

Modelling the Impacts of Predicted Environmental Change on the  
Frequency and Magnitude of Rainfall Induced Landslides in  
Central Kenya

---

Mwaniki, Mercy Wanjiru

September 2016

# Modelling the Impacts of Predicted Environmental Change on the Frequency and Magnitude of Rainfall Induced Landslides in Central Kenya

Inaugural-Dissertation

in der Fakultät Geistes und Kulturwissenschaften (GuK),

Institut für Geographie

der Otto-Friedrich-Universität Bamberg

vorgelegt von

Mercy Wanjiru Mwaniki

aus

Nairobi, Kenia

Bamberg, am 15. September 2016

„Gedruckt mit Unterstützung des Deutschen Akademischen Austauschdienstes (DAAD)“

Tag der mündlichen Prüfung: 24. Juni 2016

Dekan/ Dekanin: Prof. Dr. Markus Behmer

Erster Gutachter: PD. Dr. Matthias S. Möller

Zweiter Gutachter: Prof. Dr. Gerhard Schellmann

# Table of Contents

<b>Acknowledgements .....</b>	<b>vii</b>
<b>Dedication .....</b>	<b>viii</b>
<b>Declaration.....</b>	<b>ix</b>
<b>Disclaimer .....</b>	<b>ix</b>
<b>Abstract.....</b>	<b>x</b>
<b>Abbreviations and Acronyms .....</b>	<b>xii</b>
<b>List of Figures.....</b>	<b>xiv</b>
<b>List of Tables .....</b>	<b>xvii</b>
<b>Chapter 1: Introduction .....</b>	<b>1</b>
1.0 Introduction.....	1
1.1 Background.....	2
1.2 Problem Statement.....	4
1.3 Objectives of the Study .....	5
1.3.1 General Objective .....	5
1.3.2 Specific Objectives .....	6
1.4 Research Questions.....	6
1.5 Significance and Justification of the Study.....	6
1.6 Outline of the Research.....	8
<b>Chapter 2: Study Area.....</b>	<b>10</b>
2.1 Regional Settings .....	10
2.2 Landslide Driving Factors .....	12
2.3 Previous Landslide Studies in the Study Area.....	15
<b>Chapter 3: A Review of Landslide Mapping.....</b>	<b>18</b>
3.0 Introduction.....	18
3.1 Landslide Susceptibility Mapping Methods .....	19
3.1.1 Geomorphological Field Method.....	21
3.1.2 Combination of Maps.....	21
3.1.3 Heuristic Methods .....	21
3.1.4 Deterministic / Process- based Methods.....	22
3.1.5 Statistical Methods .....	24
3.1.6 Distribution Free Approaches .....	26
3.1.7 Empirical Analysis Methods .....	27

3.1.8 Multi-Criteria Decision Making (MCDM).....	29
3.2 Evaluation and Validation of Landslide Performance Model.....	29
3.3 The Role of Remote Sensing Data and Techniques in mapping Landslide Hazards .....	30
3.3.1 Landslide Recognition, Detection and Classification with Remote Sensing Data .....	31
3.3.1.1 Towards Automatic or Semi-automatic Detection and Classification of Landslides.....	31
3.3.1.2 Landslide Detection with Remotely Sensed Data.....	33
3.3.2 Landslide Monitoring.....	34
3.3.3 Landslide Inventory.....	37
3.4 The Role of Remote Sensing in Mapping Landslide Predisposing Factors.....	38
3.4.1 Contribution of Land-cover and Vegetation to Slope Stability .....	39
3.4.2 Geology and Lithology.....	40
3.4.3 Topographic/ Morphometric Properties .....	43
3.4.4 Geomorphology.....	44
3.4.5 Hydrology .....	45
3.4.6 Anthropogenic Factors .....	47
3.5 Landslide Triggering Factors: Rainfall .....	48
3.6 Specific Contribution of this Research to Landslide Studies.....	49
<b>Chapter 4: Land-Use Land-cover Classification, Change Detection .....</b>	<b>50</b>
4.1 Introduction.....	50
4.2 Methodology .....	51
4.2.1 Data Description and Landsat Image Enhancement .....	52
4.2.2 Knowledge Based Classification.....	54
4.2.3 Climate Variability with Rainfall and Temperature Parameters.....	57
4.3 Results.....	58
4.3.1 Land-Use Land-Cover Results .....	58
4.3.2 Post Classification Accuracy Assessment .....	63
4.3.3 Change detection.....	66
4.4 Discussion.....	70
4.4.1 Effects of Climate Variables on Land-use Land-cover (LULC).....	71
4.4.2 Land Cover/use Relation to Root Cohesion .....	74
<b>Chapter 5: Structural Geology Mapping and Lineament Visualization .....</b>	<b>76</b>
5.1 Introduction to Geology and Soil mapping.....	76
5.2 Methodology .....	79
5.2.1 Data Description.....	79

5.2.2 <i>Image Enhancement with Landsat ETM+ and OLI for Geological Mapping</i> .....	79
5.2.3 <i>Lineament Enhancement and Visualization</i> .....	81
5.2.4 <i>Knowledge Based Classification</i> .....	84
5.3 Results from Geology and Soil Mapping.....	86
5.4 Discussion.....	92
<b>Chapter 6: Landslide Inventory through Remote Sensing Image Analysis .....</b>	<b>94</b>
6.1 Introduction.....	94
6.3 Methodology .....	95
6.2.1 <i>Data Description</i> .....	95
6.2.2 <i>Image Enhancement</i> .....	96
6.2.3 <i>Knowledge-Based Classification</i> .....	99
6.4 Results.....	102
6.5 Discussion.....	112
<b>Chapter 7: Landslide Susceptibility Mapping .....</b>	<b>116</b>
7.1 Introduction to Stability Mapping.....	116
7.1.1 Methodology: CHASM.....	117
7.1.1.1. <i>Description of the Data Used</i> .....	117
7.1.1.2. <i>Combined Hydrological and Slope Instability Modelling (CHASM)</i> .....	118
7.1.2 Results.....	121
7.1.3 Discussion .....	128
7.2 Introduction to Landslide Modelling and Prediction with Artificial Neural Networks (ANN) 130	
7.2.1 Methodology: Landslide Susceptibility Mapping via ANN .....	132
7.2.1.1 <i>Data Description and Preparation</i> .....	132
7.2.1.2 <i>Landslide Susceptibility Mapping and Zonation</i> .....	134
7.2.2 Results.....	135
7.2.2.1. <i>ANN model validation</i> .....	139
7.2.3 Discussion.....	141
<b>Chapter 8: Conclusion, Recommendations and Future Outlook .....</b>	<b>144</b>
<b>References.....</b>	<b>147</b>
<b>Appendices.....</b>	<b>182</b>
Appendix A: Borehole Data.....	182
Appendix B: Description GPS landslide points.....	207
Appendix C: Curriculum Vitae.....	211

## **Acknowledgements**

I take this chance, first, to give thanks to God for bringing me this far, for the gifts of life, good health, wisdom, peace, and insights throughout the doctoral study period.

Secondly, I want to express my sincere gratitude to Privatdozent Doctor Matthias Moeller for believing in me, making me at home among his team of experts, and always working to ensure all was well and on target. Your efforts, expertise, words of wisdom, mentorship, and patience are very much appreciated. Your support has made an excellent conducive environment to bring out the very best of me in this doctorate journey. I also wish to sincerely thank Professor Schellmann, who was my second supervisor, and with whose support, comments and participation in the doctoral committee has made the research and PhD endeavour a success. I also want to sincerely thank all members of my doctoral committee, specially Professor Buchroithner who was the external examiner, and Patrick Schielein who was the rapporteur of the oral defence doctoral examination session.

I express my sincere gratitude to the German Academic Exchange Service (DAAD), in conjunction with the Kenyan National Council for Science and Technology (NACOSTI) for the financial support during my PhD research period both in Germany and for the fieldwork support in Kenya.

I also acknowledge Jomo Kenyatta University of Agriculture and Technology (JKUAT) for engaging me in the staff training programme and granting me study leave. Likewise, I greatly appreciate members of Geomatic Engineering and Geospatial Information Systems (GEGIS) department for their support, mentorship, and guidance.

I sincerely thank my friends: Nathan for always being there to offer geospatial expertise and being the first reviewer of the journal publications; Fridah and James for always cheering me on, Eric for the wonderful Berlin family; and John for always help with proof-reading of publications and thesis. Indeed, I was blessed to have all of you in my life.

The Beuth academic family: Pedro Lanz, Ulf kreuziger, Harry Ferdiansyah, Martin Grosch, Martin Vigerske, Nicole Salamanek, Prof. Ripke, and Prof. Meissner; you ensured my research environment was conducive. It was great sharing my research experience with you.

Finally, I appreciate my family, the Mwanikis: my dad Eliud for cheering me on all the way, a proud daddy; my mum Anne for the prayers, well wishes and a being role model; my sisters

Jackie and Winnie for the love, understanding, prayers and encouragement. My brother in law Isaac and nephew Gavril, your steadfast encouragement and reassurance kept me going through the hard times. My brother Ken and my nieces Jody and Fautine, your well wishes and prayers are much appreciated.

For all those who contributed to the success on my studies in one way or another, thank you very much.

## **Dedication**

I dedicate this dissertation to my family, the girl child, my mentors and those I mentor. Through the difficult times I found strength, wisdom and inspiration knowing that you believed in me and you count on me.

To those who wish to walk this journey, use time wisely knowing that the greatest enemy lies within the person you are now and the one you want to become.

## **Declaration**

I declare that this research is solely my work conducted for the purpose of PhD studies at the University of Bamberg. Therefore, this thesis has not been submitted to any other institution either in part or in whole for an award of an academic degree. All the people who assisted in the study have been mentioned in the acknowledgement. I am aware that the violation of the aforementioned conditions can have legal consequences.

Bamberg, 15th September 2016

Mercy W. Mwaniki

## **Disclaimer**

This dissertation describes the research findings as part of doctoral studies, with the guidance from the Institute of Geography, University of Bamberg. The views and opinions reflected therein are articulated solely by the author and do not necessarily reflect those of the aforementioned organisations, individuals or the institute.

## **Abstract**

The central highlands of Kenya frequently suffer the impacts of rainfall-induced landslides resulting from the interaction of slope stability and elements of environmental change (land-use and climatic variables). The impacts of rainfall-induced landslides affect the country's fight against poverty, bearing in mind the limited budgets to cope with the socioeconomic losses incurred by landslide hazards. On the other hand, a fast population growth rate puts pressure on the country's resources which is majorly agricultural based, thus contributing to more people settling on steep slopes and increasing their vulnerability to rainfall landslide hazards. Thus, this research sought to contribute to the mitigation measures by mapping the landslide areas, performing landslide susceptibility assessment, and investigating the impacts of predicted environmental change on the frequency and magnitude of rainfall-induced landslides. The role of environmental change was investigated using specific objectives which assessed the impacts of land-use on slope stability, and the impact of precipitation characteristics on landslide susceptibility. Several data types ranging from topographic, soil and geology, land-use land-cover (LULC), hydrology, and precipitation landslide controlling factors were mapped and used in the modelling process.

The methodology comprised of LULC change detection with Landsat multitemporal data for the years 1995, 2002, 2010 and 2014; structural geology and soil mapping; landslide inventory creation with Landsat multitemporal data for the years 1995, 2000, 2010 and 2014; landslide susceptibility mapping with Combined Hydrological and Slope stability Model (CHASM) and landslide modelling with Artificial Neural Network (ANN) model. The success of mapping and visualizing geology lineaments was owed to the digital image enhancement methods involving band ratioing, False Colour Composites (FCC), feature data transformation and data reduction methods of principal and independent component analysis. In addition to the feature data transformation and data reduction, the landslide inventory mapping was enhanced by utilizing a Normalized Difference Mid-Red (NDMIDR) spectral index involving Landsat geology and red bands.

The key results of this research indicated that human activities relating to land-use (mostly agricultural) did aggravate the landslide processes on the sloppy terrain. This was confirmed by the CHASM model results where forested slopes maintained low landslide susceptibility levels. In addition, the ANN model rated LULC, rainfall, and proximity to drainage network factors high in contributing to landslide occurrence in the study area. Thus, majorly shallow

types of landslides dominated, although the ANN model mapped some areas with deep-seated landslide areas along lineament features. The impacts of heavy precipitation were observed to increase slope instability, especially in bare land covers and high density drainage network areas due to rapid soil saturation, while prolonged precipitation increased infiltration thus maintaining high landslide susceptibility levels. The effects of climatic variables were associated with increased rock weathering observed on bare volcanic rocks, hence high instability rates around such areas. Landslide hazard zonation with ANN model captured several landslide types and the stability classification. The results of this study can guide targeted policies on land-use management as it has been established that rainfall induced landslides are a result of the interactions of land-use, slope and rainfall landslide conditioning factors. Moreover, creating a landslide inventory which can be updated with landslide attributes was a success since this had not been done in this geographical location to indicate the potential of landslide reactivation.

**KEY WORDS:** Landslides, susceptibility assessment, Environmental change, Landsats, Geo-hazard, Normalized Difference Mid Red (NDMIDR) spectral index, Artificial Neural Network (ANN) model, Digital Image Processing (DIP) and enhancements, Combined Hydrology and Slope Stability model (CHASM).

## Abbreviations and Acronyms

ALS	Airborne Laser Scanning
ANN	Artificial Neural Networks
AOI	Area Of Interest
ASTER	Advanced Space-borne Thermal Emission and Reflection Radiometer
AUC	Area Under Curve
AVHRR	Advanced Very High Resolution Radiometer
AVIRIS	Airborne Visible/ Infrared Imaging Spectrometer
CHASM	Combined Hydrological and Slope Stability Model
D/InSAR	Differential / Interferometric Synthetic Aperture Radar
DEM	Digital Elevation Model
DIP	Digital Image Processing
DTM	Digital Terrain Model
FCC	False Colour Composite
FOS	Factor Of Safety
GCM	Global Climate Models
GIS	Geographical Information Systems
GOK	Government Of Kenya
GPS	Global Positioning System
ICA /IC	Independent Component Analysis / Independent Component
IHS	Intensity Hue Saturation
ILRI	International Livestock Research Institute
IRS	Indian Remote Sensing satellite
km <sup>2</sup> / sq km	square kilometer
KMD	Kenya Meteorological Department
KNBS	Kenya National Bureau of Statistics
LAI	Leaf Area Index
LiDAR	Light Detection And Ranging
LULC	Land-Use Land-Cover
MSS	Multi Spectral Scanner
MTI	Multi -Temporal Interferometry
NDMIDIR	Normalized Difference Mid InfraRed

NDMIDR	Normalized Difference Mid Red
OLI	Operational Land Imager
PAN	Panchromatic band
PCA / PC	Principal Component Analysis / Principal Component
PNN	Probabilistic Neural Network
PSI	Persistent Scatterer Interferometry
RCMRD	Regional Centre for Mapping and Regional Development
RGB	Red, Green, Blue channels
ROC	Receiver Operating Characteristic
RS	Remote Sensing
SAR	Synthetic Aperture Radar
SDM	Spatial Data Modeller
SPOT	Satellite Pour l'Observation de la Terre
SRTM	Shuttle Radar Topography Mission
SVM	Support Vector Machine
SWIR	Short Wavelength Infra-Red
TCT	Tasselled Cap Transformation
TM / ETM+	Thematic Mapper / Enhanced Thematic Mapper Plus
TRMM	Tropical rainfall Measuring Mission
TMPA	TRMM Multi-satellite Precipitation Analysis
USGS	United States Geological Survey

## List of Figures

<b>Figure 1.2:</b> Graphical structure of the research flow .....	9
<b>Figure 2.1:</b> Regional settings of the study area .....	11
<b>Figure 2.2:</b> Elevation map of the study area .....	12
<b>Figure 2.3:</b> Population density map of the study area according to 2009 census .....	14
<b>Figure 2.4:</b> Slope map of the study area .....	14
<b>Figure 3.1:</b> Chart showing landslide Susceptibility/hazard assessment methods .....	20
<b>Figure 4.1:</b> False Colour Combination (a) 432, (b) 742, (c) 753 and (d) 573 .....	53
<b>Figure 4.2:</b> Spatial distribution of the meteorological stations .....	57
<b>Figure 4.3:</b> Land-cover Land-use classification map for Central Region Kenya, Year 1995.....	59
<b>Figure 4.4:</b> Land-cover Land-use classification map for Central Region Kenya, Year 2002 .....	60
<b>Figure 4.5:</b> Land-cover Land-use classification map for Central Region Kenya, Year 2010 .....	61
<b>Figure 4.6:</b> Land-cover Land-use classification map for Central Region Kenya, Year 2014 .....	62
<b>Figure 4.7:</b> Regrouped Land-covers trend for the years 1995, 2002, 2010 and 2014.....	62
<b>Figure 4.8:</b> Annual Rainfall trend (Years 1994 - 2010) .....	72
<b>Figure 4.9:</b> Maximum average annual temperature (Years 1994 - 2014).....	73
<b>Figure 4.10:</b> Minimum average annual temperature (Years 1994 - 2014).....	74
<b>Figure 5.1:</b> Summary of the methodology flow chart with Landsat 8 image enhancement .....	80
<b>Figure 5.2:</b> FCC Band ratio combination with Landsat 8	
(a) 4/2, 7/3, 6/5.....	81
(b) 4/2, 7/3*7/4, 6/5 .....	81
<b>Figure 5.3:</b> FCC {IC1,PC4, Saturation band (6,7,4)} Landsat 8 .....	82
<b>Figure 5.4:</b> Lineament map using pan-band 8 and band ratio 6/3.....	83
<b>Figure 5.5:</b> FCC PCs 3,4,5 Landsat 8 .....	84
<b>Figure 5.6:</b> Geology classification map using Landsat 8, band ratios (4/2, 7/3, 6/5) .....	86
<b>Figure 5.7:</b> Existing vector lithology map of the study area .....	87
<b>Figure 5.8:</b> Structural Geology map with Landsat 8 .....	88
<b>Figure 5.9:</b> Soil classification map .....	90
<b>Figure 5.10:</b> Existing soil texture vector map .....	91

**Figure 6.1** FCC involving Landsat:

(a) TM, year 1995 {IC1, PC4, NDMIDR}, .....	97
(b) ETM+, year 2000 {IC1, PC5, NDMIDR} .....	97
(c) TM, year 2010 {IC2, PC4, NDMIDR} .....	98
(d) OLI, year 2014 {IC1, PC4, NDMIDR} .....	98

<b>Figure 6.2:</b> Landslide mapping with Sentinel-1 SAR-C texture and roughness enhanced components .....	99
--	----

<b>Figure 6.3 (a):</b> Erodibility/landslide classification {Inputs: IC1, PC4, NDMIDR}, Landsat TM, Year 1995 .....	104
---	-----

<b>Figure 6.3 (b):</b> A blown-out section of Figure 6.3 (a) in Murang'a county overlaid with landslide GPS field landslide vector layer .....	104
--	-----

<b>Figure 6.4 (a):</b> Erodibility/landslide classification {Inputs: IC1, PC5, NDMIDR}, Landsat ETM+, Year 2000 .....	105
---	-----

<b>Figure 6.4 (b):</b> A blown-out section of Figure 6.4 (a) in Murang'a county overlaid with landslide GPS field landslide vector layer .....	105
--	-----

<b>Figure 6.4 (c):</b> A DEM Aspect map overlaid with classified landslide layer .....	105
--	-----

<b>Figure 6.5 (a):</b> Erodibility/landslide classification {Inputs: IC2, PC4, NDMIDR}, Landsat TM, Year 2010 .....	106
---	-----

<b>Figure 6.5 (b):</b> A blown-out section of Figure 6.5 (a) at Nkubu, Meru county .....	106
--	-----

<b>Figure 6.6 (a):</b> Erodibility/landslide classification {Inputs: IC1, PC4, NDMIDR, IC2}, Landsat OLI, Year 2014 .....	107
---	-----

<b>Figure 6.6 (b) &amp; (c):</b> A blown-out section of Figure 6.6 (a) in Nyeri and Murang'a counties, respectively, overlaid with landslide GPS field landslide vector layer .....	107
---	-----

<b>Figure 6.7 (a):</b> Landslide and other geomorphic processes map, from Sentinel-1 SAR-C components and NDMIDR Landsat 8, Year 2014 .....	108
---	-----

<b>Figure 6.7:</b> A blown-out section of Figure 6.7 (a): (b) Nyeri county (c) Murang'a county ...	108
--	-----

**Figure 6.8:** Identifiable landslide points on the processed satellite image

(a) Kariua road landslide .....	109
(b) Rehabilitated landslide .....	109
(c) Effect of deforestation .....	109

<b>Figure 6.9 (a):</b> The trend of landslides versus other land-uses .....	110
---	-----

(b): The trend of landslide areas .....	110
---	-----

<b>Figure 6.10 (a):</b> Landslide types extracted from Landsat classification reclassified according to other landslide factors .....	111
---	-----

<b>Figure 6.10 (b):</b> Landslide types extracted from Sentinel-1 SAR-C classification reclassified according to other landslide factors .....	111
--	-----

<b>Figure 6.11:</b> Cracks observed before landslide occurrence .....	115
<b>Figure 6.12:</b> Landslide rehabilitation efforts	
<b>(a):</b> A rehabilitated site in Karumanthi-Kathangari, Kionyo in Meru .....	115
<b>(b):</b> Possible landslide reactivation due to extra loading and shallow rooted vegetation on landslide scar .....	115
<b>Figure 7.1.1 (a):</b> Slope instability mapping, CHASM model, Nov 1997 .....	123
<b>Figure 7.1.1 (b):</b> A blown-out part of Figure 7.1.1 (a) with GPS landslides points .....	123
<b>Figure 7.1.2:</b> Slope instability trend for the epoch Oct 1997 to May 1998 .....	124
<b>Figure 7.1.3:</b> Monthly rainfall amounts in selected stations, Oct 1997 to May 1998.....	124
<b>Figure 7.1.4 (a):</b> Slope instability mapping, CHASM model, April 2010 .....	125
<b>Figure 7.1.4 (b):</b> A blown out part of Figure 7.1.4 (a) overlaid with GPS landslide points ..	125
<b>Figure 7.1.5:</b> Slope instability trend for the epoch Oct 2009 to May 2010 .....	126
<b>Figure 7.1.6:</b> Monthly rainfall amounts in selected stations, Oct 2009 to May 2010 .....	126
<b>Figure 7.1.7 (a):</b> Slope instability mapping, CHASM model, April 2015 .....	127
<b>Figure 7.1.7 (b):</b> A blown-out part of Figure 7.1.7 (a) overlaid with GPS landslides points... ..	127
<b>Figure 7.1.8:</b> Slope instability trend for the epoch February to May 2015.....	128
<b>Figure 7.2.1:</b> ANN implementation methodology flow chart .....	132
<b>Figure 7.2.2:</b> Landslide types/ stability zonation using ANN classification .....	136
<b>Figure 7.2.3:</b> Landslide susceptibility map with ANN model, year 2015 .....	138
<b>Figure 7.2.4:</b> Landslide susceptibility map with fuzzy-gamma overlay method, year 2015.....	138
<b>Figure 7.2.5:</b> Predicted landslide distribution versus GPS landslide points .....	139
<b>Figure 7.2.6 (a):</b> ANN probability model ROC curve.....	140
<b>Figure 7.2.6 (b):</b> Fuzzy overlay ROC curve.....	141

## List of Tables

<b>Table 4.1:</b> Landsat imagery scenes description .....	52
<b>Table 4.2:</b> Factor loading for PCs 1-5 for the years 1995, 2002, 2010 and 2014 .....	54
<b>Table 4.3:</b> Expert knowledge classification criteria using histogram density slicing .....	55 & 56
<b>Table 4.4:</b> Land cover area extent in percentage for the years 1995, 2002, 2010 and 2014 .....	58
<b>Table 4.5:</b> SPOT series data description. ....	63
<b>Table 4.6:</b> Error/ confusion matrix for Land-cover classification Year 1995 .....	64
<b>Table 4.7:</b> Error/ confusion matrix for Land-cover classification Year 2002 .....	64
<b>Table 4.8:</b> Error/ confusion matrix for Land-cover classification Year 2010 .....	65
<b>Table 4.9:</b> Error/ confusion matrix for Land-cover classification Year 2014 .....	65
<b>Table 4.10:</b> Cross-tabulation of classification 1995 (columns) against classification 2002 (rows) .....	67
<b>Table 4.11:</b> Change statistics extracted from Table 4.10 for the years 1995 (reference) and 2002 (classified) .....	67
<b>Table 4.12:</b> Cross-tabulation of classification 2002 (columns) against classification 2010 (rows) .....	68
<b>Table 4.13:</b> Change statistics extracted from Table 4.12 for the years 2002 (reference) and 2010 (classified) .....	68
<b>Table 4.14:</b> Cross-tabulation of classification 2010 (columns) against classification 2014 (rows) .....	69
<b>Table 4.15:</b> Change statistics extracted from Table 4.14 for the years 2010 (reference) and 2014 (classified) .....	69
<b>Table 4.16:</b> Relationship between LULC and root cohesion .....	75
<b>Table 5.1:</b> Landsat imagery scenes description .....	79
<b>Table 5.2:</b> PC Factor loading covariance-variance matrix, Landsat 8, Year 2014 .....	82
<b>Table 5.3:</b> Knowledge based classification rules with band ratios 4/2, 7/3, and 6/5 Landsat 8 ...	85
<b>Table 5.4:</b> Knowledge based classification boundaries using PCs to map Soil .....	85
<b>Table 5.5 (a):</b> Error/ confusion matrix for the Geology classification .....	89
<b>Table 5.5 (b):</b> Accuracy statistics extracted from Table 5.5 (a) .....	89
<b>Table 5.6:</b> Error/ confusion matrix for the Soil classification .....	92
<b>Table 6.1 (a):</b> Factor loading using PCs 1-5 for the years 1995, and 2000 .....	96
<b>Table 6.1 (b):</b> Factor loading using PCs 1-5 for the years 2010 and 2014 .....	97

<b>Table 6.2 (a):</b> Classification boundaries; Landsat (Years 1995, 2000, 2010).....	100
<b>Table 6.2 (b):</b> Classification boundaries; Landsat 8, Year 2014 & Sentinel-1 SAR-C .....	101
<b>Table 6.3:</b> Representation of landslide areas in percentage in comparison to other covers .	110
<b>Table 6.4:</b> GPS landslide points frequency tabulation .....	114
<b>Table 7.1.1:</b> Saturated hydraulic conductivity (Ksat) values .....	121
<b>Table 7.2.1:</b> Landslide predisposing factors reclassification and ranking .....	133 & 134
<b>Table 7.2.2:</b> Correlation matrix using the unique condition raster .....	134
<b>Table 7.2.3:</b> Landslide cells correlation to landslide causative factors .....	142

# Chapter 1: Introduction

---

## *1.0 Introduction*

Landslides are common phenomena in many parts of the world and are characterised by slope failures. They are often triggered by earthquakes, rainstorms, glacier and snowmelt, anthropogenic land-uses which interfere with slope stability, changes in pore water pressure and groundwater flow (Huang et al., 2013; Igwe et al., 2014; Pradhan and Lee, 2010a). Generally, landslide vulnerability increases with the presence of landslide predisposing factors such as faulting, steep topography and geology (Catani et al., 2011; Highland and Bobrowsky, 2008). Consequently, landslides cause deaths and enormous socioeconomic losses which are largely underestimated in many parts of the world (Akgun, 2012; Schuster, 1996). They include: loss of property and lives, loss of livelihoods, destruction of infrastructure among other detrimental impacts resulting in losses of varying magnitudes.

In particular, rainfall induced landslides are of concern to scientists and environmentalists owing to their level of destruction occasioned by the number, frequency and complexity of rainfall characteristics (Crozier, 2010; Sidle, 2007; Smith et al., 2009). The sliding mechanism of rainfall-induced landslides are further accelerated by rainfall intensity and duration, land degradation and removal of vegetation cover, water retention clayey soils, presence of perched water tables, steep topography, less cohesive soils, highly weathered rocks/soils, high density of drainage networks (Huat et al., 2006; Sidle and Ochiai, 2006; Walker and Shiels, 2013). Thus, rainfall induced landslides are related to climatic hazards, and extreme weather events (Donnelly, 2007) and are a function of environmental change.

Environmental change whether climatic or land-use may manifest changes in the size and frequency of distribution of landslides (Schlögel et al., 2011, 2013). Long-term exposure to climatic hazards which alter precipitation patterns and increase rainfall frequency and magnitude (intensity), have long-term effects and could reactivate older landslides or initiate new slope failures (Tiwari and Cepeda, 2014; Walker and Shiels, 2013). Similarly, land-use changes and anthropogenic disturbances in the form of deforestation, excavation, irrigation, and urbanization may trigger landslides on unstable slopes (Sidle and Ochiai, 2006).

Landslide processes are part of geomorphic cycles of landscape development (Korup et al., 2010) but when they interfere with human activities, they become hazardous, exposing people, infrastructure and environment to risk and making the people living in such areas vulnerable. Understanding landslides and mitigating their impacts is a serious challenge

across the world (Pradhan, 2010), which calls for scientific approaches to aid assessment and prediction of landslide mass movements in order to reduce the damages incurred, and boost preparation and mitigation measures. A variety of approaches are available to model these slope failures ranging from heuristic, deterministic, statistical, and empirical analysis (Guzzetti et al., 1999). However, the challenge is a model which can incorporate the aspects of environmental change and yet link slope stability to hydrological response. Another consideration by Bovolo and Bathurst (2012) is that although the number of landslides may increase with rainfall magnitude, rainfall frequency does not translate into landslide frequency.

The mitigation of landslides requires identification of the susceptible areas and consequently mapping the various landslide controlling factors (land use, geology, soil type, topographic attributes). This forms the basis for landslide investigation and the in-depth analysis of the processes involved during landsliding and the triggering agents. The resulting susceptibility maps are effective tools that support land-use management and decision making (Akgun, 2012), thereby guiding developments and controlling anthropogenic land-uses (e.g. road cutting, mining, deforestation) on vulnerable slopes as well as guarding the vulnerable population living in risk-prone areas.

Modelling rainfall induced landslides involve a complex analysis of the controlling factors, and understanding of the slope movements in order to map landslide susceptibility and predict landslide hazard. The quality and reliability of the landslide model is guided by the amount and quality of the data, choice of scientific method/model and the working scale (Baeza and Corominas, 2001). Geospatial technologies have greatly boosted data collection and allowed the preparation of landslide susceptibility maps with greater accuracy and efficiency (Saha et al., 2005). Remote sensing (RS) provides a means to map landslide causative factors thematic layers while Geographic Information Systems (GIS) support data management, the integration and manipulation of data (both spatial and non-spatial), computation and assignment of weight, processing platform, generation and visualization of landslide susceptibility hazard maps (Pardeshi et al., 2013).

### *1.1 Background*

The term landslide describes the movement of materials (rock, debris or earth) down a slope under the effect of gravity (Cruden, 1991; Cruden and Varnes, 1996). Various landslide types which were previously defined by the Varnes classification system (Varnes, 1978) have been updated by Hungr et al. (2014) to include the characterization of landslide material and

movement mechanisms while considering important aspects emphasized by Cruden and Varnes (1996). On the other hand, landslide undergoes several stages ranging from: pre-failure deformation and cracks, the actual sliding of the mass accelerated by gravity/slope, intense rainfall, rapid snow melting, human activities, and post failure involving flow and deposition (Hungry et al., 2014). Therefore, landslides are described by mass movement of materials in the form of flow, slide, topple/fall, spread or combination of movements (Cruden and Varnes, 1996).

Landslides can be shallow or deep-seated depending on the extent, depth or the triggering factor. Hinkelmann et al. (2011) noted heavy rainfall events, groundwater flow and pressure dynamics and vadose zone as short-term triggers, while seasonal soil moisture variations, changes in self-load, snow cover, human activities in infrastructure construction or deforestation contribute to long-term triggers. Deep-seated landslides are associated with slow movement while shallow landslides are rapid, as the main triggering factors are changes in pore pressure and heavy rains (Iverson, 2000).

Predicting shallow landslides triggered by short-term storm event can be difficult owing to the uncertainties of predicting the frequency and magnitude of extreme storm events (Coe and Godt, 2012). Godt et al. (2006) attributed changes in the frequency and magnitude of landslides to extremes in the hydrological cycle since they affect the soil moisture conditions and variation of storm scale precipitation intensity and duration. Such extremes range from prolonged and extreme rainfall events, extended drought, extreme evapotranspiration, to oversaturation which causes changes in groundwater levels, thus triggering a deep-seated landslide movement (Razak, 2014). Similarly, a further research by Randall et al. (2007) observed that changes in seasonal and annual precipitation are more likely to control deep-seated landslide occurrence. On the other hand, short-term extreme precipitation or temperature events often trigger shallow slides, rock falls and debris flows (Schmidt and Dikau, 2004; Sidle, 2007; Zêzere et al., 1999).

There is need to develop relationships between weather events (such as rainfall) and land surface response (in form of natural hazards) in order to improve the understanding of the potential impacts occasioned by changing patterns of extreme events on the society and infrastructure (Clarke and Rendell, 2006). The model should incorporate an infiltration component capable of responding to different pressure heads as controlled by soil characteristics so as to capture how precipitation events trigger shallow and deep-seated landslides (Iverson, 2000). For example, Baum et al. (2010) developed a model of the infiltration process in order to predict the timing and location of shallow landslides using a

two-layer system, i.e. unsaturated layer resting above a saturated layer. Pressure changes in the water-table placed below the saturated layer were checked as vertical infiltration diffused water in the unsaturated layer. At each cell, a factor of safety (FOS) was computed during a rainstorm while considering the initial moisture conditions and monitoring the pore pressure response.

In addition to coupled slope stability and hydrological modelling, there is need to incorporate real time precipitation and temperature data in landslide models so as to predict landslides and assist people to adapt to the impacts of climate change (Schmidt and Dehn, 2003). Thus, there is a trend to utilize regional and Global Climate Models (GCM) in landslide models which provide climatic variables and atmospheric conditions data (Coe and Godt, 2012).

### *1.2 Problem Statement*

Landslide disasters are issues of international concern due to their socioeconomic significance and the increased development pressure and urbanisation on the environment (Aleotti and Chowdhury, 1999). They pose serious challenges in developing nations, where budgets towards controlling disasters are limited or lacking (Harp et al., 2009). In addition, pressure from a rapidly increasing population, high urbanisation rates, infrastructure expansion, increasing energy demands, and the increasing demand for agricultural land-use and settlements aggravate the landslide problem, increasing pressure on the people to settle in the vulnerable areas (Beniston, 2003). Kenya (a developing country) has experienced landslide disasters in the past, with some people being buried alive in parts of central Kenya (UNDP, 2010). According to Ngecu and Mathu (1999), the impacts of the El Niño rains caused heavy economic losses, estimated at US \$ 1 billion, from which the country would take long to recover.

The need to eradicate poverty is a key development priority (GOK, 2010). Vulnerability to hazards and environmental degradation are among the greatest manifestations of household poverty and has been witnessed in the country (César et al., 2014). Census statistics show that Kenya has one of the world's fastest population growth rates, thus increasing pressure on the country's resources (Karanja and Mutua, 2000). Increased population and poverty has seen more and more people settle in the steep catchment locations and landslide prone areas. Further, human activities on the land through settlement, cultivation and deforestation, influence vegetation cover, soil texture and its organic matter content, destabilising the steep

slope areas making them more vulnerable to landsliding. By consequence, rainfall induced landslides are a serious problem to the populations living on the mountain slopes.

Climate hazards pose major challenges to Kenya's agricultural based economy and the environment (Government of Kenya, 2012; UNECA, 2013). According to McSweeney et al. (2009), Kenya's mean annual temperature has increased by 1.0°C since 1960 and it is projected to increase by 1.0°C to 2.8°C by the 2060s. This warming trend is visible with declining glacier on Mount Kenya, which has lost about 40% of its mass since 1963 (MENR, 2002). Some of the impacts of increased climate variability and extreme weather events are being witnessed in the form of recurrent droughts, changed rainfall patterns characterized by long, hot dry spells and short intense rainfall (Downing et al., 2008; UNECA, 2013). For instance, in the month of March 2010 alone, Machakos and Garrisa had recorded the total amount of rainfall normally received in the long rainy season which is March–May (KMD, 2010). Consequently, rainfall induced landslides are common in the Kenyan highlands and their frequencies are strongly attributed to the rainfall intensity (Westerberg and Christiansson, 1999).

This landslide hazard assessment study is expected to lead to the increased knowledge of landslide occurrence, provide a link between slope stability and the hydrology response in the light of changing land-use and increased climate variability, and show areas of high landslide susceptibility. Thus, by predicting areas prone to landslides, the trend of land-use as it influences vegetation cover, soil stability and erodibility has been studied to investigate its influence on the frequency and magnitude of rainfall-induced landslides. This is recommended and indeed an important factor to consider when modelling rainfall-induced landslides (Bathurst et al., 2010). Therefore, the results of the landslide hazard assessment study can assist in formulating policies on land-use which in turn can control landslide disaster and guide controlled development. In addition, by providing a landslide inventory map, the relationship between landslide controlling factors and the distribution of landslides are studied, assisting in developing mitigation measures.

### *1.3 Objectives of the Study*

#### *1.3.1 General Objective*

To model the impact of predicted environmental change on the frequency and magnitude of rainfall induced landslide in the central highlands of Kenya.

### *1.3.2 Specific Objectives*

1. To examine how human activities have affected slope stability and thus its impacts on the frequency and magnitude of rainfall induced landslides;
2. To map out geology and soil using remote sensing techniques;
3. To map out landslides and create a landslide inventory using Remote Sensing geospatial techniques;
4. To map rainfall induced landslides using a combined hydrological stability model and investigate the effect of rainfall characteristics (duration, intensity) on the landslide susceptibility;
5. To perform landslide susceptibility/ hazard zonation modelling using geospatial techniques and investigate the correlation between landslide cells and the landslide causative factors

### *1.4 Research Questions*

- To what extents do changes in land-use affect the occurrence of landslides?
- How are the changes in precipitation affecting frequency and magnitude of landslide events?
- In what ways does slope stability respond to the human activities and the changes of climate variables of rainfall and temperature?
- What are the possibilities of landslide events, and what is their spatial distribution pattern?
- Are there any relationships among landslide causative factors and the spatial distribution of the landslide/slope stability?

### *1.5 Significance and Justification of the Study*

Kenya's two thirds of the total area is semi-arid, leaving only a third for agriculture, forests and other developments. There is a high dependence on ecosystem services due to widespread poverty; evident from the change in total forest cover, i.e. 12% in the 1960s to 4.4% in 2012 (César et al., 2014). Such a low forest cover has a severe effect on the climate, water catchment areas and human population (Chacha, 2015). In addition to exposure to hazards, complex socioeconomic factors make the productive regions of the country highly vulnerable to climate driven land degradation processes. To develop robust and more responsive

landslide management system, there is need to model climate variability in order to plan for the increased uncertainty associated with climatic hazards. Success in addressing landslide susceptibility by incorporating land-use changes to assess the frequency and magnitude of landslides would also be a success on the issue of land degradation and boosting protection of three (out of five) of Kenya's water catchment towers.

Disaster and hazard management policies are vital in addressing poverty in not only catchment areas but also agricultural based regions. It would help to plan and mitigate the effects as they have impacted greatly on the country's fight against poverty and efforts to reduce the number of people living below the poverty line (GOK, 2010). Researches carried out in regard to climate change in Kenya have mostly focused on disasters of drought, food security, and floods (e.g. Rarieya and Fortun, 2009) as a result of land degradation and ecosystems, but little has been done to link land-use to landslides. This research would be helpful in formulating policies that address land degradation which is influenced by land-use, population pressure and poverty. This is important in contributing to vision 2030 as regards poverty and Kenya's economy being natural resource based.

On the other hand, the preparation of landslide susceptibility map is considered as the first step towards landslide hazard mitigation (Ercanoglu, 2005). 90% of losses occasioned by landslides can be avoided if landslide hazards are recognized before the landslide events (Brabb, 1993). This requires landslide hazard assessment maps to identify the susceptible areas and the population at risk well in advance in order to boost preparedness and mitigation measures. Consequently, the research would assist in the identification of areas where people should vacate and immediate reforestation be done to control landslide hazards. For effective and targeted policies to be developed, it is necessary to be able to identify more clearly who is at risk, where and to what extent. The results of the research could be used as basic data to assist sloppy terrain land-use management.

Landslide susceptibility maps also form the basis for assessing and evaluating landslide risks, since landslide risks are a function of the hazard, vulnerability and elements at risks (population, infrastructure or environmental features) (Courtire, 2011). This is critical for decision making in a developing country where resources are limited, yet some of its population are vulnerable to hazards which can be controlled such as landslides. Landslide susceptibility maps can also boost awareness and lead to increased knowledge about rainfall-induced landslides, which can foster preparedness and improve resilience to cope with the increasing climate variability disasters.

## *1.6 Outline of the Research*

This research study was organised using the research flow diagram as in Figure 1.1 such that:

Chapter 1 provides the framework text of the research and is comprised of the research background, problem statement, research questions, justification and significance of the study, and the dissertation structure.

Chapter 2 describes the study area; the regional settings, factors contributing to landslides, and previous landslide researches conducted within the study area and the aspects they addressed.

Chapter 3 entailed all relevant literature to landslide mapping, and the contribution of this research to landslide studies.

Chapter 4 addressed objective one and answered the research question one and partly question three; described in detail the land-use land-cover (LULC) of the study area, changes in LULC, the trends of both rainfall and LULC, and possible land degradation, possible conflicting/competing land-uses.

Chapter 5 comprised of mapping the various geological units using image enhancement techniques and Landsat datasets i.e. objective two of the research study.

Chapter 6 entailed performing image enhancement followed by knowledge-based classification that would result in a landslide inventory among other land-uses. The focus of the land-uses were related to land degradation and contribution to landslide events; thereby answering research question one and addressing objective three.

Chapter 7 comprised the landslide susceptibility mapping using the Combined Hydrological and Slope Model (CHASM) and Artificial Neural Network (ANN). The CHASM linked the ground hydrology response to slope stability. This was in line with objective four while still answering the research questions two and four. The ANN model combined the landslide factors together using a non-linear model, ANN, in order to predict future landslides, characterize landslide based on susceptibility as well as zone landslide hazard areas. This addressed objective 5 while answering research questions four and five.

Chapter 8 presented the research summary focusing on the general objective and how the research questions were addressed. Also, the conclusions and recommendations, drawn from the research were summarized.

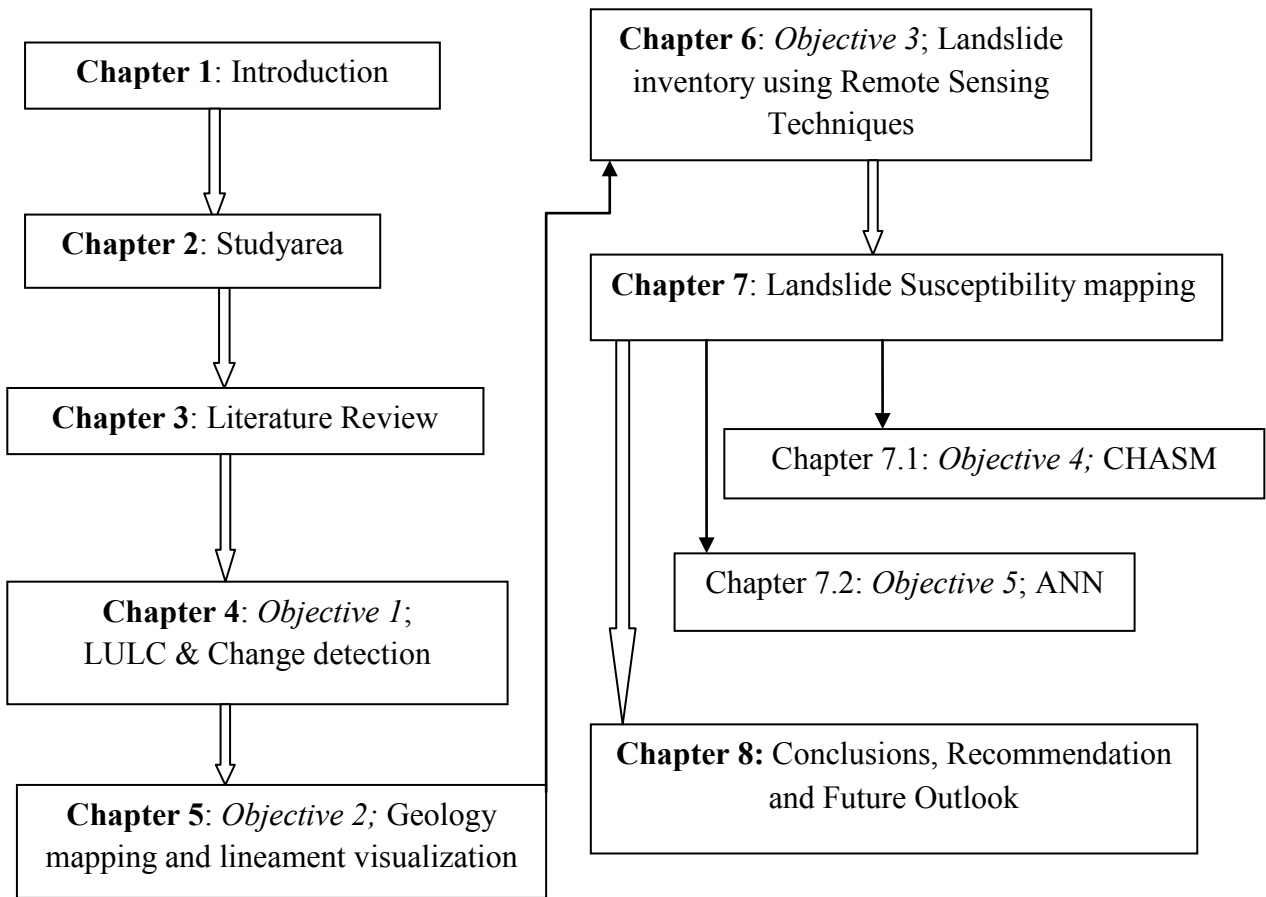


**Figure 1.1:** Graphical structure of the research flow.

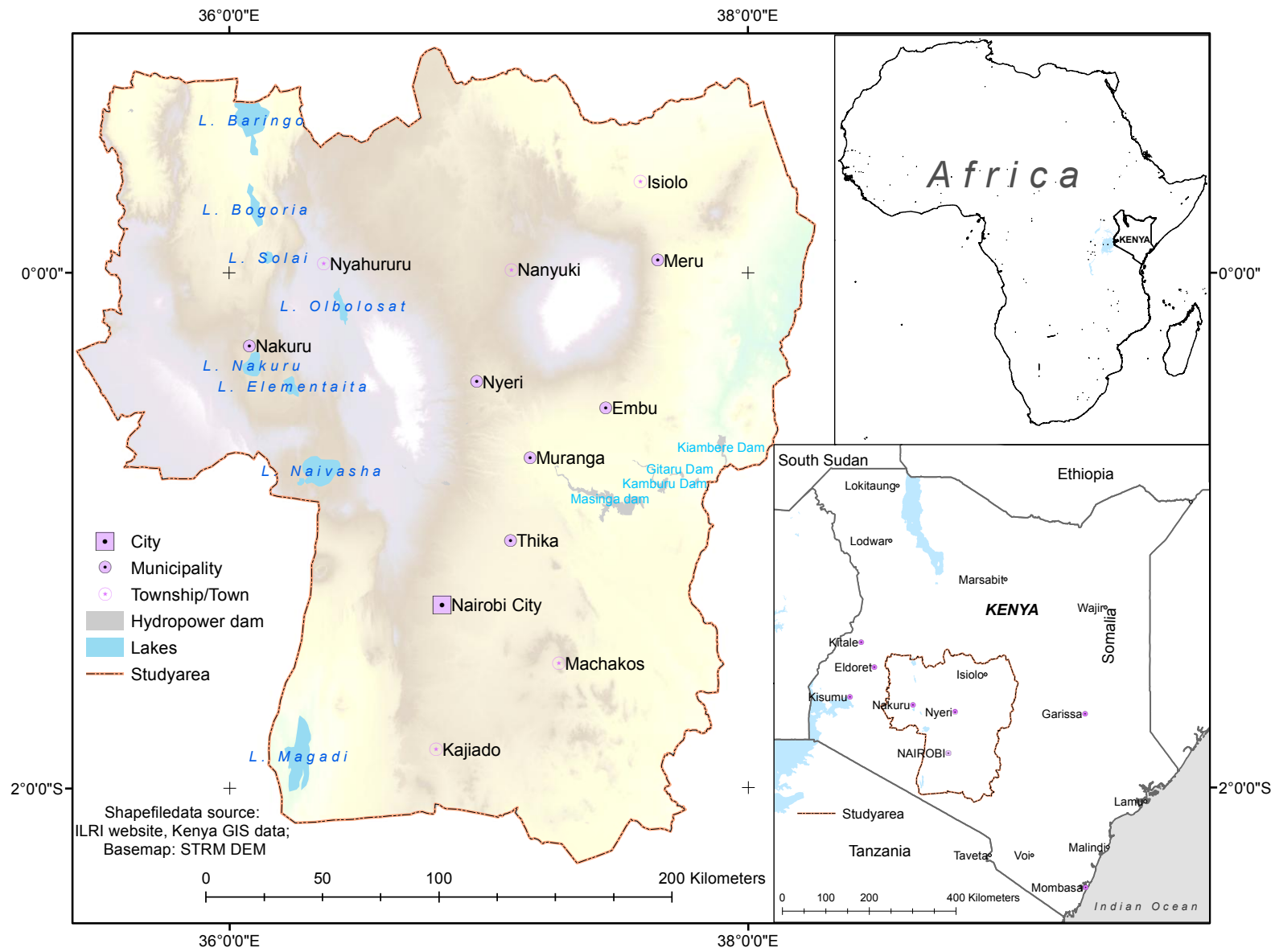
## Chapter 2: Study Area

---

### *2.1 Regional Settings*

The study area is central highlands of Kenya, covering the former Central Province, Nairobi and parts of the former Rift Valley and Eastern provinces, and it extends from longitude 35°34'00" E to 38°15'00" E and latitudes 0°53'00" N to 2°10'00" S (Figure 2.1). It has rugged mountainous terrain, with deep incised river valleys and narrow ridges in the highland regions to low-lying gentle slopes and plains in the marginal areas, and altitude varying from 397 m to 5199 m above mean sea level (Figure 2.2). Kenya's major rivers (i.e. Tana River and Athi River) originate in the study area and their major tributaries form a dendritic drainage pattern on the slopes of Mt Kenya and the Aberdare ranges. The Aberdare range constitutes the eastern rim of Gregory's Rift Valley and is exposed to the southeasterly and northeasterly winds, thus receives high orographic precipitation ranging 1100 mm yr<sup>-1</sup> at 1300 m a.s.l., to 2700 mm yr<sup>-1</sup> at 2600 m a.s.l. (Westerberg and Christiansson, 1999).

The climate of the central highlands is generally modified (tropical) by the region's higher altitude. Rainfall is fairly reliable, falling in two seasons, one from early March to May (the long rains) and a second during October and November (the short rains). Around the highland areas, the temperature ranges between 17°C to about 25°C while the average annual rainfall is about 1000 mm (McSweeney et al., 2009). The months January to February and July to September are the driest months receiving less than 30 mm of rainfall each. On the other hand, areas with savanna climate are relatively drier receiving between 50 mm to 300 mm average annual rainfall. According to Funk et al. (2010), long rains in the central Kenya region have decreased by about 100 mm since the mid-1970s and there is a drying trend which could impact densely populated areas around Nairobi. Thus, the impacts of climate change and variability are observable on rainfall and temperature parameters



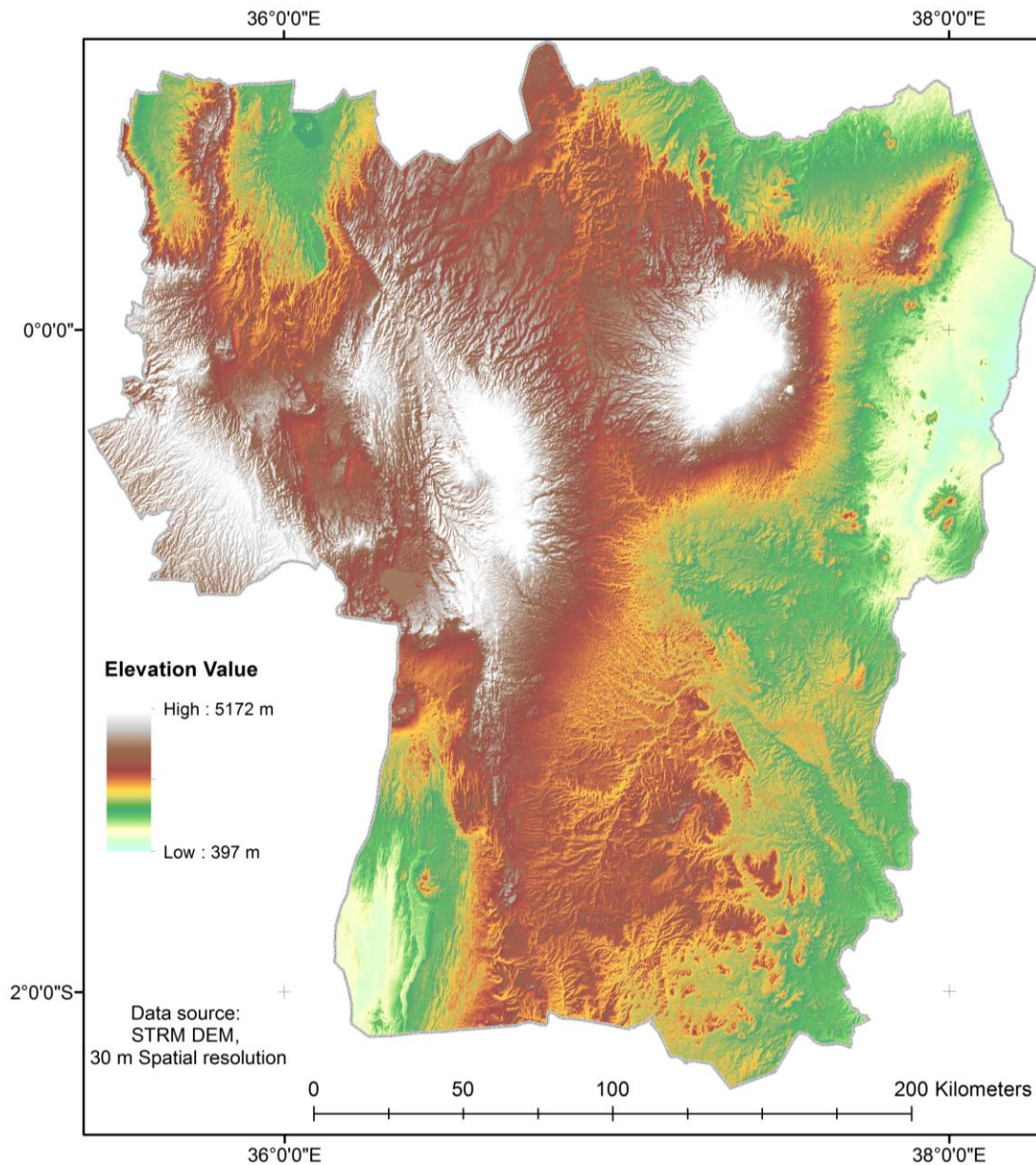


**Figure 2.2:** Elevation map of the study area.

## *2.2 Landslide Driving Factors*

In general, the central highlands of Kenya are comprised of the Neo-Proterozoic Mozambique belt rocks, the East African Rift System is associated with Tertiary volcanic and sedimentary rocks on the Rift Valley floor, as a result of faulting and rifting of the Mesozoic and Quaternary rocks, while the eastern region located east of the Rift valley is comprised extensive deposits of Quaternary sediments (Akech et al., 2013). To the East of the Great Rift Valley, volcanic activity has controlled the geologic history and geomorphological evolution. Around the Ngong area, the geology is comprised of volcanic layers of basalts, trachytes, phonolites and tuffs overlaid with a thin layer of clay soil (Mulwa et al., 2005). This forms the

ideal condition for ground water recharge where; clay water retains the water, the basalts and trachytes rocks form good aquifers, and faults filled with weathered impermeable material form excellent aquifers (Mulwa et al., 2005). Alternatively, faults can act as drains, hence lowering the groundwater table.

The geology around the former central province comprises mostly pyroclastic rocks such as tuff, agglomerates and ashes which are associated with the volcanic formation of Mt. Kenya and the Aberdare range. The interplay of heavy rainfall, steep slopes, high clay moisture absorbing andosols and the deep weathering of rocks (thereby reducing rock strength) were attributed to landslide events of 1997-1998 in the study area, according to an earlier study by Ngecu and Mathu (1999) which focussed on the geological aspects. However, the researcher also noted human activities such as alteration of natural drainage regimes, vegetation degradation on the hill slopes and slope cutting to have a landslide triggering effect. An earlier study by Ngecu et al. (2004) shows that around the Aberdare region there are three main soil types, namely: nitosols, andosols, and cambisol. Andosols are as a result of weathered volcanic material and have good physical characteristic, well drained and high available water capacity; nitosols are a result of intensive weathering of basalts and basaltic agglomerates (Davies and Nyambok, 1993).

According to the Kenya census statistics data (KNBS, 2010), the study area had a population of 14,918,698 people in the year 2009 census and the population density distribution is represented by Figure 2.3 (generated using quantile classification). The population growth rate was on the increase compared to the previous census data during the years 1999 (11,592,997 people) and 1989 (8,853,202). Moreso, the most populated areas (in Figure 2.3) were observed to coincide with the gentle to steep slopes (Figure 2.4), except for Nairobi city. This emphasized the fact that most of Kenya's population lives in the rural areas, which was estimated at 32 million (out of estimated 43 million) by César et al. (2014). The population pressure in the central highland regions has ensured rapid changes in land-use due to the need for; agricultural farming (which forms the backbone of Kenya's economy), increased infrastructure and settlements, tree harvesting to support construction as well as a source of energy (César et al., 2014; Chacha, 2015). Also, of negative impact is deforestation to allow cultivation, which loosens the soil and has led to frequent mudslides (Wendo, 2002). These anthropogenic land-uses exacerbate land degradation processes and by extension rainfall-induced landslides, which expose more people to the landslide risk (Davies and Nyambok, 1993; Mburu, 1998; Westerberg and Christiansson, 1999).

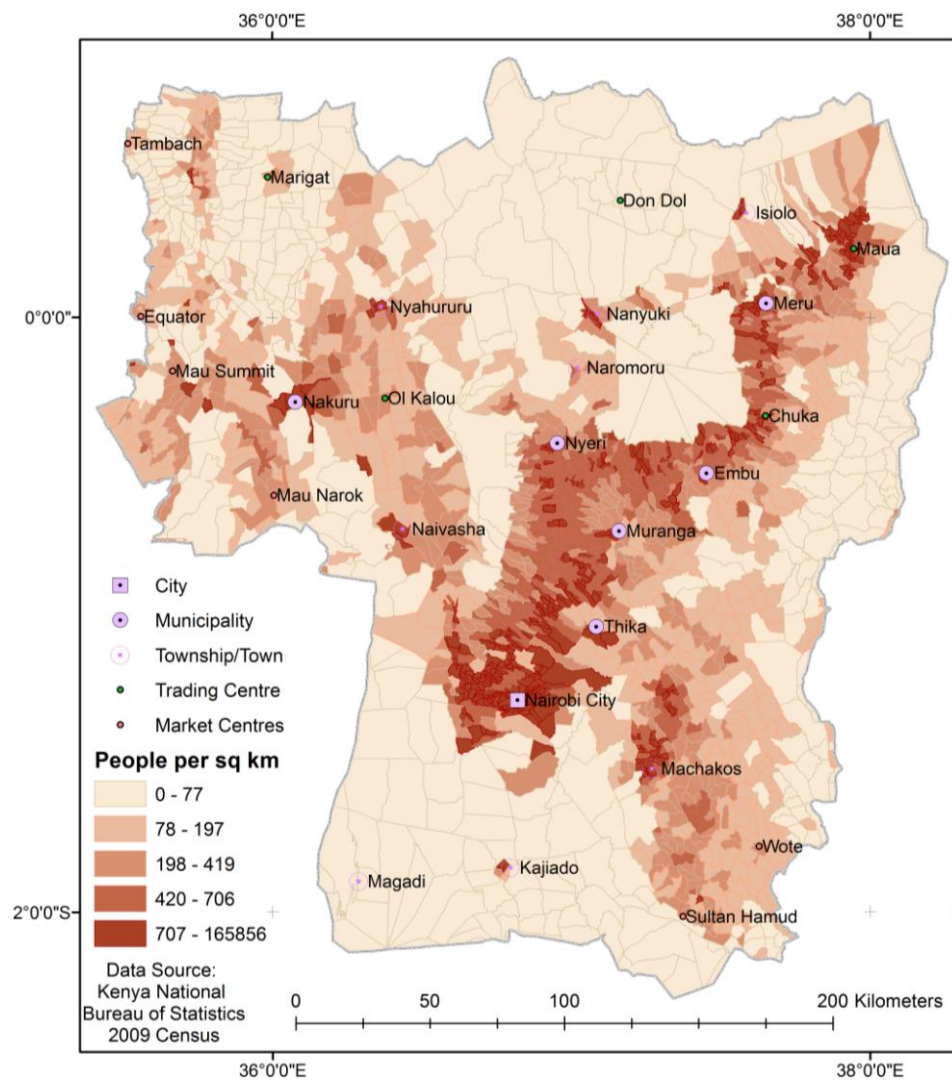


**Figure 2.3:** Population density map of the study area according to 2009 census.

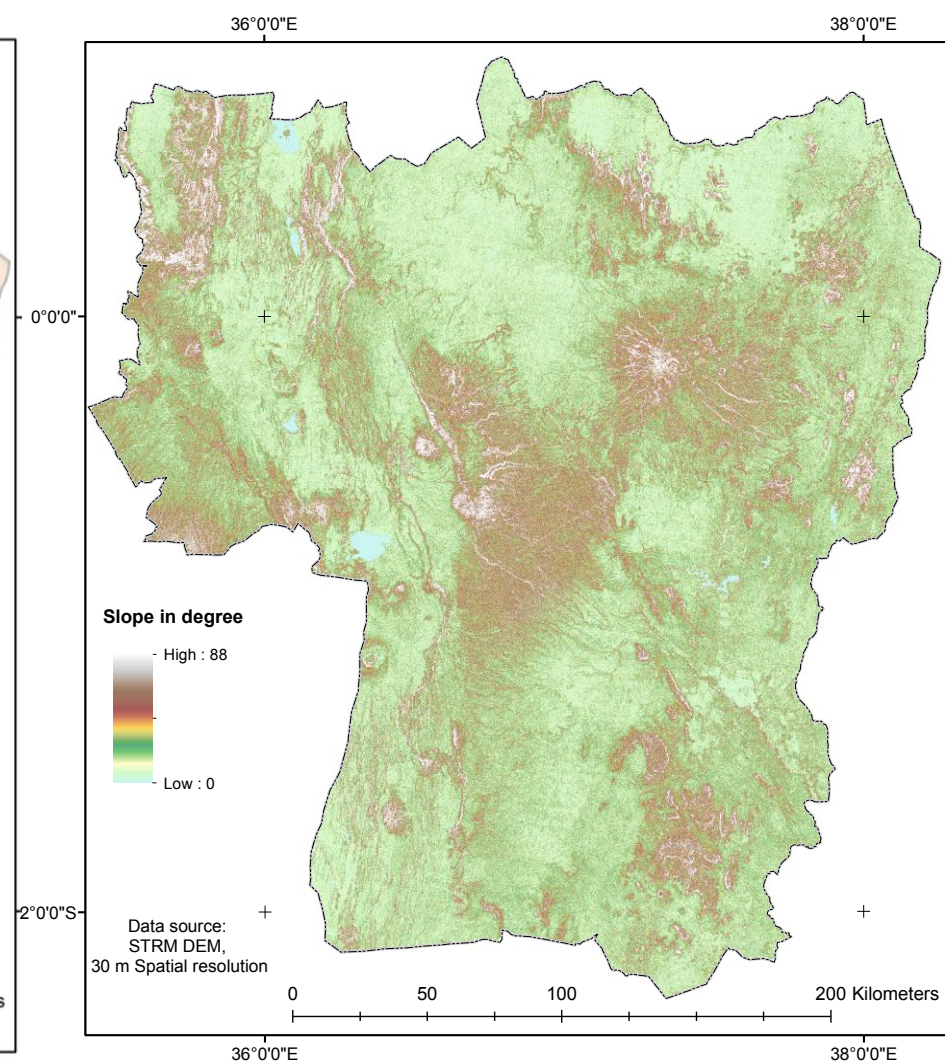


**Figure 2.4:** Slope map of the study area.

Landslides triggered by rainfall are a major threat on the south eastern slopes of Aberdare mountain ranges (Kipseba et al., 2013; Murei, 2013; Ngecu and Ichang'i, 1998; Ogallo et al., 2006), Meru County (Muthengi, 2002), Baringo and Marakwet districts in the Rift Valley (CNN, 2010; Kipchumba, 2011; Kipkiror and Towett, 2013), Yatta area in Machakos County (Ogora and Kotut, 2013), Nyandarua (Westerberg and Christiansson, 1999; Zoebisch and Johansson, 2002), Mukurweini, Nyeri County among others reported by Maina-Gichaba et al. (2013). This may be partly attributed to heavier relief rainfall on the windward side of the mountain relief features compared to the drier windy climatic conditions experienced on the leeward mountain sides. In addition, there is a changed rainfall pattern with much heavier rainfall in short durations (Downing et al., 2008). A study carried out by Makokha and Shisanya (2010) showed increased mean annual temperatures on the near earth's surface in Nairobi, which is located in the study area. This was attributed to changed land-uses, air pollution, increased population and urban and suburb development.

### *2.3 Previous Landslide Studies in the Study Area*

Existing landslide inventories are in form of reports (e.g. Njagih, 2005; OCHA, 2010) compiled using landslide incidence information collected from the National disaster operations Centre, the Kenya Red Cross Society (KRCS) and media reports. In addition, some landslide researches have recorded such landslide incidences with the aim of quantifying the aspects of landslide events and hence establish their causes (e.g. Davies, 1996; Larsson, 1986; Westerberg, 1993). Consequently, some areas in Nyeri, Muranga, Kiambu, Kijabe, Nyandarua districts and areas around Mt. Kenya, which record such incidences from time to time, have been categorised as landslide prone areas (UNDP, 2010).

A number of landslide studies have been conducted to investigate the causes, nature, and challenges resulting from landslide occurrence with a view to develop their mitigation measures. The studies range from detailed single landslide events to general overview appraisal studies which document the socioeconomic and environmental impacts of landslide events (e.g. Davies, 1996; Maina-Gichaba et al., 2013; Rowntree, 1989). For example, Ngecu and Mathu (1999) discusses in detail the socioeconomic impacts of rainfall induced landslides, which were triggered by the El-Niño rainfall between October 1997 and May 1998, in various parts of the country.

Detailed small-scale landslide studies based on field and laboratory soil geo-mechanical measurements have been conducted around Murang'a district due to the high frequency of

landslide events (Davies and Nyambok, 1993; Kamau, 1981). The results from such detailed landslide studies have shown that areas with andosol soil type around the eastern foot slope of the Aberdare ranges, which result from the rapid weathering of pyroclastic rocks under the influence of warm and wet climate, are more prone to landslides due to over-saturation of clay soils (andosol) overlying the stable basalts (Ngecu and Ichang'i, 1999). In addition, landslides and soil erosion were noted to increase with the influence of anthropogenic land-uses such as ground excavation, grazing, and poor farming practices coupled with tree felling, especially around Nyandarua region (Johansson, 1993; Larsson, 1989).

Areas which have experienced landslides in the past reveal that volcanic rocks and clayey soils overly metamorphosed basement rocks (e.g. gneiss, schist and granite) (Davies and Nyambok, 1993; Rop, 2011). These geological conditions are made more vulnerable to landslide occurrences by overlying steep slopes ( $> 70\%$ ), the interplay between rainfall characteristics (intensity and duration) and landslide predisposing factors (such as topography, hydrology, land-use, geomorphology, soil properties, and rapid weathering); have been attributed as the major cause of slope failures in the Kenyan highlands (Christiansson et al., 1993; Ngecu et al., 2004; Westerberg, 1989, 1993; Westerberg and Christiansson, 1999). Although Ngecu et al. (2004) attributes earthquakes and rainfall intensity as landslide triggers in East African highlands, the seismic activity associated with the Rift-Valley is characterized by high frequency and low magnitude events (less than 3) (Zielke and Strecker, 2009). Thus, the area is relatively stable although infrequent earthquakes could occur in the Gregory Rift-Valley, for example the Subukia earthquake (6.9 magnitude) which occurred in 1928 (Ambraseys, 1991).

Hazard assessment leading to landslide prone areas zonation was recommended by Davies and Nyambok (1993) and this was attempted at regional scale in the former central province by Mwaniki et al. (2011) using the weights of evidence statistical probability mapping. Their results showed that the probability of landslide event increased with higher rainfall amounts and non-vegetated land-use land-cover, although the effects of root cohesion were not taken into consideration. Further, the combination of the landslide factors enabled determination of stable and unstable areas during dry and wet conditions.

Morphometric GIS analysis with 36 landslides scars in a study by Wahlstrand (2015), showed that 29 landslides were within 80 m distance from the road, while only 6 landslides were within 80 m from rivers. Consequently, they attributed road drainage, overload from road

traffic, river flow or undercut to affect the occurrence of landslides. It was also evident that land-use change from forest to tea plantation, which changed forest cover from 42% in 1959 to 24% in 2012, could have contributed to increased landslide events. However their study did not conduct any susceptibility analyses due to the challenge on how to incorporate land-use data and lack of relevant data such as geology data.

Other recent landslide studies by students from the Geology department of Nairobi university, discuss in detail the landslide predisposing factors in various parts in Kenya (Kahiga, 2011; Kipchumba, 2011). Although they discuss the potential of GIS analyses in landslide hazard assessment, there is no attempt to perform any susceptibility assessment which can lead to hazard zonation. Instead, landslide susceptibility is implied using geology factor, whereby volcanic rocks are the most susceptible to landslides due to their easy of weathering. Rainfall and human activities are also emphasized as the leading triggering mechanisms.

The review of the above previous landslide studies reveals the following: that landslide inventory data is lacking the geographical spatial component which is essential to depict landslide events distribution and locations; that RS technologies have not been fully exploited to map landslide predisposing factors such as soils and geology; little has been done to model landslide hazards and perform susceptibility mapping which could guide landslide hazard zonation. Thus, this study has contributed to the increased knowledge on landslides mapping by mapping landslide factors and past landslide events, which further enabled landslide susceptibility mapping.

## Chapter 3: A Review of Landslide Mapping

---

### *3.0 Introduction*

The importance of landslide mapping cannot be underestimated given the enormous losses and damages incurred to the environment and the increasing vulnerable population. Landslide mapping may be motivated by any of the following reasons: landslide inventory, susceptibility assessment, hazard assessment/zonation mapping or risk evaluation and mitigation. Landslide inventory, distribution type of landslide map, is the simplest form of landslide map showing past and current landslides. Their significance is discussed in section 3.3. In contrast to inventories which focus on the past, hazard zonation, susceptibility maps, and risk evaluation maps are focussed into the future landslide occurrences with the aim of increasing awareness, preparedness and boosting mitigation (Hervás and Bobrowsky, 2009).

Landslide susceptibility is defined by Guzzetti et al. (2005) as the probability of landslide occurrence/slope failures, given a set of geo-environmental predisposing factors. On the other hand, a landslide hazard goes beyond the landslide susceptibility and includes the spatial distribution (location), magnitude (volume, intensity, area) and the time frame when the landslide phenomenon is expected (Guzzetti et al., 1999). Landslide risk involves measuring the likelihood and severity of the adverse consequences caused by landslide to health, property or the environment (Ercanoglu, 2008). Thus, risk analysis should involve the elements of hazard, vulnerability, and exposure (Catani et al., 2005). According to Crozier and Glade (2010), landslide vulnerability is the expected degree of loss associated with a given level of landslide hazard intensity. Therefore, vulnerability assessment requires an understanding of the elements at risk (persons or property); their location relative to the landslide, exposure; and landslide characteristics (e.g. run out distance, volume, velocity, area) (Dai et al., 2002).

This chapter aims to provide a review of landslide mapping methods, with the main focus being the importance of RS data in preparing landslides triggering and predisposing factors, source of inventory maps, use of GIS-based framework for landslide hazard assessment and modelling, and finally the contribution of this research to the existing gap.

### *3.1 Landslide Susceptibility Mapping Methods*

Landslides phenomena involve complex interrelations of various factors, and consequently no single method exists to adequately map, delineate landslide hazard and evaluate risk (Guzzetti, 2006). Instead, the choice of a landslide mapping technique is dependent on: the extent and complexity of the study area, the expertise/skills of the investigator, availability of up to date landslide inventory of the area of interest, and the available resources/data (Guzzetti et al., 2000). Generally, landslides are as a result of slope failure and thus it is assumed that they can be governed by mechanical laws using empirical, statistical or deterministic methods (Dietrich et al., 1995; Guzzetti et al., 1999).

Predicting landslide occurrence and quantifying the impact are important aspects of landslide hazard assessment (Bovolo and Bathurst, 2012). The principal goal of landslide hazard assessment is to mitigate landslide hazards and the results are the production of hazard and risk maps. The analysis of the relationship between landslides and the spatial distribution of the factors initiating landslides enables landslide hazard assessment. Thus, landslide hazard assessment requires mapping and ranking of the various slope instability factors in order to assign a hazard index (Guzzetti et al., 1999). Various landslide mapping methods are reviewed and are mainly categorized into; qualitative versus quantitative, and direct versus indirect mapping methods (Aleotti and Chowdhury, 1999; Catani et al., 2005; Kanungo et al., 2009; Pardeshi et al., 2013). A GIS enables the management of spatial data and the assessment of qualitative and quantitative aspects of landslide hazard.

Qualitative techniques are subjective in nature, in that they depend on the experts' experience and knowledge to quantify the relative importance of various landslide causative thematic layers and hence the hazard maps are shown in descriptive terms. Quantitative methods are considered more objective ways of relating landslide spatial distribution to the landslide causative factors. They result in numerical estimates/probabilities of landslide occurrence in an area. Direct mapping methods depend to a large extent on the degree of hazard and are based on the experience of the geomorphological mapper. Indirect mapping methods involve stepwise landslide hazard assessment beginning with identification and mapping of training areas (provided by landslide inventory), followed by mapping of slope instability factors, and finally generating slope failure map, according to the degree of contribution of slope instability factors and the classification into hazard zones (Guzzetti et al., 1999). Figure 3.1 is a brief overview of the various landslide susceptibility/hazard assessment mapping methods.

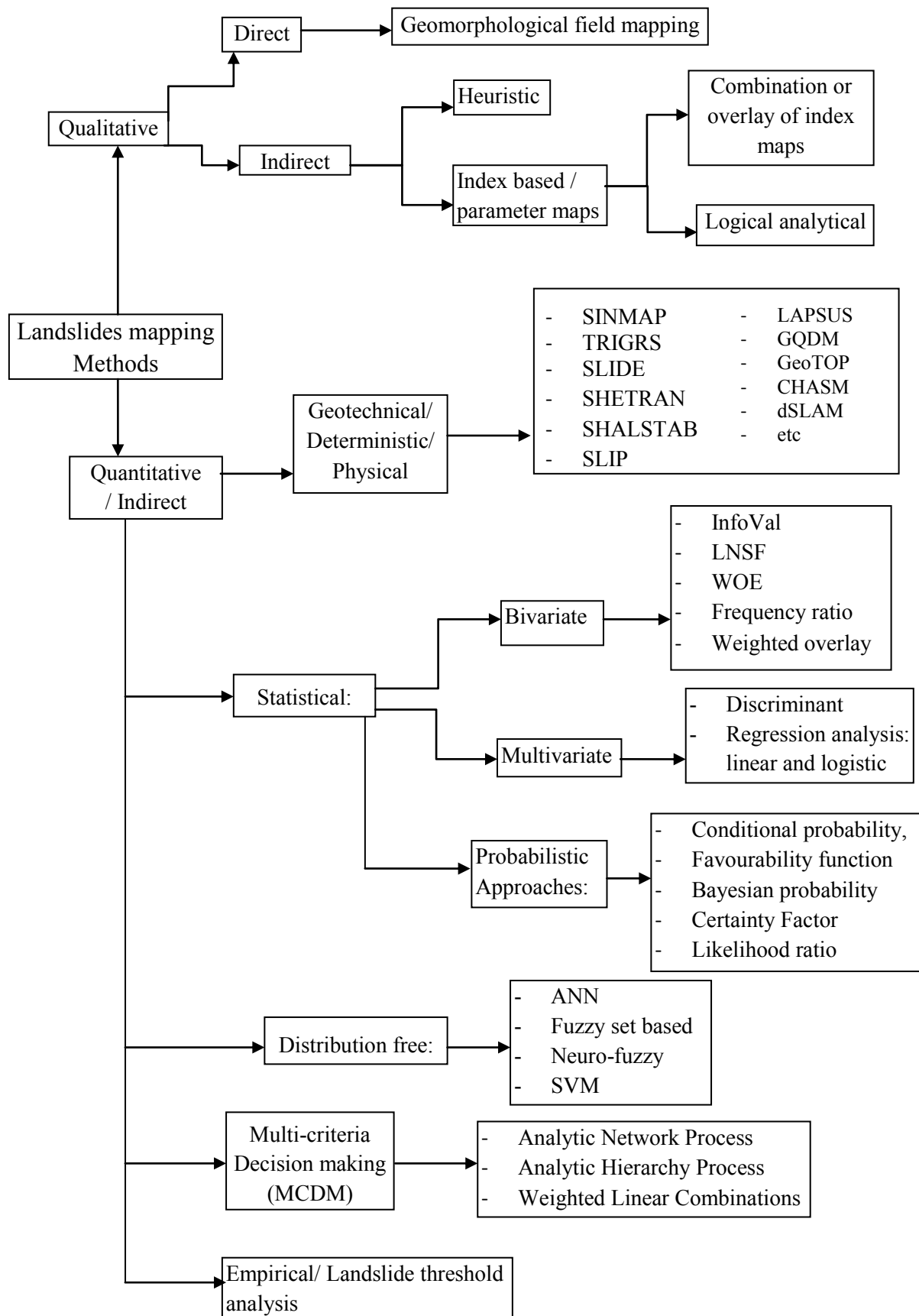


**Figure 3.1:** Chart showing landslide Susceptibility/hazard assessment methods (Source: modified from Aleotti and Chowdhury (1999)).

### *3.1.1 Geomorphological Field Method*

The method involves the direct mapping of landslides determined directly in the field by geomorphologist based on individual experience (Turner and Schuster, 1996). It is highly subjective given that there are no standard rules for the assessment (Kanungo et al., 2009). The investigator has to estimate the actual and potential slope failures based on the single particular events mapped in the field (Guzzetti et al., 1999). It is suited for single particular landslide events involving small areas as it is slow and expensive. Another challenge is mapping old landslides which is complicated by various reasons discussed in detail by Guzzetti et al. (2012), among them; vegetation regrowth, further land degradation processes dismantling the old scars, or difficulty establishing landslide boundaries.

### *3.1.2 Combination of Maps*

Index-based/ map combination approaches are indirect qualitative methods in which the expert's knowledge is applied to rank and weight landslide causative factors according to the assumed or expected importance in contributing to landslides / mass movements. Thus, they are characterized by subjective priori weight assigned to each landslide factor, where weights vary from place to place, expert to expert and hence it is not possible to extrapolate a model developed for one area and apply to another. Soeters and Van Westen (1996) have summarised the map combination steps as follows: mapping of landslide predisposing factors; categorization of each thematic layer; weight assignment to each landslide predisposing thematic layer and category; integration of the thematic layers; and production of a landslide susceptibility zonation map. Recent trends by geomorphologists is the use of Geospatial technologies of RS and GIS in preparing the landslide causative thematic layers and then using their expert knowledge to assign weights in the integration of the thematic layers (Kanungo et al., 2009).

### *3.1.3 Heuristic Methods*

Heuristic approaches are indirect landslide mapping methods where the geomorphologists/ experts are trained to detect and classify landslides from imagery based on experience, and the analysis of landslide signature (Pike, 1988). This requires training and an interpretation criterion to aid identification of landslide morphological forms using texture, pattern, colour, tone, shape, size, and topography characteristics (Antonini et al., 2002). Interpretation of aerial photographs has been the most common data source for heuristic landslide mapping. This is due to their availability, high spatial resolution, and the stereo-view capability with

additional vertical exaggeration, thereby amplifying landslide morphological/topographic signature. Interpretation of multi-temporal aerial photographs can provide essential temporal and geographical evolution of slope failure and landslide processes in an area (Fiorucci et al., 2011; Guzzetti et al., 2005).

Recent trends in heuristic/visual interpretation analysis involve use of high resolution ortho-rectified satellite images to detect and map landslides (e.g. Casagli et al., 2005; Gao and Maro, 2010; Marcelino et al., 2009; Weirich and Blesius, 2007). This presents an opportunity to map fresh landslides as well as provide complementary landslide information in areas where landslides leave clear marks. Also the use of very high resolution digital elevation models, DEMs (e.g. from Light Detection And Ranging, LiDAR) provides additional topographic and morphometric landslide characteristics by generating 3D-views in the form of hill-shaded relief, contour lines, and slope maps (Bajracharya and Bajracharya, 2008; Chi et al., 2008; Haeberlin et al., 2004; Mitasova et al., 2012; Nichol et al., 2006). Alternatively, the high-resolution DEMs from LiDAR data may be integrated with texture derived from satellite images, thus forming pseudo-stereoscopic images (Scaioni et al., 2014). High-resolution optical images such as QuickBird and IKONOS have also been used with success (e.g. Hervás et al., 2003). Other RS methods are discussed and reviewed later in section 3.3 greatly boost landslide interpretation and visualization.

### *3.1.4 Deterministic / Process-based Methods*

Deterministic models simulate the physical processes in which the slope responds to changes in ground water and rainfall, resulting in landslide initiation, subsequent slope failure and landslide occurrence. These are achieved through simple mechanical laws which evaluate stability analyses and generate a safety factor. Several methods exist for solving the safety factor, among them; infinite slope, Bishop, Janbu simplified, Morgenstein and price, Ordinary/Fellenius, Spencer, Janbu rigorous, Lowe-Karafiath, and generalised limit equilibrium method (Casagli et al., 2006). Each method has its own assumptions, hence inherent shortcomings. For example, the infinite slope model assumes that the plane of failure of the sliding mass is parallel to the ground surface. Thus, it is limited to predicting shallow landslides.

Generally, the factor of safety (stability coefficient along the slip surface) is expressed as a ratio of the available shear strength (resisting force,  $\tau_r$ ) to the shear stress (driving forces,  $\tau$ ) (Apip et al., 2010). Thus, slope failure occurs whenever the driving forces exceed the resisting forces ( $FOS < 1$ );  $FOS=1$ , indicates critical slope; and  $FS >1$  indicates stable condition. Slope

stability assessment can be calculated on the basis of static or dynamic conditions. Static conditions require the calculation of the factor of safety e.g. with a limit equilibrium stability analysis, critical rainfall. Dynamic conditions consider the changing stability condition due to changing pore pressure and the process of saturation; the velocity of the sliding mass may also be calculated. The Mohr-Coulomb failure law (Shield, 1955) is used to express the shear strength in the infinite slope model, which can be modified according to saturated or unsaturated soil conditions.

Examples of deterministic models include: Stability Index Map, SINMAP (Pack et al., 1998, 1999); Generalised Quasi Dynamic Model, GQDM (Tarolli et al., 2008); Dynamic Slope Stability Model, dSLAM (e.g. Chen and Lee, 2003); Landscape Process Modelling at Multi-dimensions and Scales, LAPSUS (Claessens et al., 2005, 2007); Shallow Landsliding Stability Mathematical Model, SHALSTAB (e.g. Listo and Carvalho, 2012; Montgomery and Dietrich, 1998); Transient Rainfall Infiltration and Grid-based Regional Slope Stability Model, TRIGRS (e.g. Baum et al., 2008; Liao et al., 2011; Vieira et al., 2010); Slope Infiltration Distributed Equilibrium, SLIDE (e.g. Liao et al., 2010); Shallow Landslide Instability Prediction, SLIP; GeoTOP (e.g. Rigon et al., 2006; Simoni et al., 2008); and CHASM (Anderson and Lloyd, 1991).

Deterministic models are complex and data intensive due to large input parameters needed by the hydrology based landslide model, laboratory test and field measurements (Crosta and Frattini, 2003; Iverson, 2000; Montgomery and Dietrich, 1994; Van Westen et al., 2006). Thus, they are recommended for detailed landslide studies limited to local extent (e.g. Ruiz-Villanueva et al., 2011). On the other hand, RS data and GIS environment can allow the models to be fed with distributed data, thereby increasing their utility to regional extents. Their added advantage is that they don't require long-term landslide inventory data. Hence, unlike quantitative methods, deterministic approaches are applicable to areas with incomplete inventories (Kuriakose, 2010).

Approaches in modelling and predicting rainfall induced triggered landslides have led to variations of physical models, incorporating stability models, hydrological models, static or dynamic conditions and probabilistic techniques in determining the factors contributing most to the hazard occurrence. This is to boost the understanding of the mechanisms involved, by allowing the simulation of pore pressure over time in the evaluation of slope stability. They enhance the estimates of landslide frequency and enable changes induced by land-use and climate variables to be obtained (Coe et al., 2004; Savage et al., 2003). This is because the

coupled hydrological-stability models capture physical processes of rain infiltration, percolation in the unsaturated zone, evapotranspiration, and ground water recharge. Other morphological and anthropogenic factors such as land-use may also be incorporated (Terlien, 1998).

Hydrological models use water infiltration models to link surface and subsurface hydrology, saturated and unsaturated soil conditions. Infiltration is considered the most important parameter in controlling pore water pressure changes and uses models such as steady-state model (Montgomery and Dietrich, 1994), a transient “piston-flow” model (Salvucci and Entekhabi, 1994), transient diffuse model (Iverson, 2000), and Richard’s equation model (water and energy budgets e.g. Rigon et al., 2006). Infiltration models enable simulation of pore water pressure while taking into account recharge, seepage, and flow.

Physically based models can also incorporate climate models as an input to assess changes in landslide activity. For example, research by Bathurst et al. (2005) used scenario runs on Hadley Centre GCM (HadRM3) for 2070-2099 in a SHETRAN physically based model and found reduced debris flow in a warmer drier climate. Tropical Rainfall Measuring Mission Multi-Satellite Precipitation Analysis (TRMM TMPA) available at 0.25° grid spatial and 3-hourly resolution obtained cumulative rainfall of the 40 days prior the landslide event. Mercogliano et al. (2013) predicted landslides using High Resolution Slope Stability Simulator (HIRESS) model based on hydrological parameters and incorporated rainfall parameters from the GCM.

Crozier (1997) emphasized the need for analysing trends in precipitation and evaluated the changes of landslide activity within the region of interest. Dikau and Schrott (1999) attributed the temporal slope instability changes to rainfall attributes (precipitation amount, frequency, duration) due to the changing climatic conditions. Their research recommended the use of hydrological factors (sudden change in permeability), mechanical factors, fissure flow and vegetation influence to be investigated in order to reconstruct a reliable landslide model reflecting the change in frequency due to changes in precipitation.

### *3.1.5 Statistical Methods*

Statistical methods are indirect and quantitative methods which aim at eliminating the subjectivity of the qualitative methods and instead compute weights using statistical techniques from landslide inventory data together with landslide predisposing factors (Aleotti and Chowdhury, 1999). The basis of landslide hazard assessments using statistical methods are landslide density distribution, and the magnitude and frequency analyses, which are

computed from the landslide inventory (Crozier and Glade, 2010; Guzzetti et al., 2005). GIS technologies have proven quite useful in these studies due to the ability to analyse spatial data, support statistical and mathematical modelling and simulation (e.g. Akgun, 2012; Neuhäuser et al., 2012; Yalcin et al., 2011).

The bivariate statistical analysis calculates the weight of each landslide causative thematic factor layer based on landslide density, derived from landslide inventory layer. The landslide density values can be computed using the following common approaches; weight of evidence (WOE) using Bayesian probability model (e.g. van Westen et al., 2003), Information value (Info Val; e.g. Jade and Sarkar, 1993), landslide nominal risk factor (LNRF; e.g. Saha et al., 2005), frequency ratio analysis approach (e.g. Karim et al., 2011), and weighted overlay model (e.g. Sarkar et al., 1995).

Multivariate statistical analyses are designed to consider the contribution of each landslide causative layer to the total landslide susceptibility (Kanungo et al., 2009) i.e. considers contributions from the relationships among the landslide causative factors, and the relationship between landslide distribution (inventory) and the landslide causative data (Pardeshi et al., 2013). Therefore, they overcome the limitations of the bivariate approaches which consider only the relationship between landslide distribution and the landslide predisposing factors. Examples of multivariate approaches are discriminant analysis (e.g. Carrara et al., 2003), regression analysis i.e. linear regression (e.g. Zhu and Huang, 2006), binary logistic regression (e.g. Ayalew and Yamagishi, 2005), and multiple logistic regression (MLR) (e.g. Mashari et al., 2012).

Probabilistic approaches are a branch of statistical analysis which computes the probability of landslide occurrence given the spatial distribution of landslides and the landslide causative thematic layers (Kanungo et al., 2009). They compute the probability of landslide occurrence based on the spatial distribution, temporal, and size of landslide events (Guzzetti et al., 2005). They include: conditional probability model (e.g. Yilmaz, 2010), Bayesian probability model (e.g. Berti et al., 2012), Poisson probability model (e.g. Guzzetti et al., 2005), certainty factor method under favorability function model (e.g. Kanungo et al., 2011), and likelihood ratio function (e.g. Lee and Min, 2001). Probabilistic approaches can also be applied within the deterministic models whereby the variability of geotechnical material parameters are considered to vary in magnitude with time (Aleotti and Chowdhury, 1999). This allows the probability density function to be computed, hence evaluate the probability of slope failure.

### *3.1.6 Distribution Free Approaches*

Distribution-free approaches are free from any distribution assumptions and they are designed to overcome the limitations of data dependent approaches (quantitative) which are highly dependent on the reliability, quality, and nature of the data (Kanungo et al., 2009). They include approaches such as fuzzy logic, ANN, and combined neural-fuzzy models.

Artificial neural networks uses artificial intelligence algorithms (i.e. mathematical methods derived from biological brain principles) to learn the behaviour of observations and extend the pattern recognition through modelling (Bhagat, 2006; Bishop, 1995; Krenker et al., 2011). ANN utilizing pattern recognition technique/clustering, essentially involves the efficient computation of the non-linear behaviour of multivariate dynamic systems without any priori assumption about data distribution. It takes into account the complex nature of landslide factors combinations and uncertainties in the landslide causative factors by computing the weights iteratively and keeping them hidden. ANN architectures allow weights adjustment correction based on the highest and training accuracies. Their resulting landslide susceptibility maps resemble the existing landslide field locations, thus in many studies they have reported satisfactory results and are recommended for landslide prediction (Arora et al., 2004; Ermini et al., 2005; Gómez and Kavzoglu, 2005; Pradhan and Lee, 2010b; Yilmaz, 2009). Another pattern recognition technique that has prediction ability like ANN, is the Support Vector machine (SVM; e.g. Peng et al., 2014).

Fuzzy logic models are intelligent systems which can capture the judgement, induction or deduction in the form of linguistic variables known as fuzzy logical rules (Saboya et al., 2006). They use the fuzzy relations to approximate expert judgement as partly true or false, while fuzzy set ensures the membership values range between 0 and 1. Thus, the inferences are mathematical operators of intersection, union, and complements, which are implemented using logical operators such as AND, OR, NOT, XOR (Vahidnia et al., 2010). They are able to capture the interrelations among landslide predisposing factors as well as the factors contributing to slope failure. However, the interrelations are largely linear models and do not support dynamic and complex interrelations for determining landslide susceptibility. Fuzzy ratings can also apply weights, thereby enabling the ranking of landslide causative factors (e.g. Wang et al., 2009). In addition, they can be implemented as purely data-driven approaches using fuzzy relations, whereby fuzzy ratings are calculated based on the actual landslide spatial data distribution while considering the relativity of the different landslide causative layers (e.g. Ercanoglu and Gokceoglu, 2004).

The Neuro-fuzzy model is an indirect quantitative landslide susceptibility method (using both data and expert's knowledge), which employs fuzzy weightings to assign membership degrees to various landslide predisposing factors and the ANN is used to solve the regression and classification problem (Elias and Bandis, 2000; Kanungo et al., 2005). The ANN's learning capability is used to automate fuzzy system, hence developing a fuzzy inference system (FIS; Vahidnia et al., 2010). The FISs are flexible, non-linear models which enable judgement "reasoning" to be applied to the data. Various combinations of landslide causative thematic layers may be tested by adjusting the fuzzy membership values and their results validated using the landslide inventory data. This adaptive Neuro-fuzzy inference system (ANFIS) has been used with success, although the success of the predictive capability depends on the membership functions used in the fuzzy membership (Tien Bui et al., 2012). Consequently, it is recommended for regional landslide susceptibility mapping, where the model applies all the landslide causative thematic layers (Oh and Pradhan, 2011; Sezer et al., 2011).

Another variation of combined Neuro-fuzzy model was implemented by Vahidnia et al. (2010) and it involved the stepwise mixing the quantitative and qualitative approaches. In the first step, the outputs from FIS were integrated into landslide depth intensity value. This was followed by training the neural network to solve the regression problem between landslide susceptibility and landslide predisposing factors. Lastly, the model was generalized to the entire study area.

### *3.1.7 Empirical Analysis Methods*

Empirical methods involve determining rainfall threshold values, beyond which, when exceeded, landslides are bound to be initiated (Reichenbach et al., 1998). Past landslide records together with rainfall characteristics of duration ( $D$ , in h) versus intensity ( $I$ ,  $\text{mm h}^{-1}$ ) or event-cumulated rainfall ( $E$ , in mm) are used to a construct landslide triggering equation. An example of such an equation which relates duration and intensity is  $I = c + \alpha D^\beta$ , where:  $\alpha$  and  $\beta$  are parameters,  $c$  is a constant (Guzzetti et al., 2007b). The empirical computation involves studying past landslides and therefore assumes that a landslide event in the future occurs under similar triggering conditions (Guzzetti et al., 2007a). This requires detailed temporal landslide records to link meteorological data to landslide events, which in most cases are incomplete or missing (Coe et al., 2004).

Empirical models based on a local scale (e.g. Vennari et al., 2014) perform better than regional (Guzzetti et al., 2007b; Reichenbach et al., 1998) and global scales (e.g. Caine, 1980) as other landslide predisposing factors differ with location (Sidle and Ochiai, 2006).

Empirical models involving heavy-event rainfall parameters are better suited for predicting shallow landslides as opposed to deep-seated landslides which may incorporate seismic data. They can be used with rainfall radar data to predict landslide occurrence, although predicting the exact landslide location poses a challenge (Walker and Shiels, 2013).

Rainfall parameters involving intensity, duration, cumulative or antecedent rainfall are the most commonly used threshold parameters for rainfall-induced landslides. However, other thresholds could also be used, such as: critical pore water pressure, slope angle, reduction of shear strength or minimum displacement for landslides to occur (Reichenbach et al., 1998). Slope stability models could also be used with critical FOS boundaries defined, allowing the safety factor equation to be resolved backwards to derive the critical pore pressure.

Empirical models could be improved by accounting other landslide predisposing factors such as soil geotechnical properties and soil moisture. For example, Ruiz-Villanueva et al. (2011) measured soil hydrological characteristics and incorporated them into a slope stability model “Generalized Quasi-Dynamic model” (GQDM) to estimate the critical rainfall intensity threshold which could be used as a predictive tool for areas prone to shallow landslides. Peres and Cancelliere (2014) combined rainfall and hydrological and slope stability physical model using Monte Carlo approach to simulate both triggering and non-triggering rainfall events, which were later analysed by receiver operating characteristics (ROC) curve to derive stochastic-input physically based thresholds.

Empirical models have been criticised on the basis of failure to provide the actual physical process which trigger landslides i.e. no relationship between infiltration and rainstorm pattern (Tsai, 2007). Instead, landslide occurrences are related to values of rainfall amount greater than the minimum triggering rainfall duration threshold. However, they have been tested for real time landslide modelling with rainfall as the dynamic variable along with other landslide predisposing factors as static variables in logistic regression approaches (Takara et al., 2010). Another criticism is the lack of temporal component which is crucial for assessing landslide hazards under changing environmental conditions. Therefore, physical models which can model minimum triggering conditions and magnitude of landslides are recommended since they consider the spatial and temporal frequency of a landslide (Terlien et al., 1995). For example, Bovolo and Bathurst (2012) using a SHETRAN model showed that although the number of landslides increased with rainfall magnitude, rainfall frequency did not translate into landslide frequency. Their research showed the importance of the ability to quantify the triggering condition and the extent of landslide occurrence as a function of the rainfall return

period, which increases the possibility of issuing warnings of landslide severity based on the weather forecast.

### *3.1.8 Multi-Criteria Decision Making (MCDM)*

Multi-criteria decision-making approaches are considered as semi-quantitative heuristic methods as they involve expert judgment to derive priority scales while using quantitative approaches to determine the relative contribution of each landslide causative thematic layer (Pardeshi et al., 2013). They include: Analytic Network Process (ANP; Neaupane and Piantanakulchai, 2006), Analytic Hierarchy Process (AHP; Yalcin, 2008), and weighted linear combination models in GIS (Ayalew et al., 2004). Unlike heuristic approaches, they are effective for medium scale landslide susceptibility studies (Akgun, 2012; Ayalew and Yamagishi, 2005; Guzzetti et al., 1999).

### *3.2 Evaluation and Validation of Landslide Performance Model*

Landslide model quality evaluation may involve three aspects: accuracy, robustness (data sensitivity) or adequacy in describing the landslide process. Accuracy in predicting the observed data is rated as the most important evaluation parameter and it involves analysing the agreement between the model results and observed data (Frattini et al., 2010). The observed data is the landslide inventory, showing the presence or absence of landslides. Predicting the presence or absence of a landslide can be judged by the number of prediction errors; false positives or false negatives. The false negative (error type II / omission error) occurs when a landslide area is identified as stable, whereas the false positive (error type I / commission error) occurs when stable area is identified as landslide area (Frattini et al., 2010). Some prediction errors may be traced to the data, and the chosen landslide model, thus the results of the model can be misleading (Fielding and Bell, 1997).

Although the true positive rate and false positive rate can be used as performance evaluators (e.g. Brenning, 2005), they are insufficient as they ignore false negatives and false positives (Frattini et al., 2010). Instead, ROC curves which use both true positive rate and false positive rate are preferred. The greater the value of the area under the ROC curve (AUC), the better the model in predicting landslides accurately (Chung and Fabbri, 2003) and the similar the ROC curve is to a diagonal (trivial model), the higher the probability of landslide classification by chance (Frattini et al., 2010). At a perfect diagonal ROC line, the AUC is equivalent to 0.5, whereas high accuracy prediction values are achieved when the AUC approaches 1.

On the other hand, Success-Rate (SR) curves are a graph of correctly classified landslide units (y axis), against the percentage area classified as unstable (x-axis) (Chung and Fabbri, 2003; Frattini et al., 2010). A Modified Success-Rate (MSR) was developed by Huang and Kao (2006) so as to avoid over and under prediction with the Success-Rate ratio/curve. The x-axis of the MSR is the total landslide sites in both actual landslide sites and in the stable cells. The economic consequences of landslide susceptibility maps are increased economic value for misclassified stable areas and decreased economic value for landslide areas/unstable areas (Fielding and Bell, 1997). The costs of misclassification can be analysed with cost curves (Drummond and Holte, 2000).

Other evaluation statistics are k-index (Landis and Koch, 1977), and cutoff dependent evaluation metrics criticized by Frattini et al. (2010) on the basis of splitting the cells/objects into stable or unstable susceptibility values, namely: Threat score, Gibert's skill score, Pierce skill score, Heidke skill score and Yule's Q. The Kappa statistic can also be used as it gives the measure of agreement between observed and predicted data, taking into account chance agreement with the prediction (Carletta, 1996). However, the Kappa statistic is criticized in landslide model evaluation as it gives inconsistent performance when landslide coverage changes (Huang and Kao, 2006).

Remote sensing landslide inventory records can also be used for validation/landslide model calibration by using them as training data and performing back analysis (Scaioni et al., 2014). Also, comparing known landslide locations with a landslide susceptibility map to evaluate overlap areas, boundaries, or simple statistics such as area ratio or pixel fraction, can provide validation for geo-statistical landslide models (e.g. Lee, 2005). Monitoring slow moving landslides data from Interferometry Synthetic Aperture Radar (InSAR) techniques can also be used for calibrating landslide models in order to forecast landslide hazards (e.g. Bai et al., 2012).

### *3.3 The Role of Remote Sensing Data and Techniques in mapping Landslide Hazards*

Remote sensing datasets are a powerful data source for landslide visualization through heuristic approaches. For instance, optical aerial photography and its interpretation are the most suitable methods for benchmarking/validating landslide maps obtained through quantitative methods (Guzzetti et al., 2012). The role of RS in landslide studies is grouped into three categories: (i) recognition, detection and classification, (ii) monitoring, and (iii) forecasting, landslide susceptibility or hazard assessment (Mantovani et al., 1996; Metternicht

et al., 2005; Qiao et al., 2013; Scaioni, 2013; Scaioni et al., 2014). These roles are closely interrelated as each role provides data for the proceeding step, i.e. monitoring requires accurate information on landslide locations, while landslide forecasting models require both landslide inventory and monitoring data.

The following section describes in detail the roles of recognition, monitoring, and inventory mapping where RS is directly involved. Besides, RS provides essential thematic data which are integrated within the GIS to process landslide susceptibility/hazard maps. Therefore, RS plays a critical role and its potential in landslide investigation has increased (Farina et al., 2005). This role is discussed independently in section 3.4.

### *3.3.1 Landslide Recognition, Detection and Classification with Remote Sensing Data*

The role of RS techniques in enabling automatic or semi-automatic recognition of landslide morphometric features has achieved a great milestone in landslide studies boosting both landslide monitoring and hazard assessment. However, the automated recognition is only possible by assuming that landslides often leave identifiable change in the morphology (morphological signature; dependent on the rate and type of movement), which can be mapped in the field or by RS methods (Cruden and Varnes, 1996; Dikau et al., 1996). Other identifiable changes at the surface or subsurface are land-use, geology, and lithology (Guzzetti, 2006).

The automated recognition of landslide features has been facilitated by the availability of various data types (e.g. LiDAR, multispectral, very-high resolution optical or Synthetic Aperture Radar, SAR), digital image processing (DIP) which enhance visual interpretation, statistical analysis of landform topographic attributes (e.g. gradient, convexity, texture, curvature), standard signal processing (e.g. discrete Fourier transform, continuous wavelet transform), and feature extraction methodologies which facilitate classification (Guzzetti et al., 2012; Scaioni et al., 2014). While automation can be fully or semi automated, many proposed solutions are still more semi-automatic than fully automatic. The quality of the final products obtained through semi-automatic methods is dependent on the pre-/processing steps such as image registration, panchromatic (PAN)-sharpening, or ortho-rectification (Behling et al., 2014).

#### *3.3.1.1 Towards Automatic or Semi-automatic Detection and Classification of Landslides*

Satellite imagery processing can lead to the automated landslide recognition and detection using methods such as index thresholding (Rosin and Hervás, 2005), image fusion

enhancement methods (Marcelino et al., 2009), band ratios (Cheng et al., 2004), colour composites (Petley et al., 2002), texture image analysis (Whitworth et al., 2005), and filtering (Haeberlin et al., 2004). These DIP image enhancements lead to more accurate landslide recognition and classification utilizing semi-automatic classification algorithms (Mondini et al., 2011a). For example, Spectral Angle Mapper (SAM) supervised classification and Normalised Difference Vegetation Index (NDVI) thresholding reported higher accuracy compared to parallelepiped, the minimum distance to mean, principal components (PCs), and multi-temporal image differencing in mapping landslides (Joyce et al., 2008a, 2008b).

Landslide recognition based on pixel-based classification, automatic algorithms (supervised or unsupervised clustering (e.g. Borghuis et al., 2007)) and change detection techniques have been exploited in the past, although their major limitation is failure to consider neighbourhood information (Scaioni et al., 2014). Change detection by differencing pre- and post-landslide disaster spectral indices or processed image bands can map landslides and land-cover changes, although image pre-processing (radiometric and geometric correction) influences the quality of the results (Cheng et al., 2004). Multi-temporal change detection with vegetation index, followed by thresholding methods based on after event vegetation change analysis is a rapid pixel based landslide mapping method (Yang and Chen, 2010).

For example, the NDVI method was used to detect fresh translation, mass movements of debris flows and earth flows (Chang and Liu, 2004; Schlögel et al., 2011; Zhao et al., 2012b). This method was successful in detecting both re(activation) of landslides and stabilizing slopes (marked by new vegetation), although Schlögel et al. (2011) noted that it is not suited for creating a landslide inventory. Mondini et al. (2011a) using a three change detection layer comprised of change in NDVI, independent and principal components, differentiated between stable areas and unstable areas (based on vegetation), and discriminated old and new landslides. The method also differentiated run-outs or sediment deposits from debris flows.

Thresholding techniques may involve the use of band ratios or spectral indices (e.g. NDVI; (Liu et al., 2002), Normalised Difference Mid-InfraRed (NDMIDIR; Vohora and Donoghue, 2004)), since they depict changes in the land surface characteristics (land-cover, geology) due to geomorphic processes such as landslides. However, the landslide signature is not unique and they must be distinguished using other data, such as DEM morphology signatures (e.g. Borghuis et al., 2007). Vegetation indices are especially recommended for investigating deep-seated landslides since they are covered by vegetation (Scaioni et al., 2014). Indices and band ratios also help solve the difference in illumination or shadowing problems in mountainous

terrain areas. In addition, threshold values can be set to indicate where major or minor changes have occurred (e.g. Teng et al., 2008).

To overcome the limitation of pixel based systems, the current trend is to utilise classification algorithms which allow integration of various data types, even allowing pseudo-stereoscopic images, e.g. object-oriented image classification methods (Lang, 2008; Lu et al., 2011; Martha et al., 2010, 2012; Moine et al., 2009; Stumpf and Kerle, 2011), ANN classifier (e.g. Brown, 2012; Gorsevski et al., 2015), and SVM (Marjanović et al., 2011). Such methods allow processed topographic signatures from DEM or texture data to be used in the classification of aerial photos or multispectral satellite imagery, thereby providing unique differentiation of landslides from other geomorphic land processes. Geomorphic feature extraction with high resolution DEMs are also explored for automatic landform detection, recognition and classification using topographic signatures, and processes such as segmentation, thresholding, and classification (Catani et al., 2005; Drăguț and Blaschke, 2006; McKean and Roering, 2004; Passalacqua et al., 2014; Tarolli, 2014; Tarolli et al., 2012). The use of high resolution DEMs is particularly recommended since landslides involve geomorphic processes which are better captured using geomorphological indicators such as breaklines (Mann et al., 2012).

#### *3.3.1.2 Landslide Detection with Remotely Sensed Data*

Landslide detection is largely dependent on the visual interpretation of satellite imagery of which optical data have provided more reliable results compared to SAR data (Joyce et al., 2009). This is attributed to higher spectral resolution and the sensor look angle provided by optical data, compared to SAR data which suffers extreme layover effects and shadowing in areas of high slope angle, where landslides and slope failures are prone (Zinck et al., 2001). For instance, the performance of IKONOS high resolution satellite imagery was rated equivalent or superior to ortho-photography in landslide mapping (Nichol and Wong, 2005a). The availability of high resolution satellite imagery, both PAN and multi-spectral scanner (MSS) has enabled detailed geological, topographic, and landslide mapping (e.g. De La Ville et al., 2002). For example, Schlögel et al. (2011) used QuickBird imagery to detect changes on the surface aided by the difference in morphological (texture) and spectral reflectance properties along discrete boundaries that result from landslide mass movement.

Multispectral medium resolution satellite imagery (e.g. Landsat Thematic Mapper (TM) / enhanced Thematic Mapper plus (ETM+) / Operational Land Imager (OLI), SPOT series and Indian Remote Sensing satellite, IRS-1) is essential for mapping landslides in non-vegetated

areas. However, advances in image enhancement techniques with multispectral imagery, have been explored for landslide applications, with vegetation stress indicators, image fusion with high resolution imagery, and geology enhancement DIPs being used to enhance landslide scars, since they are geo-hazard phenomena (Barlow et al., 2003; Li et al., 2013; Mondini et al., 2011b; Perez et al., 2006). Advanced Space-borne Thermal Emission and Reflection Radiometer (ASTER) enabled stereo capability facilitates mapping and assessment of volume changes and mass movements.

Analysis of high quality DEMs such as those provided by LiDAR data are important data source for the mapping landslide of various categories, namely: deep-seated landslides (Kasai et al., 2009), complex landslides (Corsini et al., 2009), rock slides (Oppikofer et al., 2009), rock falls (Royán et al., 2014), shallow landslides (Đomlija et al., 2014), and debris flows (Bull et al., 2010). However, the cost of LiDAR data has remained a limitation to landslide mapping. Instead, stereo viewing capability with IKONOS and QuickBird satellite sensors, which provide high-resolution DEMs are recommended (Joyce et al., 2009; Nichol et al., 2006). Another alternative source of elevation data is SAR sensors such as the German TanDEM-X mission availing global DEM at 12 m spatial resolution (Guzzetti et al., 2012).

Thermal infrared data is an indicator of high hydro-geological risk, depicting land surface temperature at different slope parts, which in turn show the status of soil moisture and groundwater circulation (Bison et al., 1990). It also provides ground surface information which is not recognisable in the visible region (Whitworth et al., 2005). However, there is difficulty in obtaining high spatial resolution thermal data, which is expected to improve with the use of passive microwave RS data (Shi et al., 2012) or the availability of Sentinel 3 data (European Space Agency, 2015). Another challenge with temperature data in landslide investigation, is the fact that temperature data is a highly variable parameter; varying with changes in altitude, LULC, time of the day, climate, and topographic attributes of slope and aspect.

### *3.3.2 Landslide Monitoring*

Landslides monitoring entails tracking the failure process for regions prone to slope failures with time and updating landslide inventories with the measurements of ground deformation and surface point displacement (Sassa et al., 2009), which are very crucial for landslide hazard assessments (e.g. Farina et al., 2006; Righini et al., 2012). Other aspects that can be monitored for landslide triggering conditions are groundwater table level and geotechnical properties. RS techniques provide essential data for quantitatively measuring slope conditions

using optical very high-resolution images, LiDAR or SAR data. Techniques that have been used successfully to measure horizontal displacement with repeated optical images are digital image correlation (e.g. Casson et al., 2003) and least squares matching (e.g. Debella-Gillo and Käab, 2012). A 3D view is possible by projecting the 2D surface displacement using heights obtained from high-resolution DEM (Travelletti et al., 2012).

Airborne laser scanning (ALS) allows topographic, and morphological analysis, and provides essential vegetation and underlying terrain data, including; surface roughness, slope, and fractal dimensions (Razak, 2014). ALS forest foliage penetration power, independence to solar incidence, and ability to generate high-resolution Digital Terrain Model (DTM) has made it superior over passive optical and active radar sensors for mountainous terrain (Van Den Eeckhaut et al., 2007; Hodgson et al., 2003; Kraus, 2007). Therefore, ALS has opened new channels, facilitating landslide; detection, characterization, hazard assessment, modelling, and monitoring (Bitelli et al., 2004; Derron and Jaboyedoff, 2010; Jaboyedoff et al., 2012; Lin et al., 2013; Prokop and Panholzer, 2009; Rohrbaugh, 2015; Royán et al., 2014; Teza et al., 2007). The challenge with ALS data remains the high cost of acquisition, making it unavailable for large areas. This challenge can be overcome by utilizing elevation data obtained from SAR sensors, such as the German TanDEM-X mission availing global DEM at 12 m spatial resolution (Guzzetti et al., 2012).

Multi-temporal analysis of the same area with LiDAR data are excellent sources of quantitative landslide volume estimates (Baldo et al., 2009; Passalacqua et al., 2014). Derivative products from LiDAR DEMs, facilitate not only visual analysis of the topographic surface, but also semi-automatic recognition of morphometric landslide features through feature extraction methodologies (e.g. Passalacqua et al., 2010; Tarolli et al., 2012). Visual analysis of LiDAR DEM has also enabled various landslide types to be mapped with success, i.e. deep-seated, shallow, debris flow, recent, old, under forested or in cultivated areas (Ardizzone et al., 2007; Chigira et al., 2004; Van Den Eeckhaut et al., 2007; Kasai et al., 2009; Razak et al., 2011). This is attributed to the high quality DEM provided by LiDAR as compared to InSAR DEM (Norheim et al., 2002).

Laser scanning techniques suit monitoring applications, especially when integrated with other RS data for the characterization of steep slopes (Jaboyedoff et al., 2012). For example, Pesci et al. (2013) determined the velocity of surface displacements on the Italian volcano slopes by comparing multi-temporal terrestrial laser scanning data integrated with airborne photogrammetry. Similarly, the integration of terrestrial and ALS data from a study by

Ghuffar et al. (2013), was successful in monitoring landslide displacement using 3D range flow algorithms on an active landslide slope in Austria.

Synthetic aperture radar data provide textural and topographical data of the ground surface, since radar waves respond to both chemical and physical characteristic of the soil, hence making it important in the mineral, lithological, and geological exploration (Rawashdeh et al., 2006). In landslide investigation, radar interferometry has proved a good method for monitoring slow moving landslides, monitoring past-landslides deformation, as well as updating landslide inventory maps (Bardi et al., 2014; Cascini et al., 2010; Greif and Vlcko, 2012; Squarzoni et al., 2003; Del Ventisette et al., 2014). This entails measuring displacements, velocities or rate of displacement, mapping new landslide boundaries and the directions in which the landslides are moving towards (Czuchlewski et al., 2003; Hilley et al., 2004; Singhroy, 2013).

Synthetic aperture radar interferometry technique enables landslide displacement measurements by computing the interference pattern resulting from the phase difference of two SAR images of the same area (Yonezawa et al., 2012). Since the phase difference contains possible ground displacement among other contributions (e.g. terrain roughness, atmospheric effects, noise) in the line of sight, differential InSAR (DInSAR) have been utilised to model and extract displacement, while filtering out unwanted effects (Wasowski and Bovenga, 2014). Such unwanted effects resulting from temporal and geometric decorrelation decrease the quality of measured phase difference. Consequently, advanced DInSAR techniques (multi-temporal interferometry, MTI) aimed at improving the coherence of SAR images have been developed (Crosetto et al., 2005). The techniques include: Permanent/Persistent Scatterer (PSInSAR or PSI), and Small Baseline Subset (SBAS) which exploit long stacks of SAR images taken with similar sensor and under similar geometry (Wasowski and Bovenga, 2014).

In the PSI technique, lack of coherence is overcome by identifying stable natural reflectors (coherent targets, called persistent scatterers, PS) such that displacement is detected as a measure of relative target velocity (multi-interferogram analysis of SAR images) along the line of sight (Lu et al., 2012). While the method can measure ground displacements to millimetre precision, it has the disadvantage in that some surfaces may not provide any coherent targets (e.g. deep slopes, vegetated areas; Scaioni, 2013). On the other hand, SBAS computes a spatial baseline displacement using the differential interferograms for multiple pairs of SAR images (Berardino et al., 2002). The resulting precision from SBAS is inferior to PSI, although it is suited for large area deformation monitoring (Guzzetti et al., 2009).

Differential interferometry synthetic aperture radar ground displacements are useful for active landslide recognition, monitoring, and characterization of landslide deformations (e.g. Crosetto et al., 2011; Tantianuparp et al., 2013). The recognition entails characterizing debris material (Singhroy and Molch, 2004) and detecting new mass movements such as rotational and translational slides, rock slides (e.g. Lauknes et al., 2010), deep-seated landslides characterized by slow movements (e.g. Agliardi et al., 2009), landslide debris (Yonezawa et al., 2012) and flows. However, DInSAR encounters challenges due to foreshortening, layover effects, temporal decorrelation especially in vegetated areas and atmospheric propagation effects (Rott and Nagler, 2006; Rott et al., 1999). Thus, InSAR data integration with in-situ sensors (e.g. GPS observations, field investigation) is recommended for providing validation and complementing data acquisition in regions lacking coherent targets (Akbarimehr et al., 2013; Strozzi et al., 2013).

The current trend is the automation of monitoring landslides using semi-automatic and automatic detection of slow moving landslides. MTI techniques might present the optimal solution for monitoring since they have overcome the limitations of the traditional DInSAR systems which affect phase de-correlation, i.e. temporal decorrelation and atmospheric propagation effects (Hölbling et al., 2012; Tofani et al., 2013). For example, Lu et al. (2012) using a spatial statistical approach known as Persistent Scatterers Interferometry Hotspot and Cluster Analysis (PSI-HCA), developed an automatic procedure for recognising slow moving landslides.

### *3.3.3 Landslide Inventory*

Landslide inventory represents the simplest form of landslide map, provides information about where landslides are located and provide the basis for studying/predicting future landslides (Guzzetti, 2006). They are considered as the first step towards assessing landslide susceptibility (Guzzetti et al., 2012). In addition to landslide location, comprehensive landslide inventory provides topology, geometrical characteristics (e.g. primary direction of displacement), possible failure mechanism, date/frequency of occurrence, state of activity, possible causal factors, and damages incurred (Guzzetti et al., 2000; van Westen et al., 2008). Such information is useful for the analysis of landslide triggering factors as well as the derivation of frequency-magnitude relationships (Dai et al., 2002) using statistical models based on the past landslide occurrence (Guzzetti et al., 2005; Lee, 2005; Malamud et al., 2004).

Landslide inventories provide the training areas necessary for landslide susceptibility mapping and enable validation testing of the landslide models. In the absence of the temporal aspect of landslide activity or rehabilitated landslide sites, numerical dating methods (e.g. dendrochronology<sup>1</sup>) followed by laboratory analyses can provide landslide age for updating a landslide inventory (e.g. Corominas and Moya, 2010; Dikau and Schrott, 1999; Van Den Eeckhaut et al., 2009). However, this is only limited to forested sloppy conditions. The inventory database can also have other attributes such as the type of movement, estimated age, activity, velocity, and depth (Guzzetti et al., 2004), which further determine categorization into shallow or deep landslides, aid landslide frequency analysis and susceptibility assessment.

Field mapping methods provide detailed, high accurate landslide inventory maps, but are often slow and expensive, thus limited to small-scale areas (Santangelo et al., 2010). RS data sources, aided by semi-automated detection methods have provided alternative, efficient means to map recent and reactivated landslides (e.g. Borghuis et al., 2007; Tsai et al., 2010). The challenge with RS methods is that they cannot detect old or rehabilitated landslides. However, they offer alternative cheaper methods of updating landslide inventories (Ciampalini et al., 2015). Thus, stereoscopic aerial photo-interpretation provides detailed morphological landslide analysis, hence aerial photography has remained a valuable source of landslide inventory data (e.g. Fiorucci et al., 2011; Moine et al., 2009), which can be enriched further by the combination of aerial photographs with SAR satellite information (Cigna et al., 2010; Strozzi et al., 2013). However, aerial photos have been criticized for lack of repetitive coverage of similar area, thereby not suiting continuous landslide monitoring (Pardeshi et al., 2013).

### *3.4 The Role of Remote Sensing in Mapping Landslide Predisposing Factors*

Landslides are assumed to leave observable changes on the land surface, thereby modifying land cover and surface topography. Post and pre-landslide event RS imagery can be useful in studying and detecting landslide effects through landslide signature. However, Guzzetti et al. (2012) noted that landslide spectral signatures are not unique and instead, indicative terrain conditions should be used to infer landslide presence or absence. Such conditions are landslide predisposing factors and include: topography, geomorphology, geology, land-cover, hydrology, and anthropogenic factors (Corominas et al., 2013; van Westen et al., 2008). These factors interact with each other and a comprehensive landslide study should ideally

---

<sup>1</sup> The science and technology of dating events, environmental change and archeological artifacts by using the characteristics patterns of growth rings in tree trunks. (Corominas and Moya, 2010)

consider their contribution. In practise, the chosen landslide model mechanism determines the relevance of the predisposing factors for landslide hazard/ susceptibility assessment (Corominas et al., 2013).

#### *3.4.1 Contribution of Land-cover and Vegetation to Slope Stability*

Vegetation provides a protective barrier, thereby controlling wind and water erosion, while intercepting rainfall through the canopy. It also bears reinforcement properties enacted through changes in mechanical and hydrological properties that enhance slope stability (Stokes et al., 2008). Different plant types offer different levels of stability, but generally they support geotechnical hydrological mechanisms of evapotranspiration, interception, surcharge root water uptake, and root reinforcement. Root moisture absorption and the loss of vegetation moisture through evapotranspiration prevent critical pore water pressure (which are responsible for triggering landslides) from being exceeded (Razak, 2014). Rainfall interception by vegetation leaves and stems reduce direct raindrops hitting the soil surface, thus controlling splash erosion and runoff. On the other hand, water drops quickly erode fine soil particles on the bare land surface, thereby creating voids which encourage more water ponding, hence increasing infiltration (Huat et al., 2006).

The mechanical mechanism of vegetation, which is provided through roots reinforcement and anchoring, can have benefits (increase shear resistance) and adverse effects (increase shear stress) on slope stability (Greenway, 1987; Sidle and Ochiai, 2006). The root reinforcement increase soil shear strength, hence increasing slope stability (McIntosh et al., 2009). In addition, root water absorption and its loss to the atmosphere through evapotranspiration decreases soil moisture, which reduce the soil pore water pressure and consequently increase the soil strength. On the contrary, vegetation root network influence subsurface flow and tends to increase infiltration (Ghestem et al., 2011). For example, Crozier (2010) observed that infiltration rates were higher in the forested slopes than in partially covered vegetated areas. Besides, the trees' weight loads increase the slope normal stress.

The role of land-use and vegetation cover to rainfall induced landslides is such that, changes in vegetation cover often result in modified landslide behaviour (Glade, 2003). The author further noted that the first rainstorm following deforestation triggered landslide activity and resulted in higher sedimentation rates. Consequently, severe fire and deforestation on slopes can reactivate old or promote new landslides by reducing the root cohesion strength (Cannon et al., 2001; Wondzell and King, 2003). Kuriakose and van Beek (2010) stressed that root cohesion is one of the most important data necessary to assess the effects of anthropogenic

disturbances on the probability of shallow landslide initiation. Their research found that root cohesion varies significantly with the type of land-use and depth of soil; hence, mixed crop land-use had the maximum root cohesion while fallow land, degraded forest, and young rubber plantation had the lowest root reinforcement. They also found that the bond between soils and root decreased when the soil was saturated. Thus, the applicable root reinforcement was limited by the root pullout strength.

Forests or deep rooted vegetation help to stabilize the top soil, an important factor in reducing landslide hazard in steep areas (Perotto-Baldiviezo et al., 2004). Kuriakose et al. (2009) discussed the effects of deforestation/ land-use change on root reinforcement and the mitigating effect of tree canopy (through interception and evapotranspiration) in providing surface protection, surcharge, and wind loading effects. Generally, root cohesion varies significantly with the type of land-use and the depth of soil and thus anthropogenic disturbances affect soil stability which then triggers landslides. Roering et al. (2003) observed that root strength can be predicted by mapping the distribution and characteristics of trees on potentially unstable slopes. Some physical landslide models have managed to capture root enforcement factor such as Wilkinson et al. (2002) who included the effect of vegetation and topography on slope stability using a combined hydrological slope stability model.

Areas that have experienced landslides in the recent past are characterized by disturbed vegetation, which are recognizable from vegetation indices computed from hyper-spectral (e.g. Airborne Visible Infrared Imaging Spectrometer, AVIRIS) or multi-spectral data (e.g. Landsat TM/ETM+ and SPOT 4 or 5). Such indices reveal vegetation health status, type, vigour and can be utilised in landslide studies, such as: NDVI (Mondini et al., 2011b), NDMIDIR (Vohora and Donoghue, 2004), Normalized Difference Mid-Red (NDMIDR; Mwaniki et al., 2015a), Physiological Reflectance Index (PRI; Sims and Gamon, 2002), and Normalized Burn Index (NBI; Epting et al., 2005). On the other hand, land-cover maps can be prepared using classification techniques and suitable post accuracy assessment performed to validate the classification. Change detection is then applied using the classified imagery and areas revealing trends of deforestation or any form of land degradation noted. Miller (2013) provides a detailed review of the methods applicable for studying soil and vegetation with an aim of investigating landslides, land degradation, and slope failures.

### *3.4.2 Geology and Lithology*

Landslides are geo-hazards which are characterized by exposure of rock layers, shifts in soils and geological substrate. Fault, joint, cleavage, fissure, rock fracture or bedding plane present

areas of geological discontinuities, which potentially indicate areas of rock property change such as orientation, roughness, permeability, or porosity (Singhal and Gupta, 2010). While these geological discontinuities may allow groundwater flow, they also control the type of slope failure such as: topples, planar, wedge, flow or circular failures (Agliardi et al., 2012). For example, highly fractured rocks with close joint spacing have low cohesion and result in circular or flow rock mass failure. On the other hand, the increase in dip orientation angle may result in toppling rock failure type.

Geology attributes provide essential information relating to landslide activity such as: distance from the major tectonic shear zone and azimuth direction, rock type, and layering (rock profile) (Gupta and Joshi, 1990). Rock types influence the type and depth of slope materials, and determine how the slope responds to the external stresses. Besides, certain rock types are more susceptible to landslides and slope failure than others. For instance, hard rocks such as igneous are resistant to erosion and form massive steep slopes (Anbalagan, 1992), while tertiary sedimentary rocks (e.g. schist, phyllites) are generally more susceptible to landslides in many parts of the world (Khazai and Sitar, 2004). In addition, Gerrard (1994) notes that specific failure types are associated with certain rock types and properties.

On the other hand, the lithology and the degree of weathering of the underlying rock materials influence the rate of geomorphological processes such as landslides and erosion. Thus, the nature of rock discontinuities and extent of weathering influences the size and shape of the detached mass in the event of slope failure (Gerrard, 1994). Consequently, the presence of structural features (e.g. joints, faults, bedding planes) increases the susceptibility of a rock mass to rock falls, planar and block slides, and may influence deep-seated landslides in strong rock types (Gerrard, 1994; Moghaddas and Ghaforri, 2006). This is because weathering begins from the discontinuities causing rock exfoliation and disintegration. On the contrary, shallow landslides (mudflows, slumps, rotational failure) are more influenced by homogenous weathered mantle in weak rock types (Moghaddas and Ghaforri, 2006).

Rock weathering reduces the strength and elasticity of the rock material, while increasing the porosity and saturation moisture content. The net effect on the rocks is decreased shear strength which may increase the susceptibility of landslides and slope failures (e.g. Regmi et al., 2013). However, rock weathering occurs in varying degrees within the rock profile, thereby creating potential failure planes. This is to a large extent determined by the rock type, which in turn influences the nature of material produced by weathering (Gerrard, 1994).

Rate of weathering is dependent upon the climate, rock type, rock structure, topography, and time elements (Gerrard, 1994). Thus, in the tropical and subtropical areas, intense weathering in the hot and humid conditions produces thick weathered material, extending to a depth of 100 metres or more (e.g. Chigira et al., 2011). Consequently, the areas around the central highlands of Kenya (the Aberdares and Mt. Kenya region) have deep-weathered volcanic soils, emanating from weathered volcanic rocks, basalts and basaltic agglomerates (Davies and Nyambok, 1993). Besides, the rapid weathering of pyroclastic rocks overlying the stable basalts, produce clay soils (Ngecu and Ichang'i, 1999), which are generally more prone to mudflows and mudslides occurrence (Gerrard, 1994). On the other hand, specific rock types are comprised of certain minerals (joined together by chemical bonding, cementing or crystallisation) which decay under the processes of hydration, carbonation, hydrolysis, and oxidation. Consequently, rocks containing limestone are more readily chemically weathered than granite rocks, while rocks bearing iron minerals are more susceptible to weathering through oxidation (Chigira and Kiho, 1994; Gerrard, 1994).

Landslides are accompanied by mass movements which result in detached large blocks of rock mass. The initiation of landslide movement is associated with the following depth (profile) attributes (DeGraff, 1994): contact between soil and unweathered bedrock, contact of well-weathered and less-weathered soil, and base of the root zone. Therefore, geology rock layers determine the soil profile and are potential failure planes where permeability and density properties change (Walker and Shiels, 2013). On the other hand, the depth of developed soils greatly determines the volume of erodible material (Kuriakose et al., 2009).

Geology factor also controls the landform elements of drainage patterns and intensity of dissection in an area. These factors may in turn influence slope stability directly (through increased infiltration) or indirectly through sub-aerial processes. Interesting studies are reported by Gerrard (1994) linking drainage basin parameters (e.g. channels) to rock strength and elasticity (function of rock type). Based on those reported studies, it was shown that 'the more the channels and deeper the incision, the more rapid the removal occurs on low strength rocks, while the fewer the channels and shallower the incision, the less rapid the removal occurs on high strength rocks'.

Remote sensing multispectral and hyper-spectral data are commonly being used to provide surface geology data (i.e. lithology, lineaments, tectonic structure). Hyper-spectral remotely sensed data is resourceful for geological mapping, enabling surface rock characterization (mineral or lithology) using spectral absorption band features (van der Meer et al., 2012).

Hyper-spectral data also facilitates characterization of soils by type, moisture, and chemical properties, which can aid further extraction of geotechnical parameters for slope stability assessment. In addition, soil characteristics influence vegetation growth and hydro-mechanical responses of the slope to water infiltration and flow (Kuriakose et al., 2009).

Several hyperspectral sensors are still expected to be launched in the near future (Ortenberg, 2016), but the utility of the data will greatly depend on the ability to process the high-dimensional data, while integrating the spatial and spectral component (Goetz, 2009; Plaza et al., 2009). As regards landslide investigation with hyperspectral data, data reduction techniques (e.g. Principal Component Analysis; PCA, Independent Component Analysis; ICA) correlated to topographic attributes from DTM (Sterzai et al., 2010), ANN image classification (Rudd, 2005), and integration of hyperspectral and LiDAR data (Smailbegovic et al., 2011) have demonstrated great potential in slope instability studies.

Lineaments can be extracted from aerial photos using edge-enhancement and filtering techniques (Ayalew and Yamagishi, 2005), likewise using Landsat ETM+ imagery (Erener and Duezguen, 2008) or ASTER multispectral data (Hung et al., 2005). Further, the lineament density is used as an indicative measure of the rocks to fracturing, which is essential in landslide susceptibility studies (e.g. Atkinson and Massari, 1998; Pachauri and Pant, 1992; Pradhan et al., 2006). Various DIP with multispectral RS data including: False Colour Composites (FCC), PCA, ICA, Intensity Hue Saturation (IHS), band ratioing, Spectral Signature Analysis (SSA) and de-correlation stretch, have also been exploited with success in lithology discrimination, and structural geological visualization, as discussed by Mwaniki (2016), Mwaniki et al. (2015b) and the references therein.

### *3.4.3 Topographic/ Morphometric Properties*

GIS environments provide geo-processing computation of DEM raster data to obtain the topographic terrain attributes such as elevation, slope angle, aspect, and curvature. The slope angle is ranked the most important factor in landslide hazard analysis (Dai et al., 2002; Guzzetti et al., 1999) and its impacts are significant at both local and regional<sup>2</sup> scales (Ayalew and Yamagishi, 2005). At the local scale, slope affects soil moisture and depth, upslope contributing area, pore water pressure, the speed of earth flow (the potential kinematic energy), the stream power index, and topographic wetness index which are important aspects of deterministic models. On steep slopes, most water runs as surface runoff with little infiltration, while gentle slopes encourage higher infiltration through the soil (Huat et al.,

---

<sup>2</sup> As used in hydrology i.e. local scale 1 m, regional scale 1 000 km (Bloeschl and Sivapalan, 1995)

2006). Perotto-Baldiviezo et al. (2004) showed that slope and land-cover type characterize landslide occurrence, with landslide susceptibility increasing with increase in slope angle, particularly for water saturated soils. This is attributed to increased weight towards the slope toe, which increases the shear stress and thus contributes to reduced stability.

On the other hand, aspect affects the rate of rock weathering by influencing the amount of sunshine and directional relief rainfall (Wieczorek et al., 1997), while the slope determines the ease of erodibility and energy of the weathering system (Robinson and Moses, 2011). Consequently, steeper slopes are associated with a dynamic weathering system compared to flat plains (Larsen, 2014; Robinson and Moses, 2011). This can be explained by the ease of erodibility (i.e. higher kinematic energy as water flows on steep rock surfaces) which exposes new rock surface layers to weathering. Curvature is a main topographic parameter affecting stability analysis and soil depth (Kuriakose et al., 2009). For example, Ohlmacher (2007) used curvature to evaluate areas prone to earth flow and slides in clay soils. It was found that areas with planar curvature were more prone to landslides compared to concave and convex curvature. Concave curvature (hollow areas) slowed the soil movement which increased stability within the hollow and towards the hill base.

At the regional scale, topographic properties affect the hydraulic conditions that enable watershed delineation and drainage basins, while at the local scale they can be used to characterize landslide types. RS techniques have been used often to provide up-to-date, high resolution DEMs such as those afforded by airborne photogrammetry and LiDAR data. Alternative sources of DEMs are possible with stereo high-resolution optical data and InSAR techniques.

#### *3.4.4 Geomorphology*

Geomorphological factors refer to distinguishable landforms in terms of mapping units and recent / past landslides. Mapping unit is thus a terrain subdivision which contains a set of ground conditions different from adjacent units and has defined boundaries (Carrara et al., 1995) i.e. maximises internal homogeneity within the units, while maximising heterogeneity among the units (Guzzetti, 2006; Guzzetti et al., 1999). The various terrain partitioning units for landslide susceptibility assessment and mapping are categorized into; grid cells, terrain units, unique condition units, slope units, geo-hydrological units, or topographic units (Van Den Eeckhaut et al., 2009; Guzzetti, 2006). The choice of the mapping unit affects the landslide model fit, ability to deal with uncertainties and consequently the reliability of the results obtained (Carrara et al., 2008; Guzzetti et al., 1999). Also important in the choice of

the mapping unit is the spatial resolution of the RS data, especially for DEMs which are processed for terrain units. For example, while deterministic models with high spatial resolution DEM may process accurate locations of recent and past landslides and unstable areas using terrain units, geo-statistical approaches are sensitive to the number of cells in the model (Scaioni et al., 2014).

#### *3.4.5 Hydrology*

Hydrological factors influence landslides and are critical elements contributing to soil shear strength in slope stability models. Such factors are groundwater table position, pore pressure changes, soil moisture, infiltration and permeability changes, lateral flow, soil saturation, and density of drainage networks. The higher the permeability /void ratio, the higher the hydraulic conductivity and consequently the higher the infiltration rate (Huat et al., 2006). Heavy infiltration can result in perched water tables when soil saturation point is reached and where a permeable layer overlies an impermeable zone. This causes elevated pore water pressure, which drastically reduces the soil shear strength resulting in a reduced factor of safety and eventually soil slip/slope failure (Deb and El-Kadi, 2009).

Subsurface water pressure responds to the rainfall amount (Baum and Reid, 1992), rainfall intensity and duration (Wilson, 2005), and rainfall seasonal patterns (Ellen et al., 1995). This is mainly dependent on soil permeability which determines rainfall infiltration, percolation, runoff, subsurface flow dynamics, and formation of perched water table; factors which directly affect the pore water pressure (e.g. Hinkelmann et al., 2011; Terlien, 1998). Landslide initiation is accelerated by a sharp rise in pore water pressure following net precipitation input (Kuriakose et al., 2009). For example, Huat et al. (2006) observed that the higher the rainfall intensity, the higher the infiltration rate, consequently lowering the slope factor of safety in high permeability soils. Similarly, Hamdhan and Schweiger (2011) showed that rainfall infiltration causes soil suction to decrease, hence lowering the FOS. However, in low permeable soils, long duration moderate rainfall intensity events may be responsible for slope failures (Casagli et al., 2006; Tofani et al., 2006). Therefore, changes in rainfall magnitudes, their timing and frequency can activate landslides of different magnitudes (Collison et al., 2000).

A rising ground water table greatly increases the potential for landslide occurrence (Walker and Shiels, 2013). This is because changes in soil moisture balance lead to changes in pore pressure and are indicative of increasing mechanical load (van der Kamp and Schmidt, 1997). On the other hand, deep infiltration capillary barriers resulting from fine-grained soil

overlying a more permeable soil surface layer (Mancarella et al., 2012) can condition the infiltration process, thereby accumulating water in the less permeable soil surface layer and consequently reduce stability through loss of soil suction (Galeandro et al., 2013).

Rapid draw down of water can reduce soil stability, since the surfaces that were previously submerged, are left unsupported and with water-filled pore spaces (Walker and Shiels, 2013). This can cause an abnormal distribution of pore water pressure at the slope toe/river banks. Clay soils are especially more prone due to their water retention ability. These types of soil failure/ slump are likely to happen following receded floods, on river banks or river valley slope. Clay soil liquefaction can also occur at the slope toe or river channels, when the clay soil loses its shear strength and behaves like liquid causing damages in the case of huge events (Walker and Shiels, 2013).

Hydrology parameters influence slope stability and together with real-time rainfall data should be incorporated into landslide models. Combined hydrological and slope stability models make provision for studying the effects of soil moisture by simulation of groundwater recharge and pore water pressure changes as part of effective stress. However, the use of infinite slope assumptions in the deterministic models, limits the prediction of slope failures to shallow landslides (Chiang et al., 2012). In addition, they require detailed geotechnical soil properties at various soil depths, and ground water table; data which is not always easily available. It is recommended that future modelling requirements should consider aspects of groundwater and understanding of bedrock or perched water tables, groundwater flow, and back pressure from within the landslide boundary extending to the whole slopes where modelling slope stability is required (Brunsden, 1999).

Remote sensing thermal infrared sensors and passive microwave can provide soil moisture data (Shi et al., 2012). For example, Younis and Iqbal (2015) showed that surface soil moisture estimated through the Temperature Vegetation Dryness Index (TVDI) adequately matched temporal variation of field soil moisture. Hence, it was recommended for evaluation of wet conditions. The author using Fourier Transform Infrared Technique (FTIR) analysis showed that as soil moisture increased, the soil reflectance decreased and vice versa. Other parameters that are indicative of soil moisture are; land-cover (Hong et al., 2007), use of Tasselled Cap Transformation (TCT) component (Vorovencii, 2007), soil water index (Brocca et al., 2012), spectral indices such as Normalised Soil Moisture index (NSMI), Water Index Soil (WISOIL) (Fabre et al., 2015). Drainage system and network may be computed in

the GIS environment using a high resolution DEM, extracted and ordered from the flow accumulation parameter (e.g. Singh et al., 2014).

#### *3.4.6 Anthropogenic Factors*

Human activities may have a negative impact on the environment and landscape, leading to land-use change, land degradation (deforestation, desertification) and climate change (Crozier and Glade, 2010). These impacts may accelerate landslide processes and other geomorphological hazards either directly or indirectly through

- i) ground shaking or vibrations (i.e. reducing resistance forces);
- ii) increasing the slope's load or weight (driving forces); and
- iii) modifying the slope substrate (Walker and Shiels, 2013).

Changes in slope self-load resulting from contribution of man-made infrastructure (buildings, artificial dams and reservoirs) are among the long-term landslide triggers (Hinkelmann et al., 2011).

Construction of road cuts and tunnels, mine and quarry activities may involve rock drilling, blasting, and cutting which causes vibration similar to seismic waves from earthquakes. In addition, the vibration and blasting reduces the soil/rock resistance strength, whereas the cutting exposes geological layers to weathering processes. On the other hand, heavy traffic on transport network built on mountainous terrain, may cause vibration, increased load and risk of sedimentation (e.g. Sidle et al., 2014). Walker and Shiels (2013) argue that seepage from reservoirs, canals, culverts or septic tanks can cause increased infiltration, thereby increasing pore pressure and weight load on a slope. Such conditions increase the probability of landslides on a sloppy terrain. Similarly, pressure from urban development and the need to erect buildings, increases the weight load whereas the construction process modifies the soil profile and reduces slope strength.

Anthropogenic land cover changes may affect geomorphic processes by reducing the strength of regolith material and climate variability, which increases the frequency of cyclonic storms and wind erosion (Glade, 2003). The human influence on the natural system by slashing, burning indigenous vegetation or deforestation can cause long-term change in vegetation and irreversible damage, thus significantly lowering the slope stability factor and triggering shallow landslides (e.g. Zêzere et al., 1999). For instance, the impacts of land-use (cattle stocking and pasturing) were found to increase landslides risk on mountainous environments where topography and climatic extremes are favourable for landslide occurrence (Meusburger and Alewell, 2008). Other anthropogenic agents interfering with slope settings include:

intensive agriculture, population growth pressure, the need for economic development, and wild fire (Aleotti and Chowdhury, 1999; Cannon et al., 2001).

### *3.5 Landslide Triggering Factors: Rainfall*

Landslide triggering factors are earthquakes, heavy rainfall, glacier and snowmelt, and anthropogenic factors. Landslide predisposing factors are static, while the triggering factors introduce a temporal dimension (Dai et al., 2002). Rainfall induced landslides are increasingly more common in many parts of the world (Gariano et al., 2015), with increased climate variability altering precipitation pattern, thereby altering the distribution of heavy rain events and intensifying storms (Scaioni et al., 2014). Since precipitation is the main triggering factor of rainfall-induced landslides, some authors argue that rainfall prediction should be considered as a landslide disposing factor because it is an event with probability of occurrence over time (Muthu et al., 2008). However, rainfall has a dynamic component and there is need to develop landslide hazard assessment models which can capture the dynamic rainfall patterns in order to predict rainfall induced landslides more accurately.

Remote sensing offers the possibility to detect meteorological conditions at regional and global scales using rainfall radar data such as: Tropical Rainfall Measurement Mission (TRMM), Precipitation Radar, and Advanced Microwave Scanning Radiometer (AMSR). The use of radar in rainfall estimation is particularly useful for orographically induced extreme rainfall and floods. Advances in satellite based precipitation observation technology and availability of high resolution satellite products are facilitating the landslide real time prediction which were previously problematic owing to the scarcity of rain gauges (Chang et al., 2008; Takara et al., 2010). Indeed, radar rainfall maps have improved the spatial distribution of mapping rainfall and consequently the prediction of terrain stability (Chiang and Chang, 2009).

Rain gauges provide direct rainfall measurement and provide validation for radar rainfall data, but their data lack accurate spatial-temporal pattern and requires dense-network of rain gauges which is not always available (Villarini et al., 2008). Therefore, rainfall radar data is preferred, although it requires validation with rain gauge data in order to improve estimated precipitation amounts (Corominas et al., 2013). Many deterministic models can incorporate rainfall data in the slope stability models, both as a dynamic variable (e.g. Hong et al., 2014; Iwahashi et al., 2012) or static rainfall estimates (Baum and Godt, 2010; Liao et al., 2012).

### *3.6 Specific Contribution of this Research to Landslide Studies*

Specific focus has been given to the role of RS in providing landslide predisposing data (geology, lineaments, land-use, vegetation cover, hydrology, and anthropogenic factors) and landslide triggering factors. In addition, the various landslide mapping techniques have been reviewed and it was noted that distribution free approaches (e.g. ANN, Neuro-fuzzy) are gaining more attention due to their ability to deal with complex interrelationships involved in landslide processes and causative factors. It has also been shown that rainfall-induced landslides need to incorporate land-use which is an indicator of environmental impact and captures vegetation cover and anthropogenic land-use (e.g. Canuti et al., 2004; Glade, 2003). Similarly, this research has investigated the role of changes in LULC and forms of land degradation in the study area as they influence landslides (Mwaniki and Moeller, 2015).

A special contribution of this research to landslide studies is the application of RS image enhancement methods to map geology (Mwaniki, 2016; Mwaniki et al., 2015b), NDMIDR spectral index capable of enhancing geological components and map landslides (Mwaniki et al., 2015a), and create landslide inventory (Mwaniki et al., 2015c). In addition, the incorporation of Sentinel-1 SAR-C data to enhance Landsat data through image fusion at feature extraction level, has greatly improved the landslide mapping, revealing fault lines and areas prone to deep-seated landslides (Mwaniki et al., 2016).

The combined hydrological and slope stability model (CHASM) has also been slightly modified, to incorporate the parameters of vegetation cover, evapotranspiration, infiltration and the changes in pore water pressure were adapted from the GeoTOP model (Bertoldi et al., 2006; Rigon et al., 2006). Using this model and stepwise incorporation of rainfall parameters following a heavy rainfall event, it was possible to monitor the ground response given the changing pore pressure effects. In addition, the threshold rainfall values which are likely to trigger landslide events can be studied. The CHASM model provided a means to combine topography, geology, rock mass strength parameters, which were noted by Moore et al. (2009) as key controls on slope failures. This is described in detail in Chapter 7.

## Chapter 4: Land-Use Land-cover Classification, Change Detection

---

### *4.1 Introduction*

Land-use land-cover studies provide essential information for environmental monitoring, such as: protected areas (forest covers, deforestation, and curbing encroachments), forms of land degradation (e.g. desertification, erosion, and landslides), urban growth and trends, and change detection. This is possible through increased RS data sources and increased technologies to process the data, thereby enabling classification into various land cover units. The suitability of RS data for environmental applications is attributed to characteristics such as high multi-temporal and multi-spectral resolution and cheap data sources covering vast areas with repeat capability. Hence, hyperspectral data (e.g. AVIRIS, Hyperion) and multispectral data (e.g. Landsat series, ASTER, SPOT, MODIS, AVHRR) are preferred owing to their ability to image a pixel in several bands (visible, Near-Infrared, Short Wave InfraRed, SWIR) thus enhance the differentiation of various land-covers (Govender et al., 2007).

On the other hand, multispectral data, such as Landsat series (30 m spatial resolution) and AVHRR have medium and low spatial resolution, respectively, which introduces the mixed pixel problem (e.g. Zhang et al., 2015). Resolving the mixed pixel problem requires tailor made solutions such as unmixing techniques (e.g. linear spectral mixture analysis, mix-unmix classifier) in order to improve image classification (Ngigi et al., 2008). In addition, DIP methods such as image enhancement to boost feature extraction, image fusion, and the use of non-parametric classifiers (e.g. ANN, decision tree, SVM, object-oriented image analysis, expert based knowledge systems) which can use multisource data, can greatly improve the classification accuracy (Lu and Weng, 2007; Stehman and Foody, 2009).

Digital image processing aids feature extraction by improving the image brightness, colour contrast, and texture thus enhancing image visual interpretation and pattern recognition. It is particularly important for non-homogenous areas, linear features and towards boundaries or edge enhancement from one class to another. Commonly used DIP techniques are FCC, band ratios and spectral indices, image space transformation (e.g. PCA, ICA, IHS, TCT, application of image filters, decorrelation stretch, and image fusion (Acharya and Ray, 2005; Campbell, 2002a; Gao, 2009; Gonzalez and Woods, 2002; Schowengerdt, 2007; Shih, 2010; Warner et al., 2009).

False colour composites involve visualizing an image using the Red, Green and Blue (RGB) channels, using actual or processed components such as band ratios, ICA or PCA processes. They are more effective in enhancing colour contrast, when the image is visualized using processed bands with little or no correlation, or real bands from different spectral regions. Methods such as PCA and ICA are effective in transforming data into a new image space where the bands are less correlated, which avoids data redundancy (Jolliffe, 2005). On the other hand, band ratios involve dividing one band by another and they reduce shadowing which may affect visual interpretation, especially in high relief areas (Campbell, 2002b). TCT gives three important measures, i.e. soil brightness, greenness measure, and canopy moisture (Huang et al., 2002; Vorovencii, 2007). Spectral indices have also been very useful in enhancing vegetation, soil or rock minerals (Bannari et al., 1995; Govender et al., 2007).

The choice of image enhancement method is a function of the final use of the classified map. For example, edge and texture filter enhancements are suitable for urban, landslide, geology and / or mineral studies (Benediktsson et al., 2003; Stumpf et al., 2012), while spectral indices are better suited for distinguishing vegetation from other land covers (Ardavan et al., 2012; Sari et al., 2005). On the other hand, the choice of a classifier is determined by complexity of the landscape, type of RS data (passive or active), and the need to obtain high classification accuracy (Mather and Tso, 2009). Non-parametric classifiers are particularly suited for complex landscapes due to their ability to combine environmental data (e.g. slope, elevation, soil, precipitation, drainage) into the classification, thereby improving the accuracy. Knowledge-based expert systems provide object-based image analysis to model complex reality and landscapes using image and geographic context rules (Lang, 2008).

The study of land-use changes are crucial in landslide studies as they help in detecting environmental change resulting from human induced surface changes such as deforestation, urban expansion and infrastructure, which could be a precursor sign to slope instability (Tarantino et al., 2007). They also help in land-use management and formulating policies towards controlling landslides and providing mitigation measures. The aim of this chapter is to investigate the land-cover changes and trends in the research area, since landslides are forms of land degradation. In addition, deforestation and farmlands have been attributed to the common occurrence of mudflow landslides within the Kenyan highlands (Kibiyy et al., 2014; UNDP, 2010). There was a need to compare the land-cover trends to climate variables (rainfall and temperatures) to investigate environmental climatic effects.

#### *4.2 Methodology*

The availability of medium resolution Landsat multi-temporal satellite imagery together with auxiliary data of slope, elevation, and processed components from Landsat datasets, enabled the land cover mapping in knowledge-based classification. Accuracy assessments and change detection followed the classification as described in the sections below.

#### 4.2.1 Data Description and Landsat Image Enhancement

Landsat series imagery for the years 1995 (TM), 2002 (ETM+), 2010 (TM) and 2014 (OLI), (described in Table 4.1), 30 m spatial resolution were downloaded from the United States Geological Survey (USGS) website and pre-processed to reduce atmospheric effects using Landsat-5 TM correction in Erdas Imagine software. There was difficulty in obtaining 100% cloud free data due to high mountain relief features in the study area. Therefore, Landsat datasets for the months of January and February (same season, dry months), 0-10% of cloud cover were used and image masking performed where necessary. Image co-registration was not necessary as the datasets were already geo-referenced and coincided well with other thematic datasets. Mosaicing was performed using histogram matching in overlap areas followed by subsetting using area of interest (AOI) file. Similarly, a DEM from the Shuttle Radar Topography Mission (SRTM), 30 m spatial resolution covering similar scenes as Landsat datasets were downloaded from the USGS site, mosaiced and subset. Slope topography variable was then computed from the elevation model for use as auxiliary information in the knowledge-based classification. The other auxiliary information were processed from Landsat datasets, i.e. NDVI spectral index and PCs.

**Table 4.1:** Landsat imagery scenes description.

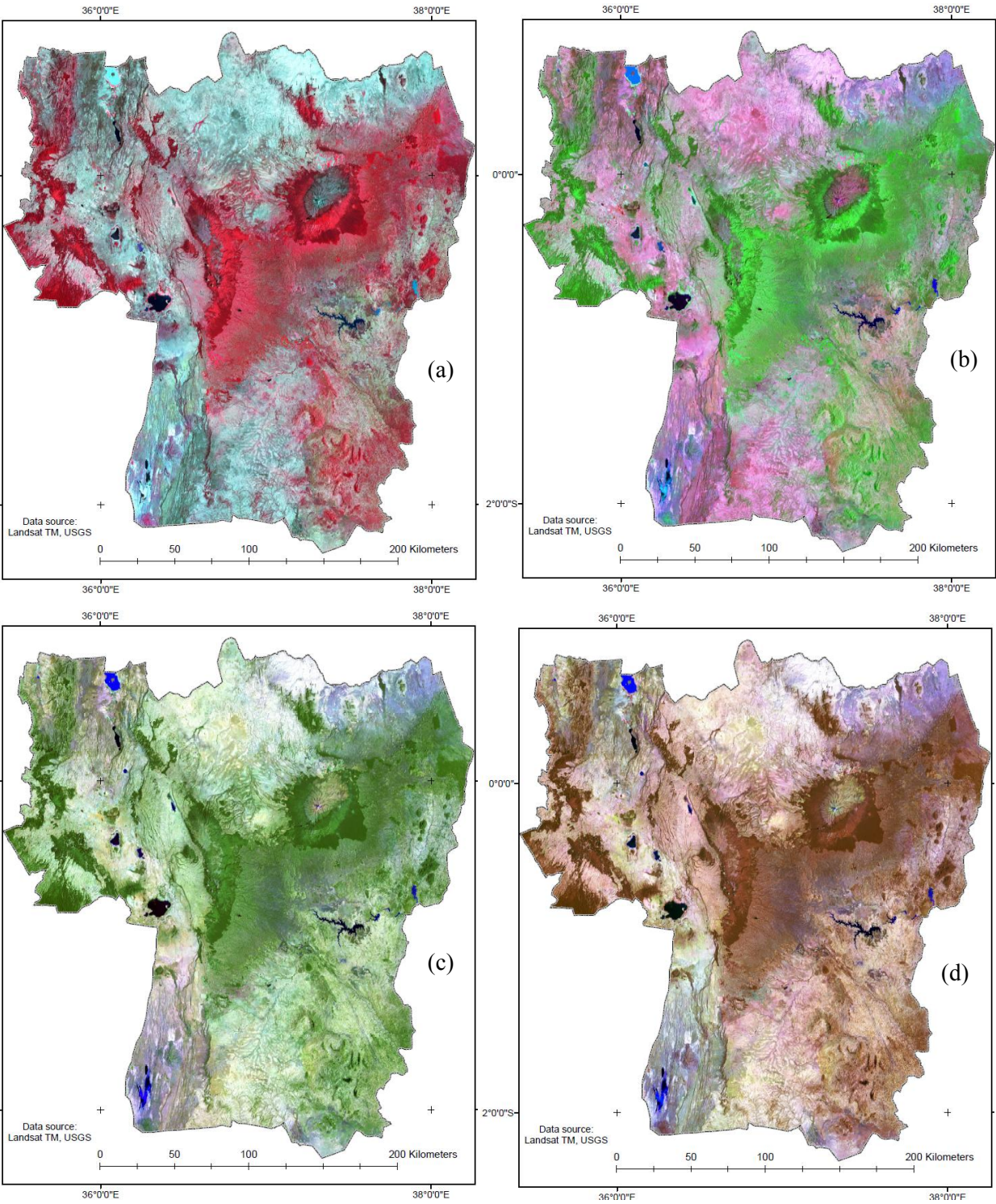
<b>Landsat 5 (1995)</b>	<b>Date of acquisition</b>	<b>Landsat 7 (2002)</b>	<b>Date of acquisition</b>
LT51680601995030XXX00	30th Jan 1995	LE71680602002041SGS00	10th Feb 2002
LT51680611995030XXX00	30th Jan 1995	LE71680612002041SGS00	10th Feb 2002
LT51690601995037XXX01	6th Feb 1995	LE71690602002032SGS01	1st Feb 2002

<b>Landsat 5 (2010)</b>	<b>Date of acquisition</b>	<b>Landsat 8 (2014)</b>	<b>Date of acquisition</b>
LT51680602010039MLK01	8th Feb 2010	LC81680602014034LGN00	3rd Feb 2014
LT51680612010039MLK01	8th Feb 2010	LC81680612014034LGN00	3rd Feb 2014
LT51690602010030MLK00	30th Jan 2010	LC81690602014025LGN00	25th Jan 2014

The Landsat subset files were then visualised using various FCC combinations, an example with Landsat TM (1995) is shown in Figure 4.1, where FCC combination 5,7,3 had enhanced contrast and allowed more land-cover discrimination compared to other band combinations. Enhanced land-cover discrimination was also investigated using standard covariance PCA and PC factor loading applied to bands 1-5, 7 of Landsat TM/ETM+ and bands 1-7 of Landsat OLI (Table 4.2). As expected, the first three components of the PCA contained most of the

information (Jolliffe, 2005). PC1 had the most information from all bands, although it was positively correlated in all bands, hence other components were needed to distinguish other land-covers. Visible bands had lower contribution in PC1 compared to SWIR bands 5 and 7 in Landsat TM/ETM+ or bands 6 and 7 in Landsat OLI. Hence, water cover were discriminated from other land-covers using PC1.



**Figure 4.1:** False Colour Combination (a) 432, (b) 742, (c) 753 and (d) 573.

On the other hand, PC2 contained most information from the vegetation band 4 in Landsat TM/ETM+, or band 5 in Landsat OLI. Thus, in addition to NDVI, it was possible to distinguish vegetation from rocks and bare soil using PC2. Besides, using PC2, additional information leading to the distinction between clear and turbid water was possible as band 3 had opposite correlation with band 1 in Landsat TM/ETM+. Most of the land-covers could be differentiated in PC1 and PC2; however, PCs 3, 4 and 5 were used when necessary, whereas PC7 had the least contribution (less than 0.01%) and therefore was not considered.

**Table 4.2:** Factor loading using PCs 1-5 for the years 1995, 2002, 2010 and 2014.

	1995					2002				
	PC1	PC2	PC3	PC4	PC5	PC1	PC2	PC3	PC4	PC5
<b>Band1</b>	0.38259	-0.25098	0.62907	0.55031	-0.11877	0.37926	-0.13078	-0.41060	-0.21206	-0.46720
<b>Band2</b>	0.19466	-0.06496	0.30232	-0.01521	0.12790	0.31493	-0.10599	-0.41305	-0.20389	-0.30389
<b>Band3</b>	0.24594	0.16360	0.43177	-0.60993	0.53252	0.37749	0.26340	-0.50416	0.13017	0.71539
<b>Band4</b>	0.42446	-0.76562	-0.29577	-0.35343	-0.14214	0.33205	-0.82765	0.16153	0.38508	0.17406
<b>Band5</b>	0.68824	0.37623	-0.46972	0.29132	0.28156	0.58275	0.13212	0.58137	-0.53100	0.15128
<b>Band7</b>	0.31844	0.42227	0.13536	-0.33933	-0.76781	0.40576	0.44701	0.20626	0.68285	-0.35271
<b>% Var</b>	94.17	4.44	1.03	0.2	0.15	95.04	3.27	1.33	0.24	0.11

	2010						2014					
	PC1	PC2	PC3	PC4	PC5		PC1	PC2	PC3	PC4	PC5	PC6
<b>Band1</b>	0.37958	-0.16216	0.67691	0.44094	-0.32967	<b>Band1</b>	0.24099	-0.05290	-0.55771	0.40784	-0.26256	0.46573
<b>Band2</b>	0.20129	-0.04220	0.33222	-0.05203	0.14573	<b>Band2</b>	0.21217	0.00164	-0.47775	0.20939	-0.08576	-0.19418
<b>Band3</b>	0.25164	0.15532	0.40481	-0.51288	0.61635	<b>Band3</b>	0.21104	0.03187	-0.37807	-0.09955	0.14961	-0.77211
<b>Band4</b>	0.42511	-0.80844	-0.28105	-0.28842	-0.04542	<b>Band4</b>	0.23250	0.22847	-0.33049	-0.62980	0.48878	0.38262
<b>Band5</b>	0.67923	0.34866	-0.43263	0.40402	0.25815	<b>Band5</b>	0.58467	-0.75238	0.21025	-0.20441	-0.06988	0.02520
<b>Band7</b>	0.33167	0.41552	-0.03721	-0.54166	-0.64923	<b>Band6</b>	0.56277	0.37244	0.37243	0.47883	0.42009	0.00958
						<b>Band7</b>	0.37386	0.48909	0.16014	-0.33498	-0.69358	-0.04594
<b>%Var</b>	92.79	4.80	1.91	0.34	0.15		91.610	6.840	1.196	0.207	0.122	0.020

#### 4.2.2 Knowledge Based Classification

Knowledge-based classification rules were set using histogram density slicing of the processed components. First, Landsat TM/ETM+ FCC 5,7,3 and PCs 1,2,3 were investigated for possible land-cover classes using density slicing aided by colours; in Landsat OLI, the FCC 6,7,4 and PC 1,2,5 were used. Secondly, at each possible land-cover, the range of the enhanced component values was noted. This was also performed with NDVI data which was helpful in distinguishing vegetation from other land-covers. Elevation data was useful in distinguishing vegetation type on high relief mountain features, where grasslands were limited to less than 3200 m. On the other hand, the slope was used to control water covers and

provide distinction from rocks in shadowed areas. In total, ten classes were identified (Table 4.3), namely: clear water, turbid water, muddy water, rocks and compact bare surfaces, dense forest, less dense forest, grassland, bare soil, fluvial deposits, and crops/agriculture areas/farmlands. The classification rules for each Landsat dataset were set as in Table 4.3, saved in an Erdas Imagine knowledge engineer file together with the enhanced components. The file was then run with the subset Landsat image as the input.

**Table 4.3:** Expert knowledge classification criteria using histogram density slicing.

Class ID	Class names	1995	2002
1	Clear water	PC1 ≤ 45, NDVI < 0.200, PC3 > 10 Elevation < 2 600 m, Slope < 20	PC1 ≤ 60, NDVI < 0, Slope < 20 Elevation < 2 600 m
	Glacier	PC3 ≥ 18, Elevation > 4 000 m	PC1 ≤ 85, NDVI < 0.400, Elevation > 4 000 m
2	Turbid water	70 < PC1 < 175, PC3 < 35 Elevation < 610 m, NDVI < 0.2	100 < PC1 < 280, Elevation < 2 600 m, NDVI < -0.340, Slope < 20
		PC3 ≥ 35, Elevation < 2 600 m	
3	Muddy/ salty water	45 < PC1 < 70, NDVI < 0.485 Elevation > 2 600 m	60 < PC1 < 100, Slope < 20 Elevation > 2 600 m, 0 < NDVI < -0.750
4	Rocks & Compact bare surfaces	70 < PC1 < 140, 0.200 < NDVI < 0.485 PC2 > -15, Elevation < 4 000 m	85 < PC1 < 180, -0.280 < NDVI < 0.05
		PC1 < 70, NDVI < 0.485 Slope > 20, Elevation < 2 600 m	Elevation > 3 000 m 60 < PC1 < 180, NDVI < 0.2
		Elevation > 3 400 m, PC3 < 18	Elevation < 3 000 m, PC1 < 180, Slope > 20
		90 < PC1 > 70, Elevation < 2 900 m, -15 < PC2 > -20, 0.485 < NDVI > 0.2	
5	Dense Forest	0.485 < NDVI < 0.650, Elevation < 4 000 m	0.28 < NDVI < 0.465, Elevation < 4 000 m
6	Light dense forest	NDVI > 0.650, Elevation < 4 000 m	NDVI > 0.465, Elevation < 4 000 m
		NDVI > 0.650, Elevation < 4 000 m	
7	Grassland	120 < PC1 < 175, Elevation < 3 200 m	180 < PC1 < 260, Elevation < 3 200 m -0.29 < NDVI < 0
8	Bare soil	175 < PC1 < 195, Elevation < 3 500 m	260 < PC1 < 330
9	Fluvial deposits	236 < PC1 > 195	330 < PC1 < 420
10	Crop, Agriculture	0.200 < NDVI < 0.485, PC2 < -15, Elevation < 2 900 m, 90 < PC1 < 175	0 < NDVI < 0.280, Elevation < 2 900 m 60 < PC1 < 260
		90 < PC1 > 70, Elevation < 2 900 m, PC2 < -20, 0.485 < NDVI > 0.200	

**Cont' Table 4.3:** Expert knowledge classification criteria using histogram density slicing.

Class ID	Class names	2010	2014
1	Clear water	PC1 < 50, Slope < 20, NDVI < 0, Elevation < 2 600 m	PC1 < 3 750, Slope < 20, NDVI < 0, Elevation < 2 600 m
	Glacier	PC1 <= 30, PC2 < -25 Elevation > 4 000 m	PC1 <= 4 000, Elevation > 4 000 m PC5 > 400, Elevation > 4 000 m
2	Turbid water	70 < PC1 < 110, PC2 < -15 NDVI < 0.1, Elevation < 2 600 m	3 750 < PC1 < 8 000, NDVI < 0.1, -1 000 < PC5 < 1 000, Elevation < 2 600 m
		110 < PC1 < 190, PC2 < -25, Elevation < 2 600 m	
3	Muddy/ salty water	50 < PC1 < 70, PC2 < -15 Elevation < 2 600 m, NDVI < 0	3 750 < PC1 < 8 000, PC5 > 1 000 NDVI < 0.1, Elevation < 2 600 m
		PC1 < 70, PC2 < 7, NDVI < 0.280, Elevation < 1 910 m	8 000 < PC1 < 12 500, PC2 < -1 000, PC5 > 1 000, Elevation < 3 200 m, NDVI < 0.1
4	Rocks & Compact bare surfaces	70 < PC1 < 145, PC2 > -25, NDVI < 0.350	12 500 < PC1 < 15 000, PC2 > -1 000, Elevation < 3 200 m, 0 < NDVI < 0.6, PC3 > -2 500, PC5 < 1 000
		110 < PC1 < 190, PC2 < -25, Elevation < 2 600 m, 0.2 < NDVI < 0.28	8 000 < PC1 < 12 500, PC2 > -1 000, 0 < NDVI < 0.6, Elevation < 3 200 m
		Elevation > 3 250 m, PC1 > 245	PC2 > -5 000, Elevation > 3 200 m
5	Dense Forest	0.5 < NDVI < 0.680, Elevation < 4 000 m	0.6 < NDVI < 0.78, Elevation < 4 000 m
		PC1 < 70, PC2 > -15, 1 910 m < Elevation < 3 250 m	
6	Light dense forest	NDVI > 0.680, Elevation < 4 000 m	NDVI > 0.78, Elevation < 4 000 m
		2 900 m < Elevation < 4 000 m 0.280 < NDVI < 0.500, PC1 < 190	
7	Grassland	145 < PC1 < 190, Elevation < 3 200 m NDVI < 0.280, PC2 < -25	12 500 < PC1 < 15 000, Elevation < 3 200 m, 0 < NDVI < 0.4, PC3 < -2 000, PC5 < 1 000
			15 000 < PC1 < 19 000, Elevation < 3 200 m, 0 < NDVI < 0.4
8	Bare soil	190 < PC1 < 225, Elevation < 3 500 m	19 000 < PC1 < 23 000, Elevation < 3 200 m, 0 < NDVI < 0.35
		Elevation > 3 500 m, 145 < PC1 < 170	12 500 < PC1 < 15 000, NDVI < 0.35, PC5 > 1 000, PC3 > -2 500, Elevation < 2 600 m
9	Fluvial deposits	225 < PC1 < 250, Elevation < 3 500 m	PC1 > 23 000
		170 < PC1 < 250, Elevation > 3 500 m	
10	Crop, Agriculture	50 < PC1 < 225, Elevation < 2 900 m 0.280 < NDVI < 0.500	3 750 < PC1 < 15 000, Elevation < 2 900 m, PC2 < -1 000, 0.4 < NDVI < 0.6
		PC1 < 70, PC2 < -15 1 910 m < Elevation < 2 900 m	15 000 < PC1 < 23 000, 0.4 < NDVI < 0.6, Elevation < 2 900 m

#### 4.2.3 Climate Variability with Rainfall and Temperature Parameters

The rain-gauge rainfall data (annual total) and temperature data (average maximum and minimum) for 14 stations within and around the study area (Figure 4.2), obtained from the Kenya meteorological department (KMD) spanning the period 1994 to 2014, were analysed and their trends compared with LULC change detection results to investigate any effect. Although raster rainfall data from TRMM satellite was available, it was limited to the beginning of the year 1998. Hence, only the vector point data was utilized.

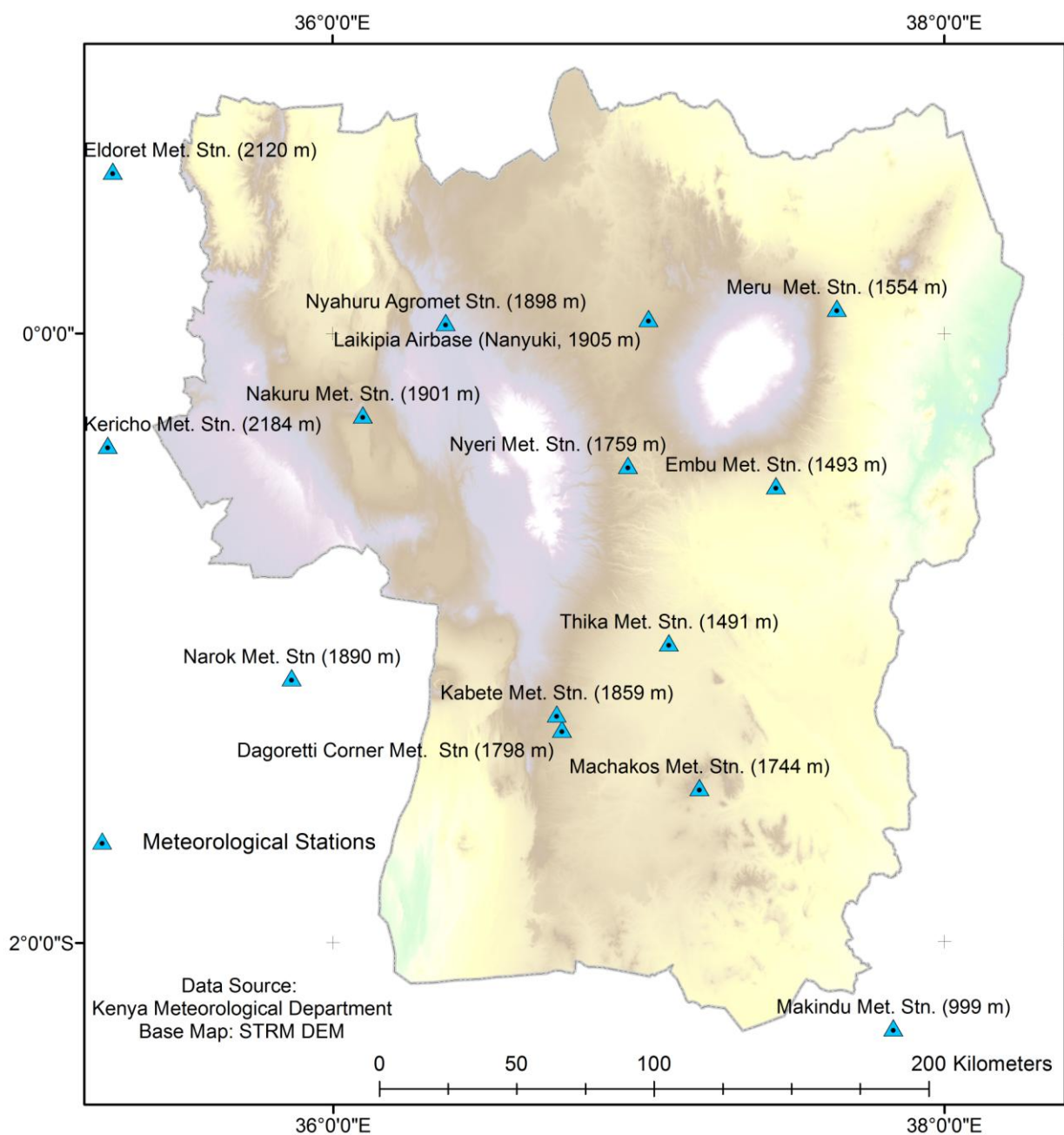


**Figure 4.2:** Spatial distribution of the meteorological stations.

### 4.3 Results

#### 4.3.1 Land-Use Land-Cover Results

Figures 4.3, 4.4, 4.5, and 4.6 are the classification results for the years 1995, 2002, 2010, and 2014 respectively, obtained after running the classification rules presented in Table 4.3. The percentage areal extent of each land cover was extracted into Table 4.4, followed by further regrouping into water, forest, grassland, bare soil/ rocks, and crops. The trend of vegetation cover against farming activities (i.e. grazing and farm land activities which could have an influence on vegetation and land degradation processes on bare lands) was analysed and visualized as in Figure 4.7. From the Figure 4.7 and Table 4.4, water cover remained almost constant with a slight increase of 0.089% by the year 2002, followed by a slight decrease of 0.056% by the year 2010, and finally another slight increase of 0.021% by the year 2014.

On the other hand, forest cover decreased by 9.14% by the year 2002, followed by an increase of 5.34% by the year 2010 and finally another slight increase of 1.42% by the year 2014. However, the forest coverage by the year 2014 is less than the initial coverage in the year 1995 by 2.38%. Grassland coverage increased by 10.09% by the year 2002, after which it took a decreasing trend, although the coverage by the year 2014 was still higher than the initial coverage by 4.95%. Rocks and bare lands decreased by 11.48% by the year 2002, followed by an increase of 10.03% by the year 2010, and finally decreased by 6.37% in the year 2014. The initial bare land coverage is higher than that mapped by the year 2014, by 7.82%. Agricultural areas increased by 10.44% in the year 2002, followed by a decrease of 11.33% by the year 2010, and finally increased by 6.10% in the year 2014. However, the final coverage by the year 2014 was still higher than the initial coverage by 5.2%.

**Table 4.4:** Land-cover area extent in percentage for the years 1995, 2002, 2010 and 2014.

Class	1995		2002		2010		2014	
Clear Water	0.486	0.971	0.338	1.060	0.493	1.004	0.388	1.025
Turbid Water	0.412		0.357		0.277		0.498	
Muddy Water	0.073		0.365		0.234		0.139	
Dense Forest (D.F.)	22.034	26.478	13.281	17.337	19.784	22.676	20.924	24.097
Light Dense Forest (L.D.F.)	4.444		4.056		2.892		3.173	
Grass	14.925	14.925	25.018	25.018	21.043	21.043	19.87	19.87
Rocks & Compact bare	22.314	30.9	7.944	19.421	17.444	29.447	14.792	23.081
Bare soil	7.325		10.105		10.502		7.269	
Fluvial deposits	1.261		1.372		1.501		1.02	
Crops	26.727	26.727	37.164	37.164	25.830	25.830	31.927	31.927
	<b>100%</b>		<b>100%</b>		<b>100%</b>		<b>100%</b>	

# Land-use Land-cover Classification, Year 1995

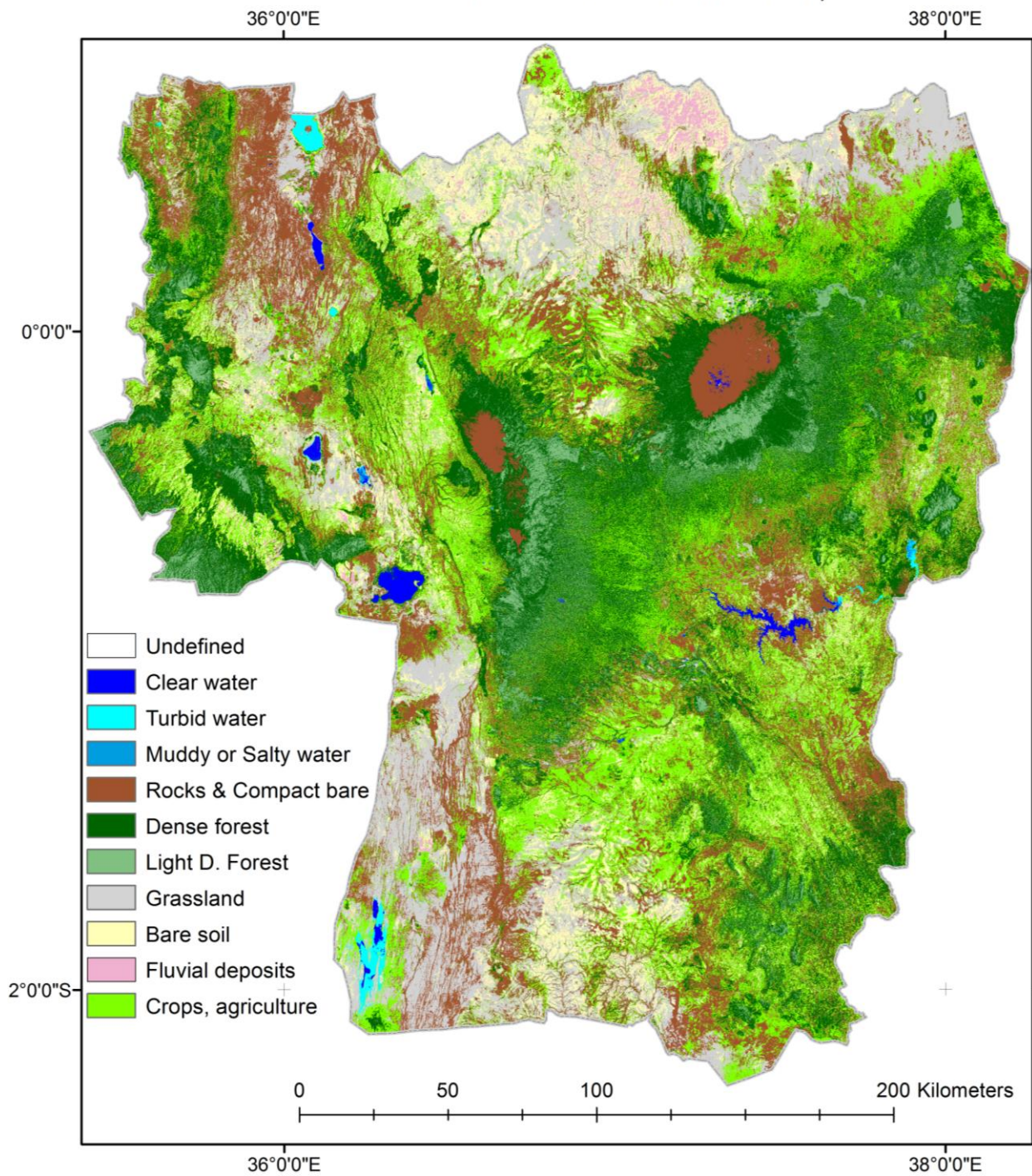


**Figure 4.3:** Land-cover Land-use classification map for Central Region Kenya, Year 1995.



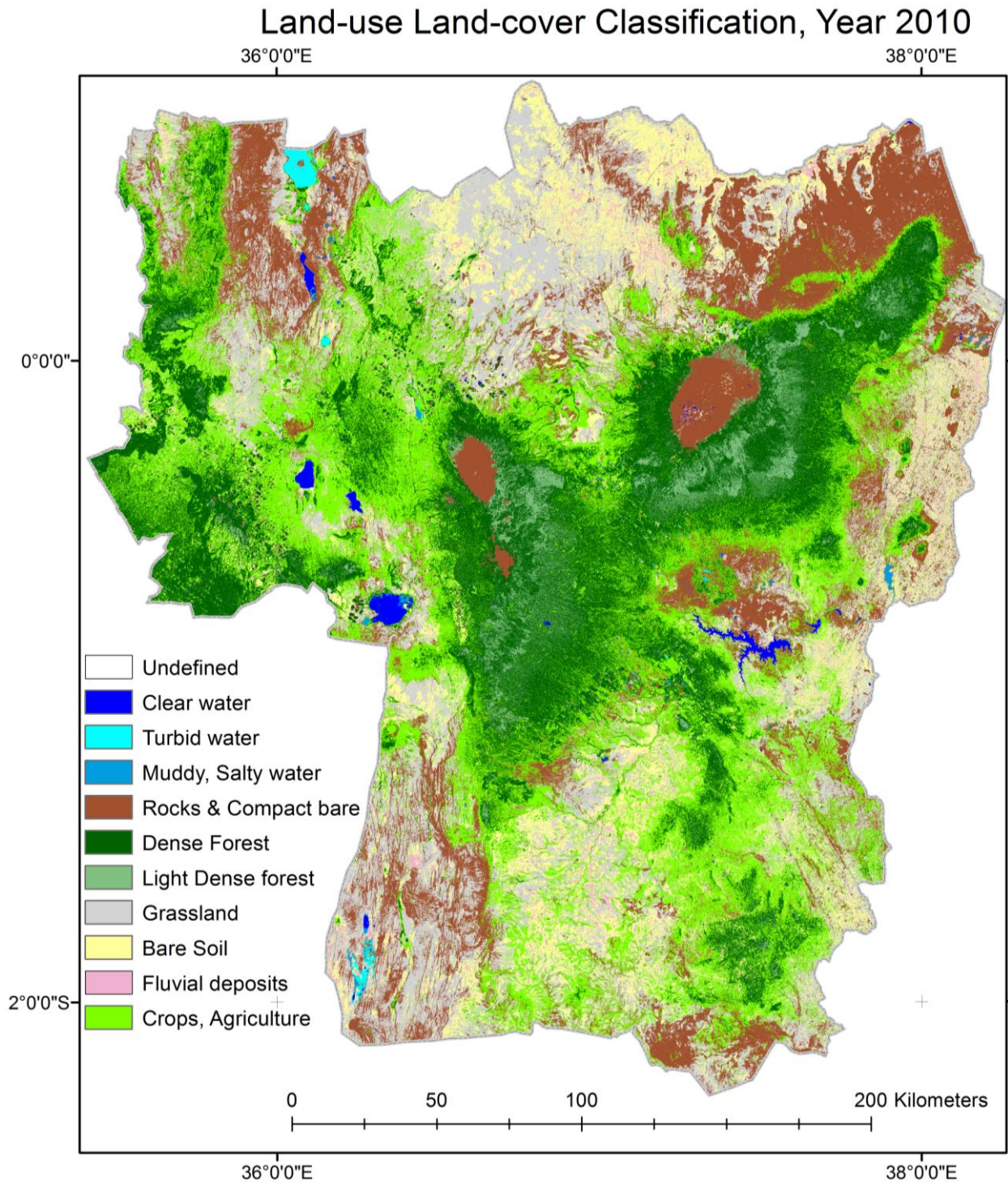


**Figure 4.5:** Land-cover Land-use classification map for Central Region Kenya, Year 2010.

## Land-use Land-cover Classification, Year 2014

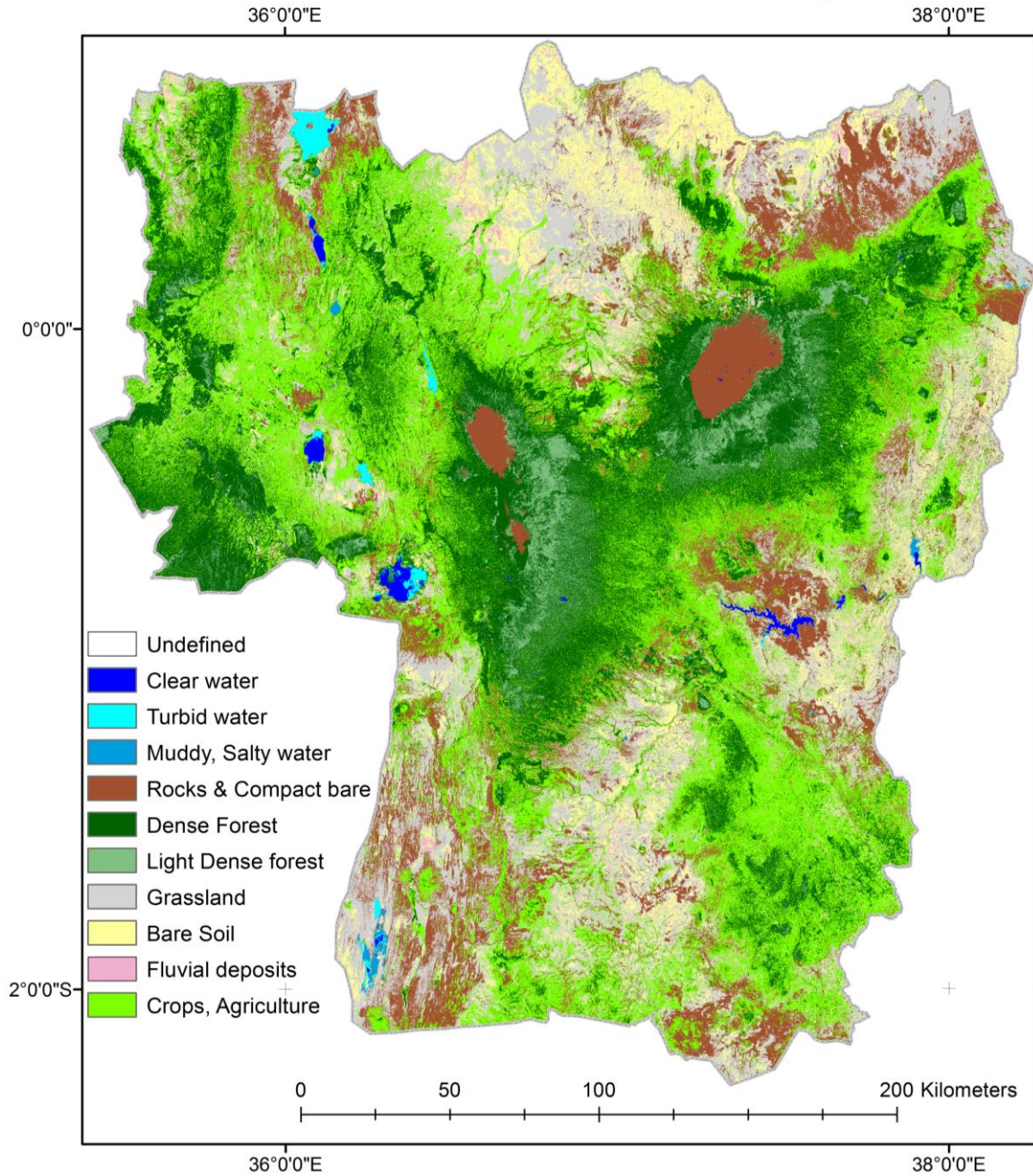


**Figure 4.6:** Land-cover Land-use classification map for Central Region Kenya, Year 2014.

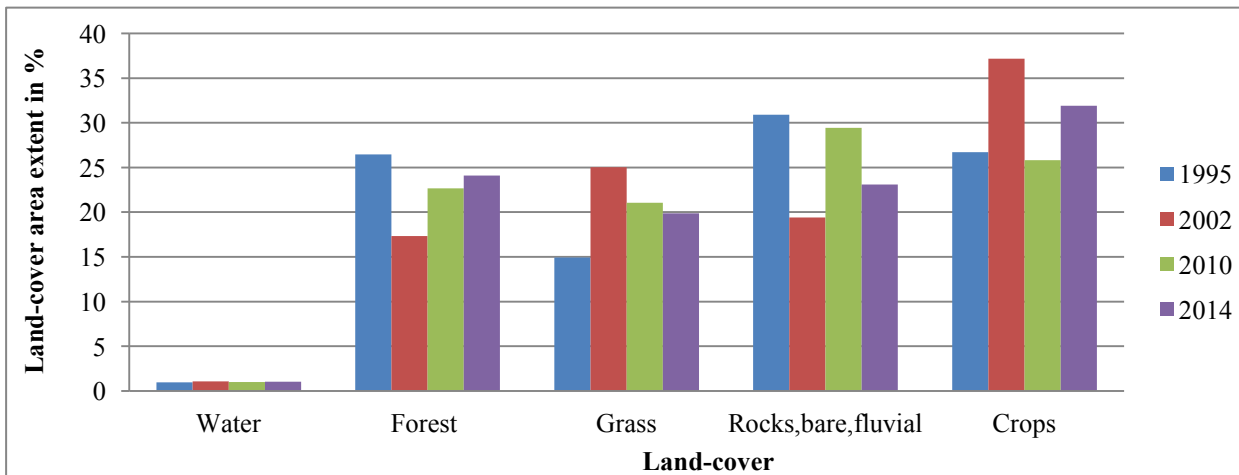


**Figure 4.7:** Regrouped Land-covers trend for the years 1995, 2002, 2010 and 2014.

### 4.3.2 Post Classification Accuracy Assessment

Post accuracy assessment was performed on each of the LULC classification i.e. SPOT 4 (20 m spatial resolution, Table 4.5) imageries were used to assess the accuracies for the years 1995 and 2002, while ALOS data (10 m spatial resolution, obtained from RCMRD<sup>3</sup>) were used to assess the accuracies for the years 2010 and 2014. A total of 500 points, of which 300 were generated using stratified random method (to ensure that all classes were represented) and 200 points were known reference points, were used in the accuracy assessment in each classification. Tables 4.6, 4.7, 4.8, and 4.9 were the resulting confusion matrices from the land-cover classification for the years 1995, 2002, 2010 and 2014, respectively. They contain the accuracy statistics, the overall kappa statistic, the user, and producer accuracies of each class per year.

The overall accuracies were 89.6%, 88.8%, 87.8%, and 87.2% for the years 1995, 2002, 2010, and 2014, respectively. The classifications were rated as satisfactory, since the overall accuracy were greater than the recommended 85% (Anderson et al., 1976; Campbell and Wynne, 2012). In addition, the kappa statistics were well above the recommended 0.8 (Jensen, 2005) i.e. 0.88, 0.87, 0.86, and 0.85 for the years 1995, 2002, 2010, and 2014, respectively. Thus, the classifications were rated good, although there were still small chances of making random errors due to error sources discussed by Congalton (1991), Congalton and Green (2009), and Foody (2002), such as choice of sampling design, 50-30 minimum points per class to be observed, and sampling size.

**Table 4.5:** SPOT series data description.

SPOT 4 - ID	Date	SPOT 1-3 <i>constellation</i> - ID	Date
41373529901220800381I	22nd Jan 1999	31383509406220755451X	22nd June 1994
41373519901220800291I	22nd Jan 1999	31373499406010759351X	1st June 1994
41403549902010808281I	1st Feb 1999	31393509402220803401X	22nd Feb 1994
41403539902010808201I	1st Feb 1999	31393529402220803571X	22nd Feb 1994
41403529902010808111I	1st Feb 1999	31383499407180755331X	18th July 1994
41383539902020749031I	2nd Feb 1999	31403549402070752361X	7th Feb 1994
41383519902020748461I	2nd Feb 1999	31393519402220803481X	22nd Feb 1994
41383529902020748551I	2nd Feb 1999		
41383499902020748291I	2nd Feb 1999		
41383509902020748381I	2nd Feb 1999		
41363499902070752222I	7th Feb 1999		
41373529902070752462I	7th Feb 1999		

<sup>3</sup> RCMRD (Regional centre for Mapping and Regional Development)

**Table 4.6:** Error/ confusion matrix for Land-cover classification Year 1995.

Classes	Reference Data										Row $\Sigma$	Producer acc. %	User acc. %
	Clear	turbid	mudd	Rocks	D. F.	L.D.F.	Grass	Bare	fluvial	Crops			
Clear Water	22	4	0	0	0	0	0	0	0	0	26	91.67	84.62
Turbid Water	0	36	0	0	0	0	0	0	0	0	36	90.00	100.00
Muddy Water	0	0	28	0	0	0	0	0	0	0	28	93.33	100.00
Rocks	2	0	2	50	2	0	4	0	0	4	64	96.15	78.13
D.For.	0	0	0	0	70	2	0	2	0	8	82	97.22	85.37
L.D.F.	0	0	0	0	0	53	0	0	0	0	53	92.98	100.00
Grass	0	0	0	0	0	0	50	2	0	0	52	73.53	96.15
Bare soil	0	0	0	0	0	0	0	38	2	0	40	90.48	95.00
Fluvial	0	0	0	0	0	0	0	0	32	0	32	94.12	100.00
Crops	0	0	0	2	0	2	17	0	0	69	87	85.19	79.31
<b>Column <math>\Sigma</math></b>	<b>24</b>	<b>40</b>	<b>30</b>	<b>52</b>	<b>72</b>	<b>57</b>	<b>68</b>	<b>42</b>	<b>34</b>	<b>81</b>	<b>500</b>		
<i>Overall Classification Accuracy = 89.60%</i>													
<i>Overall Kappa Statistics = 0.8826</i>													

**Table 4.7:** Error/ confusion matrix for Land-cover classification Year 2002.

Classes	Reference Data										Row $\Sigma$	Producer acc. %	User acc. %
	Clear	turbid	mudd	Rocks	D. F.	L.D.F.	Grass	Bare	fluvial	Crops			
Clear Water	30	2	1	0	0	0	0	0	0	0	33	90.91	90.91
Turbid Water	1	37	0	0	0	0	0	0	1	0	39	90.24	94.87
Muddy Water	1	1	35	1	0	0	2	0	0	0	40	92.11	87.50
Rocks	0	0	1	58	3	0	0	0	0	0	62	87.88	93.55
D.For.	0	0	0	2	48	2	0	0	0	3	55	88.89	87.27
L.D.F.	0	0	0	0	0	57	2	1	1	3	64	87.69	89.06
Grass	0	0	0	1	1	2	50	1	1	2	58	87.72	86.21
Bare soil	1	1	0	0	0	2	2	40	2	1	49	93.02	81.63
Fluvial	0	0	0	0	0	0	0	1	27	0	28	84.38	96.43
Crops	0	0	1	4	2	2	1	0	0	62	72	87.32	86.11
<b>Column <math>\Sigma</math></b>	<b>33</b>	<b>41</b>	<b>38</b>	<b>66</b>	<b>54</b>	<b>65</b>	<b>57</b>	<b>43</b>	<b>32</b>	<b>71</b>	<b>500</b>		
<i>Overall Classification Accuracy = 88.80%</i>													
<i>Overall Kappa Statistics = 0.8745</i>													

**Table 4.8:** Error/ confusion matrix for Land-cover classification Year 2010.

Classes	Reference Data										Row $\Sigma$	Producers Acc. %	Users Acc. %
	Clear	turbid	mudd	Rocks	D. F.	L.D.F.	Grass	Bare	fluvial	Crops			
Clear Water	36	0	2	0	0	0	0	1	0	0	39	94.74	92.31
Turbid Water	0	27	2	0	0	0	1	0	0	0	30	93.10	90.00
Muddy Water	2	1	35	1	0	0	0	0	0	0	39	83.33	89.74
Rocks	0	0	0	57	3	0	4	1	0	0	65	93.44	87.69
D. Forest	0	0	0	2	60	4	0	0	0	5	71	88.24	84.51
L.D.F.	0	0	1	0	1	55	0	1	1	3	62	82.09	88.09
Grass	0	1	2	0	0	1	48	2	0	0	54	87.27	88.89
Bare soil	0	0	0	0	0	5	1	33	1	1	41	82.50	80.49
Fluvial	0	0	0	0	0	0	0	1	36	1	38	94.74	94.74
Crops	0	0	0	1	4	2	1	1	0	52	61	83.87	85.25
<b>Column <math>\Sigma</math></b>	<b>38</b>	<b>29</b>	<b>42</b>	<b>61</b>	<b>68</b>	<b>67</b>	<b>55</b>	<b>40</b>	<b>38</b>	<b>62</b>	<b>500</b>		
<i>Overall Classification Accuracy = 87.80%</i>													
<i>Overall Kappa Statistics = 0.8634</i>													

**Table 4.9:** Error/ confusion matrix for Land-cover classification Year 2014.

Classes	Reference Data										Row $\Sigma$	Producers Acc. %	Users Acc. %
	Clear	turbid	muddy	Rocks	D. F.	L.D.F.	Grass	Bare	fluvial	Crops			
Clear Water	8	0	0	0	0	0	0	0	0	0	8	100.00	100.00
Turbid Water	0	16	0	0	0	0	0	0	0	0	16	88.89	100.00
Muddy Water	0	2	9	0	0	0	0	0	1	0	12	90.00	75.00
Rocks	0	0	0	68	0	0	4	1	0	0	74	95.77	91.89
Dense For.	0	0	1	1	85	7	1	0	0	1	105	95.51	80.95
L.D.F.	0	0	0	0	1	20	0	0	0	10	23	62.50	86.96
Grass	0	0	0	1	0	0	74	3	0	6	84	84.09	88.10
Bare soil	0	0	0	0	0	0	1	30	2	2	35	88.24	85.71
Fluvial	0	0	0	0	0	0	0	0	14	0	14	82.35	100.00
Crops	0	0	0	1	3	5	8	0	0	112	129	84.21	86.82
<b>Column <math>\Sigma</math></b>	<b>8</b>	<b>18</b>	<b>10</b>	<b>71</b>	<b>89</b>	<b>32</b>	<b>88</b>	<b>34</b>	<b>17</b>	<b>133</b>	<b>500</b>		
<i>Overall Classification Accuracy = 87.20%</i>													
<i>Overall Kappa Statistics = 0.8463</i>													

### *4.3.3 Change detection*

Change detection was performed by subtracting a latter classification from a former year classification, per epoch, and the cross tabulation change matrices generated as in Tables 4.10, 4.12 and 4.14 for the epoch years 1995-2002, 2002-2010, and 2010-2014, respectively. The diagonal elements in the cross-tabulation matrices were the unchanged pixels, while the off-diagonal elements were the misclassified and misidentified classes. Extracting the column totals as the reference class data, row totals as the classified data, and the diagonal elements as the unchanged pixels, the change statistics were analysed into Tables 4.11, 4.13 and 4.15 for the epoch years 1995-2002, 2002-2010, and 2010-2014, respectively. Thus, the changes were checked within the classes (with the increased land covers having values greater than 100%, while decreased land covers had values of less than 100%), and as a fraction of the total area.

From Tables 4.10 and 4.11, clear, muddy water, rocks, and fluvial changed the most, with over 70% changes. Clear water was lost to muddy water, muddy water was converted mostly to turbid and clear water; rocks were lost mostly to grassland and farmlands, while fluvial were lost to bare lands. However, as a percentage of the total area, changes from farmlands, grasslands, dense forest, barren lands, and rocks had the most significant effect. Areas under crop cover increased with most contribution from grassland and rocks, while dense forest increased with most contribution from light dense forest and farmlands.

On the other hand, changes between the years 2002 and 2010 were analysed using Tables 4.12 and 4.13. Muddy water changed the most (i.e. converted to crops, turbid and clear water), although it had little overall significance effect. Changes from crops, grass, dense forest, rocks, and bare lands were the most influential. Crop cover was converted into grasslands, dense forest, barren lands and rocks, while grassland was converted into crop/farm lands, barren lands, and rocks. Dense forest areas were gained from crop and light dense forest covers, barren lands gained from grassland and crops, while rocks gained most from crops, grassland, and dense forests.

Finally, changes within the time epoch 2010 and 2014 were represented by Tables 4.14 and 4.15. The most significant changes were within crops, dense forest, grasslands, rocks, and bare land covers. Crops gained most from grasslands, rocks, dense forest, and bare lands, while dense forest gained most from crops, light dense forest, and rocks. On the other hand, grasslands were converted to barren lands and silts, barren lands were converted to grasslands.

**Table 4.10:** Cross-tabulation of classification 1995 (columns) against classification 2002 (rows).

		Reference data (1995) (no. of pixels)										
Classification data (2002) , no. of pixels		Clear water	Turbid	Muddy water	Rocks	Dense F.	L.D.F.	Grass	Bare	Fluvial	Crops	Row $\Sigma$
	Clear Water	580,652	7,340	387,246	27,920	25,186	7,850	13,004	4,234	6,480	34,370	1,094,282
	Turbid Water	165,286	446,640	43,948	139,999	860	8	109,638	66,640	58,770	123,318	1,155,107
	Muddy Water	220,938	69,840	209,064	247,766	36,742	828	68,673	23,571	13,468	288,519	1,179,409
	Rocks	163,876	81,752	273,612	15,507,149	193,136	230,330	4,567,929	380,990	153,527	4,129,242	25,681,543
	Dense Forest	120,406	22,724	53,703	2,615,851	17,165,258	3,197,127	1,915,453	659,189	108,334	17,074,114	42,932,159
	L.D.F.	24,985	1,446	3,798	138,670	5,725,621	5,632,706	114,667	47,127	44,561	1,378,386	13,111,967
	Grass	282,039	93,198	182,448	12,516,203	866,095	49,067	40,022,424	14,754,933	577,143	11,541,138	80,884,688
	Bare soil	136,291	61,644	66,778	1,049,616	133,206	28,707	9,468,064	17,662,305	1,791,142	2,273,305	32,671,058
	Fluvial	6,204	5,216	6,906	53,749	3,878	91	398,902	2,816,657	1,023,409	118,830	4,433,842
	Crops	431,362	96,752	401,574	21,662,701	6,610,308	668,950	27,833,629	9,282,025	566,921	52,593,972	120,148,194
Column $\Sigma$	2,132,039	886,552	1,629,077	53,959,624	30,760,290	9,815,664	84,512,383	45,697,671	4,343,755	89,555,194	323,292,249	

**Table 4.11:** Change statistics extracted from Table 4.10 for the years 1995 (reference) and 2002 (classified).

Class	Referenced (1995)	Classified (2002)	Unchanged pixels	% unchanged (within the class)	% unchanged (fraction of total area)	% of classified pixels (2002) as a fraction of the reference classes (1995)
Clear Water	2,132,039	1,094,282	580,652	27.235	0.180	51.326
Turbid Water	886,552	1,155,107	446,640	50.379	0.138	130.292
Muddy Water	1,629,077	1,179,409	209,064	12.833	0.065	72.397
Rocks	53,959,624	25,681,543	15,507,149	28.738	4.797	47.594
Dense Forest	30,760,290	42,932,159	17,165,258	55.803	5.310	139.570
L.D.F.	9,815,664	13,111,967	5,632,706	57.385	1.742	133.582
Grass	84,512,383	80,884,688	40,022,424	47.357	12.380	95.707
Bare soil	45,697,671	32,671,058	17,662,305	38.65	5.463	71.494
Fluvial	4,343,755	4,433,842	1,023,409	23.56	0.317	102.074
Crops	89,555,194	120,148,194	52,593,972	58.728	16.268	134.161
Totals	323,292,249	323,292,249	150,843,579	46.659	46.659	

**Table 4.12:** Cross-tabulation of classification 2002 (columns) against classification 2010 (rows).

		Reference data (2002) (no. of pixels)										
Classification data (2010) , no. of pixels	Class	Clear	turbid	muddy	Rocks	Dense For.	L.D.F.	Grass	Bare	Fluvial	Crops	Row $\Sigma$
	Clear Water	852,552	52,862	348,463	110,361	17,816	2,077	70,274	43,372	7,987	80,791	1,586,555
	Turbid Water	11,311	505,364	37,105	42,812	22,471	2,297	78,747	104,166	1,380	89,430	895,083
	Muddy Water	98,787	110,383	58,830	104,230	48,563	5,354	78,620	31,575	1,749	218,840	756,931
	Rocks	34,925	247,393	471,647	18,768,091	2,643,944	109,791	14,715,124	927,846	28,488	18,450,916	56,398,165
	Dense Forest	44,987	2,476	39,432	363,343	27,897,161	7,206,858	1,800,614	479,977	30,222	26,100,213	63,965,283
	L.D.F.	13,800	115	6,420	240,558	3,056,735	5,062,341	41,023	40,798	1,958	888,408	9,352,156
	Grass	8,055	129,363	76,049	3,573,582	827,622	50,821	35,605,515	11,474,780	348,518	15,938,505	68,032,810
	Bare soil	987	60,492	23,463	281,496	371,166	30,944	9,665,922	14,259,484	2,591,604	6,670,443	33,956,001
	Fluvial	1,839	36,205	6,746	135,491	64,242	9,086	715,788	1,901,621	1,341,452	639,836	4,852,306
	Crops	27,036	10,446	111,243	2,061,499	7,985,691	632,382	18,112,868	3,407,332	81,320	51,074,885	8,350,4702
<b>Column <math>\Sigma</math></b>	1,094,279	1,155,099	1,179,398	25,681,463	42,935,411	13,111,951	80,884,495	32,670,951	4,434,678	120,152,267	323,299,992	

**Table 4.13:** Change statistics extracted from Table 4.12 for the years 2002 (reference) and 2010 (classified).

Class	Referenced (2002)	Classified (2010)	Unchanged pixels	% unchanged (within the class)	% unchanged (fraction of total area)	% of classified pixels (2010) as a fraction of the reference classes (2002)
Clear Water	1,094,279	1,586,555	852,552	77.91	0.264	144.986
Turbid Water	1,155,099	895,083	505,364	43.751	0.156	77.490
Muddy Water	1,179,398	756,931	58,830	4.988	0.018	64.179
Rocks	25,681,463	56,398,165	18,768,091	73.08	5.805	219.607
Dense Forest	42,935,411	63,965,283	27,897,161	64.975	8.629	148.980
L.D.F.	13,111,951	9,352,156	5,062,341	38.609	1.566	71.325
Grass	80,884,495	68,032,810	35,605,515	44.02	11.013	84.111
Bare soil	32,670,951	33,956,001	14,259,484	43.646	4.411	103.933
Fluvial	4,434,678	4,852,306	1,341,452	30.249	0.415	109.417
Crops	120,152,267	83,504,702	51,074,885	42.508	15.798	69.499
Totals	323,299,992	323,299,992	155,425,675	48.075	48.075	

**Table 4.14:** Cross-tabulation of classification 2010 (columns) against classification 2014 (rows).

		Reference data (2010) (no. of pixels)										
Classification data (2014) , no. of pixels	Class	Clear	turbid	muddy	Rocks	Dense F.	L.D.F.	Grass	Bare	Fluvial	Crops	Row $\Sigma$
	Clear Water	951,032	19,338	83,246	41,584	44,755	12,258	27,905	17,178	1,773	55,927	1,254,996
	Turbid Water	328,730	546,712	162,835	158,493	67,305	6,082	93,432	32,244	5,816	207,281	1,608,930
	Muddy Water	2,545	183,262	61,773	57,151	4,965	257	48,145	54,540	25,210	12,151	449,999
	Rocks	123,640	50,433	120,795	27,194,462	1,503,594	292,553	8,829,209	493,629	120,349	9,096,879	47,825,543
	Dense Forest	35,973	14,117	89,979	2,531,423	43,339,759	3,741,432	899,586	634,142	112,725	16,254,086	67,653,222
	L.D.F.	13,960	554	2,891	239,007	4,611,505	5,065,133	15,728	30,540	8,784	270,774	10,258,876
	Grass	44,001	22,386	42,182	9,688,383	577,831	17,252	33,626,409	10,883,339	696,744	8,647,132	64,245,659
	Bare soil	15,047	12,419	11,192	341,870	94,023	4,646	6,215,450	13,693,535	1,939,047	1,176,087	23,503,316
	Fluvial	3,256	2,505	1,787	48,370	80,665	5,184	187,496	1,327,616	1,457,404	144,887	3,259,170
	Crops	70,010	40,098	178,912	16,072,240	13,644,154	209,254	18,092,226	6,790,363	484,528	47,647,298	103,229,083
	<b>Column <math>\Sigma</math></b>	1,588,194	891,824	755,592	56,372,983	63,968,556	9,354,051	68,035,586	33,957,126	4,852,380	83,512,502	323,288,794

**Table 4.15:** Change statistics extracted from Table 4.14 for the years 2010 (reference) and 2014 (classified).

Class	Referenced (2010)	Classified (2014)	Unchanged pixels	% unchanged (within the class)	% unchanged (fraction of total area)	% of classified pixels (2014) as a fraction of the reference classes (2010)
Clear Water	1,588,194	1,254,996	951,032	59.88	0.294	79.02
Turbid Water	891,824	1,608,930	546,712	61.3	0.169	180.41
Muddy Water	755,592	449,999	61,773	8.18	0.019	59.56
Rocks	56,372,983	47,825,543	27,194,462	48.24	8.412	84.84
Dense Forest	63,968,556	67,653,222	43,339,759	67.75	13.406	105.76
L.D.F.	9,354,051	10,258,876	5,065,133	54.15	1.567	109.67
Grass	68,035,586	64,245,659	33,626,409	49.42	10.401	94.43
Bare soil	33,957,126	23,503,316	13,693,535	40.33	4.236	69.21
Fluvial	4,852,380	3,259,170	1,457,404	30.03	0.451	67.17
Crops	83,512,502	103,229,083	47,647,298	57.05	14.738	123.61
Totals	323,288,794	323,288,794	173,583,517	53.69	53.69	

#### *4.4 Discussion*

The results in section 4.3 have demonstrated the conflicting and competing land-uses among forest areas, crops/farmland, grassland, barren lands, and rock land covers. From the Figure 4.7, the forest cover decreased (by 9.14%) by the year 2002, depicting deforestation activities to support farmlands, an issue which jeopardized the water resources (Chacha, 2015; Lindsay and Hans, 2005) and led to declining forest reserves (Baldyga et al., 2008; Muriithi et al., 2013; Were et al., 2013). On the other hand, there were attempts to increase forest areas through government policies and campaign movements, such as the Green-belt movement (Maathai, 2003). The effects are manifested through the increasing dense forest land cover trend in the Figure 4.7, although this requires continued initiatives and goodwill, due to the increasing population and the over-reliance on forest resources as an energy source (Carter and Parker, 2009; César et al., 2014; Karanja and Mutua, 2000). Wandago (2002) recommended initiatives to support the secondary forest and the need to adopt alternative fuel sources as a forest management measure.

The effects of land degradation as a result of deforestation, increased farmlands, and grassland were also captured in the change detection analyses. The increase in grasslands and consequently the grazing land-use associated with it, together with farming activities decreased forest cover, rocks and bare lands. This may support findings by Castro's (1991) study which observed that there were proposals to convert forest reserves into tea farms in some areas within the study area. Consequently, even with increased forest cover, the net effect was increased barren lands, silt and rocks: an observation which could signify desertification effects, especially in the semi-arid parts of the study area (Otieno, 2013).

Overgrazing and nomadic pastoralism effects resulted in exposed bare lands and rocks, in the epoch 2002 to 2010. These observations were in agreement with findings by Kiage et al. (2007) who established that livestock population and deforestation have an effect on land degradation around lake Baringo catchment areas. Consequently, the lake's water turbidity increased and its actual area reduced. In this study, water cover was observed to change within its turbidity forms, i.e. decreased clear water cover by the year 2002, then an increase by the year 2010 and decrease by the year 2014. Clear and muddy water were mostly converted to turbid water: an observation which could hint to conflicts between farmers and pastoralists or water reservoir encroachments (César et al., 2014). The findings of this research were further investigated for climatic effects as in the section 4.4.1 below.

#### *4.4.1 Effects of Climate Variables on Land-use Land-cover (LULC)*

The general trend described by the rainfall data, Figure 4.8, was varying rainfall amounts with maxima peak in the years; 1994, 1997/1998, 2001/2002, 2006/2007, and 2010 and minima amounts in the years; 1996, 1999/2000, 2005, and 2008/2009. In addition, the effect of relief (orographic) rainfall on the windward side of the mountain features, and consequently the drier leeward sides, resulted in modified rainfall amounts.

The results described a pattern of high or low peaks at an interval of every 3-4 years, which may explain observations by Downing et al. (2008), who associated the events to El-Niño (heavy rainfall) and La-Niña, drought events. For example, the 1997/1998 El-Niño event and the 1999/2000 La-Niña drought event were noted as the most severe in the last 50 years (Mogaka et al., 2005). The impacts of these events were also captured by the LULC changes in this study. The green cover (i.e. both forest and crops) were high in the 1995 classification, which captured the high rainfall event in the year 1994. However, by the year 2002 the forest cover had reduced immensely due to the La-Niña event in the years 1999/2000 and forest encroachment. Instead, crop/farmlands which could flourish in short-term rainfall events were improved due to the rainfall event around the year 2001/2002. Consequently, the bare lands/rocks reduced as the areas were converted into grasslands.

On the other hand, the 2010 LULC classification had reduced grasslands and crop/farmlands, following a long dry spell in the years 2008/2009. Consequently, barren lands and rock covers were increased, whereas the forest cover was on the recovery trend as it is less affected by short-term rainfall events. Although less rainfall data were available for most stations from the year 2010, there was another rainfall peak in the years 2014/2015 (Ngethe, 2015). The impacts of this rainfall event were not captured in the 2014 LULC classification, since the Landsat imagery used in the classification was taken earlier in the year of 2014. However, it was evident that forest cover was on a recovery trend, while crop/farmlands and grasslands increased and reduced, respectively. This could be explained by the support for agriculture and the need to meet the increasing population food demands (UNECA, 2013).

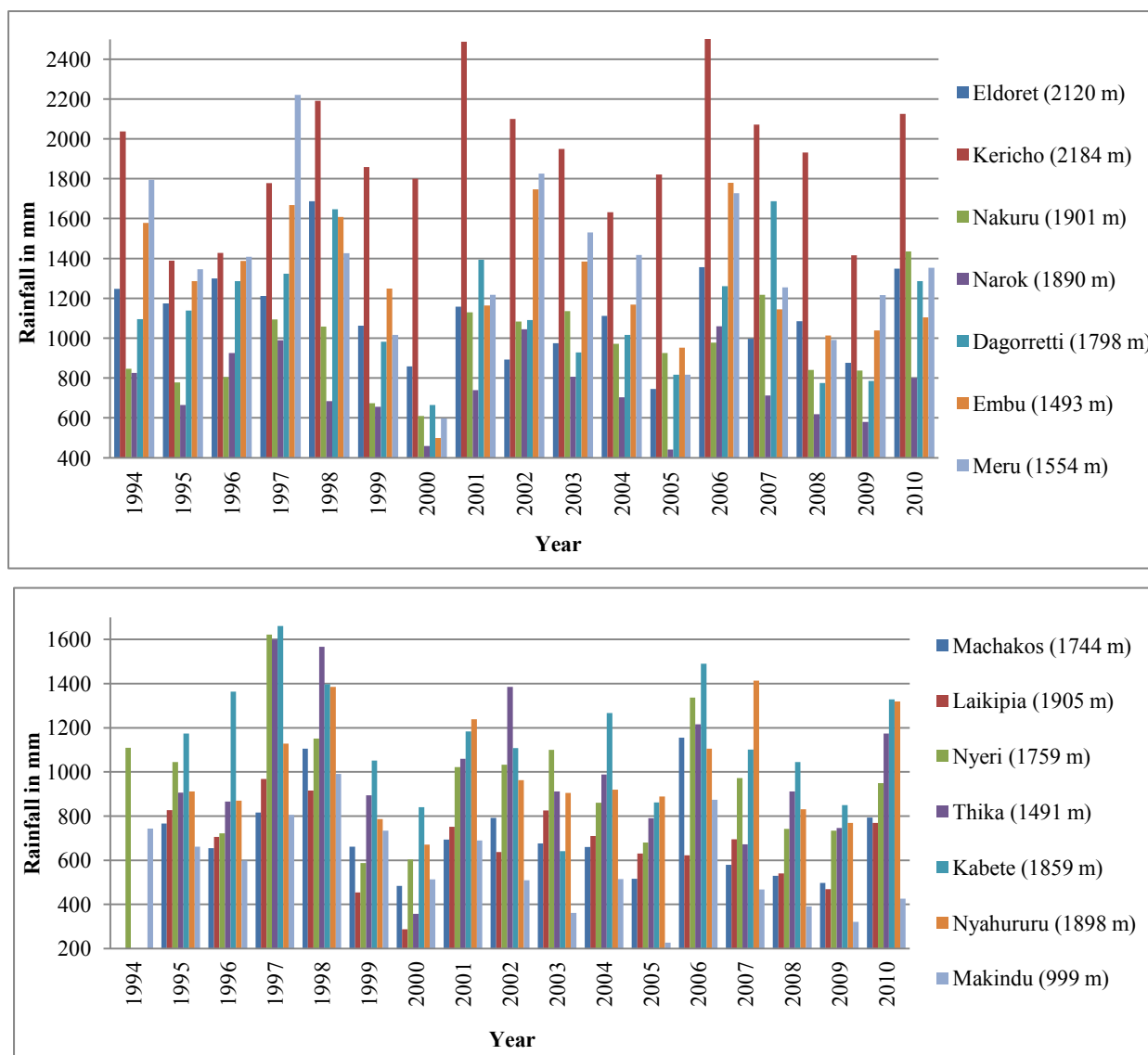


**Figure 4.8:** Total Annual Rainfall trend (Years 1994 - 2010), (Data source: KMD).

In general, the maximum average annual temperature curve (Figure 4.9) showed some inverse characteristics of the rainfall trend, i.e. higher temperatures at low peak rainfall and lower temperatures at higher peak rainfall durations. In addition, temperatures were greatly affected by altitude, i.e. temperatures are cooler with increasing altitude. Consequently, three trends were observed; at low altitude (Makindu station, 1000 m), at high altitude (Nyahururu, 2373 m) and at altitudes between 1450 m and 2150 m. The semi-arid (Makindu) areas had higher temperatures compared to highland regions. On the other hand, low temperatures were observed on the minimum average annual temperature curve (Figure 4.10) during the dry spells (La-Niña event). This could be the effect of lack of cloud cover during the nights which causes more cooling.

The high temperature during the dry spells (La-Niña events) and relatively cooler temperatures during the wet years (El-Niño), could have been partly influenced by the LULC, i.e. the epoch preceding a rainfall event, was characterized by reducing green cover which offered a heating effect. Also, the increased barren lands led to drying soil effect and consequently had an effect on the surface temperatures (e.g. Muthoka and Ndegwa, 2014). Further, urban heating and growth could exacerbate the temperature effect within urban areas (Makokha and Shisanya, 2010; Mbithi et al., 2012). Although the average temperatures are predicted to increase by 0.21°C per decade (McSweeney et al., 2009), the data used in this study was limited to a short duration and hence no substantial observation was made. On the contrary, the temperature varied greatly, with some areas recording the highest maximum (Nakuru, Makindu, Nyahururu) and lowest minimum (e.g. Narok) temperatures in the recent years. Besides, relatively higher minimum temperatures were observed at the lowlands, an observation which could signify warming effects in the lowlands (Funk et al., 2010).

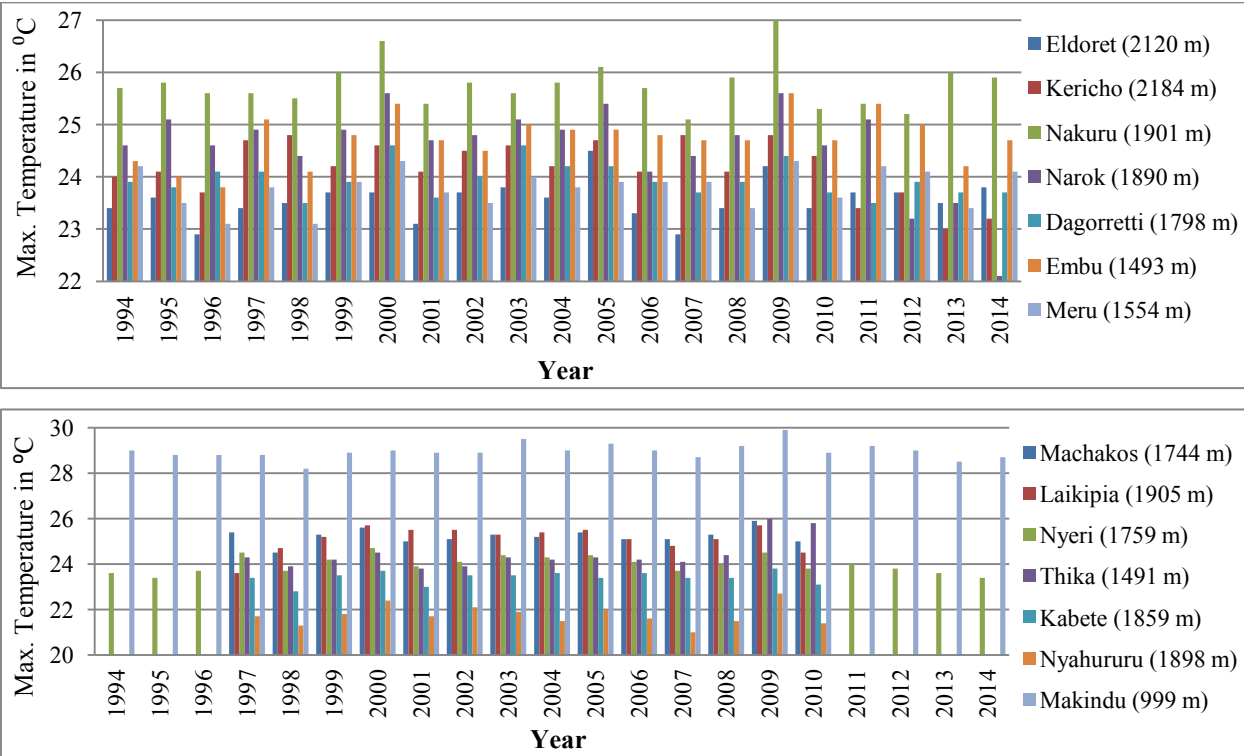


**Figure 4.9:** Maximum average annual temperature (Years 1994 – 2014), (*Data source: KMD*).

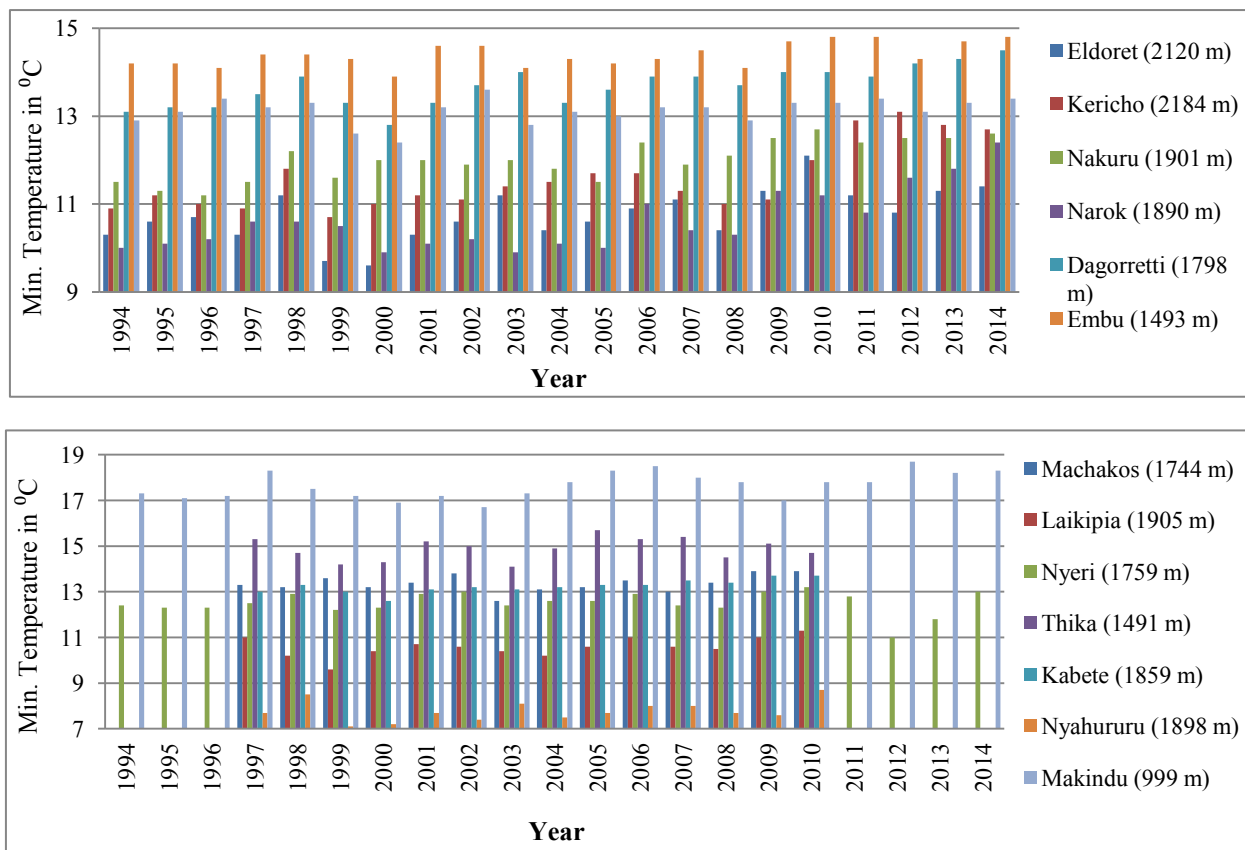


**Figure 4.10:** Minimum average annual temperature (Years 1994 – 2014), (*Data source: KMD*).

#### 4.4.2 Land Cover/use Relation to Root Cohesion

One of the aims of this chapter was to map land cover for use in landslide modelling, using the CHASM model described later in chapter 7. Based on the LULC maps for the years 1995, 2002, 2010, and 2014, each land cover unit was assigned a root cohesion value. However, only areas under vegetation contribute to root cohesion, while non-vegetated areas have only soil cohesion values. The root cohesion values were based on literature (e.g. Ekanayake et al., 1997; Nyambane and Mwea, 2011) as fieldwork did not accomplish this task due to limited resources. The values of root cohesion depend on several factors among them tree species, root network/distribution, diameter, and depth (Coder, 2010).

According to a research conducted by Nyambane and Mwea (2011) to determine the root tensile strength which contributes to soil shear strength, shrubs, tree ferns and grass were found to contribute maximum root strength values of 155 kPa, 188 kPa and 197 kPa, respectively. Their study was carried out on the back slopes of the Aberdare ranges, a region prone to shallow landslides. This study estimated root cohesion values for farmlands and modified grassland values since the study area was vast, extending from the highlands to the savannah areas as in Table 4.16. Previous studies such as Bischetti et al. (2009), Schmidt et

al. (2001), and Schwarz et al. (2010) compared root cohesion values. Barren lands were also assigned small root cohesion values as they would contain roots from dried vegetation. However, root cohesion values differed with depth, with forests having the maximum impact of greater than 1 m.

**Table 4.16:** Relationship between LULC and root cohesion modified after Nyambane and Mwea (2011).

<b>LULC</b>	<b>Root cohesion values range (kPa)</b>
Clear water	0
Turbid water	0
Muddy water	0
Rocks	0
Dense forests	200 - 250
Light dense forests	100 - 200
Grass lands	10 - 50
Bare lands	0 - 10
Fluvial	0
Crops	50 -100

## Chapter 5: Structural Geology Mapping and Lineament Visualization

---

### *5.1 Introduction to Geology and Soil mapping*

Geologic mapping is an important aspect of a landslide study as it provides information about the rock types (lithology), lineament patterns and structures, and faulting. While landslides involve the movement of the weathered rock materials under the influence of gravity (Cruden and Varnes, 1996), lineaments could accelerate landslides as they are lines of weakness, where rock properties change. Although RS provides surface geology data, important underlying rock substrata information could be deduced from surface indicators, land morphology and rock profile information. The surface indicators are derived from the interpretation of the spectral behaviour of rock forming minerals (e.g. calcite, gypsum, quartz) (Zumsprekel and Prinz, 2000). Kruse (1998) argues that the physical rock and soil characteristics (e.g. mineralogy, geochemical signature and weathering properties) form the basis for determining the spatial distribution of geologic units. In addition, the soil type, moisture and vegetation can be indicative of the underlying type of bedrock and structure (Gupta, 1991). Thus, RS data and the advances in DIP has significantly contributed to geological studies, including; lithological discrimination of rocks, rock mineralization, oil and mineral exploration, as well as delineation of structural, geological features (Chen and Campagna, 2009; Gupta, 2003a; Prost, 2001; Warner et al., 2009).

Multispectral and hyperspectral remotely sensed data have proved valuable data sources for geological applications due to their ability to record unique energy interaction with an object at every spectral (i.e. visible, near infrared and mid-infrared) region. This enables the definition of unique spectral signatures which can distinguish the minerals and elements comprised in rocks and soils (Kruse, 1998; Sabins, 1997). The higher the number of channels in the mid-infrared region, the better the sensor for lithological discrimination (van der Meer et al., 2012). Generally, spectral resolution is more appealing compared to spatial resolution for geology mapping applications, although higher spatial resolution increases the density and accuracy of the lineaments extracted (Hung et al., 2005).

Geologic features can be enhanced spectrally and spatially, consequently improving the image hue, tone, texture, fracture pattern, lineaments and their trends (Gupta, 2003b; Gupta and Joshi, 1990). These enhancements result in new detailed images which aid geology visualization, interpretation, feature extraction and categorization (Argialas et al., 2003). For example, contrast enhancement is recommended for monochrome images since it alters the

tonal range of an image (Eyers et al., 1998). The need for spectral enhancement is necessitated by the fact that bands containing most geological information are highly correlated and that they occupy a small part of the spectral region (Abdeen and Abdelghaffar, 2008). Spectral enhancement techniques which have been explored in geology mapping include: transformed feature data transform (PCA, ICA, IHS, TCT), band ratioing and spectral indices, decorrelation stretch, colour combinations, density slicing, and spectral signature analysis (SSA). On the other hand, spatial enhancement techniques, mostly involve image fusion, edge enhancements with filter applications.

Transformed feature data transform are statistical analysis methods which decorrelate the image bands and enhance the spectral response. They may also lead to the elimination of noise, e.g. the Minimum Noise Fraction (MNF) which performs two cascaded PCA, first to estimate noise covariance matrix and perform decorrelation and secondly, scale the noise in the data (Green et al., 1988). TCT is particularly suited to soil mapping as it discriminates soil from vegetation, using three indices associated with soil brightness, greenness and moisture (Crist and Cicone, 1984). IHS transform as an image enhancement method is useful for image fusion and provides an alternative method to view three-colour composite images, transforming the image into spatial (intensity) and spectral (hue and saturation) information (Koutsias et al., 2000).

Principal component analysis is a geometrical transformation which correlates variables into a number of uncorrelated variables PCs in a different orthogonal coordinate system (Richard, 1984). It is based on the global covariance matrix of the full set of image data to compute the new axis (PCs) on which classes are separable. PCA has been shown to enhance the structural differences in geology components, soil, and terrain pattern differentiation (Abdeen and Hassan, 2009; Rawashdeh et al., 2006). ICA is a more rigorous method of generating a transformed set of feature axes (Independent Components, ICs), in which class separation is optimized, i.e. data classes are separated based on class means (which maximizes the separability between the features), while at the same time minimizing the spread (Hyvärinen et al., 2001).

Band ratios involve band division such that a higher band is divided by a lower band in order to enhance geology components (Drury, 1993). They also eliminate shadowing and topographic effects, hence they are suited for complex terrain (Campbell, 2002b). In addition, band ratios are useful for resolving spectral mixture within pixels, especially where the reflectance of rocks is compromised by rock coating (e.g. Bechtel et al., 2002). On the other

hand, spectral indices are normalized band ratios which maximise the sensitivity of the target features. The successful implementation of band ratios and spectral indices is dependent on the understanding of the multispectral regions which emphasize and highlight the differences in the spectral reflectance of land surface/target material (Richards and Jia, 2006).

Colour composites (real or false, FCC) involve viewing three bands which are individually informative and collectively least correlated in the RGB channels (Ali et al., 2012; Sabins, 1997). FCC is one of the commonly used methods to visually interpret a multispectral image (Novak and Soulakellis, 2000). Methods such as PCA, Optimum Index factor, and band ratios are often used to process the bands and reduce correlation (e.g. Abdeen and Abdelghaffar, 2008; Al Muntshry, 2011; Kavak, 2005). Density slicing as an image enhancement method allows colour assignment using the histogram, often resulting in distinct colour patterns compared to the colour composite images (Sabins, 1999).

Lineament mapping is essential to landslide hazard assessment and structural geology studies as it reveals the structure of the underlying rock basement (Ramli et al., 2010). Lineament enhancement and extraction is boosted by higher spatial resolution afforded by PAN bands or some multispectral resolution satellite (e.g. WorldView-2); image fusion with SAR data which has texture and roughness information; the use of high resolution DEMs; and the improvements in automating lineament extraction through softwares such as PCI Geomatica and Canny algorithm (Kocal et al., 2004; Marghany and Hashim, 2010a, 2010b; Qari et al., 2008). Such softwares utilise edge enhancement (edge detectors, filters) to enhance boundary features and smooth internal heterogeneities (Shapiro and Stockman, 2000), and applications of thresholding and line linking.

The aim of this chapter is to map soils, discriminate lithology components, and visualize lineaments, since geology is a landslide predisposing factor. RS techniques were explored since the study area is medium scale and the available geological maps were vector maps (e.g. Kenya GIS data ILRI<sup>4</sup> website) with much generalization effects. In addition, there was need to develop a methodology which could be utilized to update geological maps. Band ratio combinations and PCA analysis were explored given the properties that: Landsat imagery is multispectral data; the mid-infrared region is more suited for rock and soil studies, i.e. Landsat TM/ETM+ band 5 has little influence from vegetation and has high soil reflectance values, Landsat band 7 is a geology band (Boettinger et al., 2008; Mia and Fujimitsu, 2012).

---

<sup>4</sup> ILRI – International Livestock Research Institute

## 5.2 Methodology

The choice of Landsat satellite imagery was based on its availability and suitability for geological mapping. However, the challenge was that existing knowledge was on geology mapping in arid and semi-arid areas, whereas this research study area contained both semi-arid and highland regions. First, Landsat OLI (year 2014) was chosen following better discrimination ability in geology mapping, in a comparison with Landsat ETM+ by Mwaniki et al. (2015d). Secondly, image enhancements were explored, followed by classification aided by density slicing of band ratios. The methodology is described in the sections below.

### 5.2.1 Data Description

Landsat satellite imagery (OLI, year 2014, described in Table 5.1), 30 m spatial resolution were downloaded from the USGS website and pre-processed to reduce atmospheric effects. The Landsat OLI imagery had 0-10% cloud cover in some areas due to high relief cloud condition. In addition, the datasets were taken within the months of January and February (dry season), thereby eliminating the need for radiometric correction. The cloud cover in Landsat 8 was eliminated by masking with band 9 and image patching. Image co-registration was not necessary as the datasets were already geo-referenced under the UTM WGS 84 system. Mosaicing was performed using histogram matching in overlap areas followed by subsetting using an AOI file.

**Table 5.1:** Landsat imagery data description.

<b>Landsat 8</b>	<b>Date of acquisition</b>
LC81680602014034LGN00	3rd Feb 2014
LC81680612014034LGN00	3rd Feb 2014
LC81690602014025LGN00	25th Jan 2014

### 5.2.2 Image Enhancement with Landsat ETM+ and OLI for Geological Mapping

Figure 5.1 is the methodology flow chart which summarizes the steps implemented to obtain a geology map. It is a summary of the various image enhancement methods prior to lineament visualization, soil mapping and structural geology mapping. Lithology enhancement aiding discrimination was explored using band ratios, since they highlight the differences in spectral reflectance of target features better than data transformation methods like PCA and ICA, which are feature enhancement methods as well as data reduction methods. From algebra combinations and permutations, there were several possible combinations of band ratios in an FCC: i.e. Landsat 8 with 7 bands (1-7) and only 3 band ratios in a FCC, then 35 combinations were possible (B n a, 2004). However, to achieve enhanced geology contrast, the principle that higher band is divided by a lower band was applied (Drury, 1993). In addition, the mid infrared region bands 7 and 6 (Landsat 8) contain most rock and soil information, thus they

were used as numerators in the band ratios. The implementation of these criteria resulted in the combinations in Figure 5.2.

According to Mwaniki et al. (2015d), geology contrast improved with less band repetition, i.e. in the numerator or denominator, and that more contrast was achieved using bands from different spectral regions. Thus, using Landsat 8 imagery, geology contrast was achieved using the FCC {4/2, 7/3, 6/5}, Figure 5.2 (a) and FCC {4/2, 7/3\*7/4, 6/5}, Figure 5.2 (b). In this case, the mid-infrared bands 6 and 7 were used to provide the rock and soil information, while band 5 emphasized vegetation.

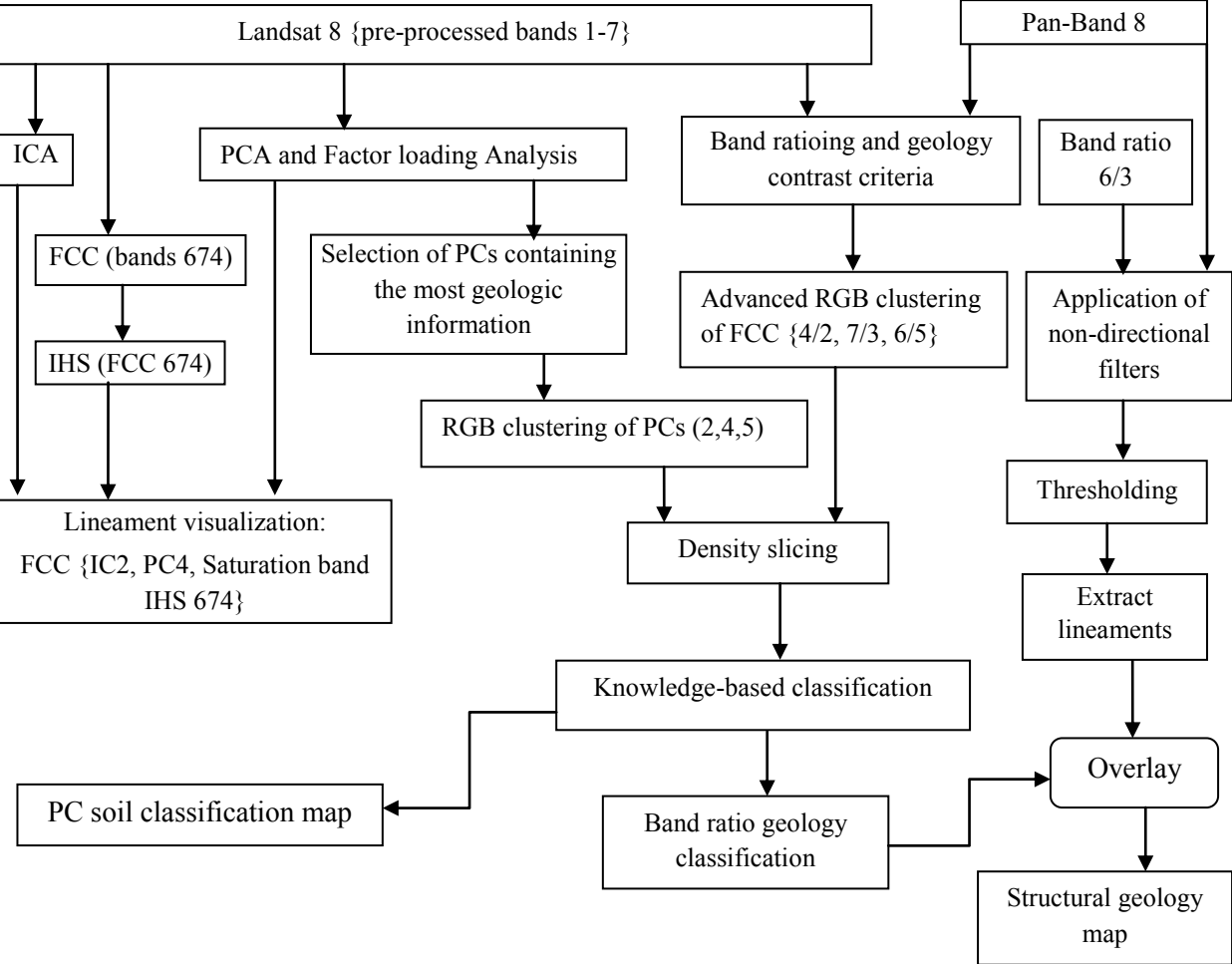


**Figure 5.1:** Summary of the methodology flow chart with Landsat 8 image enhancement.

Based on the above band ratio combinations, knowledge-based classification was performed following density slicing of the band ratios as described in the section 5.2.4. On the other hand, a soil map was implemented with a similar classification using PCs containing the most geologic information, section 5.2.4.

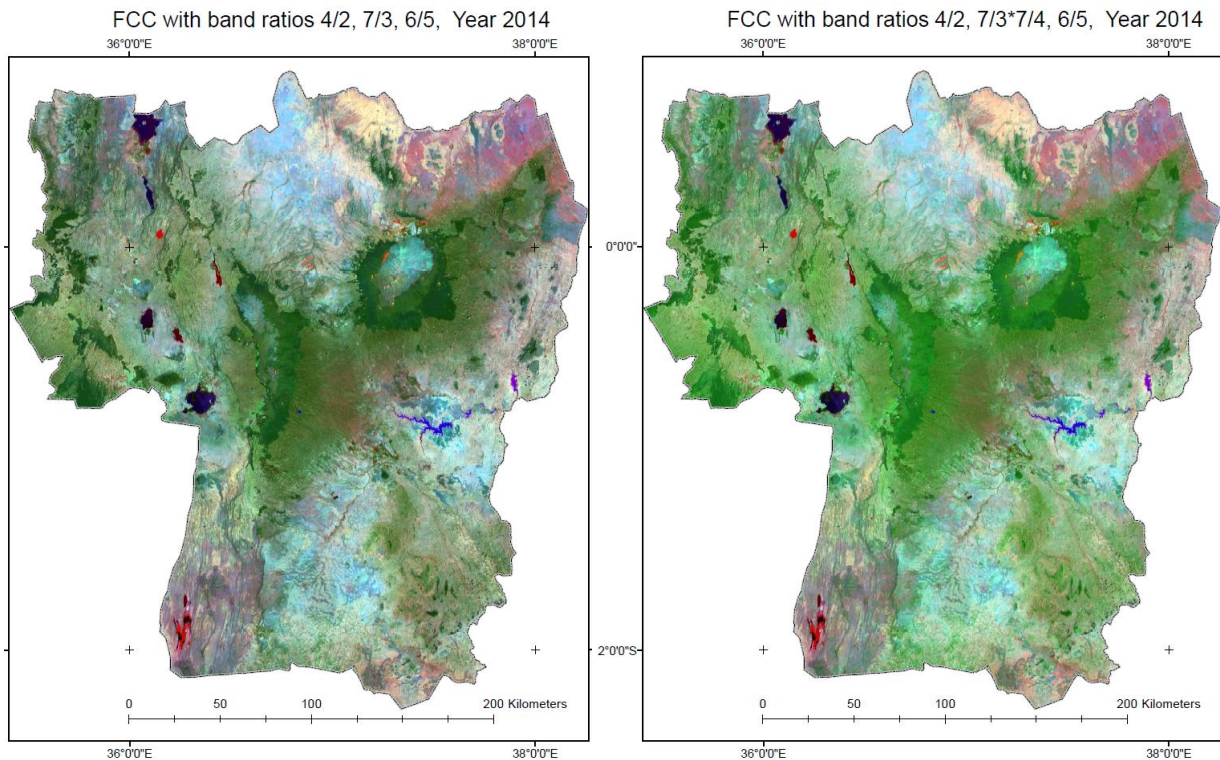


**Figure 5.2:** FCC Band ratio combination with Landsat 8: (a) 4/2, 7/3, 6/5 (b) 4/2, 7/3\*7/4, 6/5.

### 5.2.3 Lineament Enhancement and Visualization

The first step towards lineament enhancement and visualization was to investigate bands with texture information. Secondly, standard PCA was performed on the pre-processed Landsat 8 8 imagery, in order to investigate the PCs containing most geologic information as well as lineament features. The resulting covariance-variance matrix was analysed through PCA factor loading as in Table 5.2. From the Table 5.2, PC1 had a lot of information from the mid-infrared region bands. However, all the information was positively correlated and thus difficult to highlight geology or lineament information. PC2 had a lot of information from the NIR band, thus it highlighted vegetation information. Information from the mid-infrared region in PC3 had similar correlation with vegetation information from band 5. Thus, water information was well discriminated from other information as it had an opposite correlation. Both PC4 and PC5 had the geology band 7 and the mid-infrared band 6, well differentiated. Additional information was provided by the red bands where vegetation has little reflectance. Thus, PC4 had the most enhanced lineament features using the PCA enhancement technique.

**Table 5.2:** PC Factor loading covariance-variance matrix, Landsat 8, Year 2014.

	PC1	PC2	PC3	PC4	PC5	PC6	PC7
Eigvec. 1	0.24099	-0.05290	-0.55771	0.40784	-0.26256	0.46573	0.41942
Eigvec 2	0.21217	0.00164	-0.47775	0.20939	-0.08576	-0.19418	-0.79864
Eigvec 3	0.21104	0.03187	-0.37807	-0.09955	0.14961	-0.77211	0.42786
Eigvec 4	0.23250	0.22847	-0.33049	-0.62980	0.48878	0.38262	-0.05071
Eigvec 5	0.58467	-0.75238	0.21025	-0.20441	-0.06988	0.02520	-0.02421
Eigvec 6	0.56277	0.37244	0.37243	0.47883	0.42009	0.00958	0.00558
Eigvec7	0.37386	0.48909	0.16014	-0.33498	-0.69358	-0.04594	0.00235
Var. contr. in %	<b>91.596</b>	<b>6.840</b>	<b>1.209</b>	<b>0.208</b>	<b>0.122</b>	<b>0.020</b>	<b>0.005</b>

From the PCA loading analysis information, it was observed that in addition to the mid-infrared bands, the red band contributed to the lineament enhancement. Thus, the bands (7, 6, & 4) were extracted through layer-stacking into an FCC, which was enhanced further through the IHS transformation. The saturation band (which contains spectral information) was extracted to also visualise the lineaments. Finally, ICA which provides superior feature class separation compared to the PCA was also performed on the pre-processed Landsat 8 imagery. The results were enhanced lineament features from the first IC (IC1). The three lineaments enhanced bands were layer-stacked into FCC {IC1, PC4, Saturation band of IHS 674}, Figure 5.3.

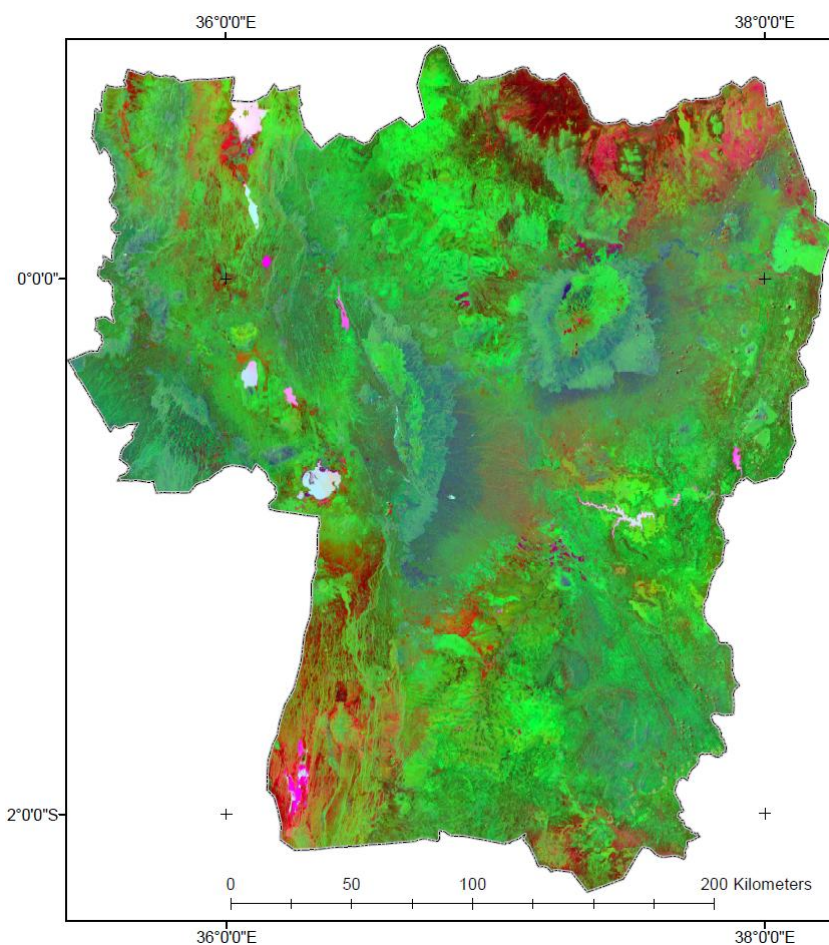


**Figure 5.3:** FCC {IC1,PC4, Saturation Band (6,7,4)} Landsat 8.

An alternative approach to extract and visualise lineaments was achieved by the application of filters on the band ratio with most texture information and also pan-band 8. Consequently, the band ratios were examined for texture enhancement, since they were more enhanced than the actual bands. It was found that the band ratio 6/3, had the most enhanced texture information compared to the other band ratios. Non-directional Sobel filter (5 X 5 kernel) was run through the 6/3 band ratio followed by thresholding to extract the significant lineament features. Similarly, the procedure was repeated with pan-band 8 and the results (from filter applications and thresholding using band ratio and band 8) were merged into a single file i.e. pan-band 8 and band ratio 6/3 (Figure 5.4). However, earlier research by Mwaniki et al. (2015d) had established that lineaments extracted from Landsat 8, pan-band 8 had more noise (unwanted edges) as compared to those extracted from Landsat 7, band 8 (Figure 5.4 b). This was attributed to the spectral coverage (only the visible region) of band 8 in Landsat 8, while Landsat 7, band 8 has wider spectral coverage (visible and NIR bands). Hence, the authors observed better clarity of the lineaments and drainage features from Landsat 7, band 8 compared to Landsat 8.

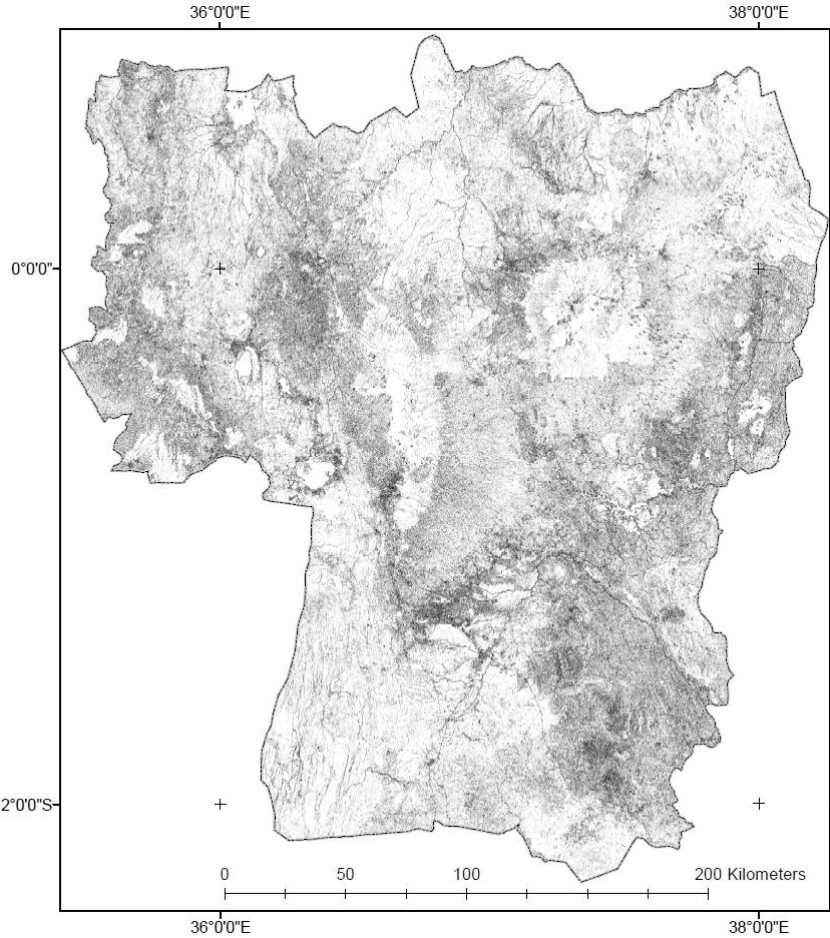


**Figure 5.4:** Lineament and drainage features map using pan-band 8 and band ratio 6/3.

### 5.2.4 Knowledge Based Classification

Geology map using Landsat 8 band ratios 4/2, 7/3, 6/5 formed the basis for the classification. Density slicing with the help of colours was the first step in class assignment. This was followed by establishing class boundaries as in the Table 5.3 (Landsat 8, band ratios). The boundary information was set and saved into a knowledge-based classification file, with the band ratio files as the variables. The following lithology categories were mapped using Landsat 8 band ratios (see, Table 5.3): igneous, basic igneous, basalt, acidic igneous, granites, intermediate igneous, intermediate A.T.P (andesite, trachyte, phonolite), ultra-basic igneous, pyroclastic unconsolidated, acidic metamorphic, basic metamorphic, eulian unconsolidated, fluvial, classic sediments, organic unconsolidated, organic, carbonates/limestone, and water classes.

The PCs containing the most geology-soil enhanced features PCs 3, 4 & 5, with an additional PC1 were used to map soil. The FCC containing the PCs, Figure 5.5 was density sliced and classified according to the boundary classes in Table 5.4. The following soil types were mapped; clay, very clayey, red volcanic, loam, sands, volcanic rocks and water types.

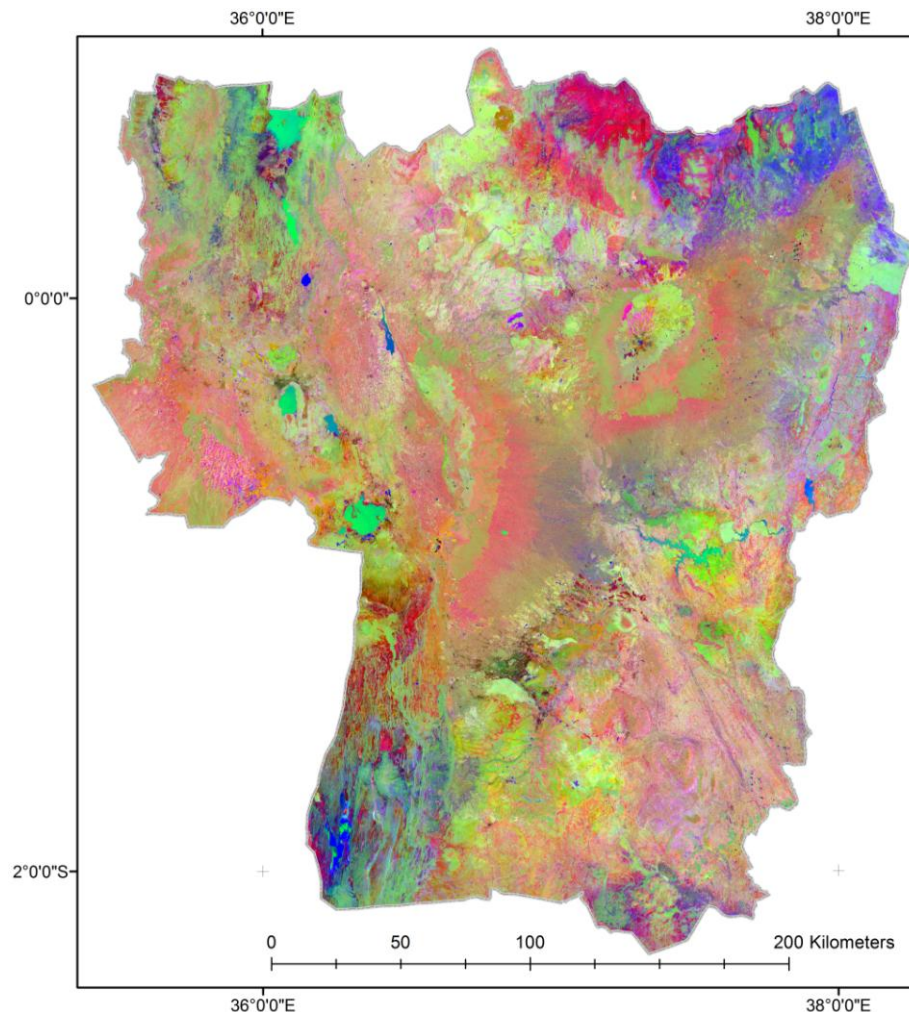


**Figure 5.5:** FCC {PCs 1,4,5} Landsat 8.

**Table 5.3** Knowledge based classification rules with band ratios 4/2, 7/3, and 6/5, Landsat 8.

Rock type	4/2 (0- 14.69)	7/3(0 – 7.91)	6/5(0 – 12.99)
Igneous rock	0.75 – 0.3	0.725 – 0.35	0.75 – 0.5
	1 – 0.8	0.7 – 0.6	0.75 – 0.35
Basic igneous	< 0.5	< 0.875	< 0.65
	1 – 0.4	0.35 – 0.150	< 0.5
Basalts	0.8 – 0.5	> 0.6	0.75 – 0.25
	1.05 – 0.8	> 0.9	< 0.75
Acidic igneous	0.85 – 0.6	0.9 – 0.6	> 0.75
Granite	0.93 – 0.5	1.175 – 0.85	> 0.9
	0.6 – 0.45	0.85 – 0.6	> 0.75
	< 0.6	< 0.6	> 0.5
Intermediate igneous	1 – 0.8	0.7 – 0.85	0.35 – 0.85
	1 – 0.8	0.85 – 0.90	0.4 – 0.75
Intermediate (A.T.P)	> 0.93	0.85 – 1.175	1.35 – 0.95
Ultra basic igneous	1 – 0.655	0.6 – 0.35	< 0.65
	1.1 – 0.75	0.6 – 0.25	0.9 – 0.5
Pyroclastic unconsolidated	0.75 – 0.5	0.6 -0.35	< 0.5
Acidic metamorphic	1 – 0.93	> 0.85	0.95 – 0.75
	> 1.2	0.85 – 0.6	> 0.85
Basic metamorphic	< 1.2	> 1.175	> 0.75
Eulian unconsolidated	> 1	1 – 0.5	0.95 – 0.25
Fluvial	> 1.2	> 1.175	> 0.8
Classic sediments	1 – 0.8	0.7 -0.6	0.85 – 0.75
	> 1	1 – 1.175	0.95 – 0.25
Organic unconsolidated	0.93 – 0.5	1.175 – 0.75	0.75 – 1.0
Organic	> 1	< 0.6	< 0.5
Carbonates/Limestone	1.1 – 0.8	0.9 – 0.52	> 0.85
	0.8 – 0.65	0.6 – 0.3	> 0.75
	> 1.05	0.5 – 0.25	0.825 – 0.5
Clear water	< 0.6	< 0.15	< 1
Turbid water	1 – 0.6	< 0.4	< 1
	< 0.6	< 0.15	< 1
Salty water	> 1	< 0.5	< 0.5
Clay deposits	< 0.6	0.55 – 0.15	> 0
	1 – 0.6	< 0.6	> 0.75

**Table 5.4:** Knowledge based classification boundaries using PCs to map soil.

Element		PC3	PC4	PC5	PC1
	Histogram range	-196 539 to 6 957.98	-6 944.88 to 1 908.32	-15 372.2 to 6 182.22	0 to 66 787.2
Volcanic rocks (agglomerates)		< 0	> 500	< 0	
Clay soils		< -1 000	< 0	> 500	
Red volcanic soils		> 500	0 – -1 000	< 0	
Very clayey soils (Tuff)		< 0	500 – 0	< 0	
Loam (volcanic ashes)		1 500 – 0	< 0	500 - 0	
Sands (sedimentary deposits)		> 500	< -1 000	< 0	
Shallow water		< -2 500	> 500		< 4 000
Turbid water		< - 4 000		1 300 – -500	< 6 000
Salt bearing rocks		< - 4 000	< - 500	> 1 300	> 4 000

### 5.3 Results from Geology and Soil Mapping

The Figure 5.6 is the result obtained from the geology classification using Landsat 8, band ratios 4/2, 7/3, and 6/5. In general, three rock types were mapped i.e. igneous, metamorphic and sedimentary rocks as provided by the provisional existing vector lithology map Figure 5.7, which was used to guide the classification. The geology classification was overlaid with the lineament and drainage feature map extracted previously (Figure 5.4) as in Figure 5.8.

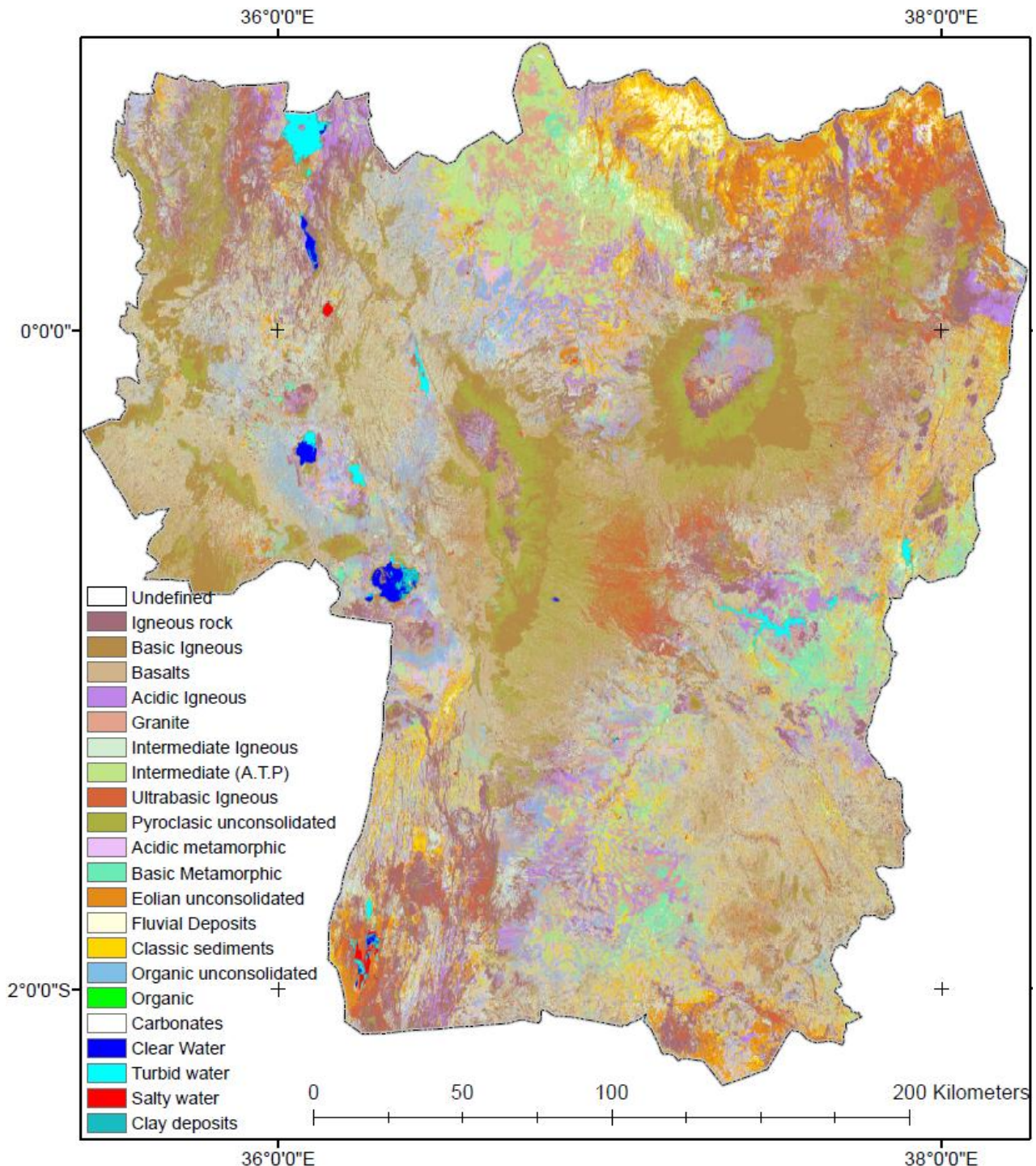


**Figure 5.6:** Geology classification map using Landsat 8, band ratios (4/2, 7/3, 6/5).

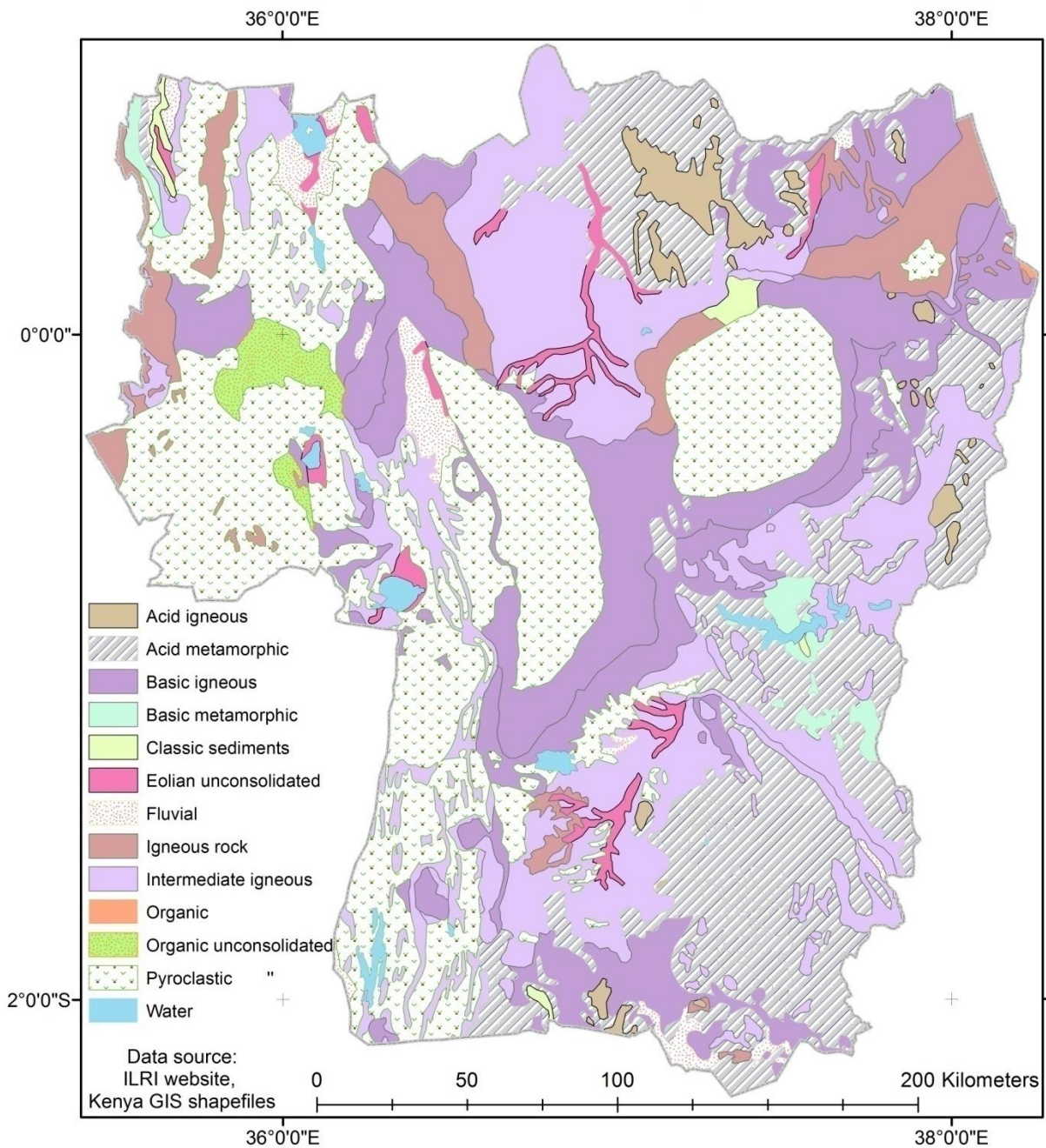


**Figure 5.7:** Existing vector lithology map of the study area.

Accuracy assessment was performed using geology information extracted from existing maps for the following areas: Nairobi, Bisil, Kajiado, Suswa, Magadi areas (Guth, 2014), Mulutu location (Kithome, 2012), Makueni (Mwanzia, 2014), Athi river (Wamwangi, 2010), and borehole data containing lithology description for the Rift –Valley region (Allen and Darling, 1992; Allen et al., 1989). A total of 480 points bearing the geology description were extracted and used to assess the accuracy of the classified geology map (Figure 5.6). This resulted in the contingency table (confusion matrix) presented by Table 5.5 (a) and (b). The overall classification accuracy was 74.38%, while the Kappa statistic was 0.7095. It was

observed in the Table 5.5 that some classes (fluvial and organic) lacked reference information because this was dependent on the availability of existing geology maps.

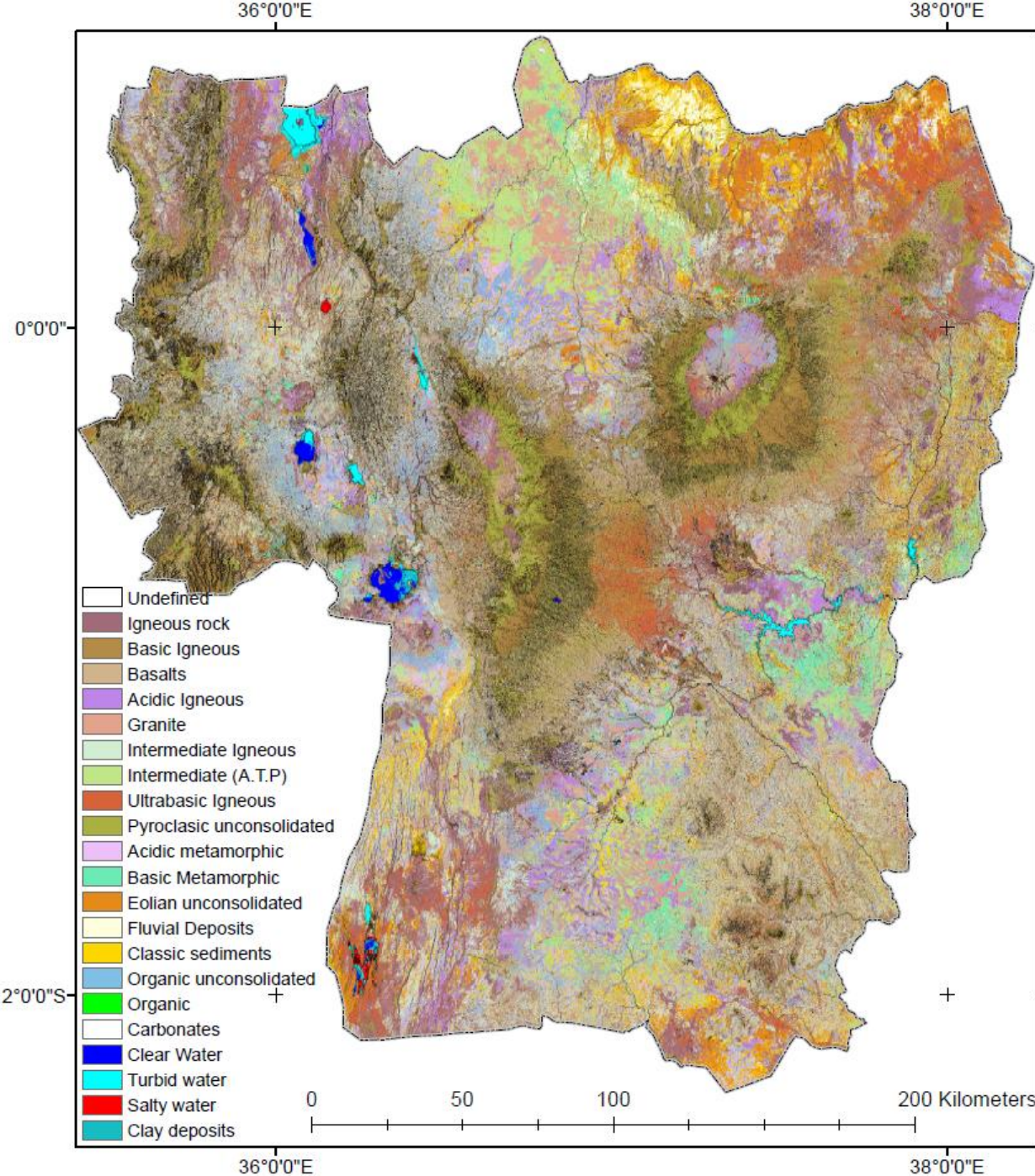


**Figure 5.8:** Structural Geology map using Landsat 8.

**Table 5.5 (a):** Error/confusion matrix for the Geology classification.

Classes	References																Row $\Sigma$	
	Igneous	Basic Igneous	Basalts	Acidic Igneous	Granite	Intermediate Igneous	Intermediate (A.T.P)	Ultrabasic Igneous	Pyroclastic uncons.	Acidic metamorphic	Basic metamorphic	Eolian Unconsolidated	Fluvial deposits	Classic sediments	Organic Unconsolidated	Organic		Carbonates
Igneous rock	40	4	1	1	0	0	0	2	1	0	0	1	0	0	0	0	0	50
Basic Igneous rock	0	4	0	0	1	0	0	0	0	0	0	0	0	1	0	0	0	6
Basalts	3	7	105	1	7	2	8	9	14	5	1	3	4	7	0	0	0	176
Acidic igneous rock	0	1	0	10	0	0	0	0	0	0	0	1	0	0	0	0	0	12
Granite	0	0	0	0	16	0	0	0	1	0	0	0	0	1	0	0	0	18
Intermediate Igneous	1	1	0	0	0	55	4	1	1	4	0	0	1	1	0	0	0	69
Intermediate (A.T.P.)	0	0	0	0	0	0	9	0	0	0	0	0	0	1	0	0	0	10
Ultrabasic igneous	0	0	0	0	0	0	1	7	0	0	0	0	1	0	0	0	0	9
Pyroclastic unconsolidated	1	1	0	0	1	1	1	2	27	0	0	0	0	1	0	0	0	35
Acidic metamorphic	0	0	0	0	0	0	0	0	0	29	1	0	0	0	0	0	0	30
Basic Metamorphic	0	0	0	0	0	0	0	1	0	0	4	0	0	0	0	0	0	5
Eolian unconsolidated	0	0	0	0	0	2	0	2	0	0	1	21	0	0	0	0	0	26
Fluvial deposit	0	0	0	0	0	0	0	0	0	0	0	0	0	0	0	0	0	0
Classic sediment	0	0	0	0	0	0	0	0	0	0	0	0	0	7	0	0	0	7
Organic unconsolidated	1	0	0	1	0	0	0	0	0	1	0	0	1	0	23	0	0	27
Organic	0	0	0	0	0	0	0	0	0	0	0	0	0	0	0	0	0	0
Carbonates	0	0	0	0	0	0	0	0	0	0	0	0	0	0	0	0	0	0
<b>Column <math>\Sigma</math></b>	46	18	106	13	25	60	23	24	44	39	7	26	7	19	23	0	0	480
<i>Overall Classification Accuracy = 74.38%</i>																		
<i>Overall Kappa Statistics = 0.7095</i>																		

**Table 5.5 (b):** Accuracy statistics extracted from Table 5.5 (a).

	Reference $\Sigma$	Classified $\Sigma$	Number correct	Producer Accuracy %	User accuracy %	Kappa statistic
Igneous rock	46	50	40	86.96	80.00	0.7791
Basic Igneous rock	18	6	4	22.22	66.67	0.6538
Basalts	106	176	105	99.06	59.66	0.4841
Acidic igneous rock	13	12	10	76.92	83.33	0.8288
Granite	25	18	16	64.00	88.89	0.8829
Intermediate Igneous	60	69	55	91.67	79.71	0.7685
Intermediate (A.T.P.)	23	10	9	39.13	90.00	0.8950
Ultrabasic igneous	24	9	7	29.17	77.78	0.7662
Pyroclastic unconsolidated	44	35	27	61.36	77.14	0.7487
Acidic metamorphic	39	30	29	74.36	96.67	0.9638
Basic Metamorphic	7	5	4	57.14	80.00	0.7971
Eolian unconsolidated	26	26	21	80.77	80.77	0.7968
Fluvial deposit	7	0	0	---	---	0.0000
Classic sediment	19	7	7	36.84	100.00	1.0000
Organic unconsolidated	23	27	23	100.00	85.19	0.8445
Organic	0	0	0	---	---	0.0000
Carbonates	0	0	0	---	---	0.0000
Totals	480	480	357			

On the other hand, the PCs (3, 4, 5) containing the most geology - soil information from Landsat 8 were the basis for the soil classification map, Figure 5.9. This was compared to the existing vector soil map Figure 5.10, which was the basis for assigning soil classes during the classification. The visual comparison of Figures 5.9 and 5.10 revealed that the classified soil map captured the general soil classes and provided the missing data in some areas on the Figure 5.10. Further, the soil distribution was revised following the distribution of the parent rock materials, i.e. red volcanic soils from igneous rocks, very clayey soils from the pyroclastic rocks, loam soils from the intermediate igneous and metamorphic rocks, sands from the fluvial rock.

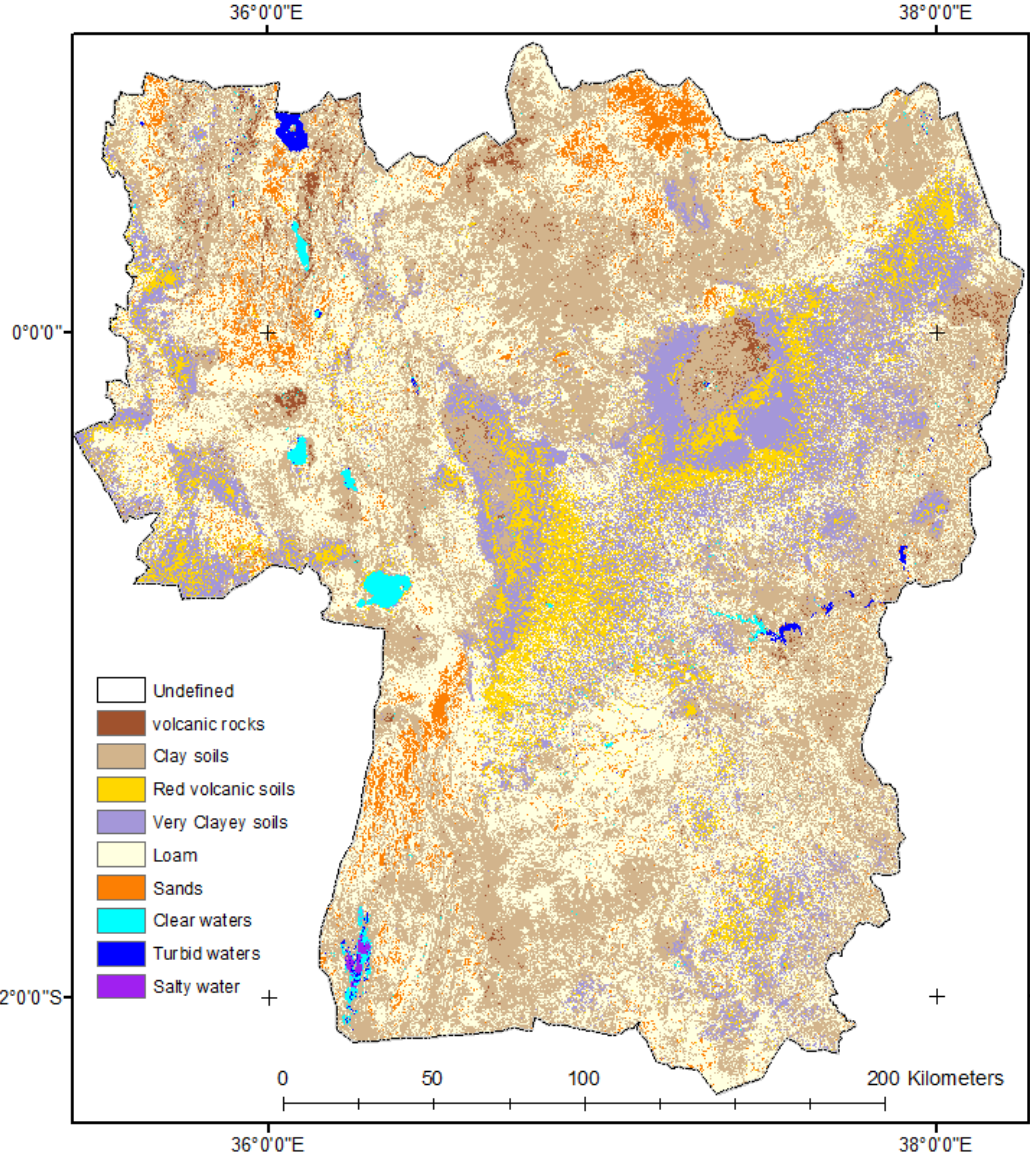


**Figure 5.9:** Soil classification map.

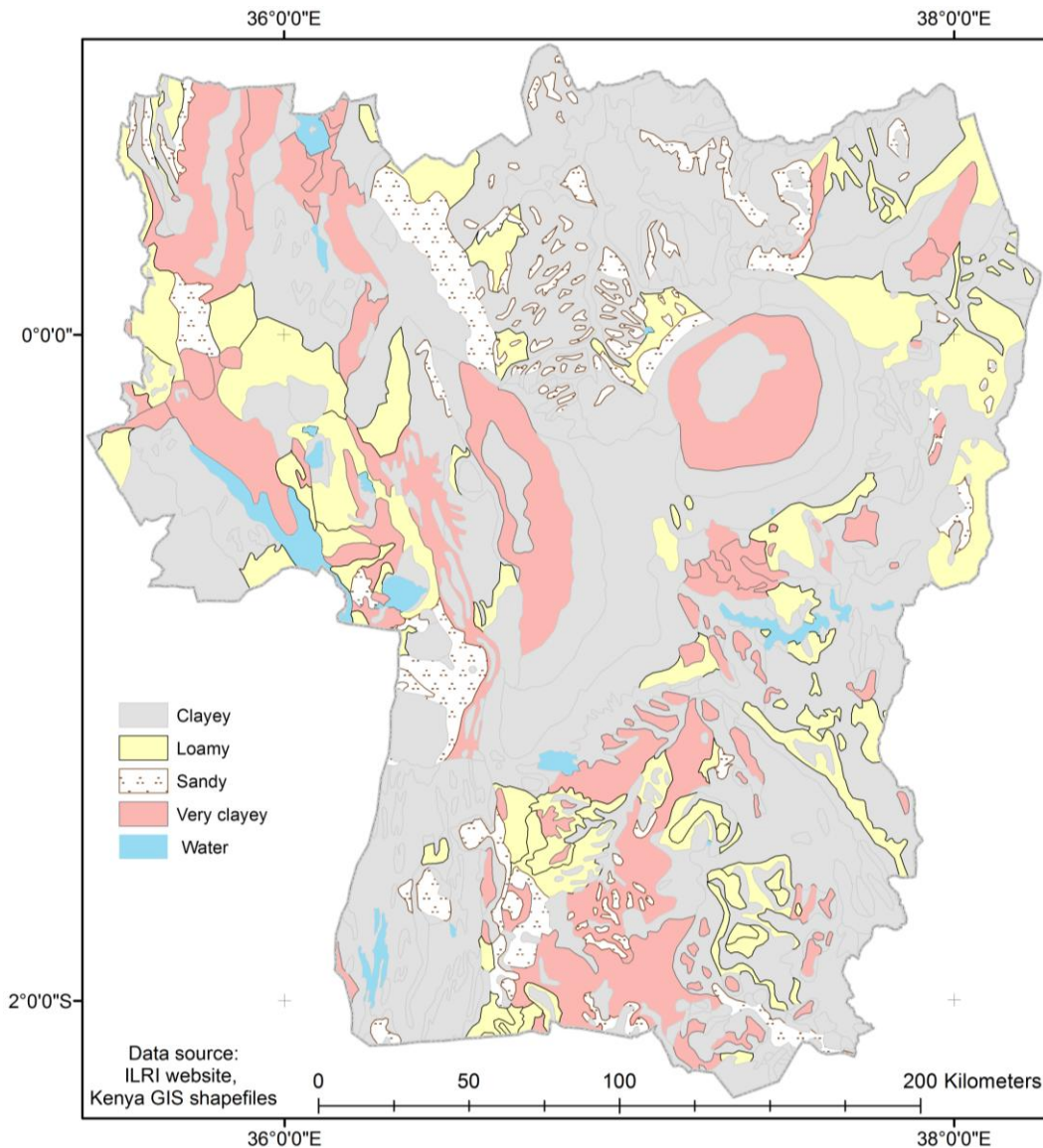


**Figure 5.10:** Existing soil texture vector map.

The Figure 5.10 and additional data extracted from secondary sources (e.g. Kariuki et al., 2004; Karuma et al., 2015; National Environment Secretariat, et al., 1980) were used to create reference points for use in the accuracy assessment. A total of 154 points were used to assess the soil accuracy as presented in Table 5.6. The overall accuracy was 51.94%, which is much lower than the recommended 85% (Foody, 2002). This could be attributed to the generalization effects of the soil data from which the reference points were extracted. In addition, the red volcanic soils class was lacking, hence the Figure 5.10 provided very basic soil classification information. Consequently, the possibility of chance agreement between the reference and the classified soil maps was very low i.e. the Kappa statistic 0.3302.

**Table 5.6:** Error/confusion matrix for the Soil classification.

Classes	References						Row $\Sigma$	Producer Accuracy %	User Accuracy %
	Volcanic rocks	Clay soils	Red volcanic soil	Very clayey soil	Loam	Sands			
Volcanic rocks	1	1	0	1	1	1	5	50.00	20.00
Clay soils	1	34	0	7	12	8	62	59.65	54.84
Red volcanic soil	0	3	0	4	1	1	9	---	---
Very clayey soil	0	1	0	11	2	0	14	37.93	78.57
Loam	0	17	0	5	28	5	55	60.87	50.91
Sands	0	0	0	1	2	6	9	28.57	66.67
<b>Column <math>\Sigma</math></b>	2	56	0	29	46	21	154		
Overall Classification Accuracy = 51.94%									
Overall Kappa Statistic = 0.3302									

#### 5.4 Discussion

Band ratioing image enhancement technique and visualization using FCC was successful in discriminating the various rock types in the study area. Knowledge-based classification using band ratios successfully captured the strength of each band ratio. Landsat 8 band ratios 4/2 and 6/5 compared to Landsat 7 band ratios 3/1 and 5/4, respectively. Consequently, the band ratio 4/2 was useful at highlighting sedimentary rocks as well as turbid water (Gad and Kusky, 2006), which appeared in cream-yellowish and red colours in Figure 5.2 (a), respectively. The band ratio 6/5 highlighted rock and soil materials rich in ferrous minerals (Carranza and Hale, 2002) which were highlighted in cyan to sky-blue colours. Lastly, the band ratio 7/3 highlighted volcanic rocks and they appeared in light green colours (Figure 5.2 a). The use of multiplication band ratio 7/3\*7/4 in the Figure 5.2 (b), improved the band combination Figure 5.2 (a) with volcanic rocks being enhanced further by the use of band ratio 7/4. However, the use of multiplication bands could introduce redundancy, which reduces geologic contrast. In addition, the choice of the band ratios should be such that they don't cause net cancellation effect through the division and multiplication (Mwaniki, 2016).

It could be observed that the bands used in the numerator of the band combination bearing the most geologic contrast (i.e. bands 7, 6, & 4), had a significant contribution when incorporated to the FCC which enhanced geology-lineament through the IHS transformation. Further, the PCA and ICA image enhancement techniques refined the lineaments and geologic information, compressing and reducing the information (Subasi and GURSOY, 2010). This reduced the quality of lithology discrimination ability compared to band ratio image

enhancement. Thus, PCA factor loading was useful at investigating the PCs which contained the most geologic information. Consequently, the PCs (1, 3, 4 & 5) were employed in the soil classification.

The strength of the band ratio 6/3 in texture enhancement was supported by the spectral difference of the bands used i.e. the combination of a SWIR and visible band. Further, band 6 in Landsat 8, which compares to band 5 in Landsat 7, has little vegetation influence (Rawashdeh et al., 2006). On the other hand, when the red (visible region) band was used as a denominator in the texture band ratio investigation, the texture was smoothed out as soil reflectance was high. Instead, the blue or green bands achieved the desired texture enhancement effect. The ability to extract lineaments using filter applications and thresholding was facilitated by the fact that lineaments had darker pixels compared to the surrounding background cells (Kocal et al., 2004). Although pan-band 8 had higher spatial resolution compared to the other Landsat bands, its wide coverage in the lower portion of the spectral region resulted in low quality texture details. The lineaments could also be improved further by data fusion of Landsat imagery with SAR data (e.g. Rawashdeh et al., 2006; Tae Hee Lee and Moon, 2002), or extraction of lineaments from the DTM (Alejandro, 2006). The former option is explored in the next chapter with Sentinel-1 SAR-C imagery.

In general, this chapter has demonstrated the strength of the mid-infrared region in mapping geology and the various image enhancements which could be applied to enhance geology features. More lithology rock type discrimination is afforded by hyperspectral data sets covering the mid-infrared region. For instance, Crisp and Bartholomew (1992) differentiated basalt and quartzite rocks using the mid-infrared spectral region. Similarly, the refinement of multispectral datasets having narrower bandwidth (e.g. Landsat 8) and the increase of bands covering the mid-infrared regions (e.g. ASTER) achieve more reliable rock discrimination effects (Amer et al., 2010; Gad and Kusky, 2007; van der Meer et al., 2012).

## Chapter 6: Landslide Inventory through Remote Sensing Image Analysis

---

### *6.1 Introduction*

Landslide inventory mapping is the first step towards any landslide hazard assessment study as it provides essential data for weighting the landslide predisposing factors, as well as show areas prone to slope instability (Guzzetti et al., 2012; Pardeshi et al., 2013). However, landslides can occur in areas with no history of slope instabilities, due to factors such as human activities, changes in topography, extreme land degradation or hydrologic conditions can lead to new landslides or accelerate the rate of the landslide processes (Highland and Bobrowsky, 2008). Therefore, environmental degradation can be a signal for future landslides (especially shallow landslides), while mapping past landslides can be considered as a precautionary measure (Lee and Pradhan, 2006).

Remote sensing data and image processing techniques come in handy to provide visual analysis and interpretation of the images in order to detect, recognise, and map past landslides. This is achieved through modifying the original image through enhancement techniques such as image contrast stretching, decorrelation stretching, application of filters and edge detectors, composite generation, band ratioing and spectral indices, image fusion, data feature space transform (PCA, ICA) (Joyce et al., 2014; Nichol and Wong, 2005a; Voigt et al., 2007; Whitworth et al., 2005). The resulting enhanced images have improved spectral characteristics, feature extraction performance and pattern recognition, which aids feature identification, classification or change detection (Joyce et al., 2009; Mantovani et al., 1996).

Incorporating topographic signatures (e.g. curvature, slope, aspect) into landslide mapping can provide a distinction between landslide scars and old mining areas or burnt landscape (Alkhasawneh et al., 2013). Besides, the identification of disturbed vegetation and land degradation can indicate areas prone to slope instability since vegetation cover contributes to shear strength through root cohesion and thus guard against shallow landslides (Roering et al., 2003; Schmidt et al., 2001). Therefore, vegetation indices and change detection leading to the detection of land degraded areas have been explored to map shallow landslides (e.g. Mondini et al., 2011b; Nichol and Wong, 2005b; Vohora and Donoghue, 2004).

On the other hand, deep-seated landslides are covered by vegetation and investigating them requires the use of active (LiDAR and SAR) data which can monitor displacements (Scaioni et al., 2014). In addition, SAR data affords the all weather, all day capability and is rich in

roughness, moisture, and topographic data. However, SAR data lack the spectral information which is necessary to characterise landslide geomorphic processes. This necessitates the integration of SAR data with optical data to complement the SAR data, while reducing temporal decorrelation effects of vegetation and soil moisture (Vrieling, 2006).

The main aim of this chapter is to explore RS techniques to map landslides and create a landslide inventory map. In addition, it was important to map the land degradation such as soil erosion, and land-use as they exacerbate landslide processes. Multi-temporal, multispectral Landsat series datasets were used to map landslides following heavy rainfall events during the periods 1997/1998 and 2010. Image enhancement methods were employed to characterise patterns which maximise separability of landslide features. In particular, this research modified the NDMIDIR (equation 6.1) spectral index developed by Vohora and Donoghue (2004) to NDMIDR (equation 6.2) for Landsat TM/ETM+ and equation 6.3 for Landsat OLI (Mwaniki et al., 2015a). These formed the basis for developing a methodology that could enhance landslide geo-hazards and lead to their successful classification among other land-uses.

$$NDMIDIR = \frac{TM4 - TM7}{TM4 + TM7} \quad (6.1)$$

$$NDMIDR = \frac{Band\ 7 - Band\ 3}{Band\ 7 + Band\ 3} \quad (6.2)$$

$$NDMIDR = \frac{Band\ 7 - Band\ 4}{Band\ 7 + Band\ 4} \quad (6.3)$$

where: TM is the Landsat Thematic Mapper band, bands 3 and 4 are the red bands in Landsat TM/ETM+ and Landsat OLI, respectively.

### *6.3 Methodology*

Landsat and Sentinel-1 SAR data acquired in C-band were processed through image enhancement methods, and landslide inventory mapping performed by classifying the landslides among other land-uses as described in the sections below. The mapped landslides were processed further using topographic signatures (slope, curvature, and aspect) and geologic information, so as to classify the landslides according to type.

#### *6.2.1 Data Description*

Landsat datasets taken in the months of January and February, during the years 2014 (OLI), 2010 (TM), 2000 (ETM+) and 1995 (TM), (scenes described by Table 4.1 and 5.1, previous

chapters), were pre-processed for image patching to remove cloud cover, layerstacked, mosaiced and subset. Geometric correction was not necessary as the images were already geo-referenced in the WGS-84 system and coincided well with the existing framework data. Radiometric correction too was unnecessary as the images were captured during the same season, thus the atmospheric conditions were relatively similar. In addition to the Landsat datasets, Sentinel-1 SAR-C band, Level 1 data (year 2014) were downloaded from the European Space Agency (ESA) Sentinel data hub and pre-processed by image registration in the ENVI software. Despeckling effects were reduced by applying a Frost filter which preserves edges, since edges and texture information are important aspects that aid landslide detection. Similarly, STRM DEM data, 30 m spatial resolution covering similar scenes were also downloaded from the USGS site, mosaicked, and subset accordingly using the study area AOI file.

### 6.2.2 Image Enhancement

Landslides are geologic hazards and therefore in this study, extensions of geological enhancements with satellite data were used to map and investigate landslide-affected areas. The basis for landslide identification and mapping was geologic components enhancement and visualization, from the previous chapter 5. Therefore, the first task was PCA to extract geologic information into one component, which was investigated using PCA factor loading Tables 6.1 (a) and (b). The last PC was eliminated on the basis of the least information and thus it was excluded in the information contained in Tables 6.1. Further analysis of the Tables 6.1 (a) and (b), revealed that PC4 (year 1995), PC5 (year 2000), PC4 (year 2010 and 2014) contained the most geologic information and were complemented by ICA components IC1 (1995, 2000 and 2014) and IC2 (2010).

**Table 6.1 (a):** Factor loading using PCs 1-5 for the years 1995, and 2000.

	1995					2000				
	PC1	PC2	PC3	PC4	PC5	PC1	PC2	PC3	PC4	PC5
<b>Band1</b>	0.38259	-0.25098	0.62907	0.55031	-0.11877	0.35043	0.14994	0.34351	-0.06653	0.41753
<b>Band2</b>	0.19466	-0.06496	0.30232	-0.01521	0.12790	0.31187	0.17774	0.41251	-0.09581	0.50378
<b>Band3</b>	0.24594	0.16360	0.43177	-0.60993	0.53252	0.40637	-0.13773	0.54636	0.35197	-0.62644
<b>Band4</b>	0.42446	-0.76562	-0.29577	-0.35343	-0.14214	0.28295	0.82872	-0.23965	-0.24133	-0.34225
<b>Band5</b>	0.68824	0.37623	-0.46972	0.29132	0.28156	0.58467	-0.13639	-0.57760	0.51478	0.19711
<b>Band7</b>	0.31844	0.42227	0.13536	-0.33933	-0.76781	0.43920	-0.47073	-0.14922	-0.73436	-0.15315
<b>% Var</b>	<b>94.17</b>	<b>4.44</b>	<b>1.03</b>	<b>0.2</b>	<b>0.15</b>	<b>96.64</b>	<b>1.91</b>	<b>1.18</b>	<b>0.17</b>	<b>0.08</b>

**Table 6.1 (b):** Factor loading using PCs 1-5 for the years 2010 and 2014.

	2010						2014					
	PC1	PC2	PC3	PC4	PC5		PC1	PC2	PC3	PC4	PC5	PC6
<b>Band1</b>	0.37958	-0.16216	0.67691	0.44094	-0.32967	<b>Band1</b>	0.24099	-0.05290	-0.55771	0.40784	-0.26256	0.46573
<b>Band2</b>	0.20129	-0.04220	0.33222	-0.05203	0.14573	<b>Band2</b>	0.21217	0.00164	-0.47775	0.20939	-0.08576	-0.19418
<b>Band3</b>	0.25164	0.15532	0.40481	-0.51288	0.61635	<b>Band3</b>	0.21104	0.03187	-0.37807	-0.09955	0.14961	-0.77211
<b>Band4</b>	0.42511	-0.80844	-0.28105	-0.28842	-0.04542	<b>Band4</b>	0.23250	0.22847	-0.33049	-0.62980	0.48878	0.38262
<b>Band5</b>	0.67923	0.34866	-0.43263	0.40402	0.25815	<b>Band5</b>	0.58467	-0.75238	0.21025	-0.20441	-0.06988	0.02520
<b>Band7</b>	0.33167	0.41552	-0.03721	-0.54166	-0.64923	<b>Band6</b>	0.56277	0.37244	0.37243	0.47883	0.42009	0.00958
						<b>Band7</b>	0.37386	0.48909	0.16014	-0.33498	-0.69358	-0.04594
<b>%Var</b>	<b>92.79</b>	<b>4.80</b>	<b>1.91</b>	<b>0.34</b>	<b>0.15</b>		<b>91.610</b>	<b>6.840</b>	<b>1.196</b>	<b>0.207</b>	<b>0.122</b>	<b>0.020</b>

The third component to facilitate visualization of an FCC was the spectral index involving geology and red bands i.e. bands 7 and 3 of Landsat TM/ETM+, and bands 7 and 4 of Landsat OLI. Thus, the following FCCs were visualized as in Figure 6.1 (a) {IC1, PC4, NDMIDR} Landsat TM, year 1995, (b) {IC1, PC5, NDMIDR} Landsat ETM+, year 2000, (c) {IC2, PC4, NDMIDR} Landsat TM, year 2010, and (d) {IC1, PC4, NDMIDR} Landsat OLI, year 2014.

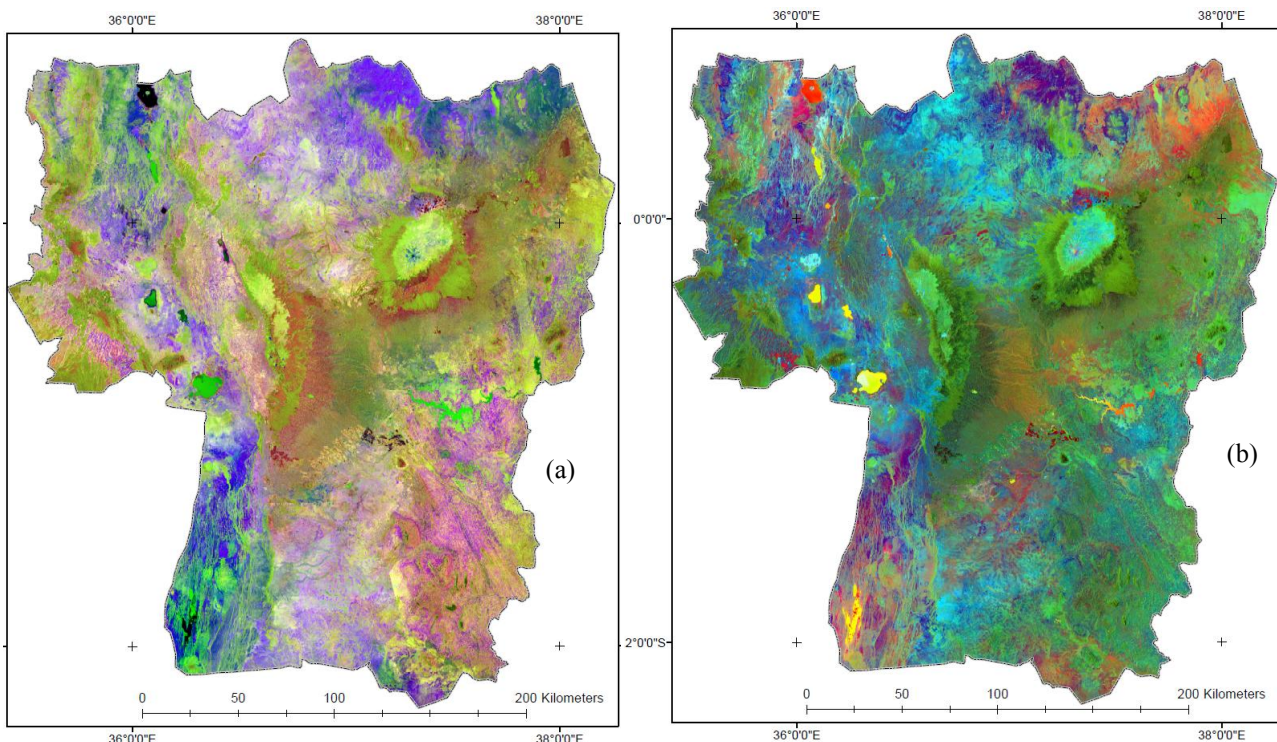


**Figure 6.1** FCC involving Landsat: (a) TM, year 1995 {IC1, PC4, NDMIDR} (b) ETM+, year 2000 {IC1, PC5, NDMIDR}.

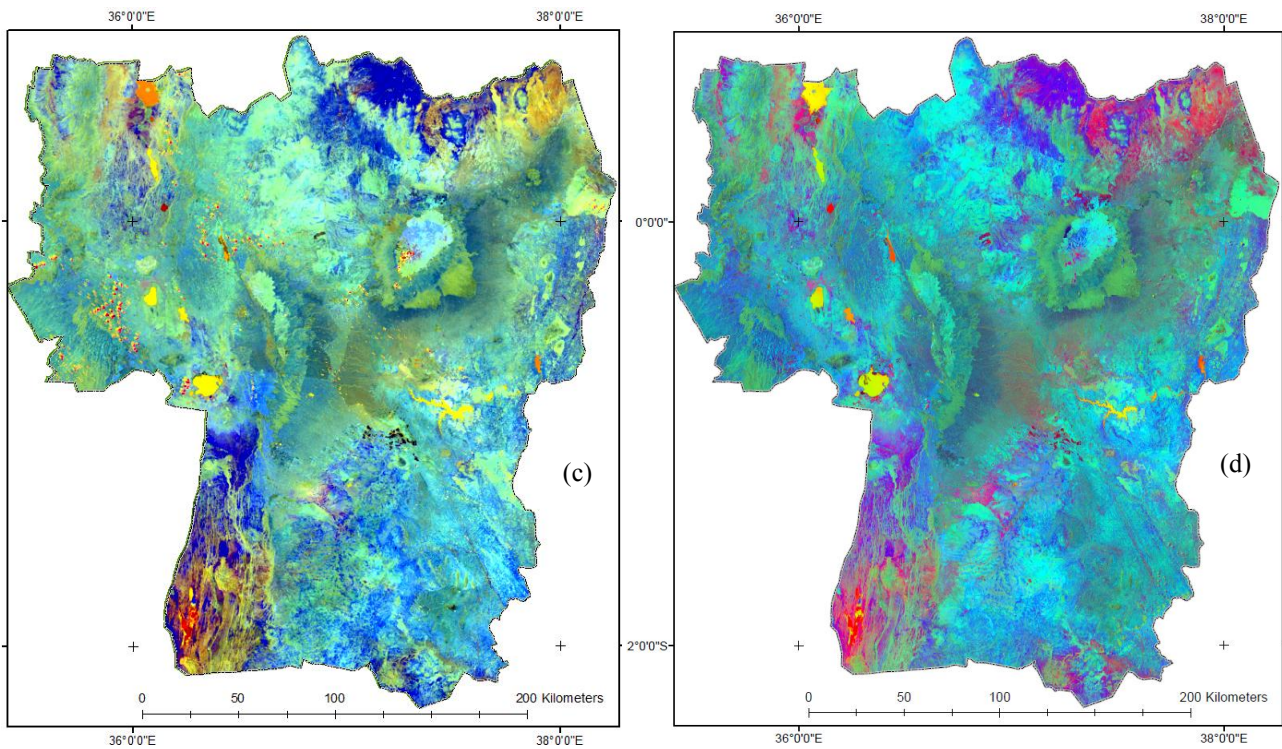


**Figure 6.1** FCC involving Landsat: (c) TM, year 2010 {IC2, PC4, NDMIDR} (d) OLI, year 2014 {IC1, PC4, NDMIDR}.

On the other hand, the Sentinel-1 SAR-C imagery was processed and used to enhance Landsat 8 NDMIDR spectral index as summarized in Figure 6.2. First, the Sentinel-1 SAR imagery was despeckled using the Lee and Frost filters separately, resulting in new images which had preserved texture and edges, respectively. The despeckled-texture preserved image was further processed by calculating texture statistics of the mean, skewness, kurtosis, variance, entropy, and range. Each component was examined and the mean and skewness were chosen to characterise ruggedness, while the mean and kurtosis statistics highlighted faults and lineaments. Through thresholding, feature extraction was performed and the results integrated into the classification with other enhanced components.

The despeckled-edge preserved image was processed further by running the Robert edge detector which resulted in enhanced edges. This was fused to Landsat 8 NDMIDR spectral index through wavelet transform method. Further, the Sentinel-1 SAR-C incoherence statistics were computed from the Frost despeckled Sentinel-1 SAR-C image and together with edges enhanced NDMIDR and texture features, were the input components of the classification. This was followed by classification which is described in the section below.

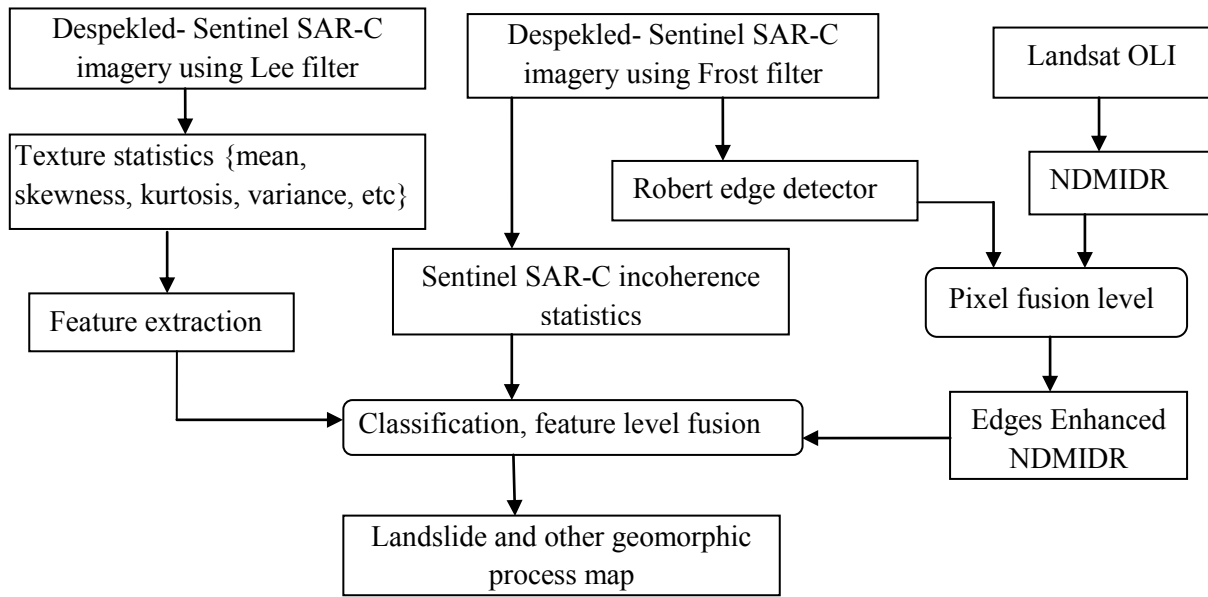


**Figure 6.2:** Landslide mapping with Sentinel-1 SAR-C texture and roughness enhanced components.

### 6.2.3 Knowledge-Based Classification

The classification was done following density slicing of the enhanced components, i.e. for each colour, the range of histogram values was established to fix the boundary. The resulting class boundaries Table 6.2 (a), were saved in an Erdas-Imagine knowledge classification file, with the enhanced components as the variables. When a class distinction was not possible with three enhanced components, a fourth component was used, e.g. IC2 was used in the Landsat 8 classification (Table 6.2 b) as it highlighted non-vegetated, built-up, and bare areas. Thus, Landsat 8 classification resulted in slightly more classes compared to the other Landsat imagery classifications. Forms of erosion were represented by the classes: extreme erosion (erosion associated with geomorphologic processes e.g. gullying), highly erodible (erosion from agricultural areas) and other erosion (erosion from barren land-cover), while those associated with deposit areas were runoff and stable areas.

On the other hand, the Landsat 8 spectral index enhanced with Sentinel-1 SAR-C texture and edge components classification had the most classes, Table 6.2 (b), because fault lines and edges (areas where the terrain change is sudden) were captured. In addition, the Sentinel-1 SAR-C incoherence component highlighted moist areas and wetlands followed by bare rocks. The Sentinel-1 SAR-C imagery had higher spatial resolution and although image fusion would have reduced the classification components, the required storage space was enormous and the processing speed of the fused components slowed down the classification. Instead, the classification with the Sentinel-1 SAR-C texture and edge information enabled feature level fusion (e.g. Hashim et al., 2013; Nyongui et al., 2002).

**Table 6.2 (a):** Classification boundaries; Landsat (Years 1995, 2000, 2010).

Classes	Variables (classification, year 1995)			Variables (classification, year 2000)			Variables (classification, year 2010)		
	IC1	PC4	NDMIDR	IC1	PC5	NDMIDR	IC2	PC4	NDMIDR
Runoff	0.5 – -5	< 0	> 95	0.35 – -0.25	< - 1.5	0 – -0.20	< -2	< 0	≥ 0.15
				1 – 0.75	< - 4.5	0 – 0.05			
Extreme erosions	< -0.90	< 1	100 – 55	6 – 1.25	6 – - 1.5	-0.70 – 0.015	2.2 – -6.5	< 0	0.15 – -0.2
Other erosions	> 1.5	> 6	> 110	6 – 0.75	-1.5 – -4.5	0.075 – -0.45	> 1.9	> 5	> 0.65
Landslide	> 2	> 6	90 – 70	< -0.11	< -1.5	< -0.035	< -1	< 0	< 0
Highly erodible	> 0.75	> 5	70 – 20	< 0.75	6 – 0.5	≥ 0.095	≤ 0.9	0 – 5	> 0.175
	2 – 0.5	> 5	> 70						
Stable	0.75 – -0.90	< 1.60	> 65	0.75 – -0.114	-1.5 – -7	-0.06 – 0.099	4.5 – 0.5	> 5	0.65 – 0.150
				1.8 – 0.75	6 – 0.75	0.05 – 0.25			
Exposed volcanic rocks	0.75 – -7	15 – 5	55 – 20	< 0.75	≥ 6.5	≥ 0.075	5 – 0.9	> 5	0.150 - 0
	< -1	1 – -1	24 – 18	3 – -2	≥ 9.2	0.20 – -0.30			
				4.5 – -1.2	9.2 – 6	0.25 – 0			
				6 – 1.5	20 – 6	-0.250 – -0.035			
Agricultural areas	3 – 0.5	5 – -1	150 – 30	0.75 – -1.75	6.5 – 0.3	0.095– 0.050	0.5 – 0	< 5	0.15 – 0
	0.75 – -0.90	5 – 1.6	> 65	1.5 – -1.5	2.5 – 0.3	0.05 – -0.06			
	< -0.90	2.0 – 1.75	100 – 55						
Green Forest	0.90 – -5	5 – -1	65 – 20	1.25 – -0.25	2.5 – 0.3	-0.06 – -0.37	< 0.9	10 - 0	< 0
				1.4 – -1	6 – 2.5	0.05 – -0.37			
				1.5 – -1.2	9.2 – 6.0	0 – -0.37			
New Forest regrowth	2.5 – -1.5	< -1	65 – 20	≤ -0.25	< 0.3	≥ 0	< 0	< 0	0.175 – 0
Clear waters	< 0	11 – 0	< 20	6 – 1	20 – 6	< -0.25	> 2.2	> 5	< -0.3
Turbid water	< -2	0 – -18	< 20	6 – 1	< 6	< - 0.30	> 2.2	< 5	< -0.6
				> 6	< 0	< 0			
Salty water	< -2	< -13	55 – 0	> 1	> 20	< 0	2.2 - 0	< 0	< - 0.3
				> 6	20 – 0	> 0			

**Table 6.2 (b):** Classification boundaries; Landsat 8, Year 2014 & Sentinel-1 SAR-C.

Classes	Variables (classification, year 2014)				Multisource image enhanced variables					
	IC1	PC4	NDMIDR	IC2	SAR_incoherence	Robert_SAR_edges	SAR Texture mean	NDMIDR index	SAR Text. Kurtosis	NDMIDR + fused SAR Robert edges
Runoff	< 0.5	< -250	> 0.1	> 3	65 375 – 65 275					25 – 15
	1.5 – 0.5	500 – -250	> 0.1							
Extreme erosions	> 2.5	< 0	0.1 – -0.3		65 485 – 65 450			0.3 – 0		
	> 2.5	< -250	> 0.1	< 2	> 65 450	< 100		> 0.3		25 – 15
Other erosions	< 0.5	500 – -250	0.3 – 0.275		65 450 – 65 375					50 – 15
	< 0.5	< -250	> 0.1	< 3						
Landslide	1 – 0	< -250	0 – -0.2		< 65 275	100 – 50	< 30	> 0		
	0.5 – 0	< -500	> 0		> 65 275	100 – 50		> 0.3		> 25
Highly erodible	2.5 – 0.5	< 0	> 0	< 3	65 275 – 62 275					15 – 5
	0.5 – 0	0 – -500	0 – 0.1							
Stable	< 1	> -250	> 0		65 375 – 65 450			< 0.3		15 – 5
	2 – 1	> 500	> -0.3							
Deposits	2.5 – 1	< -250	> 0.1	> 3	65 450 – 65 375					5 – 0
	1 – 0.5	< 0	> 0	> 3	< 65 275			0 – -0.2		
Moist deposits/ Wetland	> 2	> 500	0 – -0.3		65 536 – 65 275			0 – -0.2		
	> 1	500 – 0	0.1 – -0.3		< 65 450			-0.2 – -0.4		
Exposed rocks	< 1	> 500	> 0.15		65 375 – 65 275	< 100				5 – 0
	2.5 – 1	500 – 0	> -0.2							
Stable volcanic rocks	< 1	500 – -250	0.15 – -0.1		65 485 – 65 375			> 0.3		15 – 0
Vegetation covered rocks	< 0.5	500 – -250	0.275 – 0.15							
Human development (settlements / urban areas)	> 2.5	< 0	> 0.1	> 2	< 65 275	450 – 100	160 – 30	> 0	> 2.5	
						> 450	> 160			
Faults					< 65 275	450 – 100	160 – 30	> 0	< 2.5	
Edges_crest					< 65 275	100 – 50	160 – 30	> 0		
					> 65 275	450 – 100		> 0		
Edges_base				< 65 275	50 – 0		> 0			
Clear waters	3.9 – 2	> 500	-0.3 – -0.8		< 65 450			< -0.4		
					65 485 – 65 450			< -0.2		
Turbid water	10 – 2.5		< -0.8		> 45 485			< -0.2		
Salty water/ River channel deposits	> 3	< -500	< -0.2		> 65 485			> 0		

#### 6.4 Results

The results obtained after running the classification rules with enhanced components are the Figures: 6.3 (Landsat TM, year 1995), 6.4 (Landsat ETM+, year 2000), 6.5 (Landsat TM, year 2010), and 6.6 (Landsat OLI, year 2014). Blown-out sections of the main figures are also provided to enable viewing the mapped landslide areas among other land-uses. In addition, Figure 6.7 shows the landslide areas with additional information derived from the Sentinel SAR-C imagery, which was enhanced with Landsat 8 NDMIDR spectral index. In total, the following classes were successfully mapped: runoff, extreme erosions, other erosions, landslides, highly erodible, stable, exposed rocks, green forest, new-regrowth, agriculture, and water covers. In addition, the Landsat 8 classification mapped the aspect of human development (urban areas, settlements), which further contributes to soil disturbance during their construction. The ability of the processed satellite imagery to capture landslide processes was demonstrated in Figure 6.8 using a few Global Positioning System (GPS) landslide points and field photos of landslide scars taken during a field campaign in the year 2014.

The trend of the landslide areas was analysed against the areas prone to erosion (extreme erosions, highly erodible, other erosions), possible deposit areas (runoff, stable), exposed rocks, forested areas (green forest, new regrowth), areas under agriculture, and water bodies as in Table 6.3. These were visualized using Figure 6.9 (a) where the extents are in percentage, and as Figure 6.9 (b) where landslide areas in shown in square metres (m<sup>2</sup>). The 1995 and 2000 years classification results captured the effects of El-Niño rainfall event in the period from October 1997 to May 1998, as can be observed by the increase in landslide areas (Figure 6.9 b) and whose devastating effects were recorded by Ngecu and Mathu (1999). Similarly, there was an increase in other forms of land degradation (erosion) and exposed rocks. This is in agreement with the effects which increase the vulnerability of landslide occurrence reported by UNDP (2010).

On the other hand, the deposit areas decreased significantly, although forested areas, agriculture, and water covers remained almost unchanged. It was observed that the areas affected most by landslides were the transition areas from the forested areas to the agricultural areas where mixed farming, comprising of cash crops (mainly tea and coffee) and food crops, is practised. Similar observations were made during the epoch 2010 to 2014, although there were increased agricultural activities. Areas affected by landslides and those prone to erosion increased considerably (Figures 6.9 (a) and (b)).

An added advantage of the results obtained from the Sentinel 1-SAR enhanced components and Landsat-8 NDMIDR spectral index was the ability to capture geomorphic processes better than the classifications with Landsat enhanced components only. Therefore, there was increased possibility of mapping areas prone to deep-seated landslides (along fault lines) with the SAR enhanced components, while the Landsat classifications were limited to depicting areas prone to shallow landslides only. The obtained classes with Sentinel 1-SAR enhanced components could not be compared with the Landsat classifications since different components (in different wavelengths) were used for the classifications.

The mapped landslides were extracted into a separate layer and analysed further with topographic attributes (slope, curvature), geology, drainage networks, and flow length in a GIS environment. The results from Landsat and Sentinel 1-SAR classifications are in Figures 6.10 (a) and (b), respectively. The landslides were categorized into the following classes: debris flow, debris slide, rock slide, rotational rock slide, and earth flow. The landslides mapped from the Sentinel 1-SAR components had extra categories, namely: deep-seated landslides, areas prone to rock slides and areas prone to earth flows. It was observed that although the landslide map derived from Sentinel 1-SAR had more classes, generally the landslide density was much higher compared to the landslide map derived from the Landsat datasets.

The debris flows were characterised by slope angle less than  $25^{\circ}$ , located along drainage channels, and consisted mainly fine weathered rock materials and unconsolidated soil particles. Debris slides had similar conditions, but located along non-drainage areas. Rotational rock slides were characterised by convex curvature, rock units with over  $25^{\circ}$  slope angle, while rock (translational) slides had the opposite concave curvature. Earth flows were debris slides with slope greater than  $25^{\circ}$ , and convex curvatures. Deep-seated landslides were located along the fault lines and had steep slopes (greater than  $25^{\circ}$ ), while areas prone to rock slides and earth flows mapped on the Sentinel 1-SAR classification were located on the edge's crests and bases, respectively, with slope greater than  $25^{\circ}$ .

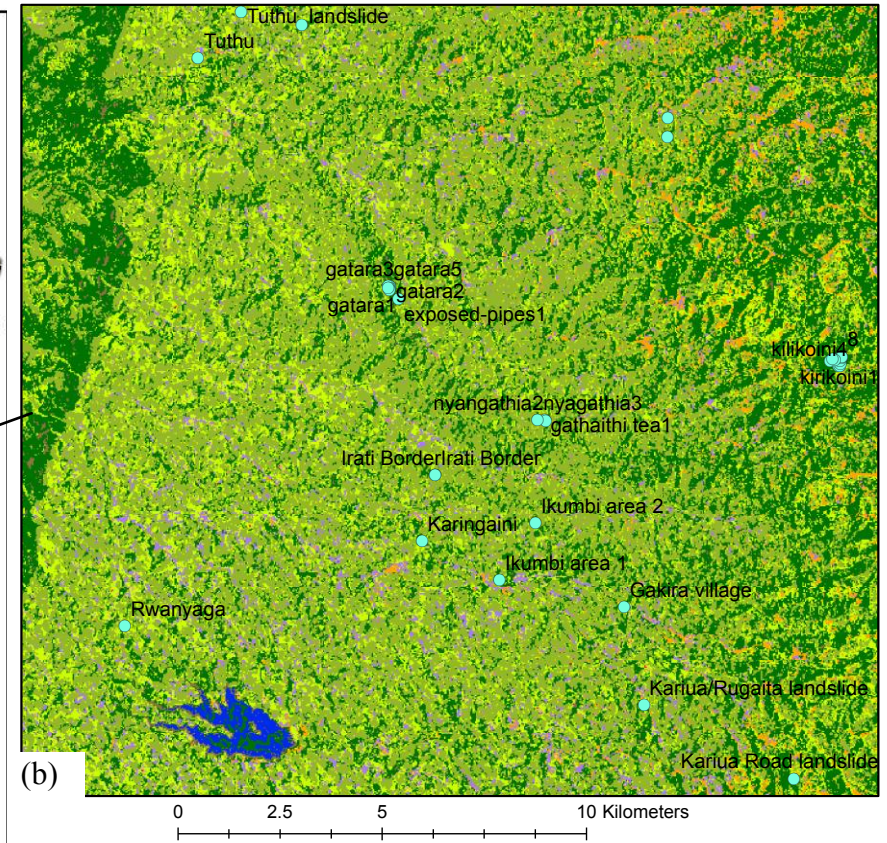
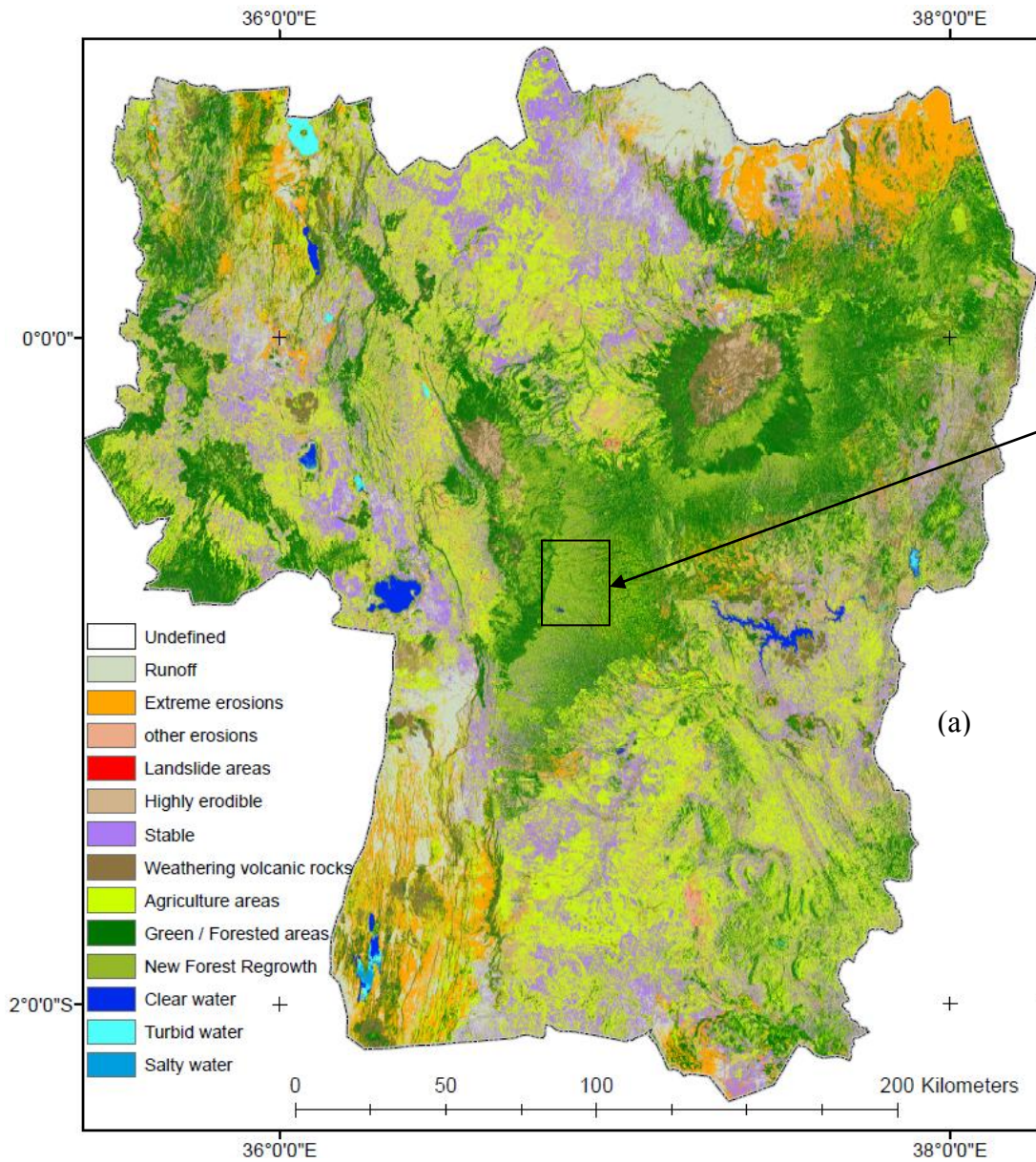


**Figure 6.3 (b):** A blown out section of Figure 6.3 (a) in Murang'a county overlaid with landslide GPS (see Appendix B) field landslide vector layer.

**Figure 6.3 (a):** Erodibility/landslide classification {Inputs: IC1, PC4, NDMIDR}, Landsat TM, Year 1995.

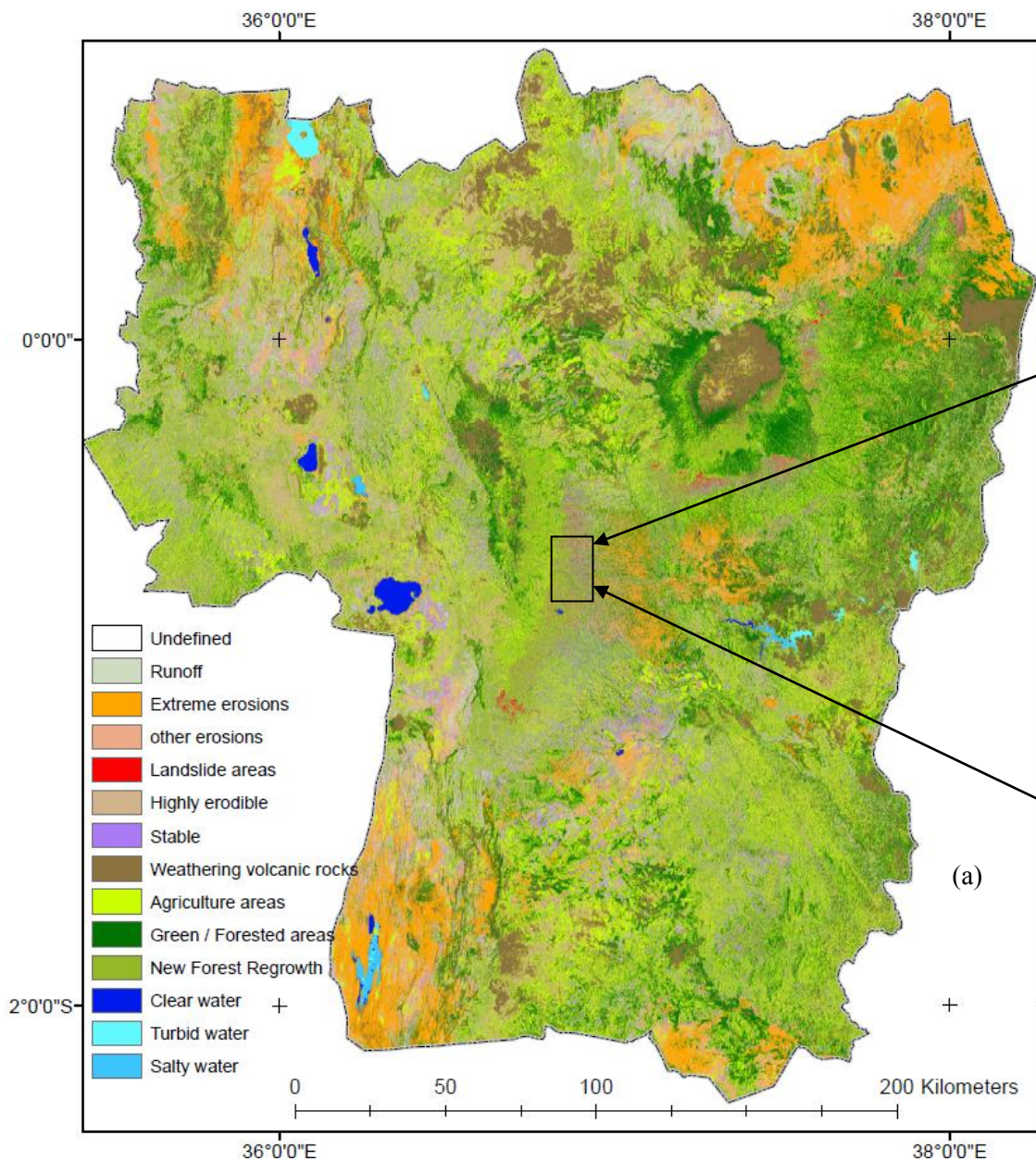


**Figure 6.4 (a):** Erodibility/landslide classification {Inputs: IC1, PC5, NDMIDR}, Landsat ETM+, Year 2000.

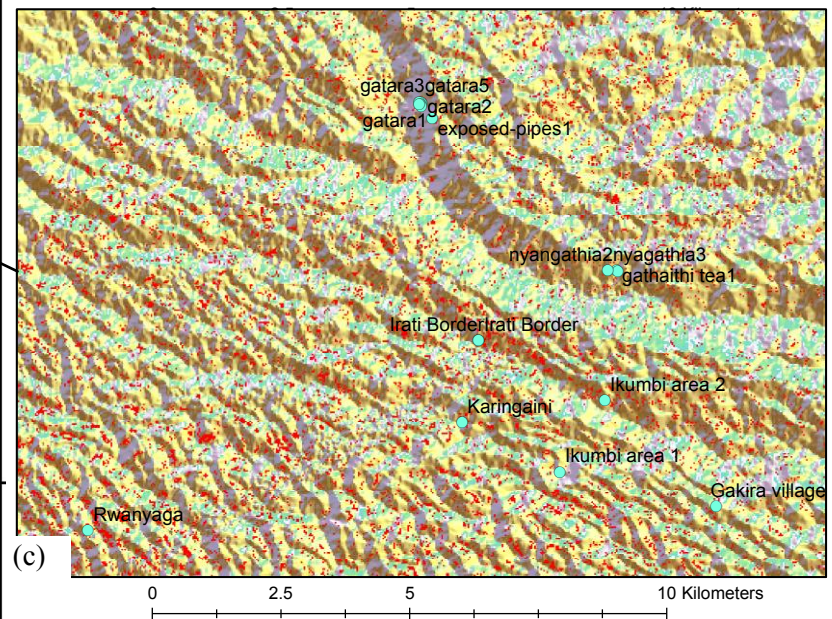
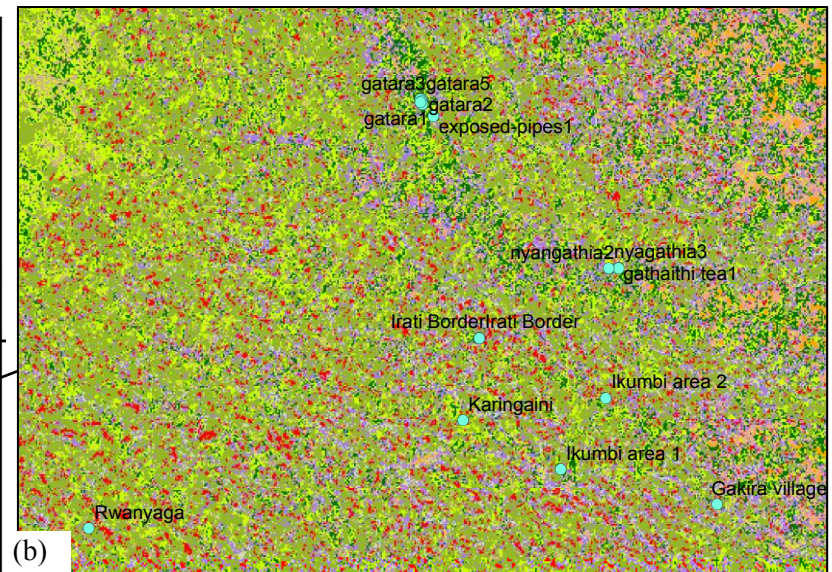


**Figure 6.4 (b):** A blown out section of Figure 6.4 (a) in Murang'a county overlaid with landslide GPS field landslide vector layer **(c):** A DEM Aspect map overlaid with classified landslide layer.

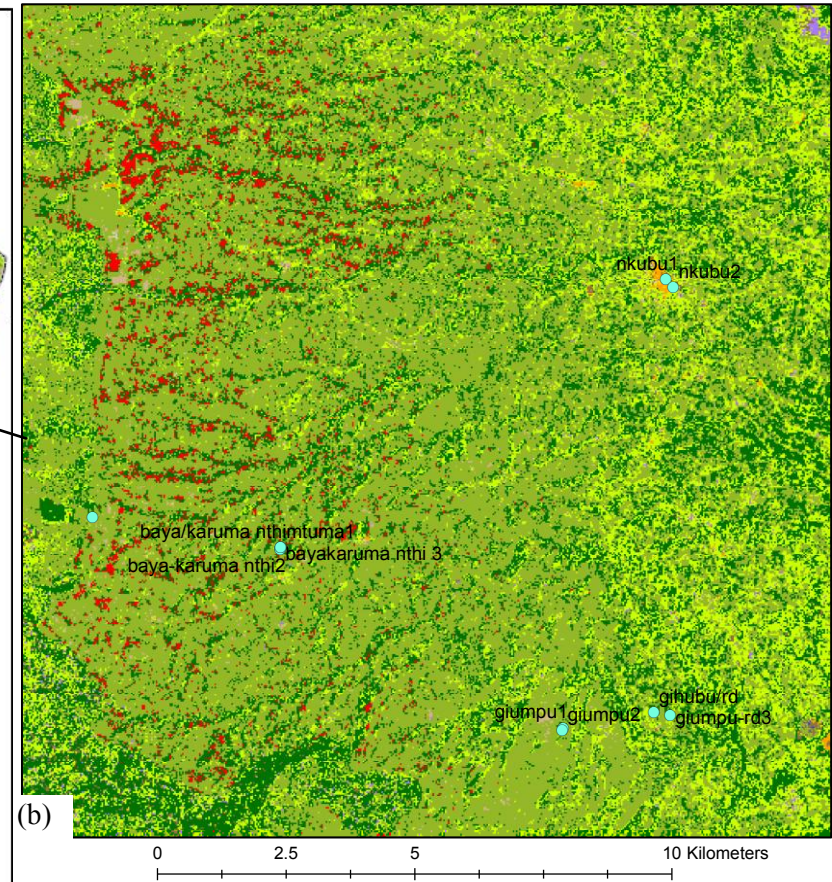
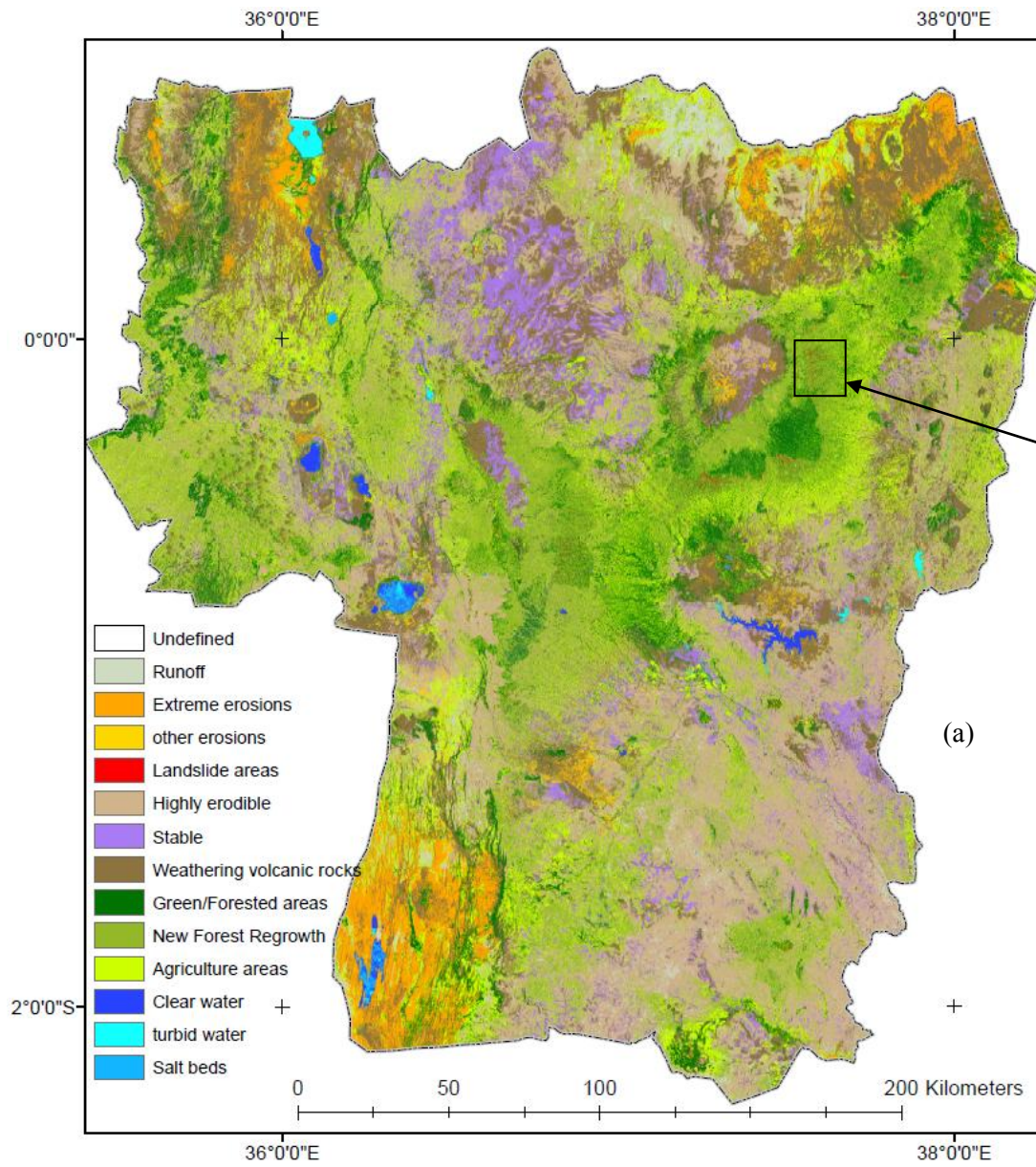


**Figure 6.5 (b):** A blown out section of Figure 6.5 (a) at Nkubu, Meru county.

**Figure 6.5 (a):** Erodibility/landslide classification {Inputs: IC2, PC4, NDMIDR}, Landsat TM, Year 2010.

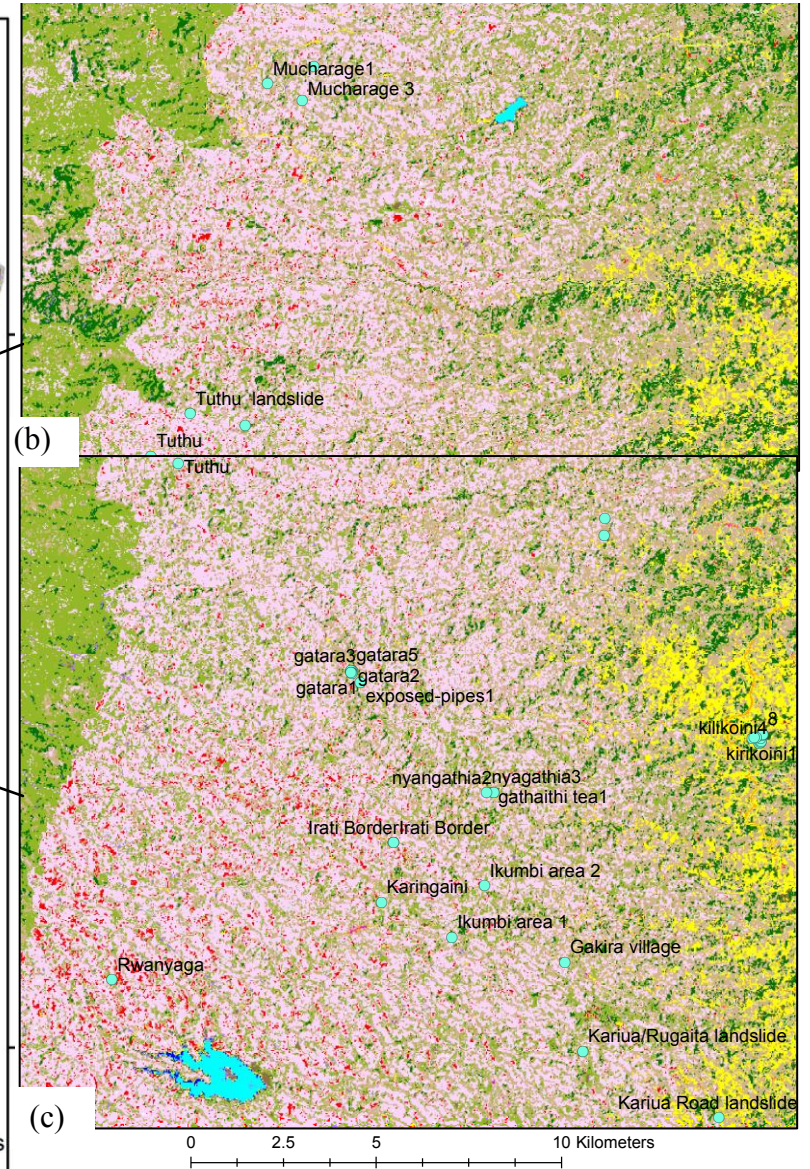
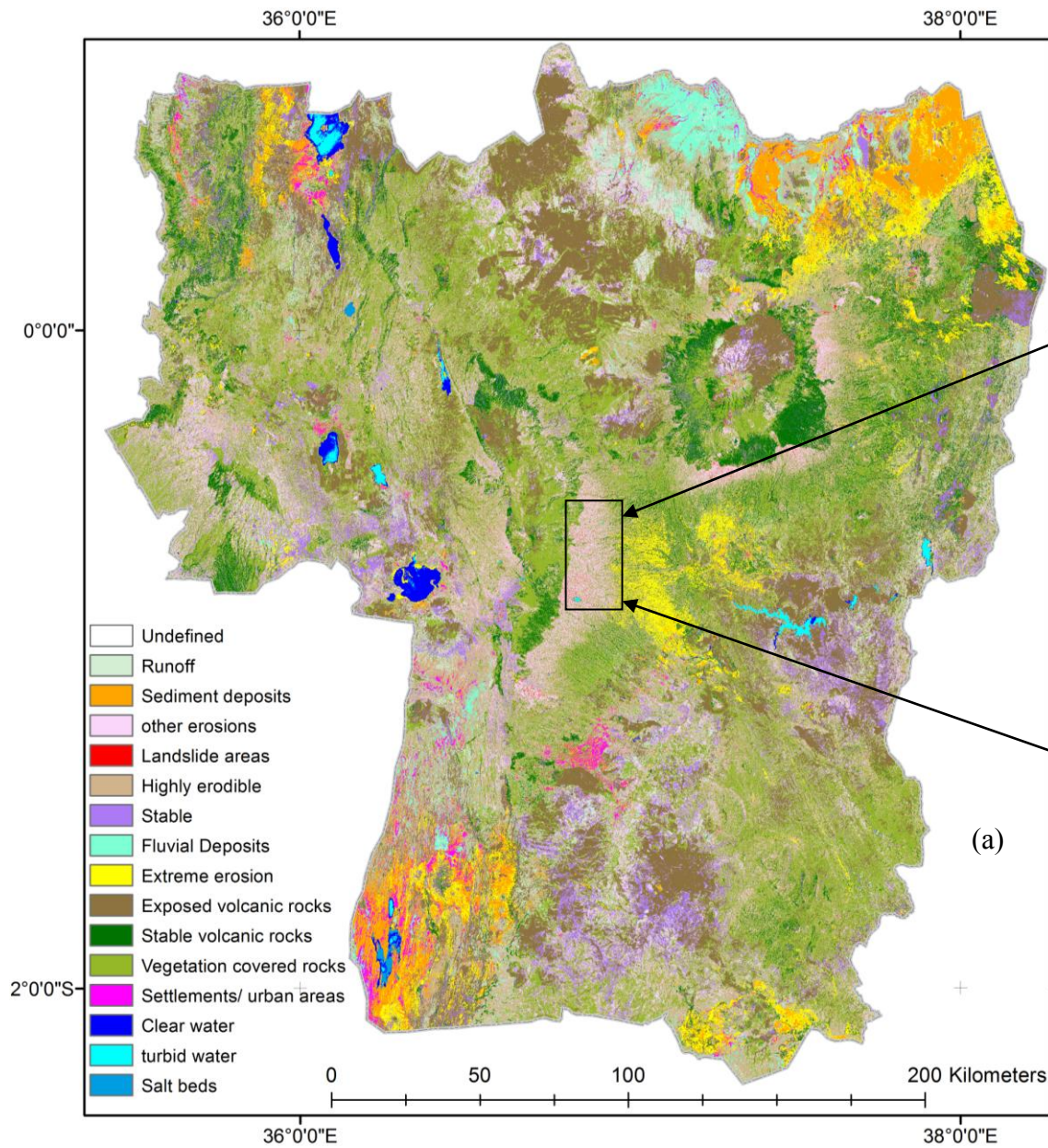


**Figure 6.6 (a):** Erodibility/landslide classification {Inputs: IC1, PC4, NDMIDR, IC2}, Landsat OLI, Year 2014.

**Figure 6.6 (b) & (c):** A blown-out section of Figure 6.6 (a) in Nyeri and Murang'a counties, respectively, overlaid with landslide GPS field landslide vector layer.

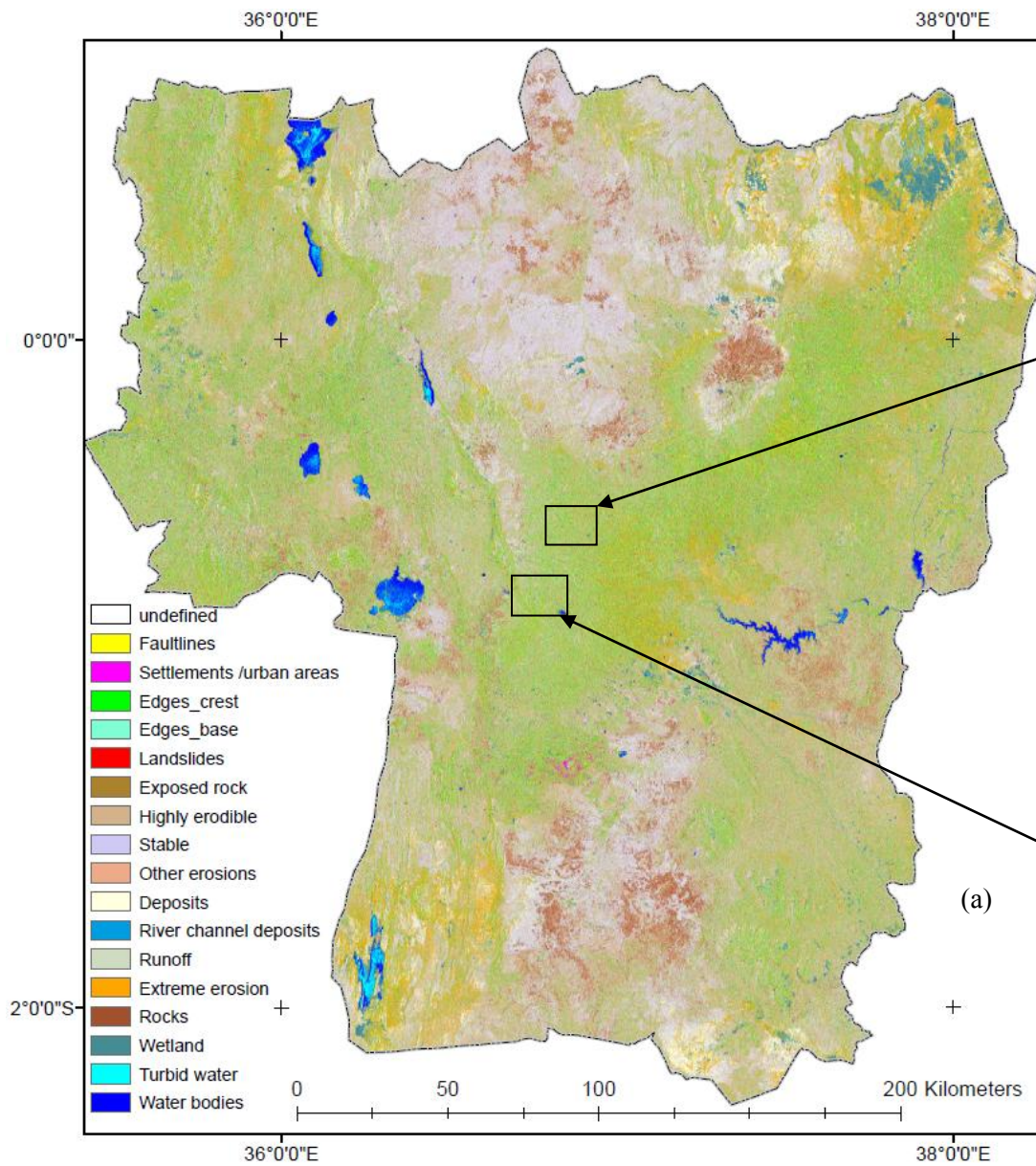


**Figure 6.7 (a):** Landslide and other geomorphic processes map, from Sentinel-1 SAR-C components and NDMIDR Landsat 8, Year 2014.

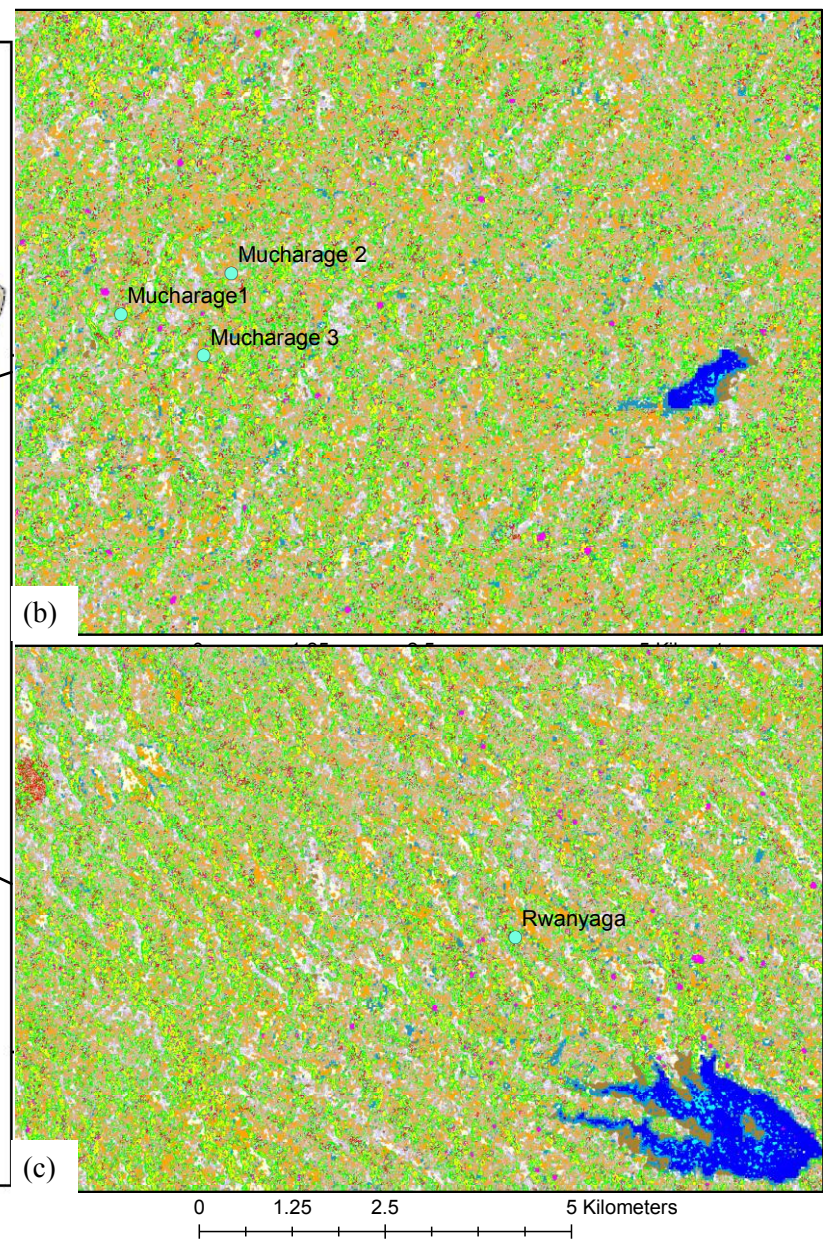


**Figure 6.7 A** blown-out section of Figure 6.7 (a): (b) Nyeri county (c) Murang'a county.

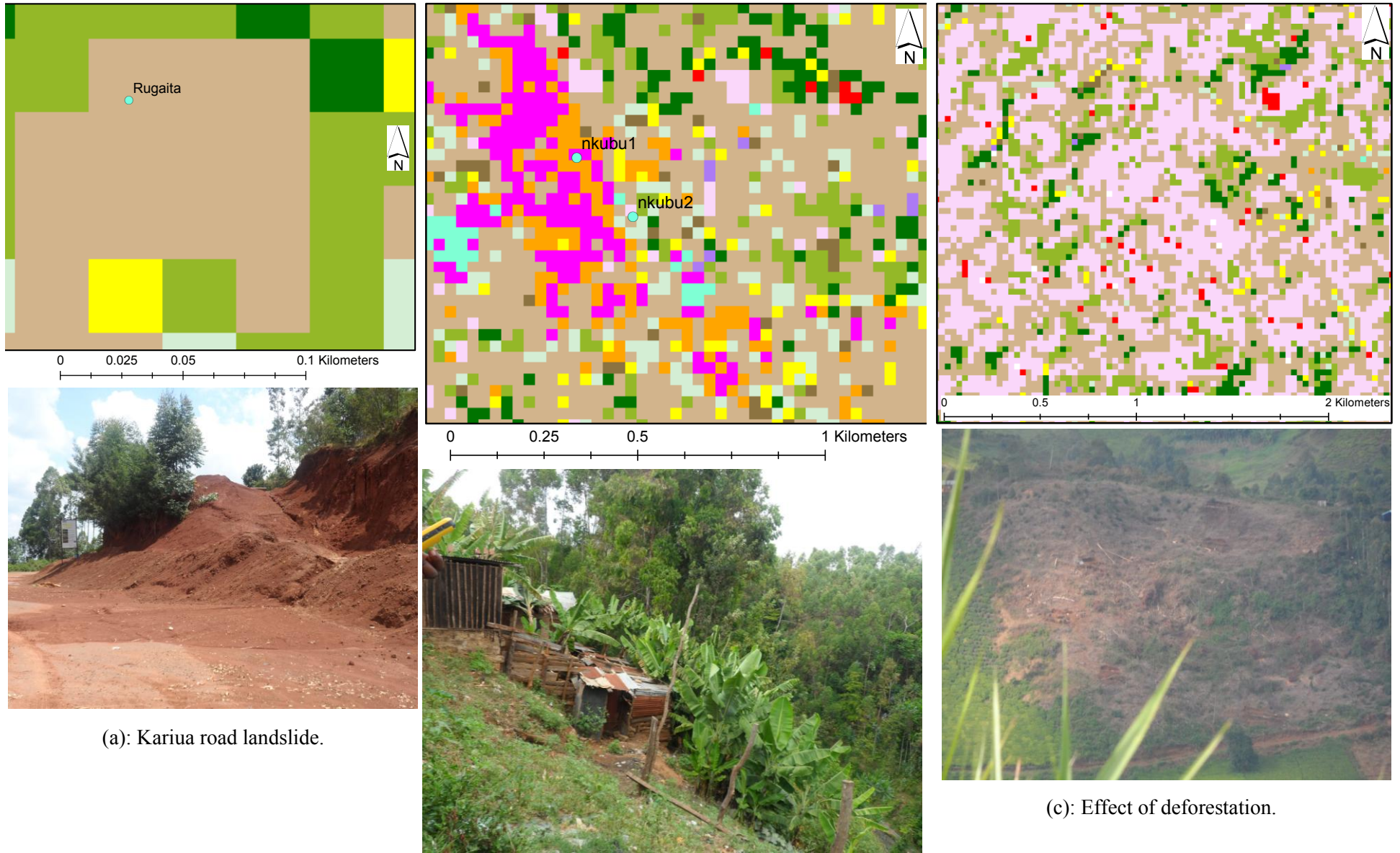


**Figure 6.8:** Identifiable landslide points on the processed satellite image.

**Table 6.3:** Representation of landslide areas in percentage in comparison to other covers.

	Classes	1995		2000		2010		2014	
Landslide areas	Landslide areas	0.19	0.19	0.25	0.25	0.09	0.09	0.18	0.18
Erodible areas	Extreme erosion	8.25	14.71	8.22	22.34	4.53	23.2	8.2	30.36
	Other erosion	0.8		8.19		0.79		1.43	
	Highly erodible	5.66		5.93		17.88		20.73	
Depositional areas	Runoff	6.37	23.60	4.09	11.50	2.13	13.5	1.78	19.31
	Stable	17.23		7.41		11.37		17.53	
Exposed volcanic rocks	Exposed volcanic rocks	5.48	5.48	10.54	10.54	19.2	19.2	9.65	9.65
Vegetated areas	Agriculture areas	27.8	27.8	27.26	27.26	8.85	8.85	14.82	14.82
	Green forest	21.44	27.41	17.48	27.30	14.25	34.22	10.26	24.68
	New forest regrowth	5.97		9.82		19.97		14.42	
Water bodies	Clear water	0.54	0.83	0.38	0.81	0.55	0.93	0.56	0.99
	Turbid water	0.24		0.22		0.31		0.12	
	Salty water	0.04		0.21		0.07		0.31	
		100		100		100		100	

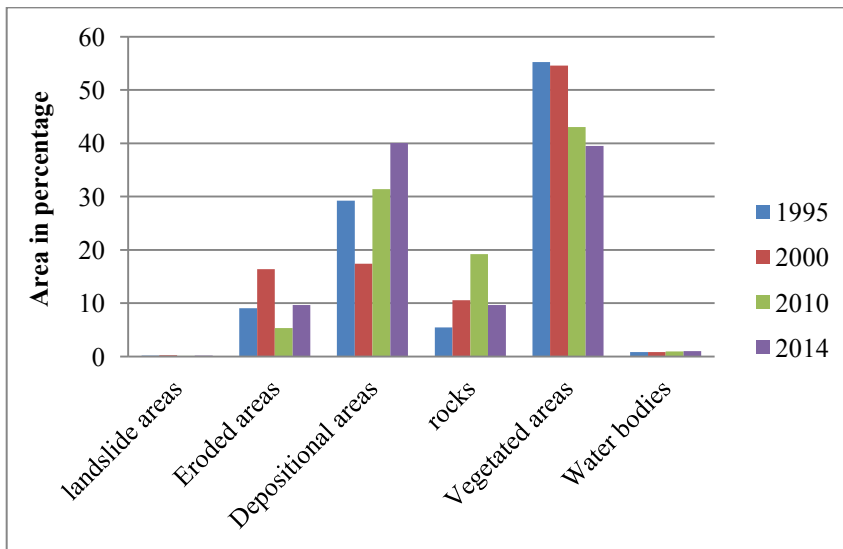


**Figure 6.9 (a):** The trend of landslides versus other land-uses.

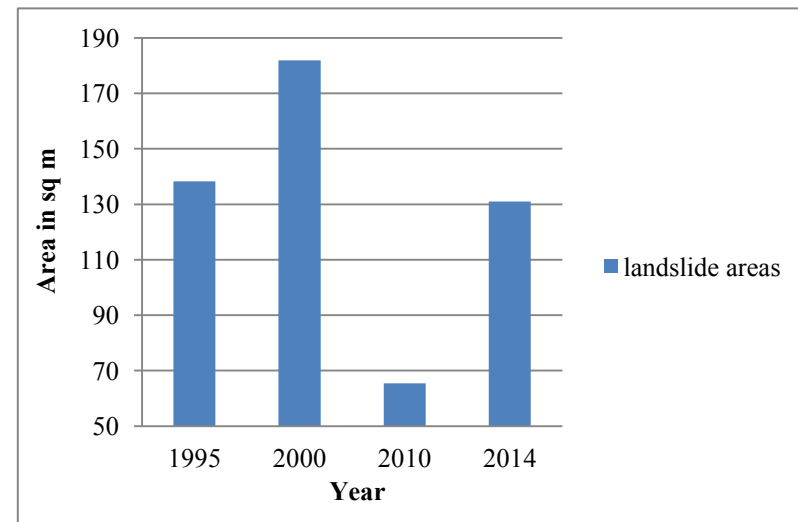


**Figure 6.9 (b):** The trend of landslide areas.

Types of shallow Landslides, Landsat classification

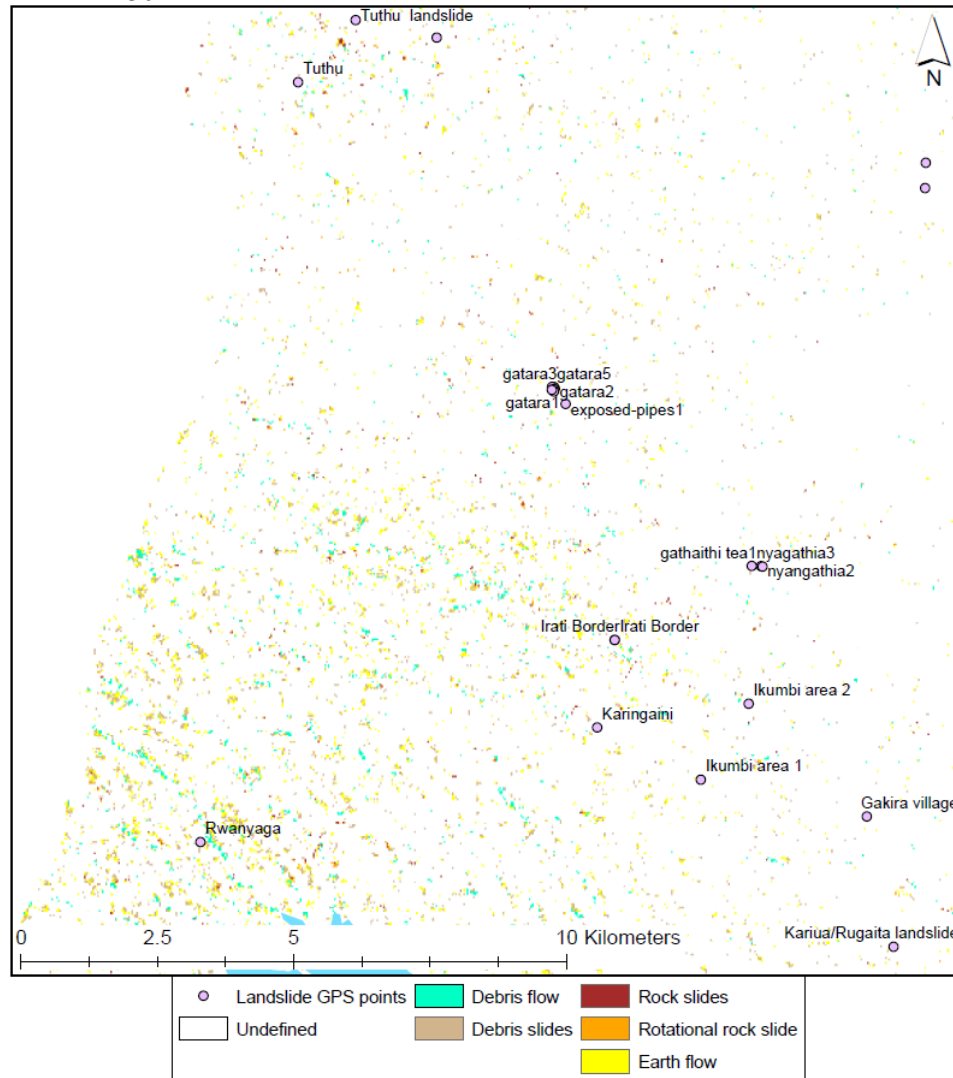


**Figure 6.10 (a):** Landslide types extracted from Landsat classification reclassified according to other landslide factors.

Types of Landslides, SAR classification

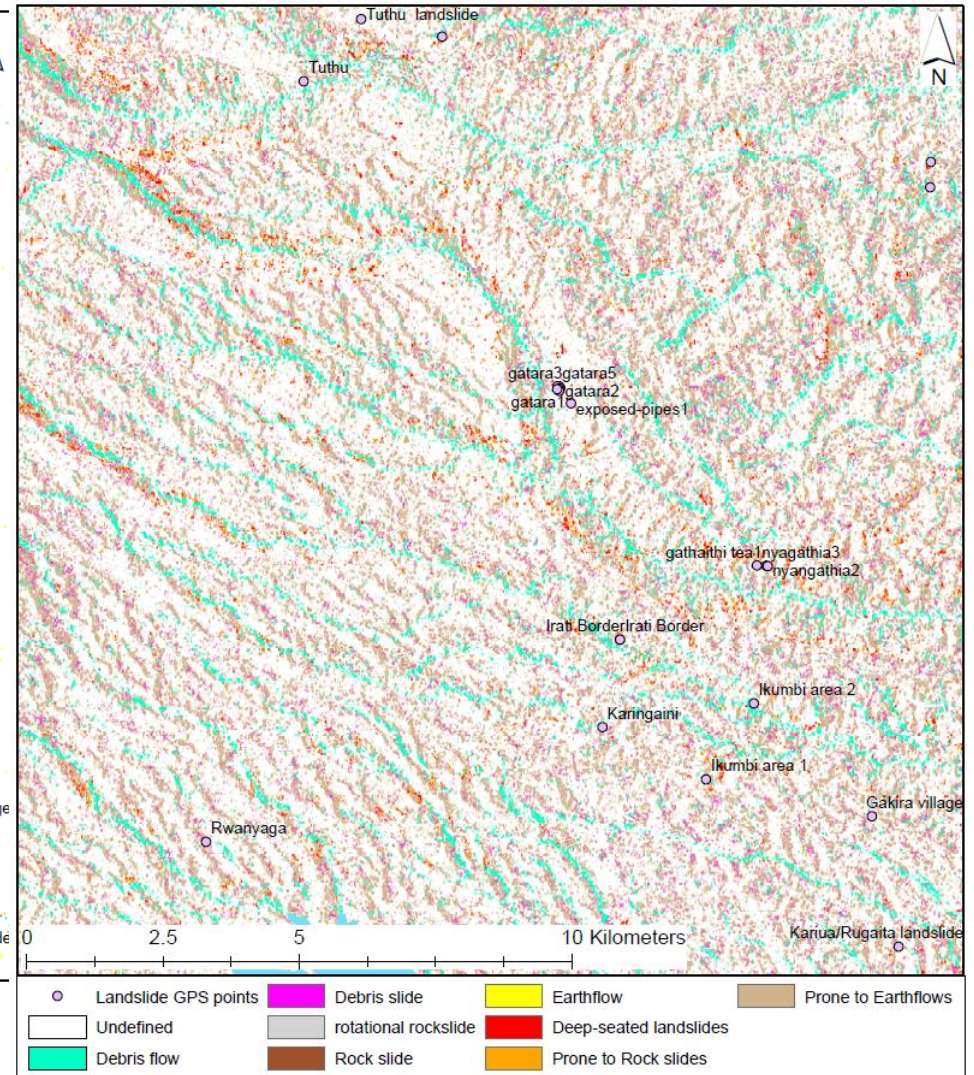


**Figure 6.10 (b):** Landslide types extracted from Sentinel-1 SAR-C classification reclassified according to other landslide factors.

## 6.5 Discussion

In general, the contribution of land-use to landslide events was captured as it was possible to observe a similar trend in landslides and land degradation processes. Other researchers' findings within the study area in the time epoch, revealed that indeed increased soil erosion activity was evident and resulted in increased sedimentation and volume change in dams such as Chinga dam (Malmstroem, 1997; Mburu et al., 2003). This could be as a result of loose soil due to poor agricultural practices (Mburu, 1998).

Although mixed root results in better root cohesion (Roering et al., 2003), less landslides are observed in forested areas and thus forest covers often result in better slope enforcement (Glade, 2003; Razak, 2014). Therefore, given that topographic and anthropogenic factors are perceived as the most important to landslides prevalence in this area (Owour, 2015), there is a need to consider afforestation as shallow rooted vegetation was observed on steep slopes (Mwaniki et al., 2015a). Indeed, the landslide density observed on the Sentinel-1 SAR-C landslide map stresses the need for alternative land-uses, since landslides are indicative of the site condition.

Earth flows were found to be the most common shallow landslide type followed by debris flow from the Landsat landslide types. This was also confirmed by the Sentinel-1 SAR-C landslide types where areas prone to earth flow dominated. This may be explained by the loose, thick top soils which often result in oversaturation during rainfall events (Zoebisch and Johansson, 2002). Further, the effects of cultivation exacerbate mudslides (Wendo, 2002). In addition, the terrain topography characterized by high density of drainage channels facilitates the movement of debris material under the influence of surface runoff.

The effectiveness of the methodology used depended on the ability to differentiate soil reflectance from the vegetated areas, use of geological information and texture data. The NDMIDR spectral index enhanced vegetation moisture properties given that Landsat band 7 is sensitive to canopy moisture content (Vohora and Donoghue, 2004) (which aided to highlight bare soil areas), and Landsat band 3 is a chlorophyll absorption band (hence soil has higher reflectance). In addition, band 7 is sensitive to clay bearing minerals (since it is located in the SWIR region) (Abdeen and Hassan, 2009), which further enhanced bare soil clayey areas. Thus, the NDMIDR spectral index overcame the challenge of using the NDVI index, which is only sensitive to vegetated areas (Mwaniki et al., 2015c). In addition, the

incorporation of the band 7 in the NDMIDR spectral index added geology information, and its use with red band maximised texture properties.

On the other hand, the use of PCA and ICA transformation analyses were essential as they led to the extraction of landslide related information onto a single component, while the changes that were not relevant to landslides were discriminated spectrally (Mondini et al., 2011b). Consequently, the use of a colour composite comprised of IC, PC and NDMIDR components, facilitated visual discrimination of landslide affected areas and those areas prone to land degradation. However, this was only limited to surface processes and by extension, shallow landslides only.

The texture and roughness information afforded by Sentinel-1 SAR-C data provided further information suited for mapping both shallow and deep-seated landslides, although it lacks the spectral information which facilitates landslide identification and mapping. This necessitates image fusion with multispectral data (e.g. Marcelino et al., 2009), which was achieved at two levels, namely: pixel and feature extraction levels. Feature extraction was enabled by thresholding of Sentinel-1 SAR-C components (texture, edges, coherence), a method applied by Zhao et al. (2012a) to combine InSAR products to detect active landslides in a large area.

The landslide map derived from Sentinel-1 SAR-C components provided information about lineaments and lines of weakness where deep-seated landslides could be triggered. This is important since a geological report after landslide occurrence in the year 2013 (Murei, 2013) and field survey, confirmed that indeed lines of weakness visualised as cracks by the local inhabitants preceded landslide occurrence, as in Figure 6.11. Inadequacy of geology and landslide expertise was cited in the report, an issue which can be handled by the use of RS expertise and automation processing with SAR imagery to detect linear geologic features (e.g. Coral, 2007; Marghany and Hashim, 2010b).

Validation was provided by overlaying GPS landslide points onto the landslide map, in selected areas where landslides are prone. The distribution of 226 GPS landslide points (Appendix B) into the various classes mapped were summarised using a frequency table in Spatial Data Modeller tool (SDM; Sawatzky et al., 2009), Table 6.4. About 25% of the GPS points coincided with the landslide areas in the Sentinel-1 SAR-C classification, while in the Landsat classification about 21% of the GPS points coincided with the mapped landslide areas. However, the additional information along the fault lines and ridge edges increased the number of GPS points in landslide areas to about 48%. The coincidence of GPS landslide

points onto forms of land degradation and erosion, 62% in Landsat 8 classification and 34% in the Sentinel-1 SAR-C classification, emphasized the high probability of landslide occurrence due to forms of erosion and land-use.

**Table 6.4:** GPS landslide points frequency tabulation.

Landsat 8 classification			Sentinel-1 SAR-C classification		
<i>Classes</i>	<i>Frequency</i>	<i>Area (sq km)</i>	<i>Classes</i>	<i>Frequency</i>	<i>Area (sq km)</i>
Landslides	47	105.5088	Landslides	57	1 897.9281
			Faults	15	2 927.6451
			Edges_crest	37	7 878.8493
			Edges_base	6	2 140.7067
Highly erodible	64	12 637.6281	Highly erodible	50	18 777.6306
Extreme erosion	23	3 453.8616	Extreme erosions	26	8 010.6948
Human development	7	755.2728	Human development	6	806.8554
Other erosions	31	7 023.8259	Other erosions	3	2 809.188
Exposed volcanic rocks	9	13 093.0614	Exposed Rocks	1	646.3548
Stable volcanic rocks	3	5 055.6024	Stable volcanic rocks	0	1 455.8364
Stable	4	4 269.2445	Stable	3	10 163.5173
vegetation covered rocks	5	17 986.5252	wetland	9	1 144.2537
Sediment deposits	24	2 474.6877	River channel deposits	3	615.2985
Runoff	9	3 779.9514	Runoff	10	6 156.2286
Fluvial deposits	0	1 401.5187	Deposits	0	6 631.3557
Water cover	0	712.413	Water cover	0	686.7585
Total	226	72 749	Total	226	72 749

Field observations revealed some landslide rehabilitation efforts on landslide scars (Figure 6.12), although in some areas it acted to increase the weight load on the loose soil which could trigger future landslides (e.g. Figure 6.12 b). Although this method is effective, it is limited to new landslides. Thus, the method can act as a guide to detailed field geomorphological analysis, while shedding light onto landslide causing factors of land-use management. It is also suited for updating existing landslide inventory maps. On the other hand, where no landslide inventories exist, older landslide scars may be mapped using earlier satellite imagery and some information from the field or literature sources.



**Figure 6.11:** Cracks observed before landslide occurrence.



(a): A rehabilitated site in Karumanthi-Kathangari, Kionyo (Meru)

(b): Possible landslide reactivation due to extra loading and shallow rooted vegetation on landslide scar

**Figure 6.12:** Landslide rehabilitation efforts.

## Chapter 7: Landslide Susceptibility Mapping

---

### *7.1 Introduction to Stability Mapping*

Landslides are consequences of slope failure and reflect the terrain instability conditions. Stability conditions are dynamic as they are functions of gravitational shear stress and the available soil shear strength: at the time of slope failure, shear stress is greater than the shear strength (Sidle and Ochiai, 2006). Thus, stability conditions change with factors affecting the local equilibrium forces (such as earthquakes), the load/weight (such as new deposit materials, rainfall) and the soil shear strength (De Blasio, 2011). Landslide triggering factors (rainfall, earthquake, volcanic eruptions, rapid erosion, physical or chemical weathering, ice melting, river undercutting, anthropogenic factors) increase the slope stresses or reduce the strength of the slope materials, thereby resulting in slope failure (Tofani et al., 2006; Wieczorek et al., 1997).

Rainfall induced landslides are increasingly common in many parts of the world (Corominas, 2000). Their occurrence is governed by the response of slopes to increased soil saturation levels / changes in pressure heads, which cause a decrease in soil suction and consequently a reduced shear strength of the soil (Galeandro et al., 2014; Iverson, 2000). Prolonged and heavy rainfall events have been shown to trigger landslides due to the variation of the pore-water pressure, according to the different degrees of weathering, fracturing, hydraulic conductivity and topography (Fannin and Jaakkola, 1999). These can result in deep-seated or shallow landslide types, whereby the frequency and magnitude of rainfall events together with other landslide predisposing factors influence the type.

Soil geotechnical properties greatly determine the hydrological response of the slope to the rainfall triggering factor. For example, rainfall induced landslides are common in areas where the slope topography angle is greater than the soil's internal friction angle (Friedel et al., 2006). In addition, the size of the soil grain particles influences the permeability, infiltration rate, and groundwater flow (Huat et al., 2006). In turn, the infiltration and subsurface water flow causes an imbalance in the hydrostatic level and suction dynamics which alters the energy balance of the slope (Liu and Li, 2015).

The main aim of this chapter is to investigate the effects of infiltration and the response of pore-water pressure due to increased saturation levels and their effect of slope stability. Although several methods are available to study rainfall and slope failures (refer to chapter

3), a physical model combining a hydrological and slope stability model was used to implement a rainfall induced landslide susceptibility model. Physical models are governed by physical laws, thus they simulate flows in the saturated and unsaturated zones of the slope using infiltration and slope stability models (Brunetti et al., 2010). Although they require much detailed soil-geotechnical data, they enhance the understanding of the rainfall induced landslide triggering mechanisms, while accounting for the differences in terrain attributes (topography, geological, hydrological) (Casagli et al., 2006). Also, the effects of environmental changes associated with rainfall patterns and land-use, which influence the frequency of landslide disasters and their severity, can be investigated and studied.

#### *7.1.1 Methodology: CHASM*

The methodology constituted of organising the various landslide predisposing factors into a geodatabase in ArcGIS, followed by combined hydrological and slope stability mapping, and finally landslide susceptibility mapping.

##### *7.1.1.1. Description of the Data Used*

The data used in the study were categorised into: topographic data (slope, aspect, curvature, flow length, flow direction, upslope contributing area, stream delineation); geology (lineaments and lithology); LULC (forest, crops, grass, bare, water); landslide inventory, soil geotechnical parameters (type, depth, soil cohesion, internal angle of friction, bulk density, porosity, root cohesion, hydraulic conductivity, saturated soil density/weight, moisture content); rainfall, water table rest surface. The LULC for various years were mapped as described in Chapter 4 and assigned root cohesion values from literature, while the lithology and lineaments were mapped and described in Chapter 5. Soil geotechnical parameters were obtained from existing soil-vector geodatabase and the attributes added to the mapped soil map (Chapter 5). However, some soil strength parameter, internal angle of friction and soil cohesion were obtained from literature and laboratory shear tests of undisturbed soil samples from few landslide points (e.g. Davies and Nyambok, 1993; Zoebisch and Johansson, 2002).

STRM DEM, a 30 m spatial resolution, was the source of the elevation data from which the topographic attributes were calculated using the spatial analyst (surface and hydrology) tool. The slope varied from 0 to 88 degrees, revealing very steep areas to gentle and flat areas. From the flow accumulation raster, a threshold value was chosen to obtain streams which were ordered according to the number of tributaries upstream (Strahler, 1952). This resulted in six classes of rivers and their tributaries which help to delineate drainage basins.

Monthly rainfall data (3B43) at a spatial resolution of 0.25° by 0.25° available from TRMM Multi-satellite precipitation Analysis (TMPA), years 1998 to 2015 were downloaded from the NASA GES DISC centre. Heavy rainfall event data were extracted and resampled at 30m to match the other available raster layers. In order to supplement the lacking rainfall data for the period earlier than the available TRMM data, 14 rain-gauge rainfall station data (from the Kenya meteorological department) were used. The spline interpolation method was used to model the monthly rainfall maps for El-Niño rainfall event (year 1997, months Oct-Dec).

On the other hand, a DEM of the groundwater table was modelled using borehole water rest level data. The datasets were obtained from secondary sources, among them hydro-geological reports and ground water assessment (e.g. Alamirew et al., 2007; Namwenya, 2014), and compiled under a common projection system as in Appendix A. The borehole distribution was random and extended to regions outside the study area boundary so as to increase the accuracy of the modelled DEM groundwater table level. The borehole points were then imported into a point shapefile with the z-dimension being the reduced level of the water table rest level. This was followed by spline interpolation to form a raster file whose output spatial resolution was fixed at 30 m, to match other data. The depth to the water table was then extracted as the difference between the terrain elevation and groundwater rest levels.

Finally, some sampled landslide GPS points collected during field campaign were imported and saved as a point shapefile for validation of the model results. In total, 226 landslide GPS points were picked and they were distributed within the landslide prone regions (see Appendix B, see Figure 7.2.5).

#### *7.1.1.2. Combined Hydrological and Slope Instability Modelling (CHASM)*

The CHASM model developed by Anderson and Lloyd (1991), combines both hydrologic model and stability models to assess slope instability and landslide hazard. It has since been applied in several researches such as: Angeli et al. (1998), Nugroho (2008), and Wilkinson et al. (2002). Groundwater flow is linked to slope stability model, and together with topographic relief and soil properties, are used to calculate pore water pressure: an input to infinite slope analysis. Slope instability modelling due to rainfall trigger can be assumed to take place due to increased air pressure ( $\mu_a$ ) and raised groundwater ( $\mu_w$ ) following infiltration (Gostelow, 1991). Thus, using an infinite slope stability model which assumes a failure plane planar to the ground surface (Casagli et al., 2006), the FOS can be expressed as the ratio of the available shear strength ( $\tau_f$ ) to the shear stress ( $\tau$ ), equation 7.1.

$$FOS = \frac{\text{shear strength}}{\text{shear stress}} = \frac{\tau_f}{\tau} \quad (7.1)$$

The shear strength is then defined for saturated and unsaturated soil conditions using equations 7.2 (a) and (b), respectively (Fredlund and Morgenstern, 1977)

$$\tau_f = c' + (\sigma - \mu_w) \tan \phi' \quad (7.2 a)$$

$$\tau_f = c' + (\sigma - \mu_a) \tan \phi' + (\mu_a - \mu_w) \tan \phi_b \quad (7.2 b)$$

Where:  $c'$  is the effective soil cohesion,  $\sigma$  is the total normal stress,  $\phi'$  is the effective friction angle,  $\mu_a$  is the pore air pressure,  $\mu_w$  is the pore water pressure,  $(\sigma - \mu_a)$  is the net normal stress,  $\phi_b$  is the angle indicating the rate of increase in shear strength relative to the matric suction  $(\mu_a - \mu_w)$  i.e.  $\phi_b = \arctan \{(C - c') / (\mu_a - \mu_w)\}$ . Therefore, the equation 7.2 (b) can be expressed in alternative means using the total cohesion,  $c$ , as equation 7.3

$$\tau_f = C + (\sigma - \mu_a) \tan \phi' \quad (7.3a) \quad \text{where: } C = c' + (\mu_a - \mu_w) \tan \phi_b \quad (7.3b)$$

As the soil approaches the saturation level, the pore air pressure approaches the pore water pressure, hence the matric suction disappears and the equation 7.3a is the extension of the Mohr-coulomb failure criterion (Fredlund et al., 1978). Therefore, the FOS equation can be represented by equation 7.4, considering the normal stress

$$FOS = \frac{C + (\sigma - \mu) \tan \phi'}{\tau} = \frac{C + (\gamma z \cos^2 \beta - \mu) \tan \phi'}{\gamma z \sin \beta \cos \beta} \quad (7.4)$$

Where;  $\gamma$  is the soil weight,  $z$  is the depth to the failure plane,  $\beta$  is the slope angle, and the denominator is the component of the shear stress,  $\tau$ . Further, the infinite slope stability model was modified to include the effects of vegetation (i.e. root cohesion) and evapotranspiration which reduces excess pore water pressure as in the equation 7.5 (Sidle, 1992)

$$FOS = \frac{C + (\gamma z \cos^2 \beta - \mu + U_v) \tan \phi'}{\gamma z \sin \beta \cos \beta + W_T Z_r \cos \beta} \quad (7.5)$$

where:  $C$  is the combined cohesion term = soil cohesion ( $c'$ ) + root cohesion ( $C_r$ ),  $W_T$  is the weight of the vegetation,  $Z_r$  is the root depth, and  $U_v$  is the correction due to evapotranspiration which leads to positive pore pressure, modelled using equation 7.6 by Simoni et al. (2008)

$$U_v = \frac{T}{\gamma_w} \times \frac{LAI}{Z_r} \times W_T \cos \beta \quad (7.6)$$

where:  $T$  is the coefficient of the transpiration rate,  $\gamma_w$  is the unit weight of water, and LAI is the leaf area index. In this study, the LAI was substituted with the second Tasselled Cap component which represents the greenness index, while the coefficient of transpiration was represented by the third Tasselled cap component which represents the canopy moisture content. On the other hand, the pore pressure term was expressed as equation 7.7 (Graham, 1984)

$$\mu = \gamma_w Z_w m \cos^2 \beta \quad (7.7)$$

where:  $m$  is the soil saturation, and  $Z_w$  is the depth to the water table. The soil saturation term was expressed considering percolation through the unsaturated layer, which was calculated based on gravitational unsaturated flow, the volumetric moisture ( $\theta$ ) is expressed as equation 7.8 (Van Beek, 2002)

$$\theta_E = \frac{\theta - \theta_r}{\theta_s - \theta_r} \rightarrow \theta = \theta_r + \theta_E(\theta_s - \theta_r) \quad (7.8)$$

where:  $\theta_s$  is the saturated soil moisture content and is set to the porosity,  $\theta_r$  is the residual moisture content, and  $\theta_E$  is the relative degree of saturation which varies between 0 and 1. However, the product of the depth of the unsaturated layer above the groundwater table and the relative degree of saturation ( $\theta_E$ ) yields the actual percolated and stored water, where percolation takes place as governed by unsaturated hydraulic conductivity. This is the condition of the Green-Ampt approach which requires the use of the water retention curves (for particular soil grain size) to solve for the unsaturated hydraulic conductivity (Tofani et al., 2006). Consequently, assuming that the depth of the unsaturated zone is equal to the depth to the groundwater table  $Z_w$ , the percolation is expressed as equation 7.9

$$P_r = Z_w(\theta - \theta_r) \frac{k(\theta_E) \cdot \Delta t}{Z_w} \quad (7.9)$$

where:  $Z_w(\theta - \theta_r)$  the amount of stored infiltrated water over the time  $\Delta t$ . Thus, the soil saturation can be estimated using infiltration parameters as equation 7.10 (a), while the pore pressure is expressed as equation 7.10(b).

$$m = K_{sat} \left( \frac{\theta - \theta_r}{\theta_s - \theta_r} \right) \quad (7.10a)$$

$$\mu = K_{sat} \left( \frac{\theta - \theta_r}{\theta_s - \theta_r} \right) \gamma_w Z_w \cos^2 \beta \quad (7.10b)$$

Finally, replacing equations 7.6, 7.10 (b) into equation 7.5 yields the final CHASM model adapted for use in this study, equation 7.11

$$FOS = \left\{ \frac{c + c_r}{\gamma z \sin \beta + W_T Z_r} \right\} \frac{1}{\cos \beta} + \left\{ \frac{\left( 1 - \left( K_{sat} \left( \frac{\theta - \theta_r}{\theta_s - \theta_r} \right) \frac{\gamma_w Z_w}{\gamma Z} \right) + \left( \frac{T}{\gamma_w} \times \frac{LAI}{Z_r} \times W_T \right) \right) \cos \beta \tan \phi}{\gamma z \sin \beta + W_T Z_r} \right\} \quad (7.11)$$

The soil geotechnical properties of porosity and the total available water capacity (TAWC) under normal conditions, supplemented the saturated soil moisture content and the residual moisture content, respectively. The saturated hydraulic conductivity values, for each soil type, were adapted from the USDA series with Van Genuchten models (Hamdhan and Schweiger, 2011) as in Table 7.1.1. The equation 7.11 was implemented stepwise, with changing pore pressure values due to infiltration, progressively in a heavy rainfall event epoch.

**Table 7.1.1:** Saturated hydraulic conductivity ( $K_{sat}$ ) values (Adapted from Hamdhan and Schweiger (2011)).

Soil type	$K_{sat}$ (m/hr)
Clay	0.00198
Very clayey	0.02592
Loam/Red volcanic	0.01044
Sand	0.2988

### 7.1.2 Results

The landslide susceptibility of three heavy rainfall events were modelled i.e. the epochs October 1997 – May 1998, October 2009 – May 2010, and March – May 2015. The epochs were chosen following the heavy rainfall amounts and the impacts of increased landslide incidences within the period (Kirimi, 2015; Momanyi, 2010; Muchui, 2015; Mwangi, 2009, 2010). Figure 7.1.1 (a) is the slope instability map chosen for the month of November 1997 which had the highest rainfall amount, as well as the highest unstable area coverage, in the first epoch i.e. October 1997 – May 1998. A blown out section of Figure 7.1.1 (a), which is prone to landslide occurrence, is the Figure 7.1.1 (b). Field GPS landslide points were overlaid on the blown out section to reveal any correlation with the mapped unstable areas of the CHASM model. The Figure 7.1.2 shows the trend of unstable areas in the first epoch, which was compared with the rainfall trend in the Figure 7.1.3.

At the onset of rainfall event in the month of October 1997, the amount of unstable cells (which were converted into areas) in the CHASM model were low. However, with increased rainfall amount in the following month of November, the unstable areas increased and they remained relatively high during the rainfall period. Although there were variations in the rainfall amount during the rainfall event, the effect of antecedent soil moisture maintained the

instability at high levels. Thus, the effects of decreasing rainfall amounts in the months of February to April 1998 were observed in the month of April by decreased unstable areas (Figure 7.1.2). However, unstable areas increased with increased rainfall in the month of May 1998.

On the other hand, the results obtained from the second rainfall epoch (October 2009 – May 2010) are represented by Figure 7.1.4 to Figure 7.1.6. The Figure 7.1.4 (a) represents only one of the months in the second epoch where rainfall amount was at the peak. A larger scale presentation of Figure 7.1.4 (a) is shown by Figure 7.1.4 (b) and is overlaid with landslide GPS points. The trend of slope instability areas is represented by Figure 7.1.5, which is compared with the effects of rainfall amounts/trend in Figure 7.1.6. The effects of soil oversaturation were observed in Figure 7.1.5, whereby the onset of rainfall season resulted in large unstable areas. The trend of instability was then controlled by rainfall amounts, i.e. reducing and increasing with rainfall amounts as in Figure 7.1.6. However, as the rainfall amount increased, the effects of accumulated antecedent soil moisture maintained instability (March – April, Figure 7.1.5).

The third epoch results were presented by Figures 7.1.7 and 7.1.8 i.e. slope instability CHASM model map and the trend of slope instability, respectively. Although the rainfall trend for this epoch was not available, the slope instability increased sharply in the month of April 2015 during which the rainfall was reported to cause floods and trigger landslides in various parts of the study area (Gitau, 2015; Ngethe, 2015). As the rainfall subsided, the slope stability improved, although the effects of antecedent soil moisture maintained higher levels of instability greater than the onset of the rainfall event.

Comparing the Figures 7.1.2, 7.1.5 and 7.1.8, it was noticeable that most unstable areas were triggered by the rainfall event in the first epoch (October 1997 – May 1998) where rainfall amounts were much higher than the second and third epochs. A common observation from the Figures 7.1.1 (b), 7.1.4 (b), and 7.1.7 (b) was the coincidence of the GPS landslide points and the unstable areas symbolized by a high density of dots. This revealed a high correlation between the unstable areas in the CHASM model and the GPS landslide points. It was also observed that exposed bare rock areas in high elevation areas had increased density of unstable areas as in Figures 7.1.1, 7.1.4, and 7.1.7. This could be attributed to the geomorphic processes which are accelerated by barren land-cover, high frequent rainfall due to modified tropical climate and orographic rain.

Slope instability map using CHASM, Nov 1997

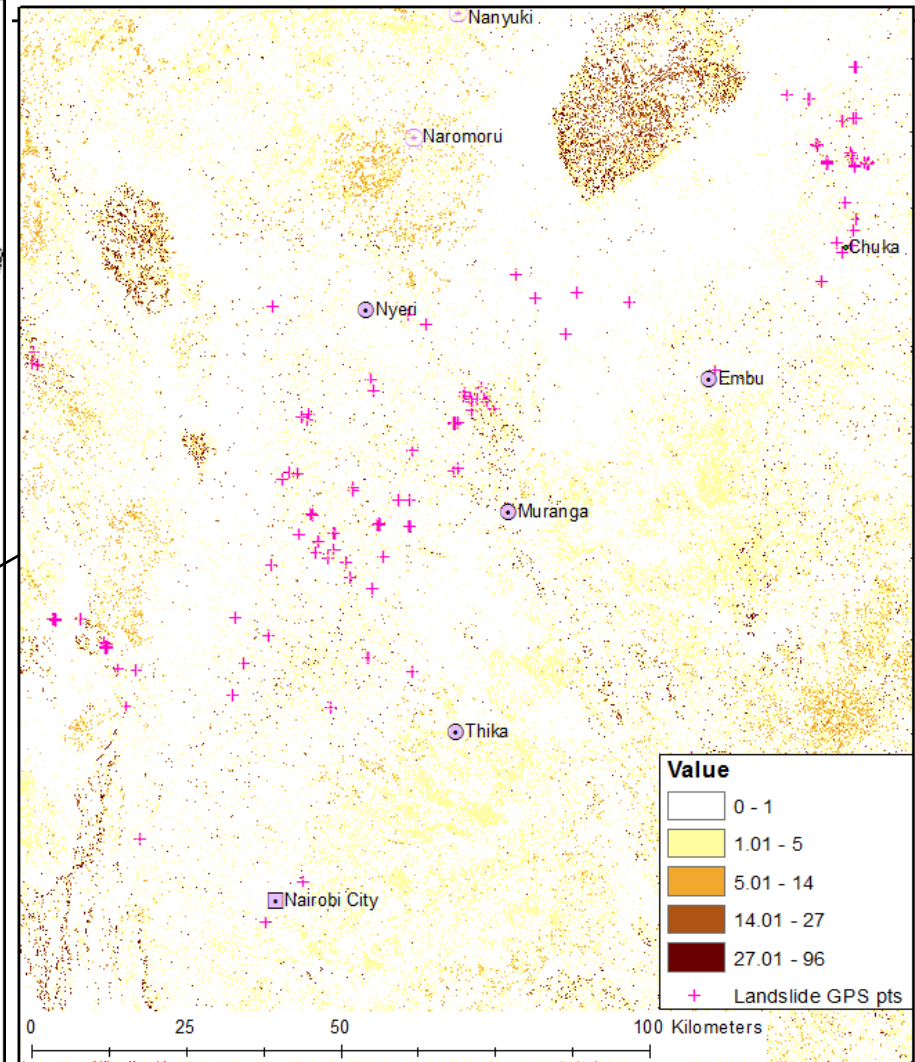
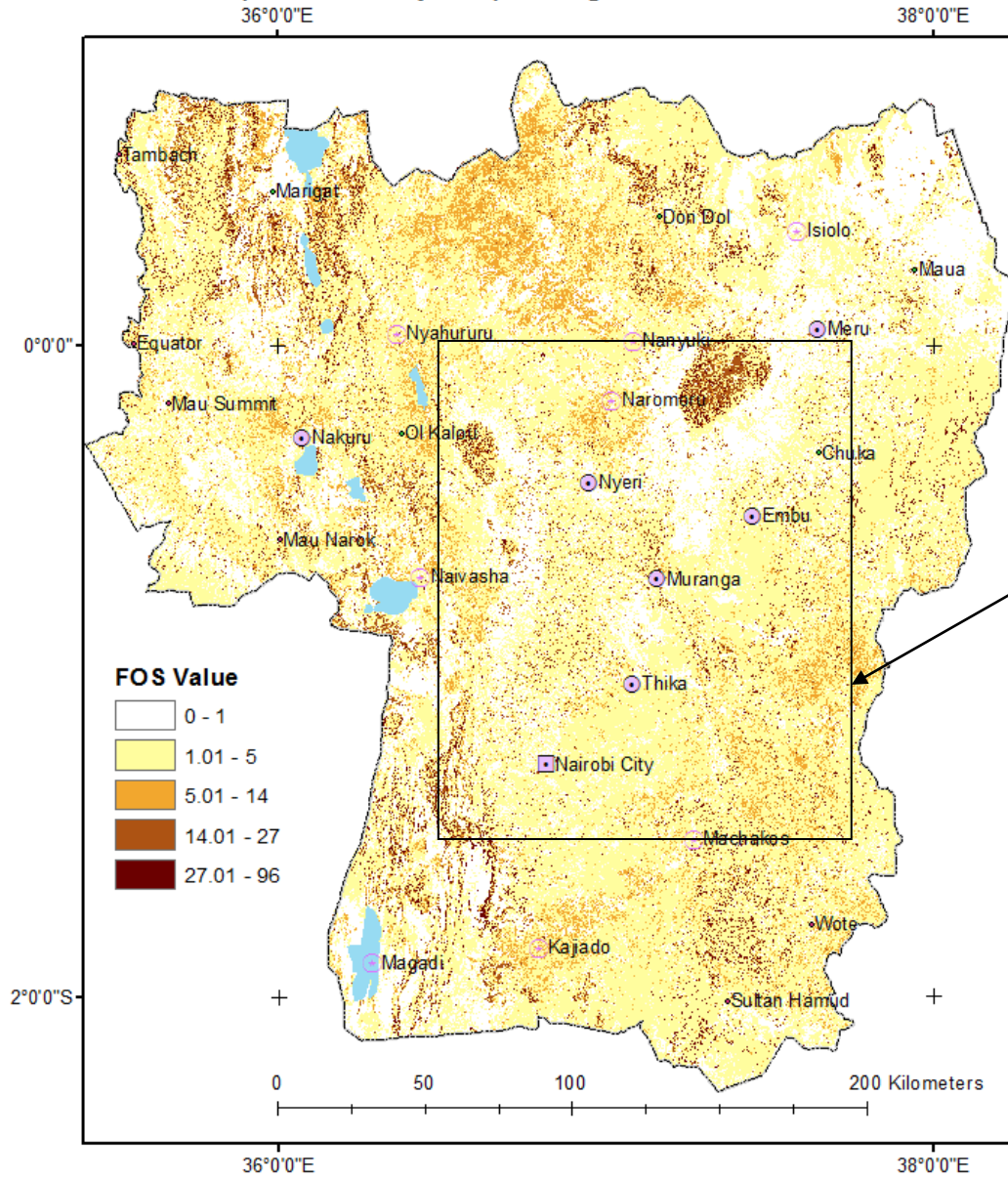
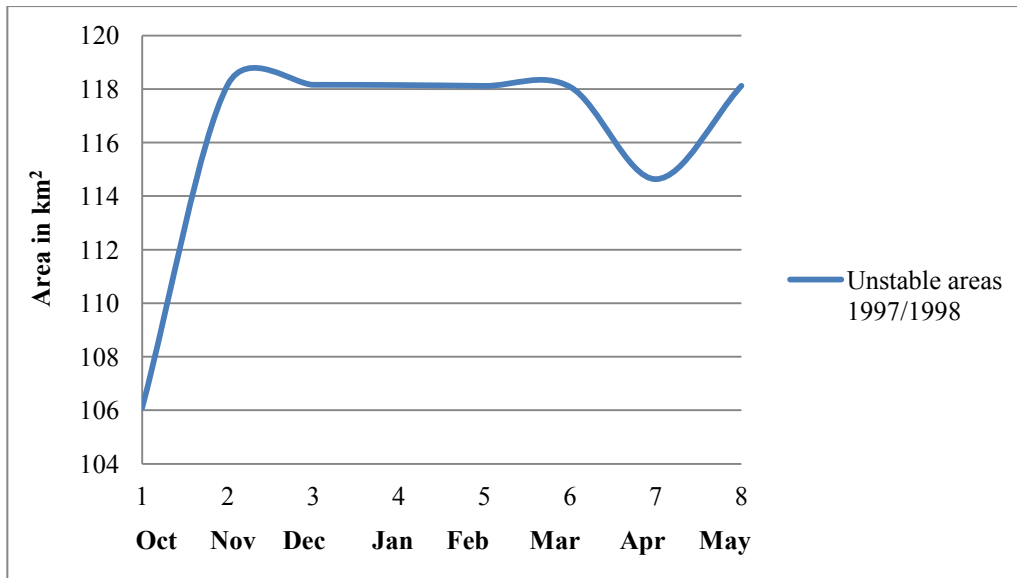
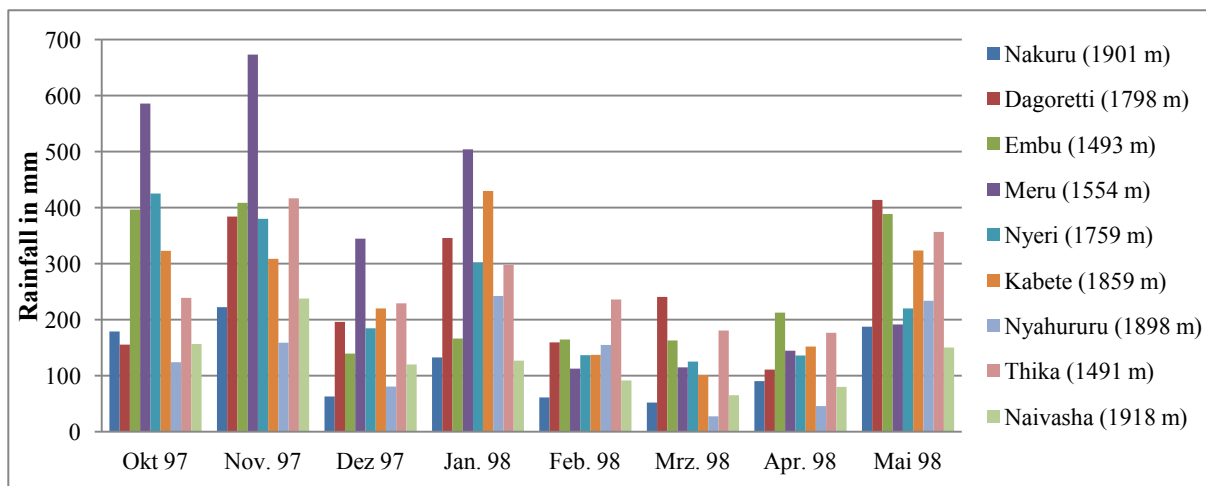


Figure 7.1.1 (b): A blown-out part of Figure 7.1.1 (a) overlaid with GPS landslides points.

Figure 7.1.1 (a): Slope instability mapping, CHASM model, Nov 1997.



**Figure 7.1.2:** Slope instability trend for the epoch Oct 1997 to May 1998.



**Figure 7.1.3:** Monthly rainfall amounts in selected stations, Oct 1997 to May 1998  
(Data source: KMD).

### Slope instability map using CHASM, April 2010

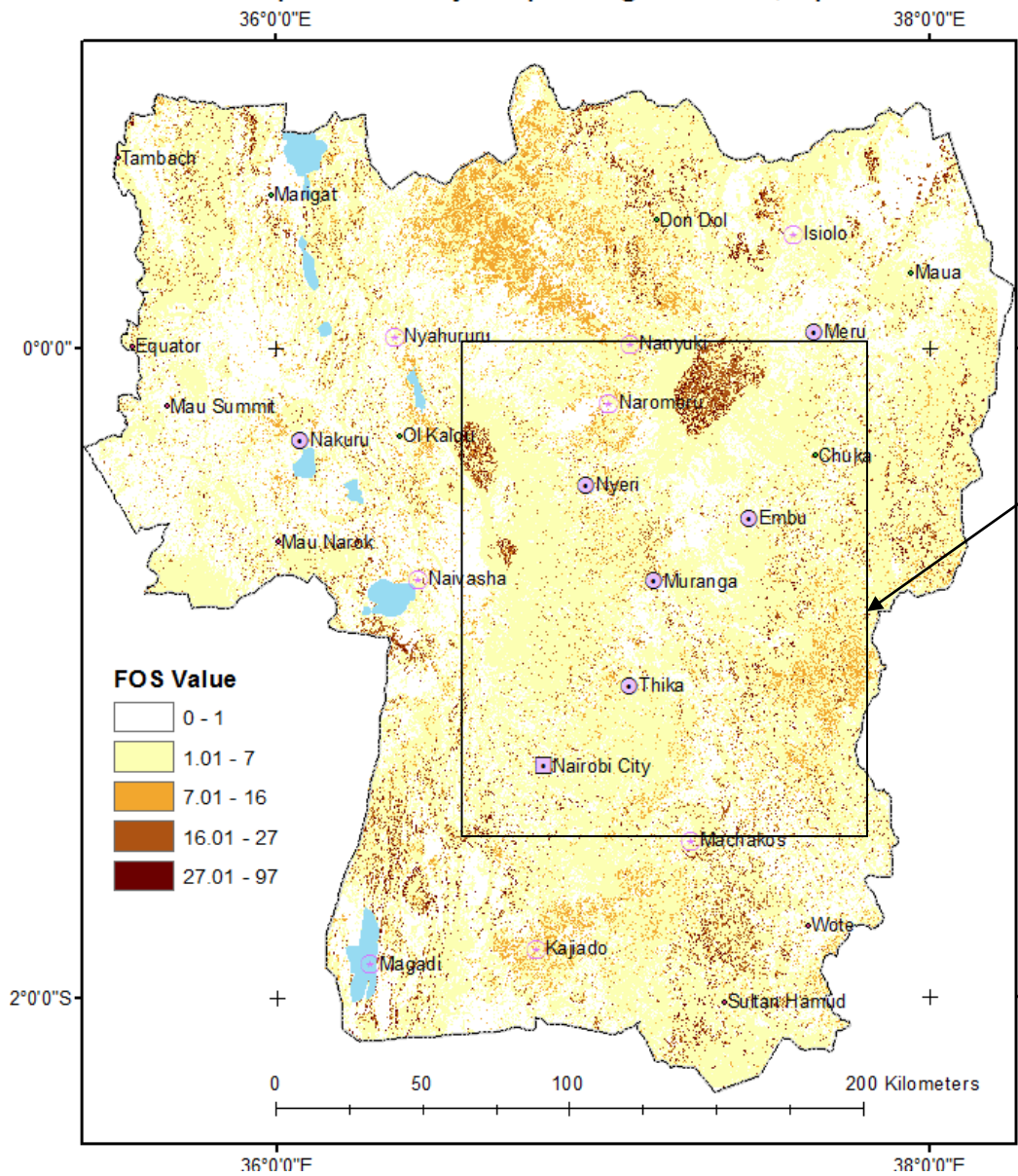


Figure 7.1.4 (a): Slope instability mapping, CHASM model, April 2010.

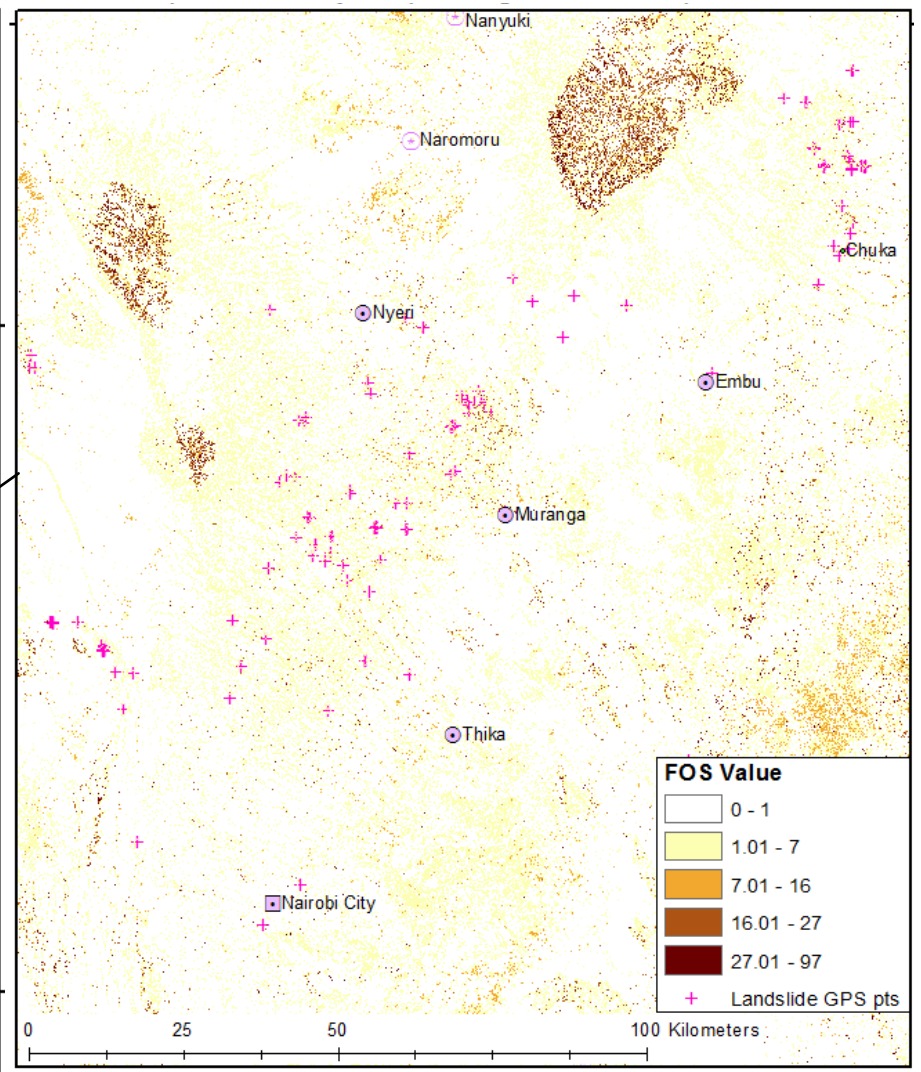
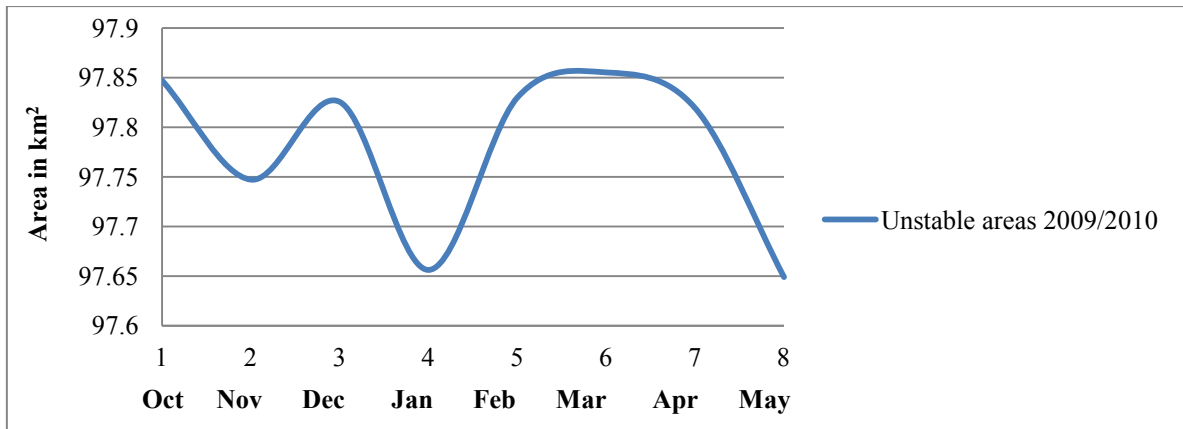
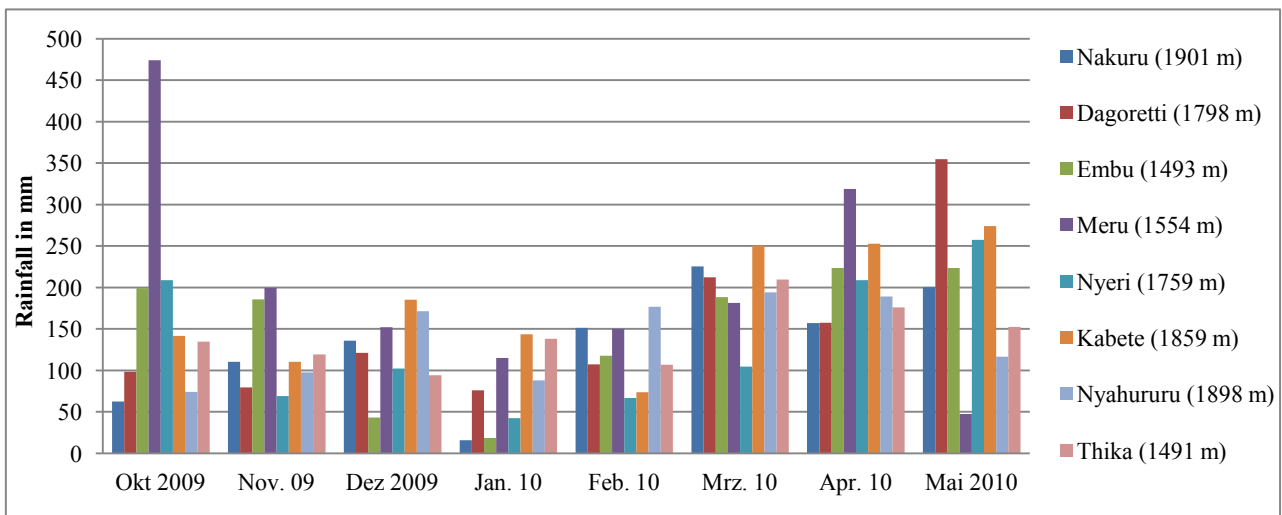


Figure 7.1.4 (b): A blown-out part of Figure 7.1.4 (a) overlaid with GPS landslides points.



**Figure 7.1.5:** Slope instability trend for the epoch Oct 2009 to May 2010.



**Figure 7.1.6:** Monthly rainfall amounts in selected stations, Oct 2009 to May 2010  
(Data Source: KMD).

### Slope instability mapping using CHASM, April 2015

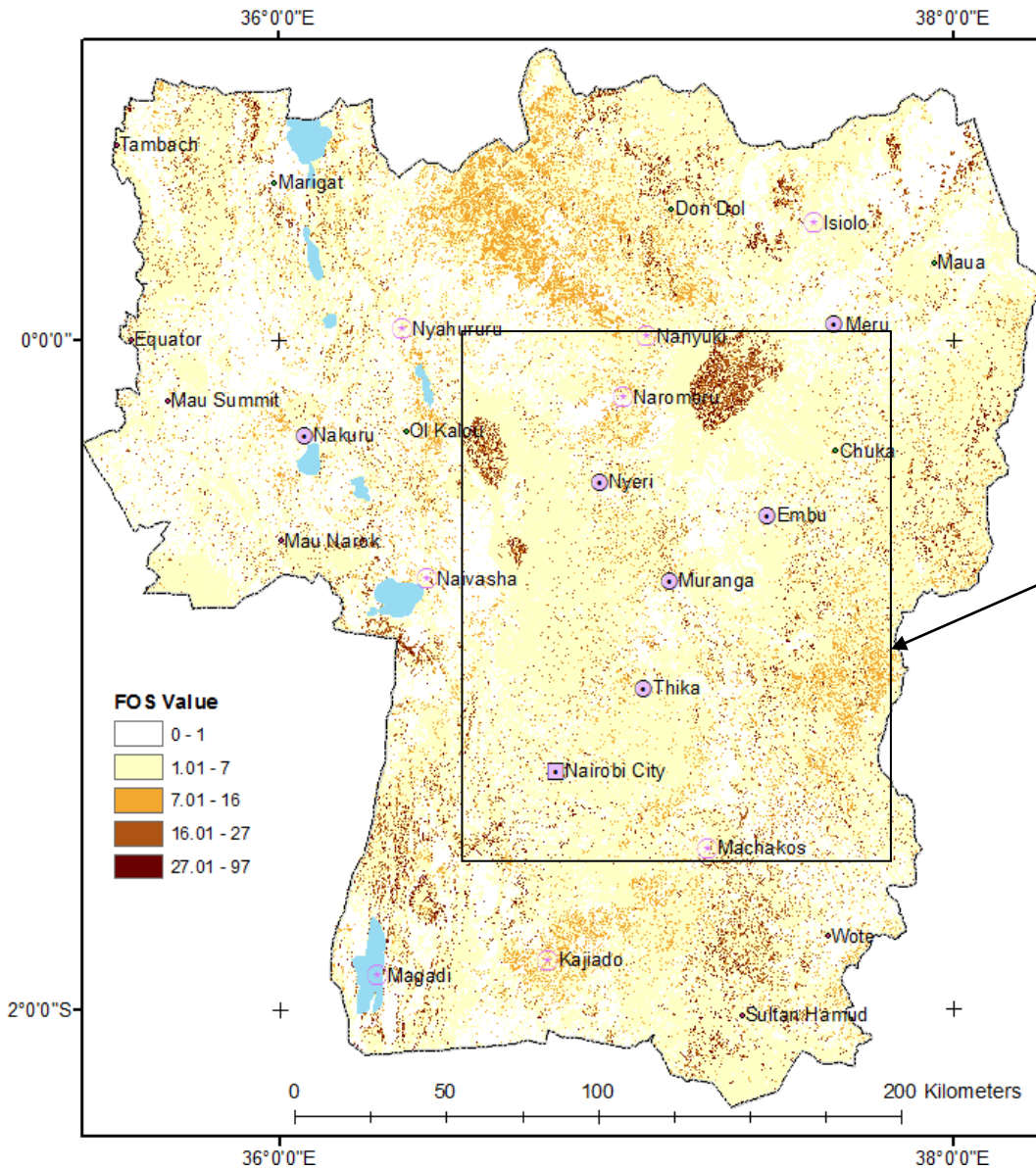


**Figure 7.1.7 (a):** Slope instability mapping, CHASM model, April 2015.

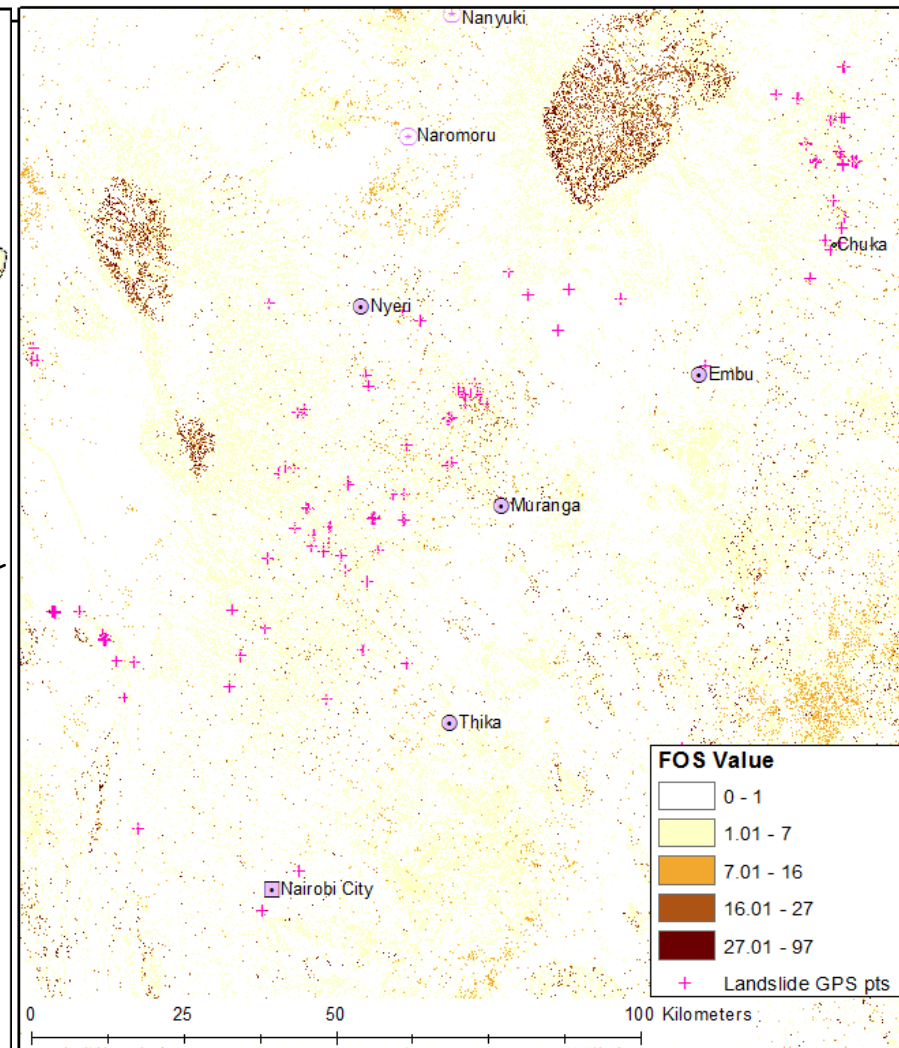


**Figure 7.1.7 (b):** A blown-out part of Figure 7.1.7 (a) overlaid with GPS landslides points.

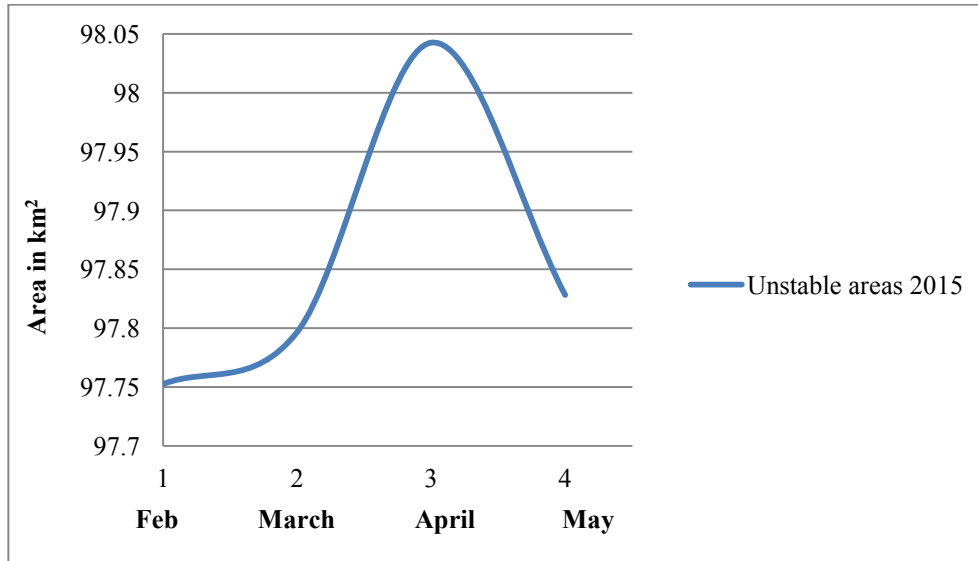


**Figure 7.1.8:** Slope instability trend for the epoch February to May 2015.

### 7.1.3 Discussion

The CHASM results depicted high densities of dots representing unstable cells closely following the terrain ridges and geology lineaments especially around the mountain areas and along the Rift Valley escarpments. However, the heavy rainfall impacts accelerated the instability and susceptibility levels. Such areas are prone to slope instabilities in the form of mudflows and shallow landslides, although they were less noticeable and are only considered hazardous when they interfere with human activities. Their effects were manifested in the lower regions (along drainage channels) in the form of dam siltation and water turbidity (Mburu et al., 2003).

On the other hand, the effects of rapid and extreme erosion exacerbated the instability, especially along drainage networks and rock lineaments. The effects of geomorphic processes were observed to increase instability on bare rocks around high mountain relief features where frequent orographic rainfall is received. In addition, temperature ranges and heavy intensity precipitation around mountainous features could accelerate the rate of weathering, which yields material with less cohesion. The fractured rock units are less compact compared to the bedrock material, which increases permeability and influences the pore pressure changes (Fannin and Jaakkola, 1999). Thus, the geology contributed to the stability after the onset of rainfall events, whereby fractured rocks allowed groundwater flow to areas of perched water table. The net effect was soil oversaturation in the layers above the perched water tables and weakened slope stability (Lourenço et al., 2006; Terlien, 1998).

The role of rainfall characteristics (duration, temporal distribution) was investigated through the effects of prolonged rainfall and amounts. Prolonged rainfall, which was noted to be more responsible for slope failure compared to intense precipitation (Galeandro et al., 2013), was also responsible for maintaining large unstable areas due to reduced matric suction (Ray 2004). Consequently, even with decreased rainfall amounts, the effects of antecedent infiltration and soil moisture from prolonged rainfall contributed to the high slope instability level. In addition, areas with intense rainfall and loose soil in the subsurface facilitated infiltration which led to reduced soil shear strength while increasing the weight load (Iverson, 2000; Ray and Jacobs, 2007). The net effect was increased negative pore pressure and increased slope instability (Huat et al., 2006). Although this study could not establish changes to the underground water table which could trigger landslides or slope instabilities, a study by Fourie (1996) showed that shallow landslides could be induced by the migration of a wetting front into the slope.

LULC played an important role in controlling stability, whereby bare sloppy areas were the most affected. However, in forested areas, stability was maintained by the processes of evapotranspiration and increased root strength (Stokes et al., 2008; Wilkinson et al., 1998). At the onset of rainfall event in the month of October, most agricultural areas were bare (in preparation for a new growing season) and thus the effects of rapid oversaturation were experienced. As the vegetation cover increased, some stabilization was achieved by the loss of soil moisture through root uptake and evapotranspiration. Hence, the role of vegetation in controlling the slope stability was demonstrated in that the areas covered by dense forest remained stable, whereas the bare soils experienced sudden oversaturation at the onset of rainfall events due to the effects of increased infiltration. A similar landslide study by Kibiiy et al. (2014) in Kerio-Valley (western Kenya) established that slope stability would be significantly improved if the study area were under forest cover, compared to agricultural land-use which increased unstable and critical areas significantly.

This study has demonstrated that CHASM model can guide large scale slope instability assessment from the high correlation of unstable areas with GPS landslide points. Also, the requirement for large, detailed datasets with deterministic models can be complemented by remotely sensed datasets, thereby enabling regional stability assessment. Such datasets could be easily updated through temporal datasets, especially to monitor the effects of vegetation, and soil moisture, which play a major role in maintaining stability.

The CHASM model results in this study could be improved further by the following: higher spatial resolution DEM to derive the topographic slope signature; higher multi-temporal resolution imagery to derive LAI indices at monthly interval; higher density borehole geotechnical water rest levels data and unconfined aquifer wells water levels; soil profiles and geotechnical parameters at various depths; and evapotranspiration parameters. In particular, high resolution DTM data would increase the potential of detailed analysis of landslide location through the ability to recognize easily the local variations in hillslope and valley morphology (Tarolli and Tarboton, 2006). Nevertheless, the study provided a guide to areas prone to slope instability, while enhancing the understanding of the interaction of slope instability factors which result in shallow landslides.

### *7.2 Introduction to Landslide Modelling and Prediction with Artificial Neural Networks (ANN)*

Landslide modelling and prediction is an essential step towards developing mitigation measures in order to safeguard the lives of the vulnerable people and prevent losses associated with the damages caused by landslides. According to Courture (2011), landslide vulnerability is the expected degree of loss associated with a given level of predicted landslide hazard in an area, while landslide hazard is a condition with the potential for causing a landslide event. The ability of the people to cope with the landslide losses (i.e. resilience), is determined to a large extent by their preparedness. Thus, landslide hazard assessment helps to address the questions, who is at risk (element), where are they located, and when are landslides expected to occur (time) (Crozier and Glade, 2004).

Landslide susceptibility mapping requires the knowledge of slope instability movements, the complex interrelationships of landslide controlling and triggering factors, and past landslide occurrences in the form of landslide inventories (Pourghasemi et al., 2012). Indeed, the vulnerability increases with the presence of landslide predisposing factors and landslide triggering events (Catani et al., 2011; Highland and Bobrowsky, 2008). In addition, areas which experienced landslides in the past are potentially unstable and hazardous due to possible landslide reactivations following landslide triggers (Guzzetti et al., 2005). Therefore, the mapping of these factors together with landslide inventory provides the basic data for further hazard susceptibility analysis. Equally important in hazard assessment is the landslide failure mechanism, which is based on landslide movement and debris involved (Hung et al., 2014).

GIS and RS are powerful tools for developing spatial models for identifying landslide prone areas and the predisposing factors. GIS environment is especially suited for landslide susceptibility assessment studies since they involve huge amounts of data, require simulation, weight assignment and ease data integration and generation of landslide maps (Pardeshi et al., 2013). On the other hand, RS provides data and enables the preparation of landslide controlling factors thematic data layers. Since landslides are the results of geomorphic processes, landslide mapping by RS alone has been criticised because it is based on spectral reflectance which is not unique to landslide debris (Martha et al., 2010). Instead, the integration of RS and GIS process-based models are recommended to characterise and classify landslide hazards (Drăguț and Blaschke, 2006; Lee, 2005).

According to Guzzetti et al. (2000), there is no generally agreed best landslide hazard assessment method. However, the general trend is the application of GIS-based quantitative methods such as Decision tree, AHP, MCDA, and ANN (see Chapter 3). Comparative studies involving ANN models have generally reported higher prediction accuracies (e.g. Kanungo et al., 2006; Pradhan and Saied, 2010; Yilmaz, 2009) and are easily implemented in GIS environment with the help of Arc-SDM extension (Sawatzky et al., 2009). In addition, ANN represents and resolves the complex relationships among landslide predisposing factors, which are related to landslide processes in non-linear relationships (Ercanoglu, 2008; Park et al., 2013). Based on landslide inventory layer, the ANN model is trained to learn the interrelationships between landslides and their causative factors, so as to recognise and predict future geo-hazards (Noack et al., 2014; Pradhan and Buchroithner, 2010). The landslide model is considered successful if the resulting landslide susceptibility map can predict the distribution of known landslide occurrences and can delineate possible landslide prone areas following strong evidence collected from the landslide thematic factor data (Brenning, 2005).

The aim of this chapter is to perform landslide susceptibility which would lead to landslide hazard zonation, identification of landslide types, and assignment of landslide occurrence probabilities. While the previous section (7.1) developed landslide susceptibility map using a CHASM physical model, this section uses the ANN statistical/ quantitative method of landslide hazard assessment to relate the landslide distribution to the landslide predisposing factors. Unlike the physical model, the ANN model could utilise all the mapped landslide factors and thus the results could include both shallow and deep-seated landslide types.

### 7.2.1 Methodology: Landslide Susceptibility Mapping via ANN

Implementing the ANN model was comprised of the following steps: preparation of landslide predisposing factors, formation of the unique condition unit (the partitioning unit for landslide mapping), ANN training and recognition, landslide classification by type, landslide susceptibility and hazard zonation, and landslide prediction. The Figure 7.2.1 is the methodology flow chart which summarized the various steps comprising the methodology. Another important step performed was model validation in order to evaluate the prediction ability of the model.

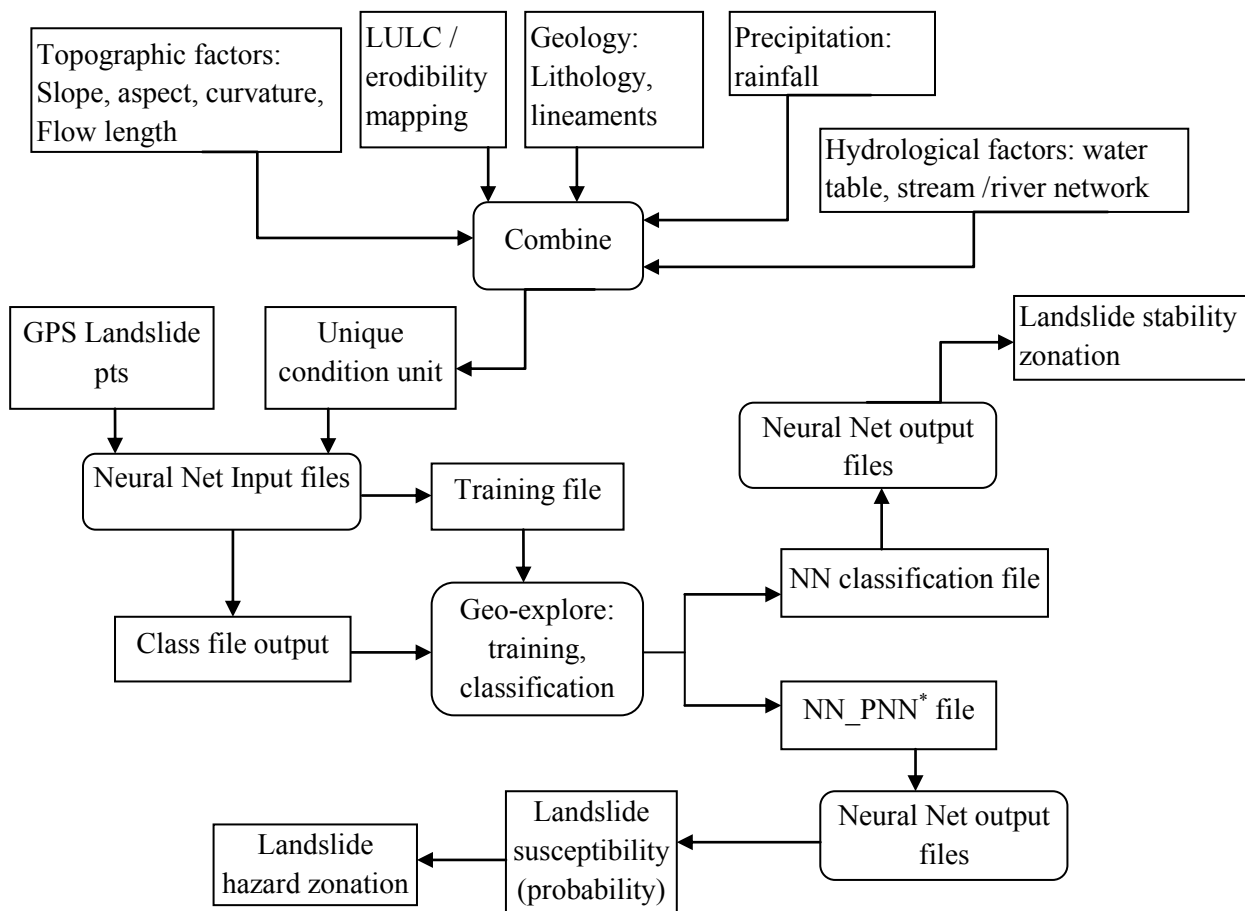


**Figure 7.2.1:** ANN implementation methodology flow chart.

#### 7.2.1.1 Data Description and Preparation

Various categories of data types were prepared (as described in previous chapters) using GIS and RS softwares, namely: topographical (slope, aspect, curvature), hydrological (flow length, watertable rest levels, river/stream network), geology (lithology, lineament), precipitation/rainfall, and LULC. GIS was particularly useful in managing and preparing the thematic maps in order to allow the processing of a combination file for use in the ANN

\*NN\_PNN: Neural Network Probability Neural Network

implementation. It was found necessary to reclassify each thematic layer into classes of integer values in order to process the unique condition unit file, which was within the capability of the computer memory and processing power. A scale of 10 to 1 was chosen to represent the new classes (captured the expert judgement), signifying the most important to the least important, respectively as in Table 7.2.1. The topographic, hydrologic and rainfall factors were adapted from section 7.1, geology classes from chapter 5, lineaments were extracted from the Sentinel-1 SAR-C classification in chapter 6 and LULC/erodibility from chapter 6. The landslide controlling thematic layers were ranked to 10 due to the possible landslide reactivation and the fact that such areas satisfy critical threshold conditions for landslide occurrence. Although elevation is a possible landslide contributing factor, this study did not use it; instead, its derivatives (slope, curvature) were considered more important.

**Table 7.2.1:** Landslide predisposing factors reclassification and ranking.

<b>Slope</b>		<b>Aspect</b>		<b>Curvature</b>	
<i>Old class (88- 0)</i>	<i>new value</i>	<i>Old class (-1 to 360)</i>	<i>new value</i>	<i>Old class (41.059 to -28.556)</i>	<i>new value</i>
88 to 83	10	337.5 to 360	10	-4.4 to -28	1
83 to 64	9	292.5 to 337.5	9	-2.2 to -4.4	2
64 to 44	8	247.5 to 292.5	8	-1.14 to -2.2	3
44 to 36	7	202.5 to 247.5	7	-0.6 to -1.14	4
36 to 29	6	157.5 to 202.5	6	-0.05 to -0.6	5
29 to 23	5	112.5 to 157.5	5	0.49 to -0.05	6
23 to 17	4	67.5 to 112.5	4	1.32 to 0.49	7
17 to 11	3	22.5 to 67.5	3	2.69 to 1.32	8
11 to 5	2	0 to 22.5	2	5.98 to 2.69	9
5 to 0	1	-1 to 0	1	41 to 5.98	10

<b>Flow Accumulation (30 630 to 0)</b>		<b>Flow length (13 519.57 to 0)</b>		<b>water table</b>		<b>Rainfall 2015</b>	
<i>Old class</i>	<i>new value</i>	<i>Old class</i>	<i>new value</i>	<i>Old class</i>	<i>new value</i>	<i>Old class</i>	<i>new value</i>
0 to 100.96	10	0 to 50.72	1	-389.69 to -129	1	744 to 590	10
100.96 to 150.13	9	50.72 to 75.91	2	-129 to 15	2	590 to 507	9
150.31 to 251.095	8	75.91 to 126.63	3	15 to 97	10	507 to 451	8
251.097 to 458.429	7	126.63 to 228.71	4	97 to 143	9	451 to 413	7
458.429 to 884.1934	6	228.71 to 434.19	5	143 to 224	8	413 to 380	6
884.193 to 1758.511	5	434.19 to 847.81	6	224 to 374	7	380 to 354	5
1758.51 to 3553.944	4	847.81 to 1680.37	7	374 to 630	6	354 to 322	4
3553.94 to 7240.911	3	1680.37 to 3356.22	8	630 to 1094	5	322 to 290	3
7240.91 to 14812.18	2	3356.22 to 6729.51	9	1094 to 1923	4	290 to 260	2
14812.18 to 30360	1	6729.509 to 13519.57	10	1923 to 3402	3	260 to 227	1

**Continued Table 7.2.1:** Landslide predisposing factors reclassification and ranking.

Enhanced SAR classification		Erodibility/LULC 2014		Geology	
<i>Old class</i>	<i>new value</i>	<i>Old class</i>	<i>new value</i>	<i>Old class</i>	<i>new value</i>
Landslide	10	Runoff	6	Basalts	10
Fault line	9	extreme erosion	9	Ultra-basic igneous	9
Edges_crest	8	other erosion	9	Intermediate Igneous /Pyroclastic	8
Edges_base	7	landslide	10	Acidic igneous /Acidic metamorphic /Organic	7
Human development	7	highly erodible	8	Igneous Rock /Eolian	6
Runoff	3	stable	5	Granite	5
Rocks/ exposed rock	3	deposits	2	Basic Metamorphic /Intermediate A.T.P	4
Highly erodible	6	moist extreme erosion	8	Fluvial/classic	3
Other erosions	4	exposed rocks	7	Basic igneous /carbonates	2
extreme erosion	5	stable volcanic rocks	3	Waters	1
Wetlands	6	veg_covered rocks	4		
Stable/deposits	2	human dev	8		
Waters	1	Waters	1		

### 7.2.1.2 Landslide Susceptibility Mapping and Zonation

The landslide predisposing factors described in section 7.2.1.1 were combined using the Spatial-analyst combine tool to form the unique condition raster. The strength of the relationships among landslide factors was examined using the correlation statistics in the band collection statistics as in Table 7.2.2, from which the absolute correlation values among the factors were less than 0.3, except when considering the factor to itself (correlation = 1). Thus, the use of linear models such as logistic regression model was inappropriate for landslide assessment using this dataset. On the other hand, the use of ANN which is a non-linear based model was justified.

**Table 7.2.2:** Correlation matrix using the unique condition raster.

	slope	Aspect	Curvat.	LULC	Linea.	Geolog.	Rain	F.length	F. Acc	W.Table
<b>1</b>	1.00000									
<b>2</b>	0.01504	1.00000								
<b>3</b>	-0.00743	-0.00659	1.00000							
<b>4</b>	-0.11592	0.01181	-0.00746	1.00000						
<b>5</b>	0.11384	-0.00324	-0.00871	0.01818	1.00000					
<b>6</b>	0.02156	0.00379	-0.00517	0.04580	0.07341	1.00000				
<b>7</b>	0.19118	-0.01476	-0.00343	-0.07872	0.25186	0.07189	1.00000			
<b>8</b>	0.27147	-0.02010	0.02955	-0.05155	0.02460	0.01614	0.04627	1.00000		
<b>9</b>	0.02491	0.00583	-0.10152	-0.02246	0.02555	0.00599	0.03049	-0.00938	1.00000	
<b>10</b>	-0.25202	0.01092	-0.01610	0.12471	0.01041	0.02037	-0.15661	-0.25188	-0.00791	1.00000

The unique condition raster file together with landslide GPS points and random non-landslide points were used as the input files in the ANN model. The output of this initial process was a training file and an output class file, which was partitioned into smaller units to allow processing with the geo-explore tool. This resulted in 90 total units, each containing 200,000 records. Each of these units was processed in the Geo-explore file resulting in Probabilistic Neural Network (PNN) and neural-fuzzy net classification file extensions. The PNN units were collected and combined after which the ANN output was executed. The output from the PNN file was a landslide susceptibility map, while that from the neural-fuzzy net file was a classification map.

The neural-fuzzy net classification was the basis for stability classification and landslide type discrimination, while the landslide susceptibility map was further reclassified into 10 classes using the natural break interval method in order allow zoning. The areas with high susceptibility were extracted as they were deemed to be the predicted landslide prone areas. On the contrast, a susceptibility map processed using fuzzy-gamma overlay method was also reclassified using the natural break interval. The areas of high susceptibility were extracted and compared with landslide GPS inventory layer in a ROC curve.

### *7.2.2 Results*

The main results from the ANN model were the stability/ landslide type classification (Figure 7.2.2) and the landslide susceptibility map (Figure 7.2.3). Besides, the susceptibility model from the fuzzy-gamma overlay (Figure 7.2.4) was also compared with the ANN results. The hazard prone areas are represented by Figure 7.2.5, where the ANN and fuzzy-gamma best represented the predicted and identified landslide prone areas, respectively.

The classification output from the ANN model (Figure 7.2.2) had 12 classes which were identified according to stability and possible landslide types. The landslide types were named according to the possible cause or type of landslide i.e. debris slide, rock slide, debris flow, river/drainage channel, and LULC landslide prone areas. The stable areas were identified as forested slopes, stable slopes, water bodies, flat/deposit areas, and relatively stable, while possible deposit areas were debris deposits, and river channel deposits. Debris and rock slides were associated with steep slopes having weathered rock materials or rock outcrops (convex curvature) respectively, while debris flows were associated with loose soil material, higher values of flow-length, pyroclastic unconsolidated rock type. On the other hand, LULC landslide prone areas were associated with activities associated with land degradation or poor

agricultural practises on sloping terrain. Deposit areas were associated with gentle to flat terrain, and concave curvature where landslide debris material could settle, whereas stable areas were mainly forested slopes. Water bodies were clearly identifiable and were characterized by zero slope values, concave curvature, low flow-length values, and were classified as water cover in the LULC classification.

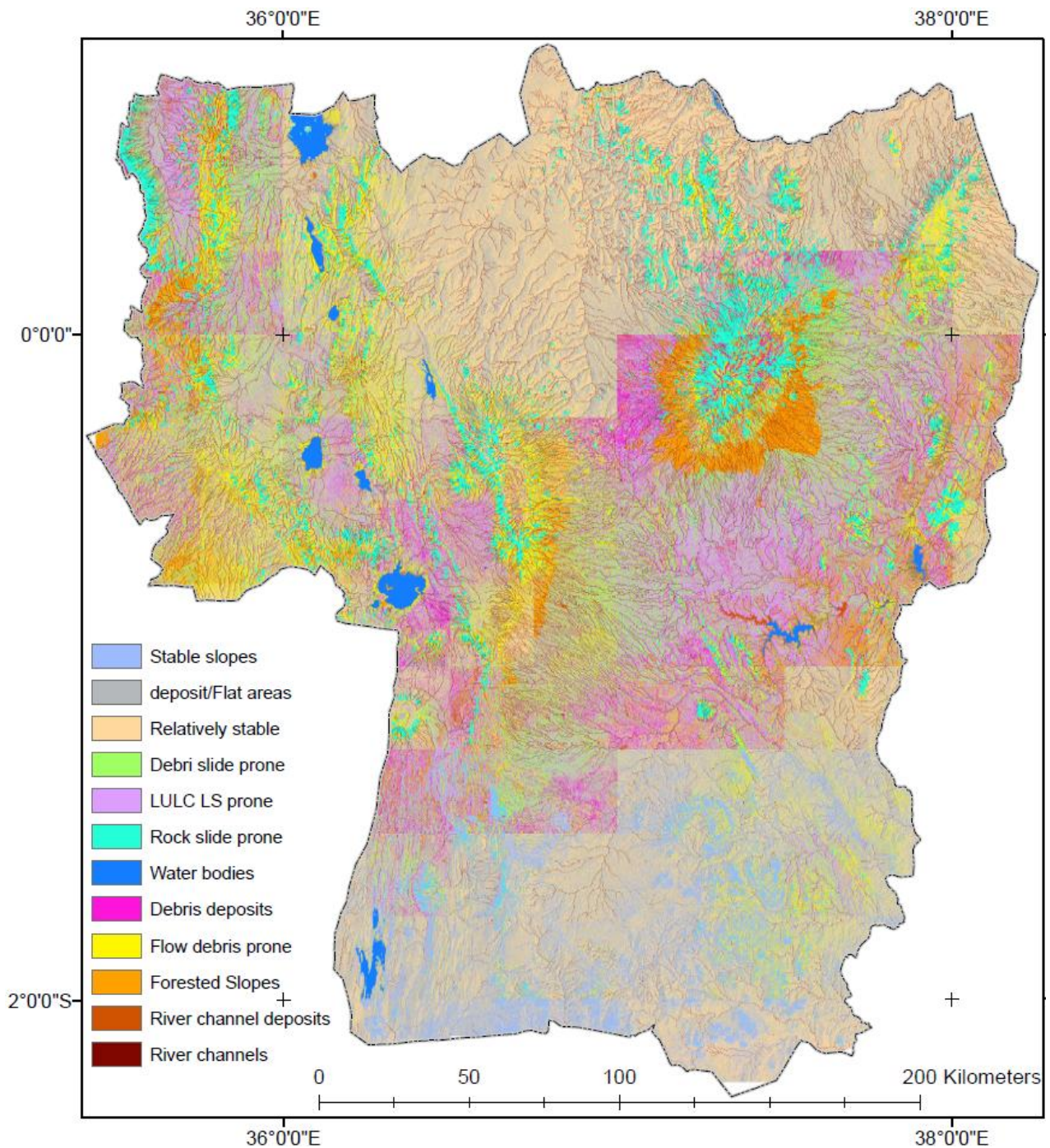


**Figure 7.2.2:** Landslide types/ stability zonation using ANN classification.

It was observed that the main classification result in the Figure 7.2.2 had sharp boundaries from one class to another. This is explained by the prior classification of each thematic layer that was used in the ANN model (i.e. Table 7.2.1). In addition, they were also influenced by the rainfall distribution pattern, since the areas which had heavy rainfall were characterized by higher probabilities of debris flow and deposits. Consequently, high susceptibility values in those areas were reflected in Figure 7.2.3 whereas forested slopes had relatively low susceptibility values. Despite the fact that ANN modelling involves a non-linear combination of landslide causative factors, those factors which contribute most to the landslide process can be determined. Therefore, in the case of the ANN model results from this study, rainfall and LULC contributed most to landslide processes. On the contrary, the fuzzy-gamma overlay susceptibility map (Figure 7.2.4), reflected high susceptibility values along the lineaments, steep slopes and areas where the volcanic rocks are exposed to weathering.

The areas of high susceptibility were extracted from both the ANN and fuzzy-gamma overlay methods into Figure 7.2.5, where they were compared with the landslide GPS points (Appendix B). Comparison of the visual distribution of the landslide GPS points and the predicted landslide areas of both methods indicate better agreement between the ANN model results and the GPS points. This can be attributed to the effect of training which was performed during the ANN modelling, a step which lacked in the fuzzy overlay susceptibility mapping. The overlap area between the two methods was 18.78 sq km, while the highly susceptible areas in the ANN and fuzzy-gamma overlay methods were 2,352.22 sq km and 1,361.04 sq km, respectively.

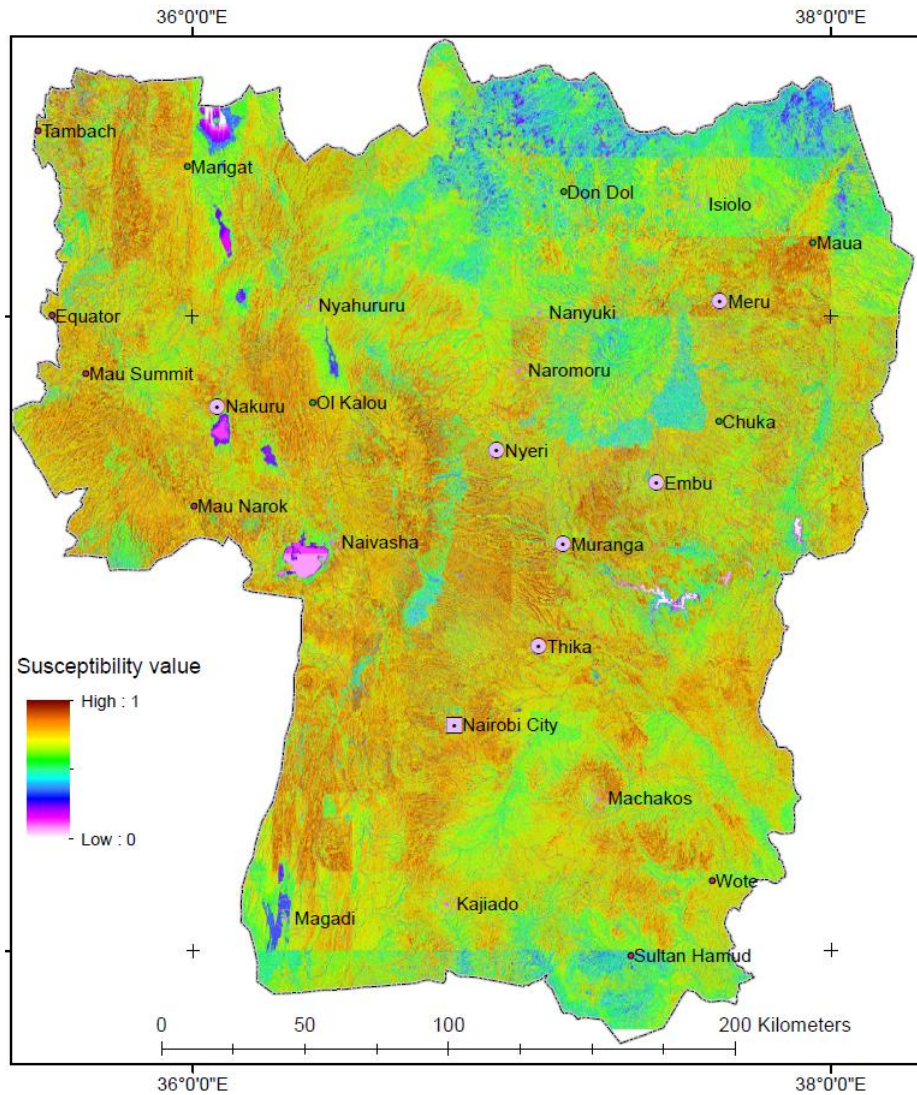


**Figure 7.2.3:** Landslide susceptibility map with ANN model, year 2015.

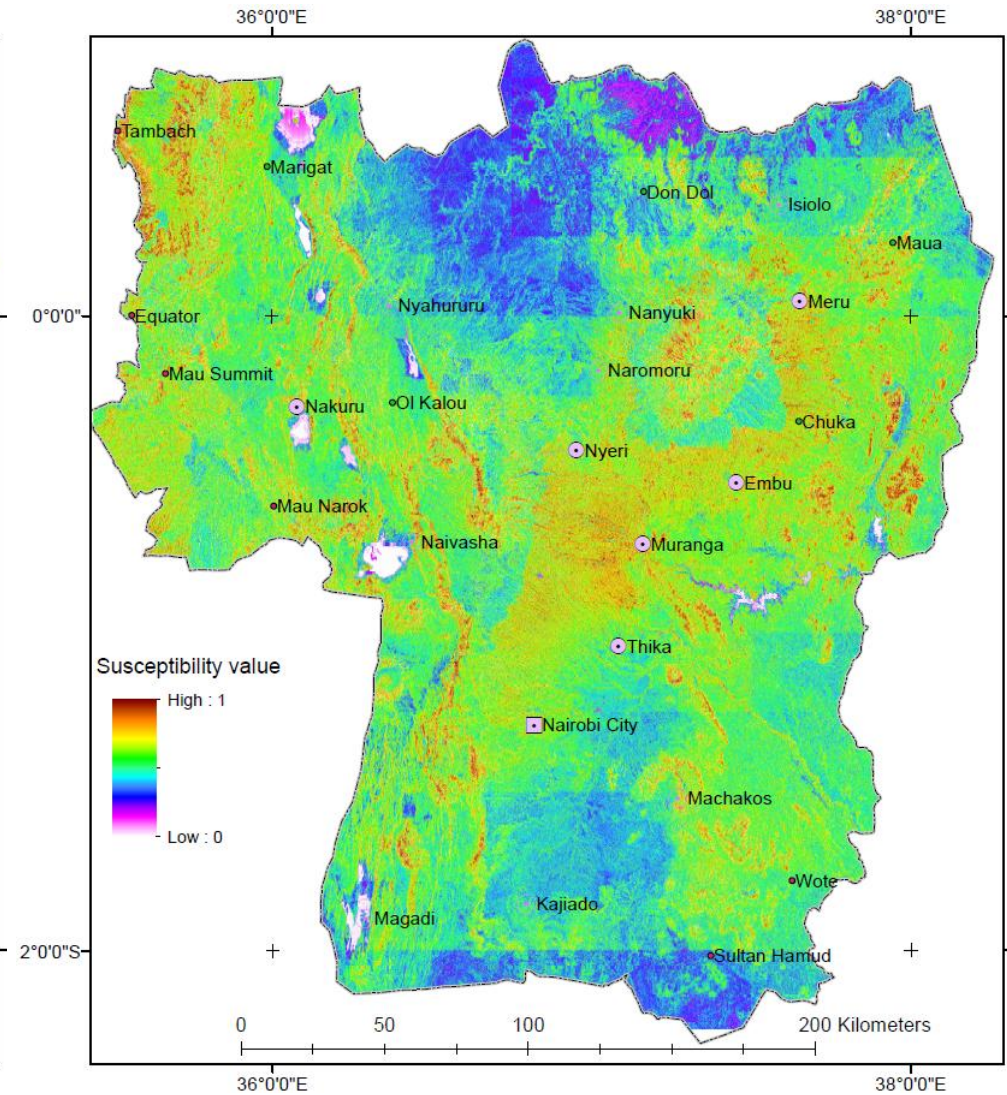


**Figure 7.2.4:** Landslide susceptibility map with fuzzy-gamma overlay method, year 2015.

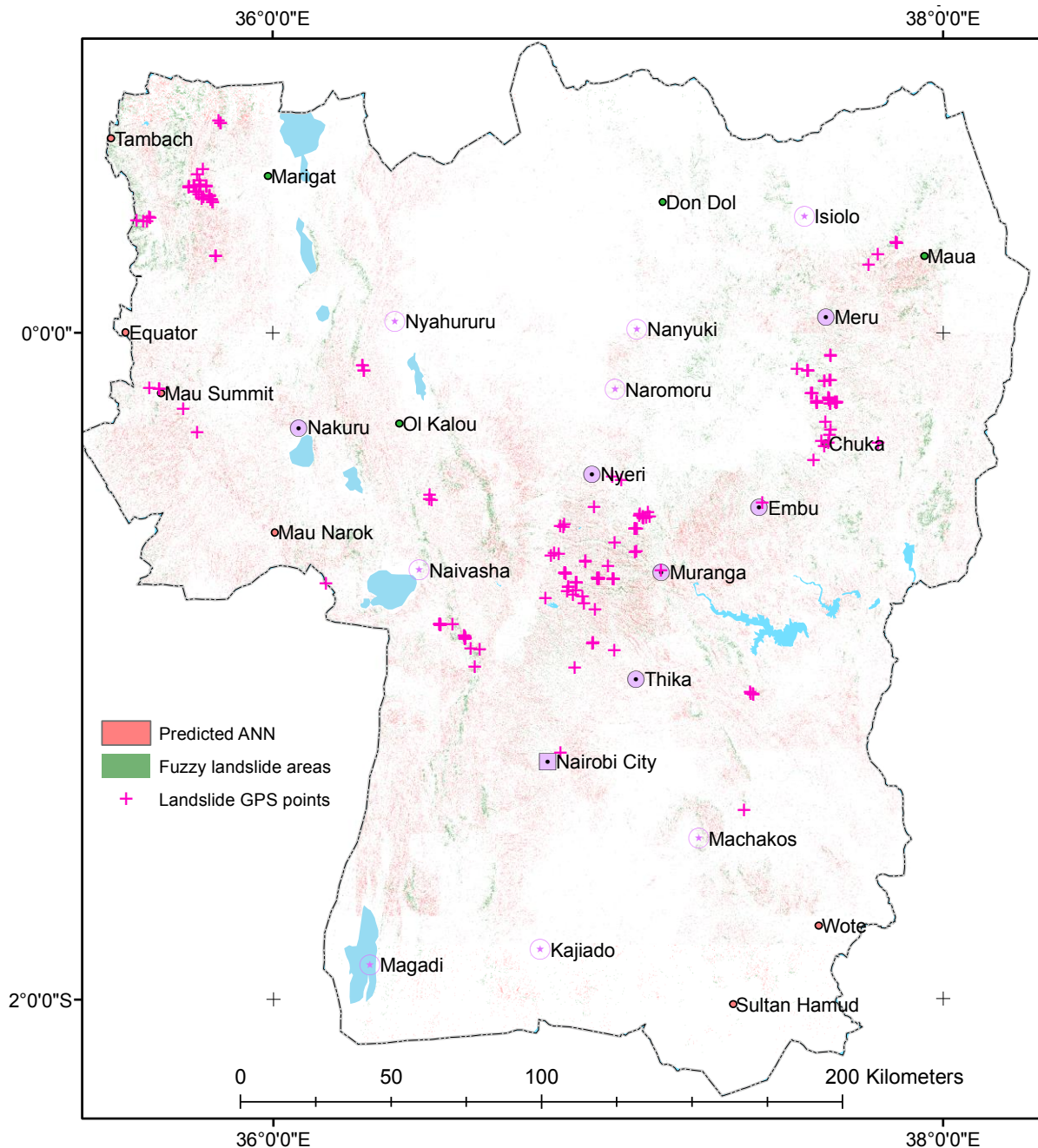


**Figure 7.2.5:** Predicted landslide distribution versus GPS landslide points.

*7.2.2.1. ANN model validation*

The landslide susceptibility maps were further evaluated for goodness of fit using training points, where random non-training sites were used to test their prediction measure. The predicted landslide areas raster layer obtained from the ANN model was tested using the training data which comprised 226 GPS landslide points (see Appendix B). The area frequency table tool (Arc-SDM; Sawatzky et al. (2009)) tabulated the efficiency curves using the training points and 126 random non-training points (consisting both landslides and non-

landslide points) to yield the training curve and prediction curves, respectively as in Figure 7.2.6. The ROC curves in Figure 7.2.6 (a) showed that the ANN model had the success rate of 0.655 (efficiency of the classification), while the prediction rate of the model was measured at 0.647 (efficiency of prediction). These statistics were obtained from the Area Under Curve (AUC) of the respective ROCs.

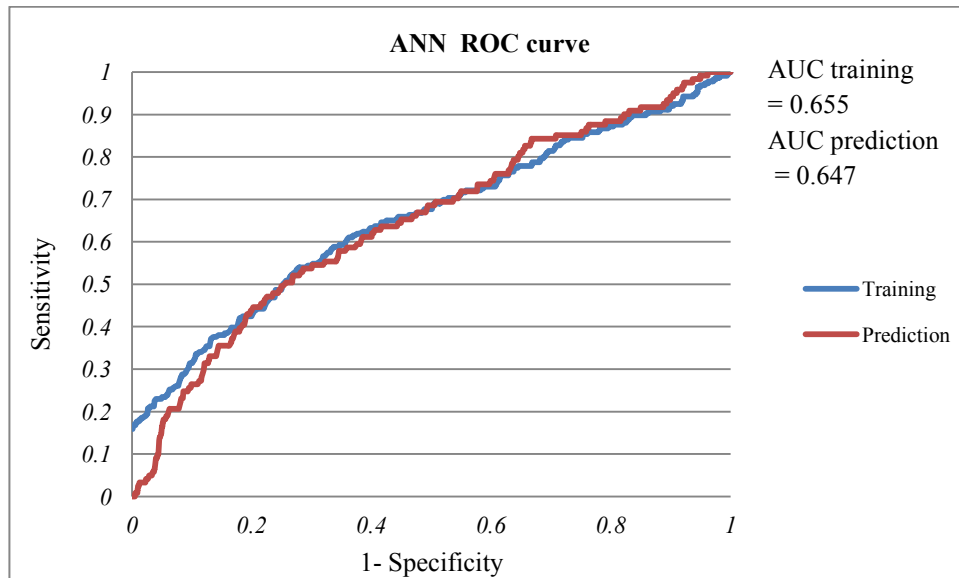


**Figure 7.2.6 (a):** ANN probability model ROC curve.

Similarly, the fuzzy-gamma overlay efficiency curves (Figure 7.2.6 (b)) were generated using the training points and the random non-training points to yield success rate value of 0.764 and the model prediction rate value of 0.663. In both models, the success rate was higher than the prediction rate, although their values were far less than the perfect efficiency value of 1 (Beguería, 2006). The higher value of the fuzzy-gamma overlay success rate explained why the obtained susceptibility map (Figure 7.2.4) had a good visual appeal of the areas prone to landslides, given that the areas were obtained from the highly ranked landslide thematic layers. On the contrast, the ANN model which involves a non-linear combination had a better visual distribution of the landslide predicted areas.

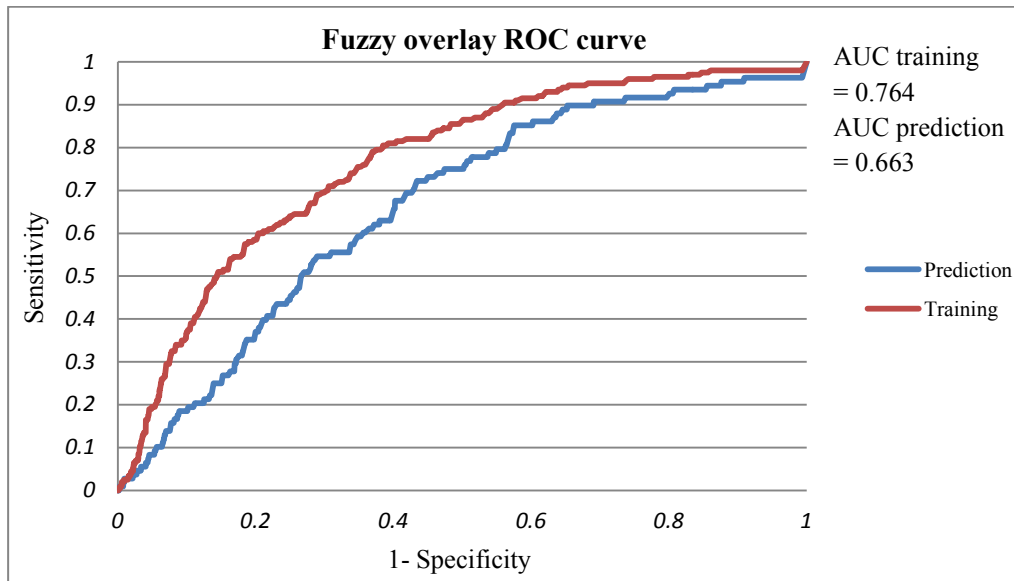


**Figure 7.2.6 (b):** Fuzzy overlay ROC curve.

### 7.2.3 Discussion

The results of the ANN model have demonstrated its strengths in landslide mapping and hazard assessment. This can be explained by the ability of the ANN to learn from the characteristics of the training areas and predict new areas based on the collected evidence (Ermini et al., 2005; Pradhan and Lee, 2010c). The learning ability equally resolves the weight ranking of the landslide causative factors in an objective manner (Chauhan et al., 2010), hence it enabled the landslide hazard zonation through classification. On the other hand, the effects of the lack of training in the fuzzy-gamma overlay susceptibility map were observable in that the character of past landslides (being reactivated) was not captured. Thus, the mapped landslide areas were more biased towards the areas where landslide causative factors were ranked high.

The ANN classification result also captured landslide debris classification by type, material and movement (learnt from the input landslide conditioning factors), which are emphasized as important aspects of landslide assessment since they explain the landslide mechanisms (Cruden and Varnes, 1996; Hungr et al., 2014; Soeters and Van Westen, 1996). In addition, the susceptibility map produced using the ANN model (a data integration model) served to relate the landslide distribution to the landslide conditioning factors (Bi et al., 2014).

The strengths of the correlation between landslide cells and the landslide predisposing factors were examined in both methods as in Table 7.2.3. This was to support the explanations of the results presented in the Figures 7.2.3 and 7.2.4, as well as their characteristic patterns.

However, since the methods applied were different, the weights were only compared to the particular method. Low correlation parameters were observed with the landslide predisposing factors in the ANN, which is in support of the non-linear nature of the method (Bishop, 1995). Utilizing the absolute weight values in the Table 7.2.3, it was noted that proximity to drainage network, LULC and rainfall weights were ranked high in predicting landslides using the ANN model. Previous research findings have associated factors of LULC and rainfall to shallow landslides (e.g. Crosta and Frattini, 2003; Glade, 2003; Montgomery and Dietrich, 1994; Wu and Sidle, 1995). Hence, it can be deduced that the ANN model predicted shallow seated landslides better compared to deep-seated landslides.

**Table 7.2.3:** Landslide cells correlation to landslide causative factors.

	Fuzzy gamma	ANN
	LS cells	LS cells
Landslide cells	1.00000	1.00000
Rainfall	0.49963	0.23140
LULC	0.18032	0.21251
Lineament	0.50813	0.10334
Aspect	0.24746	-0.03921
Geology	0.21040	0.15800
Slope	0.36668	0.10737
Curvature	0.09648	-0.03069
Flow length	0.31072	-0.03733
River/drainage network	0.12621	-0.42258
Depth to the water table	0.00565	-0.07393

On the other hand, the factors of lineament, slope, and rainfall had the most influence on the predicted landslides using fuzzy-gamma susceptibility map. Such factors have been associated with deep-seated landslides. For example, Miller (1995) found that certain deep seated landslides respond to pore water pressure (as a result of rainfall infiltration), while others react to stream-channel incision. Likewise, Lin et al. (2013) determined that deep-seated landslides were found where there were concentrations of crowns, derived from high-resolution topographic curvature signature. Therefore, the overlap areas between the fuzzy-gamma overlay and the ANN predicted landslides (18.78 km<sup>2</sup>) could be associated with deep-seated landslides, given that the factors associated with them (i.e. fault lines and very steep slopes) were present. Besides, some GPS landslide points were located in deep-seated landslide areas, and the fuzzy overlay had higher training success rate (0.764) compared to the ANN's (0.655).

The prediction results of the ANN model could be improved further by using higher resolution DEM to derive topographic signatures (slope, curvature, surface roughness), which characterise and represent landslide geomorphic processes (e.g. faulting, channelling, erosion) better and more accurately. Consequently, studies utilizing high resolution DEM topographic signatures have reported greater success at mapping deep-seated landslides (e.g. Kasai et al., 2009; Lin et al., 2013).

In addition, utilizing a complete time dimension landslide year of occurrence landslide inventory during the ANN model training, could improve the validation and prediction ability of the model (Chung and Fabbri, 2003; Guzzetti et al., 2006). This time aspect of landslide occurrence was incomplete in the landslide inventory layer that was used for this study. Hence, the landslide susceptibility could only be predicted in terms of landslide conditioning factors, where LULC and rainfall factors were rated high in contributing to shallow landslides.

## Chapter 8: Conclusion, Recommendations and Future Outlook

---

Rainfall induced landslides hazard assessment studies are important and of concern to scientists and environmentalist as rapid environmental changes manifested in the forms of land-use and climatic change, increase their frequencies and magnitude. The impacts of such changes have been investigated in this research using the central highlands of Kenya as a case study in a developing country. Firstly, LULC changes were mapped with the help of RS technologies in order to investigate the impact of anthropogenic activities which act to trigger or accelerate landslide occurrence. Secondly, structural geology which is a landslide conditioning factor was mapped using Landsat multispectral datasets and image enhancement methods. This was followed by landslide inventory mapping which is a prerequisite step to any landslide hazard/susceptibility assessment study.

In addition, the topographic signatures were processed from DEM data and together with thematic data from the above steps organised into a GIS database to enable landslide susceptibility assessment. Landslide susceptibility mapping was performed using two models; CHASM, a physical hydrological model and an ANN quantitative statistical model, which were implemented in GIS environment. The CHASM model was used to map the landslide susceptibility and investigate the impact of rainfall patterns while the ANN model was used to perform landslide hazard zonation and prediction of stability conditions.

The outcomes of the LULC changes revealed that there were competing land uses among the green cover (forested areas), agricultural/farm lands, and grazing lands. The impacts of agricultural activities were noted to encroach forested areas which are located in high relief areas and characterized by gentle to steep slopes and high rainfall amounts. On the other hand, the effects of reduced rainfall amounts and grazing land-use increased bare land areas. The net effect of decreasing vegetation cover through effects of land-use (grazing and agriculture) led to further land degradation effects upon the heavy downpour rainfall events, as was shown by the CHASM model. However, the LULC change trend revealed improving forest cover trend whose net result was reflected by decreasing landslide susceptibility levels in the CHASM model. On the other hand, comparing the rainfall and temperature trends versus the LULC trend showed that LULC responded to changed patterns of the climatic variables, with both long-term and short-term effects on the LULC green cover. Thus,

extreme climatic events marked by El-Niño and La-Niña events contributed to exacerbating the land degradation problem.

The role of geology mapping in landslide mapping was realized through the landslide hazard assessment results of the ANN and the CHASM outcomes. Thus, the ANN model which incorporated geology landslide conditioning factor showed potential to map both deep-seated and shallow landslides, while CHASM model was limited to only shallow landslides. Similarly, the landslide inventory mapping involving the Sentinel-1 SAR-C imagery mapped more landslides areas as well as areas likely to be affected by land degradation processes. This capability was drawn from the feature level fusion of the Sentinel-1 SAR-C data and the high multispectral resolution property of Landsat imagery. In addition, ICA and PCA data reduction and feature data transformation techniques coupled with the NDMIDR spectral index enhanced new landslide scars, since landslide processes expose underneath substratum and were clearly extinguished from the surrounding areas. On the other hand, the ability to enhance geology components using band ratios and the classification aided by density slicing and knowledge-based classifier was successful in geological mapping.

The CHASM model linked slope stability and hydrological response, hence allowing the impacts of rainfall characteristics (amount, distribution pattern), which contribute to landslides and slope instability, to be studied. In addition, the LULC factor was incorporated through the root cohesion component. The results of the CHASM model illustrated that shallow landslides were influenced most by rainfall, LULC, and slope landslide causative factors. Thus, the effects of soil oversaturation on bare soils at the onset of rainfall events were observed to contribute to shallow landslides especially in agricultural areas, whereas forested areas maintained low landslide susceptibility levels. On the other hand, prolonged rainfall increased infiltration effects, hence weakening the soil shear strength which increased the landslide susceptibility. The distribution of shallow landslides was biased towards steep bare slopes, high density stream incision and drainage network, and following areas with heavy rainfall distribution.

The ANN model allowed the combination of landslide conditioning factors to be integrated in a landslide susceptibility model. The training ability of the ANN model using the GPS landslide points and collecting strong evidence from the landslide causative thematic layers, enabled the characteristic properties supporting landslide geomorphic process to be learnt and applied to predict future landslide scenarios. Thus, it was demonstrated that ANN can indeed

map both deep and shallow seated landslides, although deep-seated landslides require high resolution DEM which can yield better topographic signatures that represent the geomorphic process which characterise them. The ANN model ranked factors of LULC, rainfall and proximity to drainage as the most important to landslide processes in the study area. This partly confirmed the CHASM results which found LULC and rainfall factors to be influential, hence it was in the support of common occurrence of shallow landslides in the study area.

This research study has demonstrated the usefulness of geospatial tools in an application of environmental problem of landslide mapping. In particular, the role of RS in mapping landslide predisposing factors has been demonstrated by mapping LULC, geology, and landslide inventories. The RS image enhancement methods were successful in aiding feature extraction, visualization and interpretation, and subsequent classifications. In particular, the strengths of the mid-infrared region in geology mapping were explored resulting in a new spectral index 'NDMIDR' which could enhance landslide scars. Consequently, landslide causative factors thematic layers were available for a large area which allowed subsequent hazard assessment. This illustrates that remotely sensed data can be used to overcome the limitation of physical models which are data intensive and hence limited to local scale. Also, the ability to investigate the impact of environmental change on landslide frequency and magnitude was demonstrated at regional scale, while landslide susceptibility assessment could further form the basis of risk evaluation for this study area.

In the context of future landslide studies in this area, it will be important to evaluate landslide risks using the landslide susceptibility methods tested. It is recommended that very high resolution DEM are used to extract topographic (e.g. curvature, slope, aspect) and geomorphologic signatures (e.g. breaklines and crowns) in order to accurately detect and map deep-seated landslides. Besides, the use of high-resolution DEMs in the landslide hazard assessment can lead to the estimation of the volume of landslide debris materials and the modelling of the areas affected by landslides deposit. In the light of increased climate parameters variability, it will be important to incorporate real-time climatic data in order to forecast landslides real-time and also investigate any influence of climatic change on the landslides in the study area.

## References

---

- Abdeen, M. M., & Abdelghaffar, A. A. (2008). Mapping Neoproterozoic structures along the central Allaqiheiani suture, Southeastern Egypt, using remote sensing and field data (Vol. 3). Presented at the 29th Asian Conference on Remote Sensing, Colombo, Sri Lanka: Curran Associates, Inc.
- Abdeen, M. M., & Hassan, S. M. (2009). Utilisation of Spectral Signature and PCA, of TERRA ASTER images for exploring new sites of building sand and gravels, NW Gulf of Suez, Egypt. In *30th Asian Conference on Remote Sensing*.
- Acharya, T., & Ray, A. K. (2005). *Image processing: Principles and Applications*. Hoboken, N.J.: John Wiley.
- Agliardi, F., Crosta, G. B., Zanchi, A., & Ravazzi, C. (2009). Onset and timing of deep-seated gravitational slope deformations in the eastern Alps, Italy. *Geomorphology*, *103*(1), 113–129. doi:10.1016/j.geomorph.2007.09.015
- Agliardi, F., Crosta, G. B., & Frattini, P. (2012). Slow rock-slope deformation. In J. J. Clague & D. Stead (Eds.), *Landslides: types, mechanisms, and modelling* (pp. 208–221). Cambridge: Cambridge Univ. Press.
- Akbarimehr, M., Motagh, M., & Haghshenas, M. (2013). Slope Stability Assessment of the Sarcheshmeh Landslide, Northeast Iran, Investigated Using InSAR and GPS Observations. *Remote Sensing*, *5*(8), 3681–3700. doi:10.3390/rs5083681
- Akech, N. O., Omuombo, C. A., & Masibo, M. (2013). General Geology of Kenya. In *Developments in Earth Surface Processes* (Vol. 16, pp. 3–10). Elsevier. doi:10.1016/B978-0-444-59559-1.00001-3
- Akgun, A. (2012). A comparison of landslide susceptibility maps produced by logistic regression, multi-criteria decision, and likelihood ratio methods: a case study at İzmir, Turkey. *Landslides*, *9*(1), 93–106. doi:10.1007/s10346-011-0283-7
- Alamirew, D., Korme, T., Olago, D., & Barongo, J. (2007). *Geology, Hydrogeology and hydrochemistry of the Nakuru-Elmentaita Naivasha watershed, Kenyan Rift*. Nairobi University, Department of Geology presented at the Mawari Meeting, Addis, Ethiopia.
- Alejandro, M. A. A. (2006). *Lineament extraction from Digital Terrain Models: case study San Antonio del Sur Area, South-Eastern Cuba* (Institute for Geo-Information Science and Earth Observation). ITC, Enschede, the Netherlands.
- Aleotti, P., & Chowdhury, R. (1999). Landslide hazard assessment: Summary review and new perspectives. *Bulletin of Engineering Geology and the Environment*, *58*(1), 21–44. doi:10.1007/s100640050066
- Allen, D. J., & Darling, W. G. (1992). *Geothermics and hydrogeology of the Kenya Rift Valley between Lake Baringo and Lake Turkana*. Keyworth, Nottingham: British Geological Survey.
- Allen, D. J., Burgess, W. G., Darling, W. G., Great Britain, Overseas Development Administration, & British Geological Survey. (1989). *Geothermics and hydrogeology of the southern part of the Kenya Rift Valley with emphasis on the Magadi-Nakuru area*. Keyworth [England: British Geological Survey.
- Ali, E. A., El Khidir, S. O., Babikir, A. A., & Abdelrahnam, E. M. (2012). Landsat ETM+7 Digital Image Processing Techniques for Lithological and Structural Lineament Enhancement: Case Study Around Abidiya Area, Sudan. *The Open Remote Sensing Journal*, *5*(1), 83–89. doi:10.2174/1875413901205010083
- Alkhasawneh, M. S., Ngah, U. K., Tay, L. T., Mat Isa, N. A., & Al-batah, M. S. (2013). Determination of Important Topographic Factors for Landslide Mapping Analysis Using MLP Network. *The Scientific World Journal*, *2013*, 1–12. doi:10.1155/2013/415023

- Al Muntshry, N. A. (2011). *Evaluating the effectiveness of Multispectral Remote Sensing data for Lithological Mapping in arid regions: A quantitative approach with examples from the Makkah neoproterozoic region, Saudi Arabia* (Msc Thesis). Missouri University of Science and Technology, Rolla.
- Ambraseys, N. N. (1991). Earthquake hazard in the Kenya Rift: the Subukia earthquake 1928. *Geophysical Journal International*, 105(1), 253–269. doi:10.1111/j.1365-246X.1991.tb03460.x
- Amer, R., Kusky, T., & Ghulam, A. (2010). Lithological mapping in the Central Eastern Desert of Egypt using ASTER data. *Journal of African Earth Sciences*, 56(2-3), 75–82. doi:10.1016/j.jafrearsci.2009.06.004
- Anbalagan, R. (1992). Landslide hazard evaluation and zonation mapping in mountainous terrain. *Engineering Geology*, 32(4), 269–277. doi:10.1016/0013-7952(92)90053-2
- Anderson, M. G., & Lloyd, D. M. (1991). Using a Combined Slope Hydrology/Stability Model to develop cut slope design charts. *ICE Proceedings*, 91(4), 705–718. doi:10.1680/iicep.1991.17486
- Anderson, J. R., Hardy, E. E., Roach, J. T., & Witmer, R. E. (1976). *A Land Use and Land Cover Classification System for Use with Remote Sensor Data*. Washington, DC, USA: Government Printing Office.
- Angeli, M. G., Buma, J., Gasparetto, P., & Pasuto, A. (1998). A combined hillslope hydrology/stability model for low-gradient clay slopes in the Italian Dolomites. *Engineering Geology*, 49(1), 1–13. doi:10.1016/S0013-7952(97)00033-1
- Antonini, G., Ardizzone, F., Cardinali, M., Galli, M., Guzzetti, F., & Reichenbach, P. (2002). Surface deposits and landslide inventory map of the area affected by the 1997 Umbria-Marche earthquakes. *Bollettino Della Società Geologica Italiana*, 121(1), 843–853.
- Apip, Takara, K., Yamashiki, Y., Sassa, K., Ibrahim, A. B., & Fukuoka, H. (2010). A distributed hydrological–geotechnical model using satellite-derived rainfall estimates for shallow landslide prediction system at a catchment scale. *Landslides*, 7(3), 237–258. doi:10.1007/s10346-010-0214-z
- Ardavan, G., Amir, M. M., & Abazar, E. O. (2012). Utility of the NDVI for land/canopy cover mapping in Khalkhal County (Iran). *Annals of Biological Research*, 3(12), 5494–5503.
- Ardizzone, F., Cardinali, M., Galli, M., Guzzetti, F., & Reichenbach, P. (2007). Identification and mapping of recent rainfall-induced landslides using elevation data collected by airborne Lidar. *Natural Hazards and Earth System Science*, 7(6), 637–650. doi:10.5194/nhess-7-637-2007
- Argialas, D., Mavrantza, O., & Stefouli, M. (2003). *Automatic mapping of tectonic lineaments (faults) using methods and techniques of Photointerpretation /Digital Remote Sensing and Expert Systems* (Geology No. THALES Project 1174).
- Atkinson, P. M., & Massari, R. (1998). Generalised linear modelling of susceptibility to landsliding in the central Apennines, Italy. *Computers & Geosciences*, 24(4), 373–385. doi:10.1016/S0098-3004(97)00117-9
- Arora, M. K., Das Gupta, A. S., & Gupta, R. P. (2004). An artificial neural network approach for landslide hazard zonation in the Bhagirathi (Ganga) Valley, Himalayas. *International Journal of Remote Sensing*, 25(3), 559–572. doi:10.1080/0143116031000156819
- Ayalew, L., & Yamagishi, H. (2005). The application of GIS-based logistic regression for landslide susceptibility mapping in the Kakuda-Yahiko Mountains, Central Japan. *Geomorphology*, 65(1-2), 15–31. doi:10.1016/j.geomorph.2004.06.010
- Ayalew, L., Yamagishi, H., & Ugawa, N. (2004). Landslide susceptibility mapping using GIS-based weighted linear combination, the case in Tsugawa area of Agano River, Niigata Prefecture, Japan. *Landslides*, 1(1), 73–81. <http://doi.org/10.1007/s10346-003-0006-9>

- Baeza, C., & Corominas, J. (2001). Assessment of shallow landslide susceptibility by means of multivariate statistical techniques. *Earth Surface Processes and Landforms*, 26(12), 1251–1263. doi:10.1002/esp.263
- Bai, S. B., Wang, J., Zhang, Z., & Cheng, C. (2012). Combined landslide susceptibility mapping after Wenchuan earthquake at the Zhouqu segment in the Bailongjiang Basin, China. *CATENA*, 99, 18–25. doi:10.1016/j.catena.2012.06.012
- Bajracharya, B., & Bajracharya, S. R. (2008). Landslide mapping of the Everest region using high resolution satellite images and 3D visualization. In *Proceedings of the Mountain GIS e-conference* (pp. 14–25). Kathmandu, Nepal.
- Baldo, M., Biccocchi, C., Chiocchini, U., Giordan, D., & Lollino, G. (2009). LIDAR monitoring of mass wasting processes: The Radicofani landslide, Province of Siena, Central Italy. *Geomorphology*, 105(3–4), 193–201. doi:10.1016/j.geomorph.2008.09.015
- Baldyga, T. J., Miller, S. N., Driese, K. L., & Gichaba, C. M. (2008). Assessing land cover change in Kenya's Mau Forest region using remotely sensed data. *African Journal of Ecology*, 46(1), 46–54. doi:10.1111/j.1365-2028.2007.00806.x
- Bannari, A., Morin, D., Bonn, F., & Huete, A. R. (1995). A review of vegetation indices. *Remote Sensing Reviews*, 13(1–2), 95–120. doi:10.1080/02757259509532298
- Bardi, F., Frodella, W., Ciampalini, A., Bianchini, S., Del Ventisette, C., Gigli, G., ... Casagli, N. (2014). Integration between ground based and satellite SAR data in landslide mapping: The San Fratello case study. *Geomorphology*, 223, 45–60. doi:10.1016/j.geomorph.2014.06.025
- Barlow, J., Martin, Y., & Franklin, S. E. (2003). Detecting translational landslide scars using segmentation of Landsat ETM+ and DEM data in the northern Cascade Mountains, British Columbia. *Canadian Journal of Remote Sensing*, 29(4), 510–517. doi:10.5589/m03-018
- Bathurst, J. C., Bovolo, C. I., & Cisneros, F. (2010). Modelling the effect of forest cover on shallow landslides at the river basin scale. *Ecological Engineering*, 36(3), 317–327. doi:10.1016/j.ecoleng.2009.05.001
- Bathurst, J. C., Moretti, G., El-Hames, A., Moaven-Hashemi, A., & Burton, A. (2005). Scenario modelling of basin-scale, shallow landslide sediment yield, Valsassina, Italian Southern Alps. *Natural Hazards and Earth System Science*, 5(2), 189–202.
- Baum, R. L., & Godt, J. W. (2010). Early warning of rainfall-induced shallow landslides and debris flows in the USA. *Landslides*, 7, 259–272.
- Baum, R. L., & Reid, M. E. (1992). *Geology, hydrology and mechanics of the Alani-Paty landslide, Manoa Valley, Oahu, Hawaii* (Open File Report) (pp. 92–501). U.S.: Geological Survey.
- Baum, R. L., Savage, W. Z., & Godt, J. W. (2008). *TRIGRS—A Fortran program for transient rainfall infiltration and grid-based regional slope-stability analysis, version 2.0* (Open File Report 2008-1159) (p. 75). U.S Geological Survey.
- Baum, R. L., Godt, J. W., & Savage, W. Z. (2010). Estimating the timing and location of shallow rainfall-induced landslides using a model for transient, unsaturated infiltration. *Journal of Geophysical Research*, 115(F3). doi:10.1029/2009JF001321
- Bechtel, R., Rivard, B., & Sánchez-Azofeifa, A. (2002). Spectral properties of foliose and crustose lichens based on laboratory experiments. *Remote Sensing of Environment*, 82(2–3), 389–396. doi:10.1016/S0034-4257(02)00055-X
- Beguería, S. (2006). Validation and Evaluation of Predictive Models in Hazard Assessment and Risk Management. *Natural Hazards*, 37(3), 315–329. doi:10.1007/s11069-005-5182-6

- Behling, R., Roessner, S., Kaufmann, H., & Kleinschmit, B. (2014). Automated spatiotemporal landslide mapping over large areas using rapideye time series data. *Remote Sensing*, 6, 8026–8055. doi:10.3390/rs6098026
- Benediktsson, J. A., Pesaresi, M., & Arnason, K. (2003). Classification and feature extraction for remote sensing images from urban areas based on morphological transformations. *IEEE Transactions on Geoscience and Remote Sensing*, 41(9), 1940–1949. doi:10.1109/TGRS.2003.814625
- Beniston, M. (2003). Climatic Change in Mountain Regions: A Review of Possible Impacts. In H. F. Diaz (Ed.), *Climate Variability and Change in High Elevation Regions: Past, Present & Future* (Vol. 15, pp. 5–31). Dordrecht: Springer Netherlands. doi:10.1007/978-94-015-1252-7\_2
- Berardino, P., Fornaro, G., Lanari, R., & Sansosti, E. (2002). A new algorithm for surface deformation monitoring based on small baseline differential SAR interferograms. *IEEE Transactions on Geoscience and Remote Sensing*, 40(11), 2375–2383. doi:10.1109/TGRS.2002.803792
- Berti, M., Martina, M. L. V., Franceschini, S., Pignone, S., Simoni, A., & Pizziolo, M. (2012). Probabilistic rainfall thresholds for landslide occurrence using a Bayesian approach. *Journal of Geophysical Research*, 117(F4). doi:10.1029/2012JF002367
- Bertoldi, G., Rigon, R., & Over, T. M. (2006). Impact of Watershed Geomorphic Characteristics on the Energy and Water Budgets. *Journal of Hydrometeorology*, 7(3), 389–403. doi:10.1175/JHM500.1
- Bhagat, P. (2006). *Pattern recognition in industry* (Reprinted). Amsterdam: Elsevier.
- Bi, R., Schleier, M., Rohn, J., Ehret, D., & Xiang, W. (2014). Landslide susceptibility analysis based on ArcGIS and Artificial Neural Network for a large catchment in Three Gorges region, China. *Environmental Earth Sciences*, 72(6), 1925–1938. doi:10.1007/s12665-014-3100-5
- Bischetti, G. B., Chiaradia, E. A., Epis, T., & Morlotti, E. (2009). Root cohesion of forest species in the Italian Alps. *Plant and Soil*, 324(1-2), 71–89. doi:10.1007/s11104-009-9941-0
- Bishop, C. M. (1995). *Neural networks for pattern recognition*. Clarendon Press ; Oxford University Press.
- Bison, P., Grinzato, E., Pasuto, A., & Silvano, S. (1990). Thermal IR remote sensing in landslide survey. In *Proceedings of the 6th International IAEG Congress* (pp. 873–878). Balkema, Rotterdam, The Netherlands.
- Bitelli, G., Dubbini, M., & Zanutta, A. (2004). Terrestrial laser scanning and digital photogrammetry techniques to monitor landslide bodies. *International Archives of Photogrammetry Remote Sensing and Spatial Information Sciences*, 35(Part B 5), 246–251.
- Bloeschl, G., & Sivapalan, M. (1995). Scale Issues in Hydrological Modelling: A review. *Hydrological Processes*, 9, 251–290.
- Boettinger, J. L., Ramsey, R. D., Bodily, J. M., Cole, N. J., Kienast-Brown, S., Nield, S. J., ... Stum, A. K. (2008). Landsat Spectral Data for Digital Soil Mapping. In A. E. Hartemink, A. McBratney, & M. de L. Mendonça-Santos (Eds.), *Digital Soil Mapping with Limited Data* (Vol. III, pp. 193–202). Dordrecht: Springer Netherlands. doi:10.1007/978-1-4020-8592-5\_16
- Bona, M. (2004). *Combinatorics of permutations*. Boca Raton: Chapman & Hall/CRC.
- Borghuis, A. M., Chang, K., & Lee, H. Y. (2007). Comparison between automated and manual mapping of typhoon-triggered landslides from SPOT-5 imagery. *International Journal of Remote Sensing*, 28(8), 1843–1856. doi:10.1080/01431160600935638
- Bovolo, C. I., & Bathurst, J. C. (2012). Modelling catchment-scale shallow landslide occurrence and sediment yield as a function of rainfall return period. *Hydrological Processes*, 26(4), 579–596. doi:10.1002/hyp.8158

- Brabb, E. E. (1993). Proposal for worldwide landslide hazard maps. In *Proceedings of the 7th International Conference and field workshop on landslide in Czech and Slovak Republics* (pp. 15–27).
- Brenning, A. (2005). Spatial prediction models for landslide hazards: review, comparison and evaluation. *Natural Hazards and Earth System Science*, 5(6), 853 – 862. doi:10.5194/nhess-5-853-2005
- Brocca, L., Ponziani, F., Moramarco, T., Melone, F., Berni, N., & Wagner, W. (2012). Improving landslide forecasting using ASCAT-Derived soil moisture data: A case study of the Torgiovanetto landslide in central Italy. *Remote Sensing*, 4, 1232–1244. doi:10.3390/rs4051232
- Brown, K. M. (2012). *Landslide detection and susceptibility mapping using Lidar and artificial neural network modeling: a case study in glacially dominated Cuyahoga river valley, Ohio* (Masters thesis). Bowling Green State University, Ohio.
- Brunetti, M. T., Peruccacci, S., Rossi, M., Luciani, S., Valigi, D., & Guzzetti, F. (2010). Rainfall thresholds for the possible occurrence of landslides in Italy. *Natural Hazards and Earth System Science*, 10(3), 447–485. doi:10.5194/nhess-10-447-2010
- Brunsdon, D. (1999). Some geomorphological considerations for the future development of landslide models. *Geomorphology*, 30(1-2), 13–24. doi:10.1016/S0169-555X(99)00041-0
- Bull, J. M., Miller, H., Gravley, D. M., Costello, D., Hikuroa, D. C. H., & Dix, J. K. (2010). Assessing debris flows using LIDAR differencing: 18 May 2005 Matata event, New Zealand. *Geomorphology*, 124(1-2), 75–84. doi:10.1016/j.geomorph.2010.08.011
- Caine, N. (1980). The Rainfall Intensity: Duration Control of Shallow Landslides and Debris Flows. *Physical Geography*, 62(1/2), 23–27. doi:10.2307/520449
- Campbell, J. B. (2002a). Band ratios. In *Introduction to Remote Sensing* (3rd ed., p. 505). New York: Guilford Press.
- Campbell, J. B. (2002b). *Introduction to Remote Sensing*. London; New York: Taylor & Francis.
- Campbell, J. B., & Wynne, R. H. (2012). *Introduction to Remote Sensing* (5th ed.). New York: Guildford publications.
- Cannon, S. H., Kirkham, R. M., & Parise, M. (2001). Wildfire-related debris-flow initiation processes, Storm King Mountain, Colorado. *Geomorphology*, 39(3-4), 171–188. doi:10.1016/S0169-555X(00)00108-2
- Canuti, P., Casagli, N., Ermini, L., Fanti, R., & Farina, P. (2004). Landslide activity as a geoinicator in Italy: significance and new perspectives from remote sensing. *Environmental Geology*, 45(7), 907–919. doi:10.1007/s00254-003-0952-5
- Carletta, J. (1996). Assessing agreement on classification tasks: the kappa statistic. In *Computational Linguistics* (Vol. 22, pp. 249–254). University of Edinburgh.
- Carranza, E. J. M., & Hale, M. (2002). Mineral imaging with Landsat Thematic Mapper data for hydrothermal alteration mapping in heavily vegetated terrane. *International Journal of Remote Sensing*, 23(22), 4827–4852. doi:10.1080/01431160110115014
- Carrara, A., Cardinali, M., Guzzetti, F., & Reichenbach, P. (1995). GIS technology in mapping landslide hazard. In A. Carrara & F. Guzzetti (Eds.), *Geographical Information Systems in Assessing Natural Hazards* (pp. 135–176). Dordrecht, The Netherlands: Kluwer Academic Publishers.
- Carrara, A., Crosta, G., & Frattini, P. (2003). Geomorphological and historical data in assessing landslide hazard. *Earth Surface Processes and Landforms*, 28(10), 1125–1142. doi:10.1002/esp.545
- Carrara, A., Crosta, G., & Frattini, P. (2008). Comparing models of debris-flow susceptibility in the alpine environment. *Geomorphology*, 94(3-4), 353–378. doi:10.1016/j.geomorph.2006.10.033

- Carter, R. C., & Parker, A. (2009). Climate change, population trends and groundwater in Africa. *Hydrological Sciences Journal*, 54(4), 676–689. doi:10.1623/hysj.54.4.676
- Casagli, N., Fanti, R., Nocentini, M., & Righini, G. (2005). Assessing the Capabilities of VHR Satellite Data for Debris Flow Mapping in the Machu Picchu Area (C101-1). In K. Sassa, H. Fukuoka, F. Wang, & G. Wang (Eds.), *Landslides* (pp. 61–70). Berlin/Heidelberg: Springer-Verlag. doi:10.1007/3-540-28680-2\_6
- Casagli, N., Dapporto, S., Ibsen, M. L., Tofani, V., & Vannocci, P. (2006). Analysis of the landslide triggering mechanism during the storm of 20th–21st November 2000, in Northern Tuscany. *Landslides*, 3(1), 13–21. doi:10.1007/s10346-005-0007-y
- Cascini, L., Fornaro, G., & Peduto, D. (2010). Advanced low- and full-resolution DInSAR map generation for slow-moving landslide analysis at different scales. *Engineering Geology*, 112(1-4), 29–42. doi:10.1016/j.enggeo.2010.01.003
- Casson, B., Baratoux, D., Delacourt, C., & Allemand, P. (2003). Seventeen years of the ‘La Clapière’ landslide evolution analysed from ortho-rectified aerial photographs. *Engineering Geology*, 68, 123–130. doi:10.1016/S0013-7952(02)00201-6
- Castro, A. P. (1991). The Southern Mount Kenya forest since independence: A social analysis of resource competition. *World Development*, 19(12), 1695–1704. doi:10.1016/0305-750X(91)90013-8
- Catani, F., Casagli, N., Ermini, L., Righini, G., & Menduni, G. (2005). Landslide hazard and risk mapping at catchment scale in the Arno River basin. *Landslides*, 2(4), 329–342. doi:10.1007/s10346-005-0021-0
- Catani, F., Margottini, C., Trigila, A., & Iadanza, C. (2011). *The second World Landslide Forum-Abstract Book*. Rome, FAO Headquarters, Italy: ISPRA.
- César, E., Ekbo, A., & Nyangena, W. (2014). *Environmental and Climate Change Policy Brief Kenya* (Environment and Climate Change No. 20140227). Sida.
- Chacha, J. S. (2015). Building Local Capacity and Creating Awareness in Conserving the Mau and Water Resources. In L. A. Picard, T. F. Buss, B. T. Seybolt, & M. C. Lelei (Eds.), *Sustainable development and human security in Africa: governance as the missing link* (Vol. Chapter 7, pp. 121–132). CRC Press Taylor & Francis Group.
- Chang, K.-T., & Liu, J. K. (2004). Landslide features interpreted by neural network method using a high-resolution satellite image and digital topographic data. In *Proceedings of ISPRS XX Congress, Commission VII TS WG VII/5* (pp. 574–579). Istanbul, Turkey.
- Chang, K., Chiang, S., & Lei, F. (2008). Analysing the Relationship Between Typhoon-Triggered Landslides and Critical Rainfall Conditions. *Earth Surface Processes and Landforms*, 33(8), 1261–1271. doi:10.1002/esp.1611
- Chauhan, S., Sharma, M., Arora, M. K., & Gupta, N. K. (2010). Landslide Susceptibility Zonation through ratings derived from Artificial Neural Network. *International Journal of Applied Earth Observation and Geoinformation*, 12(5), 340–350. doi:10.1016/j.jag.2010.04.006
- Cheng, K. S., Wei, C., & Chang, S. C. (2004). Locating landslides using multi-temporal satellite images. *Advances in Space Research*, 33(3), 296–301. doi:10.1016/S0273-1177(03)00471-X
- Chen, H., & Lee, C. F. (2003). A dynamic model for rainfall-induced landslides on natural slopes. *Geomorphology*, 51(4), 269–288. doi:10.1016/S0169-555X(02)00224-6
- Chen, X., & Campagna, D. J. (2009). Remote Sensing of Geology. In *The Sage handbook of remote sensing* (pp. 328–340). Thousand Oaks, CA: Sage.
- Chiang, S.-H., Chang, K.-T., Mondini, A. C., Tsai, B.-W., & Chen, C.-Y. (2012). Simulation of event-based landslides and debris flows at watershed level. *Geomorphology*, 138(1), 306–318. doi:10.1016/j.geomorph.2011.09.016

- Chi, C., Liu, Z., & Zhang, J. (2008). Interpretation of landslide from SPOT-5 imageries in the Three Gorges Reservoir Area. In *International Workshop on Earth Observation and Remote Sensing Applications, 2008* (pp. 1–5). Beijing: IEEE. doi:10.1109/EORSA.2008.4620291
- Chigira, M., & Kiho, K. (1994). Deep-seated rockslide-avalanches preceded by mass rock creep of sedimentary rocks in the Akaishi Mountains, central Japan. *Engineering Geology*, 38(3-4), 221–230. doi:10.1016/0013-7952(94)90039-6
- Chigira, M., Duan, F., Yagi, H., & Furuya, T. (2004). Using an airborne laser scanner for the identification of shallow landslides and susceptibility assessment in an area of ignimbrite overlain by permeable pyroclastics. *Landslides*, 1(3), 203–209. doi:10.1007/s10346-004-0029-x
- Chigira, M., Mohamad, Z., Sian, L. C., & Komoo, I. (2011). Landslides in weathered granitic rocks in Japan and Malaysia. *Bulletin of Geological Society of Malaysia*, 57, 1–6. doi:10.7186/bgsm2011001
- Christiansson, C., Zoebisch, M. A., Lunden, B., Davies, T. C., Westerberg, L.-O., Mburu, D. M., & Granit, J. (1993). *Landslides and related processes in Murang'a District, Central Kenya highlands* (A proposal, EDSU) (p. 10). University of Stockholm/DAE, University of Nairobi.
- Chung, C.-J., & Fabbri, A. G. (2003). Validation of spatial prediction models for landslide hazard mapping, 30, 451–472. doi:10.1023/B:NHAZ.0000007172.62651.2b
- Ciampalini, A., Raspini, F., Bianchini, S., Frodella, W., Bardi, F., Lagomarsino, D., ... Casagli, N. (2015). Remote sensing as tool for development of landslide databases: The case of the Messina Province (Italy) geodatabase. *Geomorphology*, 249, 103–118. doi:10.1016/j.geomorph.2015.01.029
- Cigna, F., Bianchini, S., Righini, G., Proietti, C., & Casagli, N. (2010). Updating landslide inventory maps in mountain areas by means of Persistent Scatterer Interferometry (PSI) and photo-interpretation: Central Calabria (Italy) case study. In *Mountain risks: bringing science to society* (pp. 24–31).
- Claessens, L., Heuvelink, G. B. M., Schoorl, J. M., & Veldkamp, A. (2005). DEM resolution effects on shallow landslide hazard and soil redistribution modelling. *Earth Surface Processes and Landforms*, 30(4), 461–477. doi:10.1002/esp.1155
- Claessens, L., Schoorl, J. M., & Veldkamp, A. (2007). Modelling the location of shallow landslides and their effects on landscape dynamics in large watersheds: An application for Northern New Zealand. *Geomorphology*, 87(1-2), 16–27. doi:10.1016/j.geomorph.2006.06.039
- Clarke, M. L., & Rendell, H. M. (2006). Hindcasting extreme events: the occurrence and expression of damaging floods and landslides in Southern Italy. *Land Degradation & Development*, 17(4), 365–380. doi:10.1002/ldr.743
- CNN, W. S. (2010). Rain halts rescue after Kenya landslide kills 8. *CNN News*. Retrieved from <http://edition.cnn.com/2010/WORLD/africa/05/01/kenya.landslides/>
- Coder, K. D. (2010). *Root Strength and Tree Anchorage* (Warnell School of Forestry and Natural Resources). University of Georgia, WSFNR 10-19.
- Coe, J. A., & Godt, J. W. (2012). Review of approaches for assessing the impact of climate change on landslide hazards, In Eberhardt. In E. Froese, A. K. Turner, & S. Leroueil (Eds.), *Proceedings of the 11th International and 2nd North American Symposium on Landslides and Engineered Slopes* (Vol. 1, pp. 371–377). Banff, Canada: Taylor & Francis Group, London.
- Coe, J. A., Michael, J. A., Crovelli, R. A., Savage, W. Z., Laprade, W. T., & Nashem, W. D. (2004). Probabilistic Assessment of Precipitation-Triggered Landslides Using Historical Records of Landslide Occurrence, Seattle, Washington. *Environmental and Engineering Geoscience*, 10(2), 103–122. doi:10.2113/10.2.103

- Collison, A., Wade, S., Griffiths, J., & Dehn, M. (2000). Modelling the impact of predicted climate change on landslide frequency and magnitude in SE England. *Engineering Geology*, 55(3), 205–218. doi:10.1016/S0013-7952(99)00121-0
- Congalton, G. R. G. (1991). A review of assessing the accuracy of classifications of remotely sensed data. *Remote Sensing of Environment*, 37(1), 35–46. doi:10.1016/0034-4257(91)90048-B
- Congalton, R. G., & Green, K. (2009). *Assessing the accuracy of remotely sensed data: principles and practices* (2. ed). Boca Raton, Fla.: CRC Press.
- Coral, R.-S. (2007). *SAR Imagery of Boquerón Bay Fault (NBBF)* (Department of Geology No. 6225). Mayaguez: University of Puerto Rico.
- Corominas, J. (2000). Landslides and Climate (Vol. 4, pp. 1–33). Presented at the Keynote lectures from the 8th international symposium on landslides, Cardiff, UK.
- Corominas, J., & Moya, J. (2010). Contribution of dendrochronology to the determination of magnitude–frequency relationships for landslides. *Geomorphology*, 124(3-4), 137–149. doi:10.1016/j.geomorph.2010.09.001
- Corominas, J., van Westen, C., Frattini, P., Cascini, L., Malet, J.-P., Fotopoulou, S., ... Smith, J. T. (2013). Recommendations for the quantitative analysis of landslide risk. *Bulletin of Engineering Geology and the Environment*, 73, 209–263. doi:10.1007/s10064-013-0538-8
- Corsini, A., Cervi, F., Daehne, A., & Ronchetti, F. (2009). Coupling geomorphic field observation and LIDAR derivatives to map complex landslides. In L. Borgatti, J.-P. Malet, & A. Remaitre (Eds.), *Proceedings of the landslide processes conference* (pp. 15–18). Strasbourg, France: CERG Editions.
- Courtire, R. (2011). *Landslide Terminology - National Technical Guidelines and Best Practices on Landslides* (No. 6824) (p. 12). Geological Survey of Canada, United States of geological Survey.
- Crisp, J., & Bartholomew, M. J. (1992). Mid-infrared spectroscopy of Pahala ash palagonite and implications for remote sensing studies of Mars. *Journal of Geophysical Research*, 97(E9), 14691. doi:10.1029/92JE01248
- Crist, E. P., & Cicone, R. C. (1984). A Physically-Based Transformation of Thematic Mapper Data—The TM Tasseled Cap. *IEEE Transactions on Geoscience and Remote Sensing*, GE-22(3), 256–263. doi:10.1109/TGRS.1984.350619
- Crosetto, M., Crippa, B., & Biescas, E. (2005). Early detection and in-depth analysis of deformation phenomena by radar interferometry. *Engineering Geology*, 79(1-2), 81–91. doi:10.1016/j.enggeo.2004.10.016
- Crosetto, M., Monserrat, O., Cuevas, M., & Crippa, B. (2011). Spaceborne Differential SAR Interferometry: Data Analysis Tools for Deformation Measurement. *Remote Sensing*, 3(12), 305–318. doi:10.3390/rs3020305
- Crosta, G. B., & Frattini, P. (2003). Distributed modelling of shallow landslides triggered by intense rainfall. *Natural Hazards and Earth System Science*, 3(1/2), 81–93. doi:10.5194/nhess-3-81-2003
- Crozier, M. J. (1997). The climate-landslide couple: a Southern Hemisphere perspective. In *Rapid mass movement as a source of climatic evidence for the Holocene* (In: Matthews, J.A., Brunsdon, D., Frenzel, B., Glaeser, B., Weiß, M.M., Vol. 19, pp. 333–354).
- Crozier, M. J. (2010). Deciphering the effect of climate change on landslide activity: A review. *Geomorphology*, 124(3-4), 260–267. doi:10.1016/j.geomorph.2010.04.009
- Crozier, M. J., & Glade, T. (2004). Landslide Hazard and Risk: Issues, Concepts and Approach. In T. Glade, M. G. Anderson, & M. J. Crozier (Eds.), *Landslide hazard and risk* (pp. 1–35). Chichester [u.a]: Wiley.

- Crozier, M. J., & Glade, T. (2010). Hazard assessment for risk analysis and risk management. In *Geomorphological Hazards and Disaster Prevention* (Alcántara-Ayala Irasema and Goudie Andrew, pp. 221–232). Cambridge University Press.
- Cruden, D. M. (1991). A simple definition of a landslide. *Bulletin of Engineering Geology and the Environment*, 43(1), 27–29. doi:10.1007/BF02590167
- Cruden, D. M., & Varnes, D. J. (1996). Landslide types and processes. In *Landslide investigation and mitigation. Transportation research board, US National Research Council. Special Report 247* (Turner AK, Schuster RL, Vol. Chapter 3, pp. 36–75). Washington, D.C.
- Czuchlewski, K. R., Weissel, J. K., & Kim, Y. (2003). Polarimetric synthetic aperture radar study of the Tsaoling landslide generated by the 1999 Chi-Chi earthquake, Taiwan. *Journal of Geophysical Research*, 108(F1). doi:10.1029/2003JF000037
- Dai, F. ., Lee, C. ., & Ngai, Y. . (2002). Landslide risk assessment and management: an overview. *Engineering Geology*, 64(1), 65–87. doi:10.1016/S0013-7952(01)00093-X
- Davies, T. C. (1996). Landslide research in Kenya. *Journal of African Earth Sciences*, 23(4), 541–545. doi:10.1016/S0899-5362(97)00017-1
- Davies, T. C., & Nyambok, I. O. (1993). The Murang’a landslide, Kenya, 21, 19–21. doi: 10.1007/BF00775046
- Debella-Gillo, M., & Kääh, A. (2012). Measurement of surface displacement and deformation of mass movements using Least Squares Matching of repeat high resolution and aerial images. *Remote Sensing*, 4, 43–67. doi:10.3390/rs4010043
- De Blasio, F. V. (2011). Friction, Cohesion and slope Stability. In *Introduction to the physics of landslides lecture notes on the dynamics of mass wasting* (Vol. Chapter 2, pp. 23–54). Springer. doi: 10.1007%2F978-94-007-1122-8\_2
- Deb, S. K., & El-Kadi, A. I. (2009). Susceptibility assessment of shallow landslides on Oahu, Hawaii, under extreme-rainfall events. *Geomorphology*, 108(3-4), 219–233. doi: 10.1016/j.geomorph.2009.01.009
- DeGraff, J. V. (1994). The geomorphology of some debris flows in the southern Sierra Nevada, California. *Geomorphology*, 10(1-4), 231–252. doi:10.1016/0169-555X(94)90019-1
- De La Ville, N., Chumaceiro, D. A., & Ramirez, D. (2002). Remote Sensing and GIS Technologies as Tools to Support Sustainable Management of Areas Devastated by Landslides - Springer. *Environment, Development and Sustainability*, 4(2), 221–229. doi:10.1023/A:1020835932757
- Del Ventisette, C., Righini, G., Moretti, S., & Casagli, N. (2014). Multitemporal landslides inventory map updating using spaceborne SAR analysis. *International Journal of Applied Earth Observation and Geoinformation*, 30, 238–246. doi:10.1016/j.jag.2014.02.008
- Derron, M.-H., & Jaboyedoff, M. (2010). Preface ‘LIDAR and DEM techniques for landslides monitoring and characterization’. *Natural Hazards and Earth System Science*, 10(9), 1877–1879. doi:10.5194/nhess-10-1877-2010
- Dietrich, W. E., Reiss, R., Hsu, M.-L., & Montgomery, D. R. (1995). A process-based model for colluvial soil depth and shallow landsliding using digital elevation data. *Hydrological Processes*, 9(3-4), 383–400. doi:10.1002/hyp.3360090311
- Dikau, R., Brunsden, D., Schrott, L., & Ibsen, M. L. (1996). *Landslide recognition. Identification, movement and causes*. England: John Wiley & Sons, Ltd.
- Dikau, R., & Schrott, L. (1999). The temporal stability and activity of landslides in Europe with respect to climatic change (TESLEC): main objectives and results. *Geomorphology*, 30(1-2), 1-12. doi: 10.1016/S0169-555X(99)00040-9

- Domlija, P., Bernat, S., Arbanas Mihalić, S., & Benac, Č. (2014). Landslide Inventory in the Area of Dubračina River Basin (Croatia). In K. Sassa, P. Canuti, & Y. Yin (Eds.), *Landslide Science for a Safer Geoenvironment* (pp. 837–842). Cham: Springer International Publishing. doi:10.1007/978-3-319-05050-8\_129
- Donnelly, L. J. (2007). Landslides associated with the Soufriere Hills Volcano, Montserrat, West Indies. In R. McInnes, J. Jakeways, H. Fairbank, & E. Mathie (Eds.), *Proceedings of the International Conference on Landslides and Climate Change* (pp. 311–320). Ventnor, Isle of Wight, UK: Taylor & Francis. isbn:9780415443180
- Downing, C., Preston, F., Parusheva, D., Horrocks, L., Edberg, O., Samazzi, F., ... Nyangena, W. (2008). *Final Report Kenya: Climate Screening and Information Exchange* (DFID Report No. ED05603-Issue 2). Oxfordshire, UK: AEA group.
- Drăguț, L., & Blaschke, T. (2006). Automated classification of landform elements using object-based image analysis. *Geomorphology*, 81(3-4), 330–344. doi:10.1016/j.geomorph.2006.04.013
- Drummond, C., & Holte, R. C. (2000). Explicitly representing expected cost: an alternative to ROC representation (pp. 198–207). ACM Press. doi:10.1145/347090.347126
- Drury, S. A. (1993). *Image interpretation in geology* (2nd ed). London ; New York: Chapman & Hall.
- Elias, P. B., & Bandis, S. C. (2000). Neuraufuzzy systems in landslide hazard assessment. In *Proceeding of the 4th International Symposium in Spatial Accuracy Assessment in Natural Resources and Environmental Sciences* (pp. 199–2002).
- Ellen, S. D., Liu, L. S. M., Fleming, R. W., Reid, M. E., & Johnsson, M. J. (1995). *Relation of slow-moving landslides on earth materials and other factors in valleys of the Honolulu District of Oahu, Hawaii* (Open File Report) (pp. 95–218). U.S.: Geological Survey.
- Ekanayake, J. C., Marden, M., Watson, A. J., & Rowan, D. (1997). Tree roots and slope stability: a comparison between *Pinus radiata* and *kanuka*. *New Zealand Journal of Forestry Science*, 27(2), 216 – 233. doi:10.1.1.700.9087
- Epting, J., Verbyla, D., & Sorbel, B. (2005). Evaluation of remotely sensed indices for assessing burn severity in interior Alaska using Landsat TM and ETM+. *Remote Sensing of Environment*, 96(3-4), 328–339. doi:10.1016/j.rse.2005.03.002
- Ercanoglu, M. (2005). Landslide susceptibility assessment of SE Bartin (West Black Sea region, Turkey) by artificial neural networks. *Natural Hazards and Earth System Science*, 5, 979–992. doi: 10.5194/nhess-5-979-2005
- Ercanoglu, M. (2008). An overview on the Landslide susceptibility assessment Techniques. In *Environment and geoscience proceedings of the 1st WSEAS international conference on environmental and geological science and engineering (EG'08)* (pp. 131–134). Malta: WSEAS (Organization).
- Ercanoglu, M., & Gokceoglu, C. (2004). Use of fuzzy relations to produce landslide susceptibility map of a landslide prone area (West Black Sea Region, Turkey). *Engineering Geology*, 75(3-4), 229–250. doi:10.1016/j.enggeo.2004.06.001
- Erener, A., & Duzguen, H. S. B. (2008). Analysis of landslide hazard mapping methods: Regression models versus weight rating. *International Archives of Photogrammetry Remote Sensing and Spatial Information Sciences*, 37/B8, 277–282.
- Ermini, L., Catani, F., & Casagli, N. (2005). Artificial Neural Networks applied to landslide susceptibility assessment. *Geomorphology*, 66(1-4), 327–343. doi:10.1016/j.geomorph.2004.09.025
- European Space Agency. (n.d.). Copernicus, ESA's Sentinel Satellites: Sentinel-3. Retrieved from [http://www.esa.int/Our\\_Activities/Observing\\_the\\_Earth/Copernicus/Sentinel-3](http://www.esa.int/Our_Activities/Observing_the_Earth/Copernicus/Sentinel-3)

- Eyers, R., Moore, J. M., Hervás, J., & Liu, J. G. (1998). Integrated use of Landsat TM and SPOT panchromatic imagery for landslide mapping: case histories from southeast Spain. *Geological Society, London, Engineering Geology Special Publications*, 15(1), 133–140. doi:10.1144/GSL.ENG.1998.015.01.14
- Fabre, S., Briottet, X., & Lesaignoux, A. (2015). Estimation of Soil Moisture Content from the Spectral Reflectance of Bare Soils in the 0.4–2.5  $\mu\text{m}$  Domain. *Sensors*, 15(2), 3262–3281. doi:10.3390/s150203262
- Fannin, R. J., & Jaakkola, J. (1999). Hydrological response of hillslope soils above a debris-slide headscarp. *Canadian Geotechnical Journal*, 36(6), 1111–1122. doi:10.1139/t99-074
- Farina, P., Catani, F., Colombo, D., Fumagalli, A., Kukavcic, M., Marks, F., & Moretti, S. (2005). Remote sensing: a tool for landslide investigations at a basin scale. In *Geophysical Research Abstracts* (Vol. 7, pp. 10157–10168). European Geosciences Union.
- Farina, P., Colombo, D., Fumagalli, A., Marks, F., & Moretti, S. (2006). Permanent Scatterers for landslide investigations: outcomes from the ESA-SLAM project. *Engineering Geology*, 88(3-4), 200–217. doi:10.1016/j.enggeo.2006.09.007
- Fielding, A. H., & Bell, J. F. (1997). A review of methods for the assessment of prediction errors in conservation presence/absence models. *Environmental Conservation*, 24(01), 38–49.
- Fiorucci, F., Cardinali, M., Carlà, R., Rossi, M., Mondini, A. C., Santurri, L., ... Guzzetti, F. (2011). Seasonal landslide mapping and estimation of landslide mobilization rates using aerial and satellite images. *Geomorphology*, 129(1-2), 59–70. doi:10.1016/j.geomorph.2011.01.013
- Foody, G. M. (2002). Status of land cover classification accuracy assessment. *Remote Sensing of Environment*, 80(1), 185–201. doi:10.1016/S0034-4257(01)00295-4
- Fourie, A. B. (1996). Predicting rainfall-induced slope instability. In *Proceedings of the Civil Engineers Geotechnical Engineering* (Vol. 119, pp. 211–218).
- Frattoni, P., Crosta, G., & Carrara, A. (2010). Techniques for evaluating the performance of landslide susceptibility models. *Engineering Geology*, 111(1-4), 62–72. doi:10.1016/j.enggeo.2009.12.004
- Fredlund, D. G., & Morgenstern, N. R. (1977). Stress state variables for unsaturated soils. *Journal of Geotechnical and Geoenvironmental Engineering*, 103(ASCE 12919), 447–466.
- Fredlund, D. G., Morgenstern, N. R., & Widger, R. A. (1978). The shear strength of unsaturated soils. *Canadian Geotechnical Journal*, 15(3), 313–321. doi:10.1139/t78-029
- Friedel, S., Thielen, A., & Springman, S. M. (2006). Investigation of a slope endangered by rainfall-induced landslides using 3D resistivity tomography and geotechnical testing. *Journal of Applied Geophysics*, 60(2), 100–114. doi:10.1016/j.jappgeo.2006.01.001
- Funk, C., Erima, G., Davenport, F., & Michaelsen, J. (2010). *A climate Trend Analysis of Kenya* (No. 3074). Nairobi, Kenya: FEWSNET. Retrieved from <http://pubs.usgs.gov/fs/2010/3074/>.
- Gad, S., & Kusky, T. (2006). Lithological mapping in the Eastern Desert of Egypt, the Barramiya area, using Landsat thematic mapper (TM). *Journal of African Earth Sciences*, 44(2), 196–202. doi:10.1016/j.jafrearsci.2005.10.014
- Gad, S., & Kusky, T. (2007). ASTER spectral ratioing for lithological mapping in the Arabian–Nubian shield, the Neoproterozoic Wadi Kid area, Sinai, Egypt. *Gondwana Research*, 11(3), 326–335. doi:10.1016/j.gr.2006.02.010
- Galeandro, A., Šimunek, J., & Simeone, V. (2013). Analysis of rainfall infiltration effects on the stability of pyroclastic soil veneer affected by vertical drying shrinkage fractures. *Bulletin of Engineering Geology and the Environment*, 72(3-4), 447–455. doi:10.1007/s10064-013-0492-5

- Galeandro, A., Doglioni, A., Simeone, V., & Šimůnek, J. (2014). Analysis of infiltration processes into fractured and swelling soils as triggering factors of landslides. *Environmental Earth Sciences*, *71*(6), 2911–2923. doi:10.1007/s12665-013-2666-7
- Gao, J. (2009). *Digital analysis of remotely sensed imagery* (1st ed.). New York [u.a.]: McGraw-Hill.
- Gao, J., & Maro, J. (2010). Topographic controls on evolution of shallow landslides in pastoral Wairarapa, New Zealand, 1979–2003. *Geomorphology*, *114*(3), 373–381. doi:10.1016/j.geomorph.2009.08.002
- Gariano, S. L., Petrucci, O., & Guzzetti, F. (2015). Changes in the occurrence of rainfall-induced landslides in Calabria, southern Italy, in the 20th century. *Natural Hazards and Earth System Science*, *15*(10), 2313–2330. doi:10.5194/nhess-15-2313-2015
- Gerrard, J. (1994). The landslide hazard in the Himalayas: geological control and human action. *Geomorphology*, *10*(1-4), 221–230. doi:10.1016/0169-555X(94)90018-3
- Ghestem, M., Sidle, R. C., & Stokes, A. (2011). The Influence of Plant Root Systems on Subsurface Flow: Implications for Slope Stability. *BioScience*, *61*(11), 869–879. doi:10.1525/bio.2011.61.11.6
- Ghuffar, S., Székely, B., Roncat, A., & Pfeifer, N. (2013). Landslide Displacement Monitoring Using 3D Range Flow on Airborne and Terrestrial LiDAR Data. *Remote Sensing*, *5*(6), 2720–2745. doi:10.3390/rs5062720
- Gitau, G. (2015). Nyeri govt promises to assist landslide victims. *Daily Nation Newspaper*. Retrieved from <http://www.nation.co.ke/counties/nyeri/Nyeri-Landslides-Victims-Kenya-Red-Cross-/1954190/2712180/-/e7us9tz/-/index.html>
- Glade, T. (2003). Landslide occurrence as a response to land use change: a review of evidence from New Zealand. *CATENA*, *51*(3-4), 297–314. doi:10.1016/S0341-8162(02)00170-4
- Godt, J. W., Baum, R. L., & Chleborad, A. F. (2006). Rainfall characteristics for shallow landsliding in Seattle, Washington, USA. *Earth Surface Processes and Landforms*, *31*(1), 97–110. doi:10.1002/esp.1237
- Goetz, A. F. H. (2009). Three decades of hyperspectral remote sensing of the Earth: A personal view. *Remote Sensing of Environment*, *113*, S5–S16. doi:10.1016/j.rse.2007.12.014
- GOK. (2010). *Kenya: Millenium Development Goals Report*. Nairobi, Kenya: Government of Kenya.
- Gómez, H., & Kavzoglu, T. (2005). Assessment of shallow landslide susceptibility using artificial neural networks in Jabonosa River Basin, Venezuela. *Engineering Geology*, *78*(1-2), 11–27. doi:10.1016/j.enggeo.2004.10.004
- Gonzalez, R. C., & Woods, R. E. (2002). *Digital image processing*. Delhi, India: Pearson Education.
- Gorsevski, P. V., Brown, M. K., Panter, K., Onasch, C. M., Simic, A., & Snyder, J. (2015). Landslide detection and susceptibility mapping using LiDAR and an artificial neural network approach: a case study in the Cuyahoga Valley National Park, Ohio. *Landslides*. doi:10.1007/s10346-015-0587-0
- Gostelow, T. P. (1991). Rainfall and landslides. In M. Almeida-Teixerira, R. Fantechi, R. Oliveira, & A. Gomes Coelho (Eds.), *Prevention and control of landslides and other mass movements* (pp. 139–161). Brussels: CEC.
- Govender, M., Chetty, K., & Bulcock, H. (2007). A review of hyperspectral remote sensing and its application in vegetation and water resource studies. *Water SA*, *33*(2), 145–152. doi:10.4314/wsa.v33i2.49049
- Government of Kenya. (2012). *National Climate Change Action Plan 2013-2017 Executive Summary* (No. NCCAP 2013-2017). Nairobi, Kenya: Ministry of Environment and Mineral Resources.
- Graham, J. (1984). Methods of Stability Analysis. In D. Brunsten (Ed.), *Slope instability* (pp. 171–215). New York: Wiley and sons.

- Green, A. A., Berman, M., Switzer, P., & Craig, M. D. (1988). A transformation for ordering multispectral data in terms of image quality with implications for noise removal. *IEEE Transactions on Geoscience and Remote Sensing*, 26(1), 65–74. doi:10.1109/36.3001
- Greenway, D. R. (1987). Vegetation and slope stability. In *Slope Stability* (M.G. Anderson, K.S. Richards, pp. 187–230). UK: Wiley, Chichester.
- Greif, V., & Vlcko, J. (2012). Monitoring of post-failure landslide deformation by the PS-InSAR technique at Lubietova in Central Slovakia. *Environmental Earth Sciences*, 66(6), 1585–1595. doi:10.1007/s12665-011-0951-x
- Gupta, R. P. (1991). Geological Applications. In R. P. Gupta, *Remote Sensing Geology* (pp. 223–309). Berlin, Heidelberg: Springer Berlin Heidelberg. doi:10.1007/978-3-662-12914-2\_13
- Gupta, R. P. (2003a). *Remote Sensing Geology*. Berlin; New York: Springer.
- Gupta, R. P. (2003b). Geological Applications. In *Remote Sensing Geology* (2nd ed., pp. 429–583). Berlin Heidelberg: Springer. doi:10.1007/978-3-662-05283-9-16
- Gupta, R. P., & Joshi, B. C. (1990). Landslide hazard zoning using the GIS approach—A case study from the Ramganga catchment, Himalayas. *Engineering Geology*, 28(1-2), 119–131. doi:10.1016/0013-7952(90)90037-2
- Guth, A. (2014). *Maps of the Southern Kenya Rift*. Geological Society of America. Retrieved from <http://www.geosociety.org/maps/2014-DMCH016/>
- Guzzetti, F. (2006). *Landslide hazard and risk assessment* (PhD Thesis). Rheinischen Friedrich-Wilhelms University of Bonn, Faculty of Mathematics and Natural Sciences, Bonn, Germany.
- Guzzetti, F., Carrara, A., Cardinali, M., & Reichenbach, P. (1999). Landslide hazard evaluation: a review of current techniques and their application in a multi-scale study, Central Italy. *Geomorphology*, 31(1-4), 181–216. doi:10.1016/S0169-555X(99)00078-1
- Guzzetti, F., Cardinali, M., Reichenbach, P., & Carrara, A. (2000). Comparing Landslide Maps: A Case Study in the Upper Tiber River Basin, Central Italy. *Environmental Management*, 25(3), 247–263. doi:10.1007/s002679910020
- Guzzetti, F., Cardinali, M., Reichenbach, P., Cipolla, F., Sebastiani, C., Galli, M., & Salvati, P. (2004). Landslides triggered by the 23 November 2000 rainfall event in the Imperia Province, Western Liguria, Italy. *Engineering Geology*, 73(3-4), 229–245. doi:10.1016/j.enggeo.2004.01.006
- Guzzetti, F., Reichenbach, P., Cardinali, M., Galli, M., & Ardizzone, F. (2005). Probabilistic landslide hazard assessment at the basin scale. *Geomorphology*, 72(1-4), 272–299. doi:10.1016/j.geomorph.2005.06.002
- Guzzetti, F., Reichenbach, P., Ardizzone, F., Cardinali, M., & Galli, M. (2006). Estimating the quality of landslide susceptibility models. *Geomorphology*, 81(1-2), 166–184. doi:10.1016/j.geomorph.2006.04.007
- Guzzetti, F., Peruccacci, S., Rossi, M., & Stark, C. P. (2007a). The rainfall intensity–duration control of shallow landslides and debris flows: an update. *Landslides*, 5(1), 3–17. doi:10.1007/s10346-007-0112-1
- Guzzetti, F., Peruccacci, S., Rossi, M., & Stark, C. P. (2007b). Rainfall thresholds for the initiation of landslides in central and southern Europe. *Meteorology and Atmospheric Physics*, 98(3-4), 239–267. doi:10.1007/s00703-007-0262-7
- Guzzetti, F., Manunta, M., Ardizzone, F., Pepe, A., Cardinali, M., Zeni, G., ... Lanari, R. (2009). Analysis of Ground Deformation Detected Using the SBAS-DInSAR Technique in Umbria, Central Italy. *Pure and Applied Geophysics*, 166(8-9), 1425–1459. doi:10.1007/s00024-009-0491-4

- Guzzetti, F., Mondini, A. C., Cardinali, M., Fiorucci, F., Santangelo, M., & Chang, K.-T. (2012). Landslide inventory maps: New tools for an old problem. *Earth-Science Reviews*, *112*(1-2), 42–66. doi:10.1016/j.earscirev.2012.02.001
- Haerberlin, Y., Turberg, P., Retiere, A., & Senegas, O. (2004). Validation of Spot-5 satellite imagery for geological hazard identification and risk assessment for landslides, mud and debris flows in Matagalpa, Nicaragua. *International Archives of Photogrammetry Remote Sensing and Spatial Information Sciences*, *35*, B1.
- Hamdhan, I. N., & Schweiger, H. F. (2011). Slope Stability Analysis of Unsaturated Soil with Fully Coupled Flow-Deformation Analysis. *Mathematical Geosciences at the Crossroads of Theory and Practice, IAMG 2011*. doi:10.5242/iamg.2011.0063
- Harp, E. L., Reid, M. E., McKenna, J. P., & Michael, J. A. (2009). Mapping of hazard from rainfall-triggered landslides in developing countries: Examples from Honduras and Micronesia. *Engineering Geology*, *104*(3-4), 295–311. doi:10.1016/j.enggeo.2008.11.010
- Hashim, M., Ahmad, S., Johari, M. A. M., & Pour, A. B. (2013). Automatic lineament extraction in a heavily vegetated region using Landsat Enhanced Thematic Mapper (ETM+) imagery. *Advances in Space Research*, *51*(5), 874–890. doi:10.1016/j.asr.2012.10.004
- Hervás, J., & Bobrowsky, P. (2009). Mapping: Inventories, Susceptibility, Hazard and Risk. In K. Sassa & P. Canuti (Eds.), *Landslides – Disaster Risk Reduction* (Vol. 19, pp. 321–349). Berlin, Heidelberg: Springer Berlin Heidelberg. doi:10.1007/978-3-540-69970-5\_19
- Hervás, J., Barredo, J. I., Rosin, P. L., Pasuto, A., Mantovani, F., & Silvano, S. (2003). Monitoring landslides from optical remotely sensed imagery: the case history of Tessina landslide, Italy. *Geomorphology*, *54*(1-2), 63–75. doi:10.1016/S0169-555X(03)00056-4
- Highland, L., & Bobrowsky, P. T. (2008). *The Landslide handbook: a guide to understanding landslides*. Reston, VA: US Geological Survey.
- Hilley, G. E., Bürgmann, R., Ferretti, A., Novali, F., & Rocca, F. (2004). Dynamics of Slow-Moving Landslides from Permanent Scatterer Analysis. *Science*, *304*(5679), 1952–1955. doi:10.1126/science.1098821
- Hinkelmann, R., Zehe, E., Ehlers, W., & Joswig, M. (2011). Special Section on Landslides: Setting the Scene and Outline of Contributing Studies. *Vadose Zone Journal*, *10*(2), 473. doi:10.2136/vzj2011.0032
- Hodgson, M. E., Jensen, J. R., Tullis, J. A., Riordan, K. D., & Archer, C. M. (2003). Synergistic Use of Lidar and Color Aerial Photography for Mapping Urban Parcel Imperviousness. *Photogrammetric Engineering & Remote Sensing*, *69*(9), 973–980. doi:10.14358/PERS.69.9.973
- Hölbling, D., Füreder, P., Antolini, F., Cigna, F., Casagli, N., & Lang, S. (2012). A Semi-Automated Object-Based Approach for Landslide Detection Validated by Persistent Scatterer Interferometry Measures and Landslide Inventories. *Remote Sensing*, *4*(12), 1310–1336. doi:10.3390/rs4051310
- Hong, Y., Adler, R. F., & Huffman, G. J. (2007). Use of satellite remote sensing data in the mapping of global landslide susceptibility. *Natural Hazards*, *43*, 245–256. doi: 10.1007/s11069-006-9104-z
- Hong, Y., He, X., Cerato, A., Zhang, K., Hong, Z., & Liao, Z. (2014). Predictability of a physically-based model for rainfall-induced shallow landslides: Model development and case studies. In M. Scaioni (Ed.), *Modern Technologies for Landslide Investigation and prediction*. Berlin, Germany: Springer. doi:10.1007/978-3-662-45931-7\_9
- Huang, J. C., & Kao, S. J. (2006). Optimal estimator for assessing landslide model performance. *Hydrology and Earth System Sciences*, *10*(6), 957–965. doi:10.5194/hess-10-957-2006

- Huang, C., Wylie, B., Yang, L., Homer, C., & Zylstra, G. (2002). Derivation of a tasseled cap transformation based on Landsat 7 at-satellite reflectance. *International Journal of Remote Sensing*, 23(8), 1741–1748. doi:10.1080/01431160110106113
- Huang, H.-P., Yang, K.-C., & Lin, B.-W. (2013). Statistical evaluation of the effect of earthquake with other related factors on landslide susceptibility: using the watershed area of Shihmen reservoir in Taiwan as a case study. *Environmental Earth Sciences*, 69(7), 2151–2166. doi:10.1007/s12665-012-2044-x
- Huat, B. B. K., Ali, F. H., & Low, T. H. (2006). Water infiltration characteristics of unsaturated soil slope and its effect on suction and stability. *Geotechnical and Geological Engineering*, 24(5), 1293–1306. doi:10.1007/s10706-005-1881-8
- Hung, L. Q., Batelaan, O., & De Smedt, F. (2005). Lineament extraction and analysis, comparison of LANDSAT ETM and ASTER imagery. Case study: Suoimuoi tropical karst catchment, Vietnam. In M. Ehlers & U. Michel (Eds.), *Proceedings of SPIE Remote sensing for Environmental monitoring, GIS applications and Geology* (Vol. 5983, p. 59830T–59830T–12). International Society for Optics and Photonics. doi:10.1117/12.627699
- Hungr, O., Leroueil, S., & Picarelli, L. (2014). The Varnes classification of landslide types, an update. *Landslides*, 11(2), 167–194. doi:10.1007/s10346-013-0436-y
- Hyvärinen, A., Karhunen, J., & Oja, E. (2001). *Independent Component Analysis*. New York: Wiley.
- Igwe, O., Mode, W., Nnebedum, O., Okonkwo, I., & Oha, I. (2014). The analysis of rainfall-induced slope failures at Iva Valley area of Enugu State, Nigeria. *Environmental Earth Sciences*, 71(5), 2465–2480. doi:10.1007/s12665-013-2647-x
- Iverson, R. M. (2000). Landslide triggering by rain infiltration. *Water Resources Research*, 36(7), 1897–1910. doi:10.1029/2000WR900090
- Iwahashi, J., Kamiya, I., & Yamagishi, H. (2012). High-resolution DEMs in the study of rainfall- and earthquake-induced landslides: Use of a variable window size method in digital terrain analysis. *Geomorphology*, 153–154, 29–38. doi:10.1016/j.geomorph.2012.02.002
- Jaboyedoff, M., Oppikofer, T., Abellán, A., Derron, M.-H., Loye, A., Metzger, R., & Pedrazzini, A. (2012). Use of LIDAR in landslide investigations: a review. *Natural Hazards*, 61(1), 5–28. doi:10.1007/s11069-010-9634-2
- Jade, S., & Sarkar, S. (1993). Statistical models for slope instability classification. *Engineering Geology*, 36(1-2), 91–98. doi:10.1016/0013-7952(93)90021-4
- Jensen, J. R. (2005). Thematic map accuracy assessment. In *Introductory digital image processing: a remote sensing perspective* (3rd edition, Vol. Section C, pp. 495–515). Upper Saddle River, N.J: Prentice Hall.
- JICA, G. (1997). *The study on the water supply for seven towns in Eastern Province in the Republic of Kenya* (No. 52). JICA & The ministry of Land Reclamation, Regional and water development, The Republic of Kenya.
- Johansson, A. (1993). *A study of earth flow features and the relation to soil and rainfall characteristics in Ol'Joro Orok Division, Nyandarua District, Kenya* (Bsc degree project report, Department of Physical Geography). Stockholm University.
- Jolliffe, I. (2005). *Principal Component Analysis* (2nd ed.). John Wiley & Sons, Ltd.
- Joyce, K. E., Dellow, G. D., & Glassey, P. J. (2008a). Assessing Image Processing Techniques for Mapping Landslides (Vol. 2, pp. II–1231–II–1234). Presented at the Geoscience and Remote Sensing Symposium, Boston, MA: IEEE. doi:10.1109/IGARSS.2008.4779224

- Joyce, K. E., Dellow, G. D., & Glassey, P. J. (2008b). Methods for mapping landslides in New Zealand using satellite optical remote sensing. Presented at the 14th Australasian Remote Sensing and Photogrammetry Conference, Darwin: electronic proceedings.
- Joyce, K. E., Belliss, S. E., Samsonov, S. V., McNeill, S. J., & Glassey, P. J. (2009). A review of the status of satellite remote sensing and image processing techniques for mapping natural hazards and disasters. *Progress in Physical Geography*, 33(2), 183–207. doi:10.1177/0309133309339563
- Joyce, K. E., Samsonov, S. V., Levick, S. R., Engelbrecht, J., & Belliss, S. (2014). Mapping and monitoring geological hazards using optical, LiDAR, and synthetic aperture RADAR image data. *Natural Hazards*, 73(2), 137–163. doi:10.1007/s11069-014-1122-7
- Kahiga, E. W. (2011). *Comparative factors that influence landslide occurrence: Application of GIS and rainfall thresholds in landslide assessment in Kenya* (Bsc Project). University of Nairobi, Kenya.
- Kamau, N. R. (1981). *A study of mass movements in Kangema area, Murang'a District, Kenya* (postgraduate diploma in Soil conservation). University of Nairobi, Kenya.
- Kanungo, D. P., Arora, M. K., Gupta, R. P., & Sarkar, S. (2005). GIS based landslide hazard zonation using neuro-fuzzy weighting. In *Proceedings of the 2nd Indian International Conference on Artificial intelligence* (pp. 1222–1237). Pune, India.
- Kanungo, D. P., Arora, M. K., Sarkar, S., & Gupta, R. P. (2006). A comparative study of conventional, ANN black box, fuzzy and combined neural and fuzzy weighting procedures for landslide susceptibility zonation in Darjeeling Himalayas. *Engineering Geology*, 85(3-4), 347–366. doi:10.1016/j.enggeo.2006.03.004
- Kanungo, D. P., Arora, M. K., Sarkar, S., & Gupta, R. P. (2009). Landslide Susceptibility Zonation (LSZ) Mapping - A Review. *Journal of South Asia Disaster Studies*, 2(1), 81–105.
- Kanungo, D. P., Sarkar, S., & Sharma, S. (2011). Combining neural network with fuzzy, certainty factor and likelihood ratio concepts for spatial prediction of landslides. *Natural Hazards*, 59(3), 1491–1512. doi:10.1007/s11069-011-9847-z
- Karanja, F. K., & Mutua, F. M. (2000). *Reducing the impact of environmental emergencies through early warning and preparedness - The case of El-Nino Southern Oscillation (ENSO)*. Nairobi, Kenya: UNFIP, UNEP, NCAR, WMO, IDNDR, UNU.
- Karim, S., Jalileddin, S., & Ali, M. T. (2011). Zoning Landslide by Use of Frequency Ratio Method (Case Study: Deylaman Region). *Middle East Journal of Scientific Research*, 9(5), 578–583.
- Kariuki, P. C., Woldai, T., & Van der Meer, F. (2004). The Role of Remote Sensing in Mapping Swelling Soils. *Asian Journal of Geoinformatics*, 5(1), 43–54.
- Karuma, A., Gachene, C., Msanya, B., Mtakwa, P., Amuri, N., & Gicheru, P. (2015). Soil Morphology, Physico - Chemical Properties and Classification of Typical Soils of Mwala District, Kenya. *International Journal of Plant & Soil Science*, 4(2), 156–170. doi:10.9734/IJPSS/2015/13467
- Kasai, M., Ikeda, M., Asahina, T., & Fujisawa, K. (2009). LiDAR-derived DEM evaluation of deep-seated landslides in a steep and rocky region of Japan. *Geomorphology*, 113(1-2), 57–69. doi:10.1016/j.geomorph.2009.06.004
- Kavak, K. S. (2005). Determination of palaeotectonic and neotectonic features around the Mendere Massif and the Gediz Graben (West. Turkey) using Landsat TM image. *International Journal of Remote Sensing*, 26(1), 59–78. doi:10.1080/01431160410001709994
- Khazai, B., & Sitar, N. (2004). Evaluation of factors controlling earthquake-induced landslides caused by Chi-Chi earthquake and comparison with the Northridge and Loma Prieta events. *Engineering Geology*, 71(1-2), 79–95. doi:10.1016/S0013-7952(03)00127-3

- Kiage, L. M., Liu, K. B., Walker, N. D., Lam, N., & Huh, O. K. (2007). Recent land cover/use change associated with land degradation in the Lake Baringo catchment, Kenya, East Africa: evidence from Landsat TM and ETM+. *International Journal of Remote Sensing*, 28(19), 4285–4309. doi:10.1080/01431160701241753
- Kibiiy, J., Koskei, K., Sitters, C., & Ndambuki, J. (2014). Development of a regional landslide prediction model for Kerio Valley in Kenya. *International Journal of Development and Sustainability*, 3(4), 662–678.
- Kipchumba, I. K. (2011). *Landslide Hazard Assessment in Kenya* (Bsc Project). University of Nairobi, Nairobi, Kenya.
- Kipkiror, L. J., & Towett, J. (2013). Towards Ensuring a supply of sufficient and Quality water in the Lagam Escapment and the kerio valley in Marakwet District, Kenya. *International Journal of Humanities and Social Science*, 3(13), 231–241.
- Kipseba, E. K., Ogora, M., Maina, G., & Kotut, J. (2013). *Preliminary reports on Kijabe Landslides, Lari District, Kiambu County* (Mines and Geology Department). Nairobi, Kenya: Ministry of Environment and Mineral Resources.
- Kirimi, M. (2015). Four killed in Meru quarry landslide. *The Star Newspaper*. Retrieved from <http://www.the-star.co.ke/news/four-killed-meru-quarry-landslide>
- Kithome, C. N. (2012). *Detailed Hydrogeological /Geophysical Survey Report for Borehole site investigation at Muluu village, Muluu location, Kitui county*. Nairobi, Kenya.
- KMD (2010). *Weather review during March and the outlook for April 2010* (p. 2). Nairobi, Kenya: Kenya Meteorological Department (KMD).
- KNBS. (2010). Population and Housing Censuses, Kenya National Bureau of Statistics.
- Kocal, A., Duzgun, H. S., & Karpuz, C. (2004). Discontinuity mapping with automatic lineament extraction from high resolution satellite imagery. In *Proceedings of the XXth ISPRS Congress*. Istanbul, Turkey.
- Korup, O., Densmore, A. L., & Schlunegger, F. (2010). The role of landslides in mountain range evolution. *Geomorphology*, 120(1-2), 77–90. doi:10.1016/j.geomorph.2009.09.017
- Koutsias, N., Karteris, M., & Chuvieco, E. (2000). The Use of Intensity-Hue-Saturation transformation of Landsat-5 Thematic mapper for Burned Land Mapping. *Photogrammetric Engineering & Remote Sensing*, 66(7), 829–839.
- Kraus, K. (2007). *Photogrammetry: Geometry from Images and Laser Scans*. (I. Harley, Trans.) (2. ed). Berlin: de Gruyter.
- Krenker, A., Bester, J., & Kos, A. (2011). Introduction to the Artificial Neural Networks. In *Artificial Neural Networks- Methodological advances and Biomedical applications* (Vol. 1, pp. 3–18). INTECH Open Access Publisher.
- Kruse, A. F. (1998). Advances in Hyperspectral Remote Sensing for Geologic Mapping and Exploration. In *9th Australasian Remote Sensing Conference*. Sydney, Australia.
- Kuriakose, S. L. (2010). Physically-based dynamic modeling of the effect of land use changes on shallow landslide initiation in the Western Ghats of Kerala. India: University of Twente, Netherlands.
- Kuriakose, S. L., & van Beek, L. P. H. (2010). Root reinforcement and its contribution to slope stability in the western Ghats of Kerala, India. In *EGU General Assembly 2010* (Vol. 34, p. 8505). Vienna, Austria.
- Kuriakose, S. L., Devkota, S., Rossiter, D. G., & Jetten, V. G. (2009). Prediction of soil depth using environmental variables in an anthropogenic landscape, a case study in the Western Ghats of Kerala, India. *CATENA*, 79(1), 27–38. doi:10.1016/j.catena.2009.05.005

- Landis, J. R., & Koch, G. G. (1977). The Measurement of Observer Agreement for Categorical Data. *Biometrics*, 33(1), 159–174. doi:10.2307/2529310
- Lang, S. (2008). Object-based image analysis for remote sensing applications: modeling reality - dealing with complexity. In *Object-based image analysis spatial concepts for knowledge-driven remote sensing applications* (pp. 3–28). Berlin; London: Springer. doi:10.1007/978-3-540-77058-9\_1
- Larsen, I. J. (2014). *Hillslope erosion and weathering rates in Earth's most rapidly uplifting mountains* (PhD Thesis). University of Washington, Department of Earth and Space Sciences, Washington, D.C.
- Larsson, M. (1986). *Landslides in the mountain areas of Kenya: comparative studies of different slopes within the Nyandarua Range* (Department of Physical Geography). Stockholm University.
- Larsson, M. (1989). Landslides in the mountain areas of Kenya: comparative studies of different slopes within the Nyandarua Range. In D. B. Thomas, E. K. Biamah, A. M. Kilewe, L. Lundgren, & B. O. Mochoge (Eds.), *Proceedings Third national Workshop* (pp. 123–136). University of Nairobi, Kenya.
- Lauknes, T. R., Piyush Shanker, A., Dehls, J. F., Zebker, H. A., Henderson, I. H. C., & Larsen, Y. (2010). Detailed rockslide mapping in northern Norway with small baseline and persistent scatterer interferometric SAR time series methods. *Remote Sensing of Environment*, 114(9), 2097–2109. doi:10.1016/j.rse.2010.04.015
- Lee, S. (2005). Application of logistic regression model and its validation for landslide susceptibility mapping using GIS and remote sensing data. *International Journal of Remote Sensing*, 26(7), 1477–1491. doi:10.1080/01431160412331331012
- Lee, S., & Min, K. (2001). Statistical analysis of landslide susceptibility at Yongin, Korea. *Environmental Geology*, 40(9), 1095–1113. doi:10.1007/s002540100310
- Lee, S., & Pradhan, B. (2006). Probabilistic landslide hazards and risk mapping on Penang Island, Malaysia. *Journal of Earth System Science*, 115(6), 661–672. doi:10.1007/s12040-006-0004-0
- Liao, Z., Hong, Y., Wang, J., Fukuoka, H., Sassa, K., Karnawati, D., & Fathani, F. (2010). Prototyping an experimental early warning system for rainfall-induced landslides in Indonesia using satellite remote sensing and geospatial datasets. *Landslides*, 7(3), 317–324. doi:10.1007/s10346-010-0219-7
- Liao, Z., Hong, Y., Kirschbaum, D., & Liu, C. (2011). Assessment of shallow landslides from Hurricane Mitch in central America using a physically based model. *Environmental Earth Sciences*, 66(6), 1697–1705. doi:10.1007/s12665-011-0997-9
- Liao, Z., Hong, Y., Kirschbaum, D., & Liu, C. (2012). Assessment of shallow landslides from Hurricane Mitch in central America using a physically based model. *Environmental Earth Sciences*, 66(6), 1697–1705. doi:10.1007/s12665-011-0997-9
- Lin, C.-W., Tseng, C.-M., Tseng, Y.-H., Fei, L.-Y., Hsieh, Y.-C., & Tarolli, P. (2013). Recognition of large scale deep-seated landslides in forest areas of Taiwan using high resolution topography. *Journal of Asian Earth Sciences*, 62, 389–400. doi:10.1016/j.jseaes.2012.10.022
- Lindsay, M., & Hans, P. L. (2005). Monitoring and Modelling for the Sustainable Management of Water Resources in Tropical Mountain Basins: The Mount Kenya Example. In *Global change and mountain regions: an overview of current knowledge* (pp. 605–616). Dordrecht: Springer. doi:10.1007/1-4020-3508-X\_60#page-1
- Listo, F. de L. R., & Carvalho, V. B. (2012). Mapping of risk and susceptibility of shallow-landslide in the city of São Paulo, Brazil. *Geomorphology*, 169-170, 30–44. doi:10.1016/j.geomorph.2012.01.010

- Liu, J. K., Wong, C. C., Huang, J. H., & Yang, M. J. (2002). Landslide-enhancement images for the study of torrential-rainfall landslides. In *Proceedings of the 23rd Asian Conference on Remote Sensing*. Kathmandu, Nepal.
- Liu, Q. Q., & Li, J. C. (2015). Effects of Water Seepage on the Stability of Soil-slopes. *Procedia IUTAM*, 17, 29–39. doi:10.1016/j.piutam.2015.06.006
- Li, Y., Chen, G., Wang, B., Zheng, L., Zhang, Y., & Tang, C. (2013). A new approach of combining aerial photography with satellite imagery for landslide detection. *Natural Hazards*, 66(2), 649–669. doi:10.1007/s11069-012-0505-x
- Lourenço, S. D. N., Sassa, K., & Fukuoka, H. (2006). Failure process and hydrologic response of a two layer physical model: Implications for rainfall-induced landslides. *Geomorphology*, 73(1-2), 115–130. doi:10.1016/j.geomorph.2005.06.004
- Lu, D., & Weng, Q. (2007). A survey of image classification methods and techniques for improving classification performance. *International Journal of Remote Sensing*, 28(5), 823–870. doi:10.1080/01431160600746456
- Lu, P., Casagli, N., Catani, F., & Tofani, V. (2012). Persistent Scatterers Interferometry Hotspot and Cluster Analysis (PSI-HCA) for detection of extremely slow-moving landslides. *International Journal of Remote Sensing*, 33(2), 466–489. doi:10.1080/01431161.2010.536185
- Lu, P., Stumpf, A., Kerle, N., & Casagli, N. (2011). Object-Oriented Change Detection for Landslide Rapid Mapping. *IEEE Geoscience and Remote Sensing Letters*, 8(4), 701–705. doi:10.1109/LGRS.2010.2101045
- Maathai, W. (2003). *The Green Belt Movement: sharing the approach and the experience*. New York: Lantern Books.
- Maina-Gichaba, C., Kipseba, E. K., & Masibo, M. (2013). Overview of Landslide Occurrences in Kenya. In *Developments in Earth Surface Processes* (Vol. 16, pp. 293–314). doi:10.1016/B978-0-444-59559-1.00020-7
- Makokha, G. L., & Shisanya, C. A. (2010). Trends in Mean Annual Minimum and Maximum Near Surface Temperature in Nairobi City, Kenya. *Advances in Meteorology*, 2010, 1–6. doi:10.1155/2010/676041
- Malamud, B. D., Turcotte, D. L., Guzzetti, F., & Reichenbach, P. (2004). Landslide inventories and their statistical properties. *Earth Surface Processes and Landforms*, 29(6), 687–711. doi:10.1002/esp.1064
- Malmstroem, M. (1997). *Volume change of Chinga Dam, Othaya Division, Kenya: A study of sedimentation related to mass movements, soil erosion and precipitation* (Minor Field Studies No. 4). Uppsala: Swedish University of Agriculture Sciences.
- Mancarella, D., Doglioni, A., & Simeone, V. (2012). On capillary barrier effects and debris slide triggering in unsaturated layered covers. *Engineering Geology*, 147-148, 14–27. doi:10.1016/j.enggeo.2012.07.003
- Mann, U., Pradhan, B., Prechtel, N., & Buchroithner, M. F. (2012). An automated Approach for detection of shallow landslides from LiDAR derived DEM using geomorphological indicators in a tropical Forest. In B. Pradhan & M. F. Buchroithner (Eds.), *Terrigenous Mass Movements: Detection, Modelling, Early Warning and Mitigation using Geoinformation Technology* (pp. 1–22). Berlin: Springer. doi:10.1007/978-3-642-25495-6\_1
- Mantovani, F., Soeters, R., & Van Westen, C. J. (1996). Remote sensing techniques for landslide studies and hazard zonation in Europe. *Geomorphology*, 15(3-4), 213–225. doi:10.1016/0169-555X(95)00071-C

- Marcelino, E. V., Formaggio, A. R., & Maeda, E. E. (2009). Landslide inventory using image fusion techniques in Brazil. *International Journal of Applied Earth Observation and Geoinformation*, 11(3), 181–191. doi:10.1016/j.jag.2009.01.003
- Marghany, M., & Hashim, M. (2010a). Lineament Mapping using Multispectral Remote Sensing Satellite Data. *Research Journal of Applied Sciences*, 5(2), 126–130. doi:10.3923/rjasci.2010.126.130
- Marghany, M., & Hashim, M. (2010b). Developing adaptive algorithm for automatic detection of geological linear features using RADARSAT-1 SAR data. *International Journal of the Physical Sciences*, 5(14), 2223–2229.
- Marjanović, M., Kovačević, M., Bajat, B., & Voženilek, V. (2011). Landslide susceptibility assessment using SVM machine learning algorithm. *Engineering Geology*, 123(3), 225–234. doi:10.1016/j.enggeo.2011.09.006
- Martha, T. R., Kerle, N., Jetten, V., van Westen, C. J., & Kumar, K. V. (2010). Characterising spectral, spatial and morphometric properties of landslides for semi-automatic detection using object-oriented methods. *Geomorphology*, 116(1-2), 24–36. doi:10.1016/j.geomorph.2009.10.004
- Martha, T. R., Kerle, N., van Westen, C. J., Jetten, V., & Vinod Kumar, K. (2012). Object-oriented analysis of multi-temporal panchromatic images for creation of historical landslide inventories. *ISPRS Journal of Photogrammetry and Remote Sensing*, 67, 105–119. doi:10.1016/j.isprsjprs.2011.11.004
- Mashari, S., Solaimani, K., & Omidvar, E. (2012). Landslide Susceptibility Mapping Using Multiple Regression and GIS Tools in Tajan Basin, North of Iran. *Environment and Natural Resources Research*, 2(3). doi:10.5539/enrr.v2n3p43
- Mather, P. M., & Tso, M. (2009). *Classification methods for remotely sensed data* (2. ed). Boca Raton, Fla.: CRC Press/Taylor & Francis.
- Mbithi, D. M., Demessie, E. T., & Kashiri, T. (2012). The impact of Land use Land Cover (LULC) changes on Land Surface Temperature (LST); a case study of Addis Ababa City, Ethiopia.
- Mburu, D. M. (1998). Landslide problems in agricultural land and farmers' perception. In *Proceedings of the International Conference of the Kenya Society of Agricultural Engineers* (pp. 1–4). Nairobi, Kenya.
- Mburu, D. M., Westerberg, L.-O., Sandel, J., & Malmstroem, M. (2003). Mass movement and sedimentation of Chinga Dam in Othaya Division, Kenya. In *Proceedings of the International Conference on Local Land use Strategies ina Globalizing World* (Vol. 4, pp. 329–339). Institute of Geography, University of Copenhagen, Denmark.
- McIntosh, P. D., Price, D. M., Eberhard, R., & Slee, A. J. (2009). Late Quaternary erosion events in lowland and mid-altitude Tasmania in relation to climate change and first human arrival. *Quaternary Science Reviews*, 28(9-10), 850–872. doi:10.1016/j.quascirev.2008.12.003
- McKean, J., & Roering, J. J. (2004). Objective landslide detection and surface morphology mapping using high-resolution airborne laser altimetry. *Geomorphology*, 57(3-4), 331–351. doi:10.1016/S0169-555X(03)00164-8
- McSweeney, C., New, M., & Lizcano, G. (2009). *UNDP climate change country profile: Kenya*. UNDP. Retrieved from <http://ncsp.undp.org/sites/default/files/Kenya.oxford.report.pdf>
- MENR. (2002). *First national communication of Kenya to the Conference of the Parties of the United Nations Framework Convention on Climate Change*. Nairobi, Kenya: Ministry of Environment and Natural Resources. Retrieved from <http://unfccc.int/resource/docs/natc/kenncl.pdf>
- Mercogliano, P., Segoni, S., Rossi, G., Sikorsky, B., Tofani, V., Schiano, P., ... Casagli, N. (2013). Brief communication 'A prototype forecasting chain for rainfall induced shallow landslides'. *Natural Hazards and Earth System Science*, 13(3), 771–777. doi:10.5194/nhess-13-771-2013

- Metternicht, G., Hurni, L., & Gogu, R. (2005). Remote sensing of landslides: An analysis of the potential contribution to geo-spatial systems for hazard assessment in mountainous environments. *Remote Sensing of Environment*, 98(2-3), 284–303. doi:10.1016/j.rse.2005.08.004
- Meusburger, K., & Alewell, C. (2008). Impacts of anthropogenic and environmental factors on the occurrence of shallow landslides in an alpine catchment (Urseren Valley, Switzerland). *Natural Hazards and Earth System Science*, 8(3), 509–520. doi:10.5194/nhess-8-509-2008
- Mia, B., & Fujimitsu, Y. (2012). Mapping hydrothermal altered mineral deposits using Landsat 7 ETM+ image in and around Kuju volcano, Kyushu, Japan. *Journal of Earth System Science*, 121(4), 1049–1057. doi:10.1007/s12040-012-0211-9
- Miller, A. J. (2013). Remote Sensing Proxies for Deforestation and Soil Degradation in Landslide Mapping: A Review: Remote Sensing Proxies. *Geography Compass*, 7(7), 489–503. doi:10.1111/gec3.12050
- Miller, D. J. (1995). Coupling GIS with physical models to assess deep-seated landslide hazards. *Environmental and Engineering Geoscience*, 1(3), 263–276. doi:10.2113/gseegeosci.1.3.263
- Mitasova, H., Harmon, R. S., Weaver, K. J., Lyons, N. J., & Overton, M. F. (2012). Scientific visualization of landscapes and landforms. *Geomorphology*, 137(1), 122–137. doi:10.1016/j.geomorph.2010.09.033
- Mogaka, H., Gichere, S., Davis, R., & Hirji, R. (2005). *Climate Variability and Water Resources Degradation in Kenya: Improving Water Resources Development and Management*. The World Bank. doi:10.1596/978-0-8213-6517-5
- Moghaddas, H. N., & Ghaforri, M. (2006). The role of weathering in the occurrence of landslides in central Alborz, Iran (Vol. Paper 813). Presented at the IAEG 2006, The Geology Society of London.
- Moine, M., Puissant, A., & Malet, J.-P. (2009). Detection of landslides from aerial and satellite images with a semi-automatic method. Application to the Barcelonnette basin (Alpes-de-Hautes-Provence, France). In *Landslide processes from geomorphologic mapping to dynamic modelling* (pp. 63–68). Strasbourg, France.
- Mondini, A. C., Guzzetti, F., Reichenbach, P., Rossi, M., Cardinali, M., & Ardizzone, F. (2011a). Semi-automatic recognition and mapping of rainfall induced shallow landslides using optical satellite images. *Remote Sensing of Environment*, 115(7), 1743–1757. doi:10.1016/j.rse.2011.03.006
- Mondini, A. C., Chang, K.-T., & Yin, H.-Y. (2011b). Combining multiple change detection indices for mapping landslides triggered by typhoons. *Geomorphology*, 134(3-4), 440–451. doi:10.1016/j.geomorph.2011.07.021
- Montgomery, D. R., & Dietrich, W. E. (1994). A physically based model for the topographic control on shallow landsliding. *Water Resources Research*, 30(4), 1153–1171. doi:10.1029/93WR02979
- Montgomery, D. R., & Dietrich, W. E. (1998). SHALSTAB: A Digital Terrain Model for Mapping Shallow Landslide Potential. University of California and University of Washington: Berkeley, CA.
- Moore, R. D., Fleming, S. W., Menounos, B., Wheate, R., Fountain, A., Stahl, K., ... Jakob, M. (2009). Glacier change in western North America: influences on hydrology, geomorphic hazards and water quality. *Hydrological Processes*, 23(1), 42–61. doi:10.1002/hyp.7162
- Muchui, D. (2015). Two dead in Meru landslide. *Daily Nation Newspaper*. Nairobi, Kenya. Retrieved from <http://www.nation.co.ke/counties/meru/Meru-Kithangene-Quarry-Landslide-Deaths/-/1183302/2676944/-/8yxmjez/-/index.html>
- Mulwa, J. K., Gaciri, S. J., Barongo, J. O., Opiyo, A. N., & Kianji, G. K. (2005). Geological and Structural influence on groundwater distribution and flow in Ngong area, Kenya. *African Journal of Science and Technology*, 6(1), 105–115.

- Murei, B. K. (2013). *Geo-hazard report of Kiriko-ini land crack of Kahuro district, Murang'a county* (Geohazard report No. MG/TECH/1(3)) (pp 12). Nyeri, Kenya: Mines and geology department.
- Muriithi, Z., Ako, E., Kiplagat, J., Maingi, S., & Olang, L. O. (2013). Assessment of Land Cover Changes in Lake Olbolosat Region of the Central Kenyan Highlands using Landsat Satellite Imagery Aided by Indigenous Knowledge. *Journal of Biodiversity Management & Forestry*, 2(2). doi:10.4172/2327-4417.1000107
- Muthengi, A. (2002). 11 feared dead in Kenya landslides. *BBC News*. UK. Retrieved from <http://news.bbc.co.uk/2/hi/africa/1962450.stm>
- Muthoka, J. M., & Mundia, C. N. (2014). Dynamism of Land use Changes on Surface Temperature in Kenya: A Case Study of Nairobi City. *International Journal of Science and Research*, 3(4), 38–41.
- Muthu, K., Petrou, M., Tarantino, C., & Blonda, P. (2008). Landslide possibility mapping using fuzzy approaches. *IEEE Transactions on Geoscience and Remote Sensing*, 46, 1253–1265. doi:10.1109/TGRS.2007.912441
- Mwangi, J. (2009). El Nino rain cause havoc in Kenya. *DEMOTIX News*. Retrieved from <http://www.demotix.com/news/el-nino-rain-cause-havoc-kenya#media-172030>
- Mwangi, J. (2010a). Landslide kills two in Mukurweini, Kenya. *DEMOTIX News*. Retrieved from <http://www.demotix.com/news/327790/landslide-leaves-34-families-homeless-kenya#media-327780>
- Mwangi, J. (2010b). Landslide leaves 34 families homeless in Kenya. *DEMOTIX News*. Retrieved from <http://www.demotix.com/news/327790/landslide-leaves-34-families-homeless-kenya#media-327780>
- Mwaniki, M. W. (2016). Geology mapping and lineament visualization using image enhancement techniques: comparison of Landsat 8 (OLI) and Landsat 7 (ETM+). *Researchgate Resource*.
- Mwaniki, M. W., & Moeller, M. S. (2015). Knowledge based multi-source, time series classification: A case study of central region of Kenya. *Applied Geography*, 60, 58–68. doi:10.1016/j.apgeog.2015.03.005
- Mwaniki, M. W., Ngigi, T. G., & Waithaka, E. H. (2011). Rainfall Induced Landslide Probability Mapping for Central Province. In *Fourth International Summer School and Conference* (Vol. 1, 2011, pp. 203–213). JKUAT, Kenya: Publications of AGSE Karlsruhe, Germany. doi:10.13140/RG.2.1.4509.9046
- Mwaniki, M. W., Agutu, N. O., Mbaka, J. G., Ngigi, T. G., & Waithaka, E. H. (2015a). Landslide scar/soil erodibility mapping using Landsat TM/ETM+ bands 7 and 3 Normalised Difference Index: A case study of central region of Kenya. *Applied Geography*, 64, 108–120. doi:10.1016/j.apgeog.2015.09.009
- Mwaniki, M. W., Matthias, M. S., & Schellmann, G. (2015b). Application of Remote Sensing Technologies to Map the Structural Geology of Central Region of Kenya. *IEEE Journal of Selected Topics in Applied Earth Observations and Remote Sensing*, 8(4), 1855–1867. doi:10.1109/JSTARS.2015.2395094
- Mwaniki, M. W., Moeller, M. S., & Schellmann, G. (2015c). Landslide inventory using knowledge based multisources classification time series mapping: A case study of central region of Kenya. *GI Forum - Journal of Geographic Information Science*, 1, 209–219. doi:10.13140/RG.2.1.1645.4241
- Mwaniki, M. W., Moeller, M. S., & Schellmann, G. (2015d). A comparison of Landsat 8 (OLI) and Landsat 7 (ETM+) in mapping geology and visualising lineaments: A case study of central region Kenya. *ISPRS - International Archives of the Photogrammetry, Remote Sensing and Spatial Information Sciences*, XL-7/W3, 897–903. doi:10.5194/isprsarchives-XL-7-W3-897-2015

- Mwaniki, M. W., Kuria, D. N., Boitt, M. K., & Ngigi, T. G. (2016). Image enhancements of Landsat 8 (OLI) and SAR data for Preliminary Landslide identification and mapping applied to the central region of Kenya. *Geomorphology*.
- Mwanzia, J. K. (2014). *Assessment of groundwater potential in Makueni subcounty, Makueni County, Kenya* (Bachelor thesis, Department of Geology). University of Nairobi.
- Naeslund, J., & Snell, I. (2005). *GIS-mapping of Fluoride Contaminated Groundwater in Nakuru and Baringo district, Kenya* (Masters thesis). Lulea University of Technology, Sweden.
- Namwenya, B. (2014). *Hydrogeological analysis using borehole data within Kitengela area, Kijiado County, Kenya* (Bsc Project). University of Nairobi, Nairobi, Kenya.
- National Environment Secretariat, Clark University, & U.S. Agency, for International Development (1980). *Nyeri District Environmental Assessment Report*. Ministry of Environment and Natural Resources.
- Neaupane, K. M., & Piantanakulchai, M. (2006). Analytic network process model for landslide hazard zonation. *Engineering Geology*, 85(3-4), 281–294. doi:10.1016/j.enggeo.2006.02.003
- Neuhäuser, B., Damm, B., & Terhorst, B. (2012). GIS-based assessment of landslide susceptibility on the base of the Weights-of-Evidence model. *Landslides*, 9(4), 511–528. doi:10.1007/s10346-011-0305-5
- Ngecu, M. W., & Ichang'i, D. W. (1998). The environmental impact of landslides on the population living on the eastern footslopes of the Aberdare ranges in Kenya: a case study of Maringa Village landslide. *Environmental Geology*, 38(3), 259–264. doi:10.1007/s002540050423
- Ngecu, M. W., & Mathu, M. E. (1999). The El-Nino triggered landslides and their socio-economic impacts on Kenya, 22(4), 284–289. doi: 10.1007/s002540050425
- Ngecu, W. M., Nyamai, C. M., & Erima, G. (2004). The extent and significance of mass-movements in Eastern Africa: case studies of some major landslides in Uganda and Kenya. *Environmental Geology*, 46(8), 1123–1133. doi:10.1007/s00254-004-1116-y
- Ngethe, V. (2015). 5 things to know about El Nino and why Nairobi's bad floods is not it yet. *Daily Nation Newspaper*. Nairobi, Kenya. Retrieved from [http://www.nation.co.ke/el\\_nino](http://www.nation.co.ke/el_nino)
- Ngigi, T. G., Tateishi, R., Shalaby, A., Soliman, N., & Ghar, M. (2008). Comparison of a new classifier, the Mix–Unmix Classifier, with conventional hard and soft classifiers. *International Journal of Remote Sensing*, 29(14), 4111–4128. doi:10.1080/01431160701772559
- Nichol, J., & Wong, M.-S. (2005a). Satellite remote sensing for detailed landslide inventories using change detection and image fusion. *International Journal of Remote Sensing*, 26(9), 1913–1926. doi:10.1080/01431160512331314047
- Nichol, J., & Wong, M.-S. (2005b). Detection and interpretation of landslides using satellite images. *Land Degradation & Development*, 16(3), 243–255. doi:10.1002/ldr.648
- Nichol, J. E., Shaker, A., & Wong, M.-S. (2006). Application of high-resolution stereo satellite images to detailed landslide hazard assessment. *Geomorphology*, 76(1-2), 68–75. doi:10.1016/j.geomorph.2005.10.001
- Njagih, J. K. (2005). *Landslide hazard mapping in Murang'a*. ITC, Netherlands.
- Noack, S., Knobloch, A., Eitzold, S. H., Barth, A., & Kallmeier, E. (2014). Spatial predictive mapping using artificial neural networks. *ISPRS - International Archives of the Photogrammetry, Remote Sensing and Spatial Information Sciences*, XL-2, 79–86. doi:10.5194/isprsarchives-XL-2-79-2014
- Norheim, R. A., Queija, V. R., & Haugerud, R. A. (2002). Comparison of LIDAR and INSAR DEMs with dense ground control. In *Proceedings of the Environmental Systems Research Institute*.

- Novak, I. D., & Soulakellis, N. (2000). Identifying geomorphic features using Landsat-5/TM data processing techniques on Lesvos, Greece. *Geomorphology*, 34(1-2), 101–109. doi:10.1016/S0169-555X(00)00003-9
- Nugroho, C. (2008). *Hydrological – Slope Stability Modeling for Landslide Hazard Assessment by means of GIS and Remote Sensing Data* (Msc Thesis). Gadjah University International Institute for Geo-Information and Earth Observation, Indonesia.
- Nyambane, O. S., & Mwea, S. K. (2011). Root tensile strength of 3 typical plant species and their contribution to soil shear strength; a case study: Sasumua backslope, Nyandarua District, Kenya. *Journal of Civil Engineering and Practice*, 8(1), 57–73.
- Nyoungui, A. N., Tonye, E., & Akono, A. (2002). Evaluation of speckle filtering and texture analysis methods for land cover classification from SAR images. *International Journal of Remote Sensing*, 23(9), 1895–1925. doi:10.1080/01431160110036157
- OCHA. (2010). *Kenya: Floods and Landslides: Focus on Nyeri* (Floods No. No. 3). Nairobi, Kenya: UN office for the coordination of Humanitarian Affairs (OCHA).
- Ogallo, S. N., Gaya, C. O., & Omuterema, S. O. (2006). Landslide Hazard Zonation Mapping for Murang'a District, Kenya. In *Proceedings of the 1st International Conference on Disaster Management & Human Security in Africa* (pp. 303– 308). Masinde Muliro University of Science & Technology, Kakamega, Kenya: Center for Disaster Management & Humanitarian Assistance.
- Ogora, M., & Kotut, J. (2013). *Report on Yatta Landslide, Machakos County* (Mines and Geology Department). Nairobi, Kenya: Ministry of Environment and Mineral Resources.
- Oh, H.-J., & Pradhan, B. (2011). Application of a neuro-fuzzy model to landslide-susceptibility mapping for shallow landslides in a tropical hilly area. *Computers & Geosciences*, 37(9), 1264–1276. doi:10.1016/j.cageo.2010.10.012
- Ohlmacher, G. C. (2007). Plan curvature and landslide probability in regions dominated by earth flows and earth slides. *Engineering Geology*, 91(2-4), 117–134. doi:10.1016/j.enggeo.2007.01.005
- Oppikofer, T., Jaboyedoff, M., Blikra, L., Derron, M.-H., & Metzger, R. (2009). Characterization and monitoring of the Åknes rockslide using terrestrial laser scanning. *Natural Hazards and Earth System Science*, 9(3), 1003–1019. doi:10.5194/nhess-9-1003-2009
- Ortenberg, F. (2016). Hyperspectral Sensor Characteristics: Airborne, Hand-Held, and Truck-Mounted; Integration of Hyperspectral Data with LIDAR. In P. S. Thenkabail, J. G. Lyon, & A. Huete (Eds.), *Hyperspectral remote sensing of vegetation* (pp. 39–68). Boca Raton, Fla.: CRC Press. doi:10.1201/b11222
- Otieno, R. (2013). Rapid desertification in Kenya threatening livelihood. *Standard Newspaper*. Nairobi, Kenya. Retrieved from <http://www.standardmedia.co.ke/lifestyle/article /2000086318/rapid-desertification-in-Kenya-threatening-livelihood>
- Owour, P. (2015). *The disaster profile of Kenya* (Emergency and Disaster Reports No. Vol 2, Number 3) (pp. 1–45). University of Oviedo.
- Pachauri, A. K., & Pant, M. (1992). Landslide hazard mapping based on geological attributes. *Engineering Geology*, 32(1-2), 81–100. doi:10.1016/0013-7952(92)90020-Y
- Pack, R. T., Tarboton, D. G., & Goodwin, C. N. (1998). The SINMAP approach to terrain stability mapping. In *Proceedings of the Eighth Congress of the International Association of Engineering Geology*. Vancouver, British Columbia, Canada.
- Pack, R. T., Tarboton, D. G., & Goodwin, C. N. (1999). GIS-based landslide susceptibility mapping with SINMAP. In *Proceedings of the 34th symposium on engineering geology and geotechnical engineering* (pp. 219–231). Utah State University, Logan, UT, United States.

- Pardeshi, S. D. D., Autade, S. E., & Pardeshi, S. S. (2013). Landslide hazard assessment: recent trends and techniques. *SpringerPlus*, 2(1), 523. doi:10.1186/2193-1801-2-523
- Park, S., Choi, C., Kim, B., & Kim, J. (2013). Landslide susceptibility mapping using frequency ratio, analytic hierarchy process, logistic regression, and artificial neural network methods at the Inje area, Korea. *Environmental Earth Sciences*, 68(5), 1443–1464. doi:10.1007/s12665-012-1842-5
- Passalacqua, P., Tarolli, P., & Fofoula-Georgiou, E. (2010). Testing space-scale methodologies for automatic geomorphic feature extraction from lidar in a complex mountainous landscape. *Water Resources Research*, 46(11), 1–17. doi:10.1029/2009WR008812
- Passalacqua, P., Hillier, J., & Tarolli, P. (2014). Innovative analysis and use of high-resolution DTMs for quantitative interrogation of Earth-surface processes. *Earth Surface Processes and Landforms*, 39(10), 1400–1403. doi:10.1002/esp.3616
- Peng, L., Niu, R., Huang, B., Wu, X., Zhao, Y., & Ye, R. (2014). Landslide susceptibility mapping based on rough set theory and support vector machines: A case of the Three Gorges area, China. *Geomorphology*, 204, 287–301. doi:10.1016/j.geomorph.2013.08.013
- Peres, D. J., & Cancelliere, A. (2014). Derivation and evaluation of landslide-triggering thresholds by a Monte Carlo approach. *Hydrology and Earth System Sciences*, 18(12), 4913–4931. doi:10.5194/hess-18-4913-2014
- Perez, F. G., Higgins, C. T., & Real, C. R. (2006). Evaluation of use of remote sensing imagery in refinement of geological mapping for seismic hazard zoning in northern los angeles county, California. In *Proceedings of ISPRS XXXVI Congress* (Vol. XXXVI Part 7).
- Perotto-Baldviezo, H. L., Thurow, T. L., Smith, C. T., Fisher, R. F., & Wu, X. B. (2004). GIS-based spatial analysis and modeling for landslide hazard assessment in steeplands, southern Honduras. *Agriculture, Ecosystems & Environment*, 103(1), 165–176. doi:10.1016/j.agee.2003.10.011
- Pesci, A., Teza, G., Casula, G., Fabris, M., & Bonforte, A. (2013). Remote Sensing and Geodetic Measurements for Volcanic Slope Monitoring: Surface Variations Measured at Northern Flank of La Fossa Cone (Vulcano Island, Italy). *Remote Sensing*, 5(5), 2238–2256. doi:10.3390/rs5052238
- Petley, D. N., Crick, W. D. ., & Hart, A. B. (2002). The use of satellite imagery in landslide studies in high mountain area. In *Proceedings of the 23rd Asian Conference on Remote Sensing* (pp. 2–9). Kathmandu, Nepal.
- Pike, R. J. (1988). The geometric signature: Quantifying landslide-terrain types from digital elevation models. *Mathematical Geology*, 20(5), 491–511. doi:10.1007/BF00890333
- Plaza, A., Benediktsson, J. A., Boardman, J. W., Brazile, J., Bruzzone, L., Camps-Valls, G., ... Trianni, G. (2009). Recent advances in techniques for hyperspectral image processing. *Remote Sensing of Environment*, 113, S110–S122. doi:10.1016/j.rse.2007.07.028
- Pourghasemi, H. R., Pradhan, B., & Gokceoglu, C. (2012). Application of fuzzy logic and analytical hierarchy process (AHP) to landslide susceptibility mapping at Haraz watershed, Iran. *Natural Hazards*, 63(2), 965–996. doi:10.1007/s11069-012-0217-2
- Pradhan, B. (2010). Remote sensing and GIS-based landslide hazard analysis and cross-validation using multivariate logistic regression model on three test areas in Malaysia. *Advances in Space Research*, 45(10), 1244–1256. doi:10.1016/j.asr.2010.01.006
- Pradhan, B., & Buchroithner, M. F. (2010). Comparison and Validation of Landslide Susceptibility Maps Using an Artificial Neural Network Model for Three Test Areas in Malaysia. *Environmental and Engineering Geoscience*, 16(2), 107–126. doi:10.2113/gseegeosci.16.2.107
- Pradhan, B., & Lee, S. (2010a). Delineation of landslide hazard areas on Penang Island, Malaysia, by using frequency ratio, logistic regression, and artificial neural network models. *Environmental Earth Sciences*, 60(5), 1037–1054. doi:10.1007/s12665-009-0245-8

- Pradhan, B., & Lee, S. (2010b). Landslide susceptibility assessment and factor effect analysis: backpropagation artificial neural networks and their comparison with frequency ratio and bivariate logistic regression modelling. *Environmental Modelling & Software*, 25(6), 747–759. doi:10.1016/j.envsoft.2009.10.016
- Pradhan, B., & Lee, S. (2010c). Regional landslide susceptibility analysis using back-propagation neural network model at Cameron Highland, Malaysia. *Landslides*, 7(1), 13–30. doi:10.1007/s10346-009-0183-2
- Pradhan, B., & Saied, P. (2010). Comparison between prediction capabilities of neural network and fuzzy logic techniques for landslide susceptibility mapping. *Disaster Advances*, 3(3), 26–34.
- Pradhan, B., Singh, R. P., & Buchroithner, M. F. (2006). Estimation of stress and its use in evaluation of landslide prone regions using remote sensing data. *Advances in Space Research*, 37(4), 698–709. doi:10.1016/j.asr.2005.03.137
- Prokop, A., & Panholzer, H. (2009). Assessing the capability of terrestrial laser scanning for monitoring slow moving landslides. *Natural Hazards and Earth System Science*, 9(6), 1921–1928. doi:10.5194/nhess-9-1921-2009
- Prost, L. G. (2001). *Remote sensing for geologists: a guide to image interpretation*. [Amsterdam]; New York; Abingdon: Gordon & Breach ; Marston.
- Qari, M. H. T., Madani, A. A., Matsah, M. I. M., & Hamimi, Z. (2008). Utilization of Aster and Landsat data in geologic mapping of basement rocks of Arafat area, Saudi Arabia. *The Arabian Journal for Science and Engineering*, 33(1C), 99–117.
- Qiao, G., Lu, P., Scaioni, M., Xu, S., Tong, X., Feng, T., ... Li, R. (2013). Landslide Investigation with Remote Sensing and Sensor Network: From Susceptibility Mapping and Scaled-down Simulation towards in situ Sensor Network Design. *Remote Sensing*, 5(9), 4319–4346. doi:10.3390/rs5094319
- Ramli, M. F., Yusof, N., Yusoff, M. K., Juahir, H., & Shafri, H. Z. M. (2010). Lineament mapping and its application in landslide hazard assessment: a review. *Bulletin of Engineering Geology and the Environment*, 69(2), 215–233. doi:10.1007/s10064-009-0255-5
- Randall, D. A., Wood, R. A., Bony, S., Colman, R., Fichet, T., & Fyfe, J.; Kattsov, V.; Pitman, A.; Shukla, J.; Srinivasan, J.; Stouffer, R. J.; Sumi, A.; Taylor, K. E. (2007). Climate models and their evaluation. In *Climate Change 2007: The physical science basis. Contribution of Working Group I to the Fourth Assessment Report of the Intergovernmental Panel on Climate Change (IPCC)* (pp. 589–662). Cambridge University Press, Cambridge, U.K.
- Rarieya, M., & Fortun, K. (2009). Food security and seasonal climate information: Kenyan challenges. *Sustainability Science*, 5(1), 99–114. doi:10.1007/s11625-009-0099-8
- Rawashdeh, S. A., Saleh, B., & Hamzah, M. (2006). The use of Remote Sensing Technology in geological Investigation and mineral Detection in El Azraq-Jordan. *Cybergeo : European Journal of Geography*, (358). doi:10.4000/cybergeo.2856
- Ray, R. L., & Jacobs, J. M. (2007). Relationships among remotely sensed soil moisture, precipitation and landslide events. *Natural Hazards*, 43(2), 211–222. doi:10.1007/s11069-006-9095-9
- Razak, K. A. (2014). *Airborne laser scanning for forested landslides: investigation in temperate and tropical environments* (PhD Thesis). University of Twente, ITC, Faculty of Geo-Information Science and Earth Observation, Enschede, The Netherlands.
- Razak, K. A., Straatsma, M. W., van Westen, C. J., Malet, J.-P., & de Jong, S. M. (2011). Airborne laser scanning of forested landslides characterization: Terrain model quality and visualization. *Geomorphology*, 126(1-2), 186–200. doi:10.1016/j.geomorph.2010.11.003

- Regmi, A. D., Yoshida, K., Nagata, H., Pradhan, A. M. S., Pradhan, B., & Pourghasemi, H. R. (2013). The relationship between geology and rock weathering on the rock instability along Mugling–Narayanghat road corridor, Central Nepal Himalaya. *Natural Hazards*, *66*(2), 501–532. doi:10.1007/s11069-012-0497-6
- Reichenbach, P., Cardinali, M., De Vita, P., & Guzzetti, F. (1998). Regional hydrological thresholds for landslides and floods in the Tiber River Basin (central Italy). *Environmental Geology*, *35*(2-3), 146–159. doi:10.1007/s002540050301
- Richard, J. A. (1984). Thematic mapping from multitemporal image data using the principal components transformation. *Remote Sensing of Environment*, *16*, 35–46. doi:10.1016/0034-4257(84)90025-7
- Richards, J. A., & Jia, X. (2006). *Remote sensing digital image analysis* (4th ed.). Berlin, Heidelberg: Springer.
- Righini, G., Pancioli, V., & Casagli, N. (2012). Updating landslide inventory maps using Persistent Scatterer Interferometry (PSI). *International Journal of Remote Sensing*, *33*(7), 2068–2096. doi:10.1080/01431161.2011.605087
- Rigon, R., Bertoldi, G., & Over, T. M. (2006). GEOtop: A Distributed Hydrological Model with Coupled Water and Energy Budgets. *Journal of Hydrometeorology*, *7*(3), 371–388. doi:10.1175/JHM497.1
- Robinson, D. A., & Moses, A. (2011). Rock surface and Weathering: Process and Form. In *The SAGE handbook of geomorphology* (pp. 291–309). Los Angeles; London: SAGE.
- Roering, J. J., Schmidt, K. M., Stock, J. D., Dietrich, W. E., & Montgomery, D. R. (2003). Shallow landsliding, root reinforcement, and the spatial distribution of trees in the Oregon Coast Range. *Canadian Geotechnical Journal*, *40*(2), 237–253. doi:10.1139/t02-113
- Rohrbaugh, N. B. (2015). *A new technique for modelling the geomorphology of a slow moving, soft-slope landslide using terrestrial LiDAR* (Masters thesis). Missouri University of Science and Technology, Department of Geosciences and Geological and Petroleum Engineering.
- Rop, B. K. (2011). Landslide disaster vulnerability in Western Kenya and mitigation options: a synopsis of evidence and issues of Kuvasali landslide. *Journal of Environmental Science Engineering*, *5*(1), 110–115.
- Rosin, P. L., & Hervás, J. (2005). Remote sensing image thresholding methods for determining landslide activity. *International Journal of Remote Sensing*, *26*(6), 1075–1092. doi:10.1080/01431160512331330481
- Rott, H., & Nagler, T. (2006). The contribution of radar interferometry to the assessment of landslide hazards. *Advances in Space Research*, *37*(4), 710–719. doi:10.1016/j.asr.2005.06.059
- Rott, H., Scheuchl, B., Siegel, A., & Grasemann, B. (1999). Monitoring very slow slope movements by means of SAR interferometry: A case study from a mass waste above a reservoir in the Ötztal Alps, Austria. *Geophysical Research Letters*, *26*(11), 1629–1632. doi:10.1029/1999GL900262
- Rowntree, K. M. (1989). Landslides in Kenya: a geographical appraisal. In E. E. Brabb & B. L. Harrod (Eds.), *Proceedings of the International Geological Congress* (Vol. 28, pp. 253–259).
- Royán, M. J., Abellán, A., Jaboyedoff, M., Vilaplana, J. M., & Calvet, J. (2014). Spatio-temporal analysis of rockfall pre-failure deformation using Terrestrial LiDAR. *Landslides*, *11*(4), 697–709. doi:10.1007/s10346-013-0442-0
- Rudd, L. P. (2005). *Using AVIRIS hyperspectral imagery to study the role of clay mineralogy in Colorado Plateau debris flow initiation* (PhD Thesis). University of Arizona.

- Ruiz-Villanueva, V., Bodoque, J. M., Díez-Herrero, A., & Calvo, C. (2011). Triggering threshold precipitation and soil hydrological characteristics of shallow landslides in granitic landscapes. *Geomorphology*, *133*(3-4), 178–189. doi:10.1016/j.geomorph.2011.05.018
- Sabins, F. F. (1997). *Remote Sensing: Principles and Applications* (3rd ed.). New York: W.H. Freeman and Co.
- Sabins, F. F. (1999). Remote sensing for mineral exploration. *Ore Geology Reviews*, *14*(3), 157–183. doi:10.1016/S0169-1368(99)00007-4
- Saboya, F., da Glória Alves, M., & Dias Pinto, W. (2006). Assessment of failure susceptibility of soil slopes using fuzzy logic. *Engineering Geology*, *86*(4), 211–224. doi:10.1016/j.enggeo.2006.05.001
- Saha, A. K., Gupta, R. P., Sarkar, I., Arora, M. K., & Csaplovics, E. (2005). An approach for GIS-based statistical landslide susceptibility zonation- with a case study in the Himalayas. *Landslides*, *2*(1), 61–69. doi:10.1007/s10346-004-0039-8
- Salvucci, G. D., & Entekhabi, D. (1994). Explicit expressions for Green-Ampt (delta function diffusivity) infiltration rate and cumulative storage. *Water Resources Research*, *30*(9), 2661–2663. doi:10.1029/94WR01494
- Santangelo, M., Cardinali, M., Rossi, M., Mondini, A. C., & Guzzetti, F. (2010). Remote landslide mapping using a laser rangefinder binocular and GPS. *Natural Hazards and Earth System Science*, *10*(12), 2539–2546. doi:10.5194/nhess-10-2539-2010
- Sari, D. K., Hermawan, E. T., & Hudman, G. G. (2005). Study on vegetation cover changes in the province of south Kalimantan using RGB-NDVI unsupervised classification method. Presented at the Map Asia 2005, Jakarta, Indonesia.
- Sarkar, S., Kanungo, D. P., & Mehrotra, G. S. (1995). Landslide Hazard Zonation: A Case Study in Garhwal Himalaya, India. *Mountain Research and Development*, *15*(4), 301. doi:10.2307/3673806
- Sassa, K., Tsuchida, S., Ugai, K., Wakai, A., & Uchimura, T. (2009). Landslides: A review of achievements in the first 5 years (2004 - 2009). *Landslides*, *6*, 275–286. doi:10.1007/s10346-009-0172-5
- Savage, W. Z., Godt, J. W., & Baum, R. L. (2003). A model for spatially and temporally distributed shallow landslide initiation by rainfall infiltration. In *Proceedings of the Third International Conference on Debris-Flow Hazards Mitigation: mechanics, Prediction, and Assessment* (pp. 179–187). Davos, Switzerland: Millpress.
- Sawatzky, D. L., Raines, G. L., Bonham-Carter, G. ., & Looney, C. G. (2009). Spatial Data Modeller (SDM): ArcMAP 9.3 Geoprocessing tools for spatial data modelling using weights of evidence, logistic regression, fuzzy logic and neural networks (Version ArcMAP 9.3).
- Scaioni, M. (2013). Remote Sensing for Landslide Investigations: From Research into Practice. *Remote Sensing*, *5*(11), 5488–5492. doi:10.3390/rs5115488
- Scaioni, M., Longoni, L., Melillo, V., & Papini, M. (2014). Remote Sensing for Landslide Investigations: An Overview of Recent Achievements and Perspectives. *Remote Sensing*, *6*(10), 9600–9652. doi:10.3390/rs6109600
- Schlögel, R., Torgoev, I., De Marneffe, C., & Havenith, H.-B. (2011). Evidence of a changing size-frequency distribution of landslides in the Kyrgyz Tien Shan, Central Asia. *Earth Surface Processes and Landforms*, *36*(12), 1658–1669. doi:10.1002/esp.2184
- Schlögel, R., Braun, A., Torgoev, A., Fernandez-Steeger, T. M., & Havenith, H.-B. (2013). Assessment of Landslides Activity in Maily-Say Valley, Kyrgyz Tien Shan. In C. Margottini, P. Canuti, & K. Sassa (Eds.), *Landslide Science and Practice* (pp. 111–117). Berlin, Heidelberg: Springer Berlin Heidelberg. doi:10.1007/978-3-642-31325-7\_14

- Schmidt, J., & Dikau, R. (2004). Modeling historical climate variability and slope stability. *Geomorphology*, 60(3-4), 433–447. doi:10.1016/j.geomorph.2003.11.001
- Schmidt, M., & Dehn, M. (2003). Examining Links Between Climate Change and Landslide Activity Using GCMs. In S. J. McLaren & D. R. Kniveton (Eds.), *Linking Climate Change to Land Surface Change* (Vol. 6, pp. 123–141). Dordrecht: Kluwer Acad. Publishers. doi:10.1007/0-306-48086-7\_7
- Schmidt, K. M., Roering, J. J., Stock, J. D., Dietrich, W. E., Montgomery, D. R., & Schaub, T. (2001). The variability of root cohesion as an influence on shallow landslide susceptibility in the Oregon Coast Range. *Canadian Geotechnical Journal*, 38(5), 995–1024. doi:10.1139/t01-031
- Schowengerdt, R. A. (2007). *Remote sensing: models, and methods for image processing* (3rd ed). Burlington, MA: Academic Press.
- Schuster, R. L. (1996). *Socioeconomic significance of landslides* (Landslides: Investigation and Mitigation, Special Report No. 247) (pp. 12–35). National Academy Press: Washington, DC, USA: National Research Council, Transportation Research Board.
- Schwarz, M., Preti, F., Giadrossich, F., Lehmann, P., & Or, D. (2010). Quantifying the role of vegetation in slope stability: A case study in Tuscany (Italy). *Ecological Engineering*, 36(3), 285–291. doi:10.1016/j.ecoleng.2009.06.014
- Sezer, E. A., Pradhan, B., & Gokceoglu, C. (2011). Manifestation of an adaptive neuro-fuzzy model on landslide susceptibility mapping: Klang valley, Malaysia. *Expert Systems with Applications*, 38(7), 8208–8219. doi:10.1016/j.eswa.2010.12.167
- Shapiro, L. G., & Stockman. (2000). Filtering and Enhancing Images. In *Computer Vision* (Vol. Chapter 5). Washington, DC.
- Shield, R. T. (1955). On Coulomb's law of failure in soils. *Journal of the Mechanics and Physics of Solids*, 4(1), 10–16. doi:10.1016/0022-5096(55)90043-0
- Shih, F. Y. (2010). *Image processing and pattern recognition fundamentals and techniques*. Piscataway, NJ; Hoboken, N.J.: IEEE Press ; Wiley.
- Shi, J., Du, Y., Du, J., Jiang, L., Chai, L., Mao, K., ... Wang, Y. (2012). Progresses on microwave remote sensing of land surface parameters. *Science China Earth Sciences*, 55(7), 1052–1078. doi:10.1007/s11430-012-4444-x
- Sidle, R. C. (1992). A theoretical model of the effects of timber harvesting on slope stability. *Water Resources Research*, 28(7), 1897–1910. doi:10.1029/92WR00804
- Sidle, R. C. (2007). Using Weather and Climate Information for Landslide Prevention and Mitigation. In M. V. K. Sivakumar & N. Ndiang'ui (Eds.), *Climate and Land Degradation* (Vol. Chapter 15, pp. 285–307). Berlin, Heidelberg: Springer. doi:10.1007/978-3-540-72438-4\_15
- Sidle, R. C., & Ochiai, H. (2006). *Landslides: Processes, Prediction, and Land Use*. Washington, DC: American Geophysical Union. doi:10.1029/WM018
- Sidle, R. C., Ghestem, M., & Stokes, A. (2014). Epic landslide erosion from mountain roads in Yunnan, China – challenges for sustainable development. *Natural Hazards and Earth System Science*, 14(11), 3093–3104. doi:10.5194/nhess-14-3093-2014
- Simoni, S., Zanotti, F., Bertoldi, G., & Rigon, R. (2008). Modelling the probability of occurrence of shallow landslides and channelized debris flows using GEOTop-FS. *Hydrological Processes*, 22(4), 532–545. doi:10.1002/hyp.6886
- Sims, D. A., & Gamon, J. A. (2002). Relationships between leaf pigment content and spectral reflectance across a wide range of species, leaf structures and developmental stages. *Remote Sensing of Environment*, 81(2-3), 337–354. doi:10.1016/S0034-4257(02)00010-X

- Singhal, B. B. S., & Gupta, R. P. (2010). Fractures and Discontinuities. In *Applied Hydrogeology of Fractured Rocks* (pp. 13–33). Dordrecht: Springer Netherlands. doi:10.1007/978-90-481-8799-7
- Singh, P., Gupta, A., & Singh, M. (2014). Hydrological inferences from watershed analysis for water resource management using remote sensing and GIS techniques. *The Egyptian Journal of Remote Sensing and Space Science*, 17(2), 111–121. doi:10.1016/j.ejrs.2014.09.003
- Singhroy, V. (2013). Operational Applications of Radar Images. In J. N. Pelton, S. Madry, & S. Camacho-Lara (Eds.), *Handbook of Satellite Applications* (pp. 739–756). New York, NY: Springer New York. doi:10.1007/978-1-4419-7671-0\_43
- Singhroy, V., & Molch, K. (2004). Characterizing and monitoring rockslides from SAR techniques. *Advances in Space Research*, 33(3), 290–295. doi:10.1016/S0273-1177(03)00470-8
- Smailbegovic, A., Mendenhall, M., Clark, J., Gray, K., & Wooten, R. (2011). Hyperspectral image and signal processing: Evolution in remote sensing. In *Proceedings of the 3rd Workshop, WHISPERS*. Lisbon, Portugal.
- Smith, J. B., Schneider, S. H., Oppenheimer, M., Yohe, G. W., Hare, W., Mastrandrea, M. D., ... van Ypersele, J.-P. (2009). From the Cover: Assessing dangerous climate change through an update of the Intergovernmental Panel on Climate Change (IPCC) ‘reasons for concern’. *Proceedings of the National Academy of Sciences*, 106(11), 4133–4137. doi:10.1073/pnas.0812355106
- Soeters, R., & Van Westen, C. J. (1996). Slope instability recognition, analysis and zonation. In *Landslide: investigations and mitigation. Special Report 247* (Turner AK, Schuster RL (eds), Vol. Chapter 8, pp. 129–177). Washington, D.C.: National Academy Press.
- Squarzoni, C., Delacourt, C., & Allemand, P. (2003). Nine years of spatial and temporal evolution of the La Valette landslide observed by SAR interferometry. *Engineering Geology*, 68(1-2), 53–66. doi:10.1016/S0013-7952(02)00198-9
- Stehman, S. V., & Foody, G. M. (2009). Accuracy Assessment. In *The Sage handbook of remote sensing* (pp. 297–310). Thousand Oaks, CA: Sage.
- Sterzai, P., Vellico, M., Berti, M., Coren, F., Corsini, A., Rosi, A., ... Zambonelli, F. (2010). Innovative integrated airborne and wireless systems for landslide monitoring. In *Proceedings of the International Symposium GeoInformation for Disaster Management (GI4DM)*. Torino, Italy.
- Stokes, A., Norris, J. E., van Beek, L. P. H., Bogaard, T., Cammeraat, E., Mickovski, S. B., ... Fourcaud, T. (2008). How Vegetation Reinforces Soil on Slopes. In J. E. Norris, A. Stokes, S. B. Mickovski, E. Cammeraat, R. van Beek, B. C. Nicoll, & A. Achim (Eds.), *Slope Stability and Erosion Control: Ecotechnological Solutions* (pp. 65–118). Dordrecht: Springer Netherlands. doi:10.1007/978-1-4020-6676-4\_4
- Strahler, A. N. (1952). Dynamic basis of geomorphology. *Geological Society of America Bulletin*, 63(9), 923–938. doi:10.1130/0016-7606(1952)63[923:DBOG]2.0.CO;2
- Strozzi, T., Ambrosi, C., & Raetzo, H. (2013). Interpretation of Aerial Photographs and Satellite SAR Interferometry for the Inventory of Landslides. *Remote Sensing*, 5(5), 2554–2570. doi:10.3390/rs5052554
- Stumpf, A., & Kerle, N. (2011). Object-oriented mapping of landslides using Random Forests. *Remote Sensing of Environment*, 115(10), 2564–2577. doi:10.1016/j.rse.2011.05.013
- Stumpf, A., Lampert, T. A., Malet, J.-P., & Kerle, N. (2012). Multi-scale line detection for landslide fissure mapping (pp. 5450–5453). IEEE. doi:10.1109/IGARSS.2012.6352373
- Subasi, A., & Gursoy, I. M. (2010). EEG signal classification using PCA, ICA, LDA and support vector machines. *Expert Systems with Applications*, 37(12), 8659–8666. doi:10.1016/j.eswa.2010.06.065

- Tae Hee Lee, & Moon, W. M. (2002). Lineament extraction from Landsat TM, JERS-1 SAR, and DEM for geological applications (Vol. 6, pp. 3276–3278). IEEE. doi:10.1109/IGARSS.2002.1027154
- Takara, K., Yamashiki, Y., Sassa, K., Ibrahim, A. B., & Fukuoka, H. (2010). A distributed hydrological–geotechnical model using satellite-derived rainfall estimates for shallow landslide prediction system at a catchment scale. *Landslides*, 7(3), 237–258. doi:10.1007/s10346-010-0214-z
- Tantianuparp, P., Shi, X., Zhang, L., Balz, T., & Liao, M. (2013). Characterization of Landslide Deformations in Three Gorges Area Using Multiple InSAR Data Stacks. *Remote Sensing*, 5(6), 2704–2719. doi:10.3390/rs5062704
- Tarantino, C., Blonda, P., & Pasquariello, G. (2007). Remote sensed data for automatic detection of land-use changes due to human activity in support to landslide studies. *Natural Hazards*, 41(1), 245–267. doi:10.1007/s11069-006-9041-x
- Tarolli, P. (2014). High-resolution topography for understanding Earth surface processes: Opportunities and challenges. *Geomorphology*, 216, 295–312. doi:10.1016/j.geomorph.2014.03.008
- Tarolli, P., & Tarboton, D. G. (2006). A new method for determination of most likely landslide initiation points and the evaluation of digital terrain model scale in terrain stability mapping. *Hydrology and Earth System Sciences*, 10, 633–677. doi: 10.5194/hess-10-663-2006
- Tarolli, P., Borga, M., & Fontana, G. D. (2008). Analysing the influence of upslope bedrock outcrops on shallow landsliding. *Geomorphology*, 93(3-4), 186–200. doi:10.1016/j.geomorph.2007.02.017
- Tarolli, P., Sofia, G., & Dalla Fontana, G. (2012). Geomorphic features extraction from high-resolution topography: landslide crowns and bank erosion. *Natural Hazards*, 61(1), 65–83. doi:10.1007/s11069-010-9695-2
- Teng, S. P., Chen, Y. K., Cheng, K. S., & Lo, H. C. (2008). Hypothesis-test-based landcover change detection using multi-temporal satellite images – A comparative study. *Advances in Space Research*, 41(11), 1744–1754. doi:10.1016/j.asr.2007.06.064
- Terlien, M. T. J. J. (1998). The determination of statistical and deterministic hydrological landslide-triggering thresholds. *Environmental Geology*, 35(2-3), 124–130. doi:10.1007/s002540050299
- Terlien, M. T. J., van Asch, T. W. J., & Van Westen, C. J. (1995). Deterministic modelling in GIS-based landslide hazard assessment. In *Geographical Information systems in Assessing Natural Hazards* (A. Carrara and F. Guzzetti, pp. 57–77). Kluwer Academic Publishers.
- Teza, G., Galgaro, A., Zaltron, N., & Genevois, R. (2007). Terrestrial laser scanner to detect landslide displacement fields: a new approach. *International Journal of Remote Sensing*, 28(16), 3425–3446. doi:10.1080/01431160601024234
- Tien Bui, D., Pradhan, B., Lofman, O., Revhaug, I., & Dick, O. B. (2012). Landslide susceptibility mapping at Hoa Binh province (Vietnam) using an adaptive neuro-fuzzy inference system and GIS. *Computers & Geosciences*, 45, 199–211. doi:10.1016/j.cageo.2011.10.031
- Tiwari, B., & Cepeda, J. (2014). Introduction: Rain Induced Landslides. In K. Sassa, P. Canuti, & Y. Yin (Eds.), *Landslide Science for a Safer Geoenvironment* (pp. 271–271). Cham: Springer International Publishing. doi:10.1007/978-3-319-04996-0\_41
- Tofani, V., Dapporto, S., Vannocci, P., & Casagli, N. (2006). Infiltration, seepage and slope instability mechanisms during the 20-21 November 2000 rainstorm in Tuscany, central Italy. *Natural Hazards and Earth System Science*, 6(6), 1025–1033. doi:10.5194/nhess-6-1025-2006
- Tofani, V., Raspini, F., Catani, F., & Casagli, N. (2013). Persistent Scatterer Interferometry (PSI) Technique for Landslide Characterization and Monitoring. *Remote Sensing*, 5(3), 1045–1065. doi:10.3390/rs5031045
- Travelletti, J., Delacourt, C., Allemand, P., Malet, J.-P., Schnittbuhl, J., Toussaint, R., & Bastard, M. (2012). Correlation of multi-temporal ground-based optical images for landslide monitoring:

- Application, potential and limitations. *ISPRS Journal of Photogrammetry & Remote Sensing*, 70, 39–55. doi: 10.1016/j.isprsjprs.2012.03.007
- Tsai, T.-L. (2007). The influence of rainstorm pattern on shallow landslide. *Environmental Geology*, 53(7), 1563–1569. doi:10.1007/s00254-007-0767-x
- Tsai, F., Hwang, J.-H., Chen, L.-C., & Lin, T.-H. (2010). Post-disaster assessment of landslides in southern Taiwan after 2009 Typhoon Morakot using remote sensing and spatial analysis. *Natural Hazards and Earth System Science*, 10(10), 2179–2190. doi:10.5194/nhess-10-2179-2010
- Turner, A. K., & Schuster, R. L. (1996). *Landslides: investigation and mitigation*. Washington, DC: National Academy Press.
- UNDP, E. S. U. (2010). *Kenya Natural Disaster Profile*. United Nations Development Programme. Retrieved from <http://www.gripweb.org/gripweb/sites/default/files/KenyaDisasterProfile.pdf>
- UNECA. (2013). *An Assessment of Agricultural Sector Policies and Climate Change in Kenya: Nexus between Climate Change Related Policies, Research and Practice*. United Nations Economic Commission for Africa.
- Vahidnia, M. H., Alesheikh, A. A., Alimohammadi, A., & Hosseinali, F. (2010). A GIS-based neuro-fuzzy procedure for integrating knowledge and data in landslide susceptibility mapping. *Computers & Geosciences*, 36(9), 1101–1114. doi:10.1016/j.cageo.2010.04.004
- Van Beek, L. P. H. (2002). *Assessment of the influence of changes in land use and climate on landslide activity in a Mediterranean environment* (PhD Thesis). University of Utrecht.
- Van Den Eeckhaut, M., Poesen, J., Verstraeten, G., Vanacker, V., Nyssen, J., Moeyersons, J., ... Vandekerckhove, L. (2007). Use of LIDAR-derived images for mapping old landslides under forest. *Earth Surface Processes and Landforms*, 32(5), 754–769. doi:10.1002/esp.1417
- Van Den Eeckhaut, M., Reichenbach, P., Guzzetti, F., Rossi, M., & Poesen, J. (2009). Combined landslide inventory and susceptibility assessment based on different mapping units: an example from the Flemish Ardennes, Belgium. *Natural Hazards and Earth System Science*, 9(2), 507–521. doi:10.5194/nhess-9-507-2009
- van der Kamp, G., & Schmidt, R. (1997). Monitoring of total soil moisture on a scale of hectares using groundwater piezometers. *Geophysical Research Letters*, 24(6), 719–722. doi:10.1029/97GL00521
- van der Meer, F. D., van der Werff, H. M. A., van Ruitenbeek, F. J. A., Hecker, C. A., Bakker, W. H., Noomen, M. F., ... Woldai, T. (2012). Multi- and hyperspectral geologic remote sensing: A review. *International Journal of Applied Earth Observation and Geoinformation*, 14(1), 112–128. doi:10.1016/j.jag.2011.08.002
- van Westen, C. J., Rengers, N., & Soeters, R. (2003). Use of Geomorphological Information in Indirect Landslide Susceptibility Assessment. *Natural Hazards*, 30(3), 399–419. doi:10.1023/B:NHAZ.0000007097.42735.9e
- Van Westen, C. J., Van Asch, T. W. J., & Soeters, R. (2006). Landslide hazard and risk zonation—why is it still so difficult? *Bulletin of Engineering Geology and the Environment*, 65(2), 167–184. doi:10.1007/s10064-005-0023-0
- van Westen, C. J., Castellanos, E., & Kuriakose, S. L. (2008). Spatial data for landslide susceptibility, hazard, and vulnerability assessment: An overview. *Engineering Geology*, 102(3-4), 112–131. doi:10.1016/j.enggeo.2008.03.010
- Varnes, D. J. (1978). *Slope movement types and processes* (Transportation Research Board Special Report No. 176) (pp. 11–33). Washington, D.C.

- Vennari, C., Gariano, S. L., Antronico, L., Brunetti, M. T., Iovine, G., Peruccacci, S., ... Guzzetti, F. (2014). Rainfall thresholds for shallow landslide occurrence in Calabria, southern Italy. *Natural Hazards and Earth System Science*, 14(2), 317–330. doi:10.5194/nhess-14-317-2014
- Vieira, B. C., Fernandes, N. F., & Filho, O. A. (2010). Shallow landslide prediction in the Serra do Mar, São Paulo, Brazil. *Natural Hazards and Earth System Science*, 10(9), 1829–1837. doi:10.5194/nhess-10-1829-2010
- Villarini, G., Mandapaka, P. V., Krajewski, W. F., & Moore, R. J. (2008). Rainfall and sampling uncertainties: A rain gauge perspective. *Journal of Geophysical Research*, 113(D11). doi:10.1029/2007JD009214
- Vohora, V. K., & Donoghue, S. L. (2004). Application of remote Sensing data to Landslide mapping in Hong Kong. *International Archives of Photogrammetry, Remote Sensing & GIS*, V(XXXV-B4), 489–494.
- Voigt, S., Kemper, T., Riedlinger, T., Kiefl, R., Scholte, K., & Mehl, H. (2007). Satellite Image Analysis for Disaster and Crisis-Management Support. *IEEE Transactions on Geoscience and Remote Sensing*, 45(6), 1520–1528. doi:10.1109/TGRS.2007.895830
- Vorovencii, I. (2007). Use of the ‘Tasseled Cap’ Transformation for the Interpretation of Satellite Images. *Cadastrre Journal RevCAD*, 75–82.
- Vrieling, A. (2006). Satellite remote sensing for water erosion assessment: A review. *CATENA*, 65(1), 2–18. doi:10.1016/j.catena.2005.10.005
- Wahlstrand, A. (2015). *Landslide scars in the Kenyan highlands* (PhD Thesis). Stockholm University, Institute for Natural Earth Sciences.
- Walker, L. R., & Shiels, A. B. (2013). *Landslide ecology* (1. publ). Cambridge: Cambridge Univ. Press.
- Wamwangi, E. (2010). *Geology and Hydrogeology Report* (No. 201004-EIA-004). Nairobi, Kenya: NEMA.
- Wandago, B. (2002). *Reality and perspectives Kenya Country paper* (Tropical secondary forest management in Africa No. J0628E54). Nairobi, Kenya: Forest Department. Retrieved from FAO corporate document repository.
- Wang, W., Xie, C., & Du, X. (2009). Landslides susceptibility mapping in Guizhou province based on fuzzy theory. *Mining Science and Technology (China)*, 19(3), 399–404. doi:10.1016/S1674-5264(09)60075-2
- Wanyama, C. B. (2009). *Hydrogeological Survey Report for Our Lady of Assumption Catholic Mission, Kampi ya Juu, Isiolo*. Nairobi, Kenya: Adebwi Geoconsult.
- Warner, T. A., Nellis, M. D., & Foody, G. M. (2009). *The Sage handbook of remote sensing*. Thousand Oaks, CA: Sage.
- Wasowski, J., & Bovenga, F. (2014). Investigating landslides and unstable slopes with satellite Multi Temporal Interferometry: Current issues and future perspectives. *Engineering Geology*, 174, 103–138. doi:10.1016/j.enggeo.2014.03.003
- Weirich, F., & Blesius, L. (2007). Comparison of satellite and air photo based landslide susceptibility maps. *Geomorphology*, 87(4), 352–364. doi:10.1016/j.geomorph.2006.10.003
- Wendo, B. (2002). Mudslides in Kenya. *Daily Nation Newspaper*. Nairobi, Kenya. Retrieved from <http://news.bbc.co.uk/2/hi/africa/1976946.stm>
- Were, K. O., Dick, Ø. B., & Singh, B. R. (2013). Remotely sensing the spatial and temporal land cover changes in Eastern Mau forest reserve and Lake Nakuru drainage basin, Kenya. *Applied Geography*, 41, 75–86. doi:10.1016/j.apgeog.2013.03.017

- Westerberg, L.-O. (1989). *Rainfall characteristics, soil properties, land-use and landslide erosion in the Kanyenyaini area, Nyandarua Range, Kenya* (Msc Thesis, Department of Physical Geography). Stockholm University.
- Westerberg, L.-O. (1993). *Slope movements in the Kenyan highlands -three case studies in Murang'a District, Central Province, Kenya* (SUAS Working Papers) (p. 123). Uppsala: Swedish University of Agriculture Sciences.
- Westerberg, L.-O., & Christiansson, C. (1999). Highlands in East Africa: Unstable Slopes, Unstable Environments? *Ambio*, 28(5), 419–429.
- Whitworth, M. C. Z., Giles, D. P., & Murphy, W. (2005). Airborne remote sensing for landslide hazard assessment: a case study on the Jurassic escarpment slopes of Worcestershire, UK. *Quarterly Journal of Engineering Geology and Hydrogeology*, 38(3), 285–300. doi:10.1144/1470-9236/04-057
- Wieczorek, G. F., Mandrone, G., & DeCola, L. (1997). The influence of hillslope shape on debris-flow initiation. In *Debris-flow hazards mitigation: mechanics, prediction, and assessment* (pp. 21–31). New York: American Society of Civil Engineers.
- Wilkinson, P. L., Brooks, S. M., & Anderson, M. G. (1998). Investigating the effect of moisture extraction by vegetation upon slope stability: further developments of a combined hydrology and stability model (CHASM). In *Proceedings of the British hydrological society international symposium on hydrology in a changing environment* (Vol. 4, pp. 165–178).
- Wilkinson, P. L., Anderson, M. G., & Lloyd, D. M. (2002). An integrated hydrological model for rain-induced landslide prediction. *Earth Surface Processes and Landforms*, 27(12), 1285–1297. doi:10.1002/esp.409
- Wilson, R. C. (2005). The rise and fall of a debris-flow warning system for the San Francisco Bay region, California. In *Landslide Hazard and Risk* (Glade T., Anderson M., Crozier M.J., pp. 493–516). UK: Wiley, Chichester.
- Wondzell, S. M., & King, J. G. (2003). Postfire erosional processes in the Pacific Northwest and Rocky Mountain regions. *Forest Ecology and Management*, 178(1-2), 75–87. doi:10.1016/S0378-1127(03)00054-9
- WRMA, G. (2013). *Annual water resources situation Report 2012 - 2013*. Water Resources Management Authority.
- Wu, W., & Sidle, R. C. (1995). A Distributed Slope Stability Model for Steep Forested Basins. *Water Resources Research*, 31(8), 2097–2110. doi:10.1029/95WR01136
- Yalcin, A. (2008). GIS-based landslide susceptibility mapping using analytical hierarchy process and bivariate statistics in Ardesen (Turkey): Comparisons of results and confirmations. *CATENA*, 72(1), 1–12. doi:10.1016/j.catena.2007.01.003
- Yalcin, A., Reis, S., Aydinoglu, A. C., & Yomralioglu, T. (2011). A GIS-based comparative study of frequency ratio, analytical hierarchy process, bivariate statistics and logistics regression methods for landslide susceptibility mapping in Trabzon, NE Turkey. *CATENA*, 85(3), 274–287. doi:10.1016/j.catena.2011.01.014
- Yang, X., & Chen, L. (2010). Using multi-temporal remote sensor imagery to detect earthquake-triggered landslides. *International Journal of Applied Earth Observation and Geoinformation*, 12(6), 487–495. doi:10.1016/j.jag.2010.05.006
- Yilmaz, I. (2009). Landslide susceptibility mapping using frequency ratio, logistic regression, artificial neural networks and their comparison: A case study from Kat landslides (Tokat—Turkey). *Computers & Geosciences*, 35(6), 1125–1138. doi:10.1016/j.cageo.2008.08.007

- Yilmaz, I. (2010). The effect of the sampling strategies on the landslide susceptibility mapping by conditional probability and artificial neural networks. *Environmental Earth Sciences*, 60(3), 505–519. doi:10.1007/s12665-009-0191-5
- Yonezawa, C., Watanabe, M., & Saito, G. (2012). Polarimetric Decomposition Analysis of ALOS PALSAR Observation Data before and after a Landslide Event. *Remote Sensing*, 4(12), 2314–2328. doi:10.3390/rs4082314
- Younis, S. M. Z., & Iqbal, J. (2015). Estimation of soil moisture using multispectral and FTIR techniques. *The Egyptian Journal of Remote Sensing and Space Science*, 18(2), 151–161. doi:10.1016/j.ejrs.2015.10.001
- Zêzere, J. L., de Brum Ferreira, A., & Rodrigues, M. L. (1999). The role of conditioning and triggering factors in the occurrence of landslides: a case study in the area north of Lisbon (Portugal). *Geomorphology*, 30(1-2), 133–146. doi:10.1016/S0169-555X(99)00050-1
- Zhang, C., Chen, Y., & Lu, D. (2015). Mapping the land-cover distribution in arid and semiarid urban landscapes with Landsat Thematic Mapper imagery. *International Journal of Remote Sensing*, 36(17), 4483–4500. doi:10.1080/01431161.2015.1084552
- Zhao, C., Lu, Z., Zhang, Q., & de la Fuente, J. (2012a). Large-area landslide detection and monitoring with ALOS/PALSAR imagery data over Northern California and Southern Oregon, USA. *Remote Sensing of Environment*, 124, 348–359. doi:10.1016/j.rse.2012.05.025
- Zhao, J., Liu, C., Tingting, L., & Lijun, D. (2012b). Identification of landslide spatial distribution and their types along the Riviere Frose Drainage Basin triggered by earthquake in Haiti on 12 January 2010. *Disaster Advances*, 5(1), 5–13.
- Zhu, L., & Huang, J. (2006). GIS-based logistic regression method for landslide susceptibility mapping in regional scale. *Journal of Zhejiang University SCIENCE A*, 7(12), 2007–2017. doi:10.1631/jzus.2006.A2007
- Zielke, O., & Strecker, M. R. (2009). Recurrence of Large Earthquakes in Magmatic Continental Rifts: Insights from a Paleoseismic Study along the Laikipia-Marmanet Fault, Subukia Valley, Kenya Rift. *Bulletin of the Seismological Society of America*, 99(1), 61–70. doi:10.1785/0120080015
- Zinck, J. A., López, J., Metternicht, G. I., Shrestha, D. P., & Vázquez-Selem, L. (2001). Mapping and modelling mass movements and gullies in mountainous areas using remote sensing and GIS techniques. *International Journal of Applied Earth Observation and Geoinformation*, 3(1), 43–53. doi:10.1016/S0303-2434(01)85020-0
- Zoebisch, M. A., & Johansson, A. (2002). Erosion Scars Caused by Earth Flows-A Case Study from Central Kenya. In *12th ISCO Conference* (pp. 429–437). Beijing.
- Zumsprekel, H., & Prinz, T. (2000). Computer-enhanced multispectral remote sensing data: a useful tool for the geological mapping of Archean terrains in (semi)arid environments. *Computers & Geosciences*, 26(1), 87–100. doi:10.1016/S0098-3004(99)00042-4

## Appendices

### Appendix A: Borehole Data

Data sources: Alamirew et al. (2007), JICA (1997), Kithome (2012), Mwanzia (2014), Naeslund and Snell (2005), Namwenya (2014), Wamwangi (2010), Wanyama (2009), and WRMA (2013).

Locality	Longitude	Latitude	BH*	Elev.	Depth	RL_WRL <sup>†</sup>	WRL <sup>&amp;</sup>
				Units in metres			
Grahams farm_Naro	37.04469	-0.16288	C286	2022	121.92	1957.99	64.01
Poolman Farm Nyk	37.09802	-0.01204	C1704	2022	109.73	1953.4	68.58
Fowler Farm_Nyk	37.13353	0.06483	C290	1992	127.71	1954.51	37.49
Paice Farm Burguret	37.0759	-0.07353	C291	2049	108.51	2025.23	23.77
Paice Farm Burguret	36.99156	-0.03692	C2638	1858	69.19	1844.3	13.72
Allens Farm Burguret	37.01553	-0.07905	C1619	1882	159.11	1858.5	23.47
Kianyaga police post	37.35367	-0.5005	C2030	1494	189.89	1403.17	90.83
JKUAT BH3	37.0147	-1.08742		1519	162.88	1466.7	52.3
JKUAT BH5	37.01512	-1.09346		1524	182.88	1469.8	54.2
Juja Farm BH1	37.06406	-1.14226		1483	198.2	1381.8	101.2
Juja Farm BH2	37.12013	-1.18147		1467	0	1368.5	98.5
Murera East	36.96852	-1.11316		1539	131.1	1459.8	79.2
Murera Kimbo/Gsu BH	36.9905	-1.15989		1500	150	1416	84
	36.78436	-1.41668	C11044	1700	253	1566	134
	36.78575	-1.29752	C13881	1720	250	1580	140
	36.75213	-1.25918	C10770	1820	240	1698	122
	36.77935	-1.26141	C13958	1760	155	1734	26
	36.78824	-1.26418	C12821	1720	250	1603	117
	36.79297	-1.26557	C13169	1720	250	1638	82
	36.79881	-1.26557	C14412	1720	268	1573	147
	36.80658	-1.26529	C14354	1700	250	1564	136
	36.80603	-1.25863	C12117	1720	201	1587	133
Muslim world league	36.79575	-1.25946	C14054	1720	235	1577	143

	36.79158	-1.25557	C14260	1760	230	1629	131
	36.79158	-1.25334	C10522	1720	240	1699.8	20.2
	36.79408	-1.25223	C12866	1720	250	1600	120
	36.80075	-1.25002	C12997	1720	215	1560	160
	36.81103	-1.27224	C13756	1800	240	1675	125
	36.8038	-1.25418	C13541	1705	232	1642.6	62.4
Njiru	36.99168	-1.2639	C13217	1518	130	1455	63
Kiserian	36.77778	-1.47834	C13448	1722	262	1685	37
Kitengela	36.84777	-1.39721	C12569	1611	156	1564	47
Emakoko	36.83332	-1.41946	C14220	1640	152	1579	61
Kitengela	36.95778	-1.51832	C14593	1622	122	1585	37
Kitengela	36.91943	-1.52445	C14567	1630	150	1571	59
Kitengela	36.94306	-1.56778	C14933	1616	150	1578	18
	36.93444	-1.56861	C12430	1600	179	1577	23
	36.92917	-1.55278	C12479	1600	100	1574	26
	36.75445	-1.48889	C14147	1740	146.96	1713.5	26.5
	36.80139	-1.55917	C11320	1720	120	1673.6	46.4
	36.82083	-1.56278	C11710	1695	124	1659	36
	36.81306	-1.55945	C11705	1700	168.2	1665	35
Kiserian	36.81944	-1.56889	C13213	1690	120	1638.8	51.2
Kisaju	36.91389	-1.61	C11151	1630	150	1576.2	53.8
Olooitikoshi	36.08063	-1.56528	C13062	1460	180	1363.1	96.9
Kitengela	36.93642	-1.3924	C11808	1620	100	1581	39
Edonyo Sidai pri sch	36.67616	-1.65248		1884	250	1836	48
Esilanke	36.67591	-1.66784		1947	160	1877	66
Mr. Christian	36.70124	-1.70946		1977	220	1903	74
Aga Khan Hosp	36.82326	-1.26034	C5050	1678	171	1657	21
CBK	36.82501	-1.29005	C10734	1620	220	1566	54
Utalii College	36.8541	-1.25369	C10072	1600	218	1503.6	96.4
Twiga chemicals	36.86478	-1.30665	C10301	1685	204	1575	110
Farmers choice	36.90954	-1.1861	C10857	1570	139	1539.5	30.5
Consolata sisters	36.80246	-1.26762	C10053	1720	252	1585	135
Kenya re_Insurance plaza	36.8246	-1.28716	C9771	1660	200	1537	123

\*BH: Borehole,

<sup>†</sup>RL\_WRL: Reduced Level Water Rest Level,

<sup>&</sup>WRL: Water Rest Level

Shah Suresh	36.8235	-1.28053	C14221	1730	250	1670	60
Polish embassy	36.80315	-1.23496	C9764	1760	181	1673.6	86.4
Nairobi Hilton	36.82496	-1.28514	C9765	1660	200	1538	122
Embassy of Japan	36.81506	-1.29701	C10431	1723	250	1695	28
UNICEF	36.81534	-1.23233	C10696	1790	315	1677	113
St. Francis sisters	36.91615	-1.22582	C9733	1600	120	1524	76
Mater hospital	36.8343	-1.30694	C10122	1662	170	1575	87
St. Lawrence University	36.71015	-1.31244	C13069	1873	320	1753.2	119.8
KICC	36.82275	-1.28834	C13594	1666	250	1532.7	133.3
Kenya Polytechnic	36.8238	-1.29225	C12885	1669	200	1582.7	86.3
Kabansora millers	36.90705	-1.3189	C14559	1627	200	1524.2	102.8
KEWI South C	36.82406	-1.31438	C6310	1661	169	1584	77
Trufoods	36.85469	-1.29608	C8697	1643	164	1539.3	103.7
State House	36.8018	-1.28289	C4790	1736	200	1590	146
Uchumi Hyper	36.7909	-1.30056	C11592	1760	250	1609.09	150.91
Unilever	36.83135	-1.29624	C4147	1662	258	1583	79
Hurlingham	36.79888	-1.2959	C10333	1744	250	1592	152
Sarit centre	36.80218	-1.26122	C11590	1715	220	1589	126
Hindu Temple	36.83358	-1.26891	C12357	1663	204	1503	160
Hotel Boulevard	36.81313	-1.27503	C13860	1670	255	1557.7	112.3
Hill Crest Karen	36.79672	-1.26179	C10883	1724	300	1600.9	123.1
Riverside Park	36.80436	-1.27088	C14539	1697	280	1548	149
Arboretum view apart	36.80145	-1.27371	C11329	1696	217	1571	125
Shretta Y.A.	36.82411	-1.28456	C10076	1650	180	1541	109
Getrudes Garden C. Shop	36.88932	-1.3299	C9006	1640	181	1528	112
Bristol Apartments	36.89459	-1.31324	C16044	1615	240	1412	203
Kenya High School	36.84113	-1.3451	C13981	1651	292	1524	127
Sankara Hotel	36.80201	-1.26271		1714	290	1566.3	147.7
1339/ACB/WRMA	36.78294	-1.26659		1728	273	1555	173
Parklands_Plaza	36.81014	-1.26972		1694	250	1557.1	136.9
Kabete NCC	36.75638	-1.26123	C168	1828	17.3	1802	11
Riverside Park	36.80596	-1.26997	C14539	1690	280	1550.1	139.9
Jorgen L Karen	36.70613	-1.31167	C15129	1880	170	1795.6	84.4

Karen Country Club	36.71575	-1.33813	C3958	1857	142.6	1740.5	116.5
Anthony Ngotho	36.79107	-1.29357	C10333	1740	192.2	1591.3	148.7
George Kinyua	36.92972	-1.34823	C15222	1618	200	1521.91	96.09
Faulu Pamoja & patners	36.94836	-1.34691		1613	175	1517	96
All Pack industries	36.93469	-1.38214	C10291	1617	154	1510	107
	36.99661	-1.4738	C2303	1528	140	1509	19
	36.99526	-1.47086	C2301	1530	127	1506	24
Youth for Christ	37.02852	-1.44851	C11719	1543	101	1523	20
BAT	36.99618	-1.44867	C4001	1504	200	1470.3	33.7
Athi river steel	36.99932	-1.44939	C13717	1505	175	1458.7	46.3
New borehole	37.00247	-1.44849		1525	160	1461.8	63.2
New BH_superior homes	37.01351	-1.45475		1517	110	1490.6	26.4
Kamiti Prison BH	36.91413	-1.17333		1554	177	1467.5	86.5
kwihota sec BH	36.99448	-1.1699		1501	190	1415.4	85.6
Dandora	36.88	-1.24		1582	245	1467	115
Kahawa sukari	36.93	-1.19		1542	162	1464.5	77.5
Ruiru	36.93	-1.13		1494	162	1363	131
L. Kabete	36.76	-1.24		1790	262	1663	127
Ruaraka	36.86	-1.23		1619	233	1505	114
Roysambu	36.87	-1.21		1615	200	1528.5	86.5
Mbagathi ridge	36.70788	-1.35033		1874	310	1757.7	116.3
Kenol Makuyu	37.12098	-0.93807		1532	200	1433.3	98.7
Karen	36.63	-1.27		2031	181	1919	112
Subukia	36.1667	-0.0333		2088	184	2044	44
Naivasha	35.4567	-0.5083		2314	175	2175.9	138.1
Nakuru	36.0833	-0.1333		1795	166	1772	23
Elementatita	36.1333	-0.4667		1797	35	1757	40
Njoro Canning	35.9417	-0.3667		2213	30	2125	88
Naivasha	36.4417	-0.7725		1939	52	1879	60
Olongai	36.0083	-0.1333		1796	46	1757	39
Kerma_Njoro	36.9719	-0.3167		1862	95	1770	92
Lanet	36.1303	-0.3056		1875	115	1766	109
	36.95711	-2.32502	C1534	1298	63	1277	21

	36.95927	-2.30061	C9444	1305	110	1248.7	56.3
	36.86132	-2.27877	C3532	1398	121.93	1352.92	45.08
	36.85049	-2.30858	C3474	1386	58.2	1358	28
	36.86891	-2.31223	C3835	1371	108.5	1345.8	25.2
	36.84196	-2.30315	C3741	1398	107.9	1367.5	30.5
	36.91116	-2.31591	C9374	1327	150	1278.29	48.71
	36.70789	-1.37182	C4938	1827	116	1783	44
	36.67111	-1.32659	C9725	1872	172	1860	12
	36.7429	-1.39988	C11361	1756	177	1617.9	138.1
	36.68251	-1.38536	C4186	1888	101	1855	23
	36.66477	-1.38376	C11131	1996	75	1836	60
	36.70656	-1.35374	C8069	1857	85	1808	39
	36.65623	-1.38398	C6979	2030	167	1938	92
	36.73823	-1.34676	C5563	1820	148	1711	109
	36.58888	0.9344	C7921	2040	100	2014	26
Wamagana	36.925	-0.47306	D087/C336	1909	130	1877	27
Joytown Sch BH_Thika	37.0851	-1.05026	C8716	1486	70.4	1469.8	16.2
King'Atua BH_Kijabe	36.60745	-1.15438	C3921	2152	61	2136.15	15.85
Kagunduini	37.05	-0.9	C3471	1545	143	1506	35
Kagunduini	37.03	-0.87	C3640	1577	124	1545	26
Makuyu Police Stn	37.19222	-0.90309	C118	1396	181	1332	64
Maragua Muslim Mosq	37.13249	-0.78707	C1154	1351	87	1316	12
Aikan	37.00877	-0.1456		1946	72.07	1892.75	53.25
Lolalick b/h3	37.03644	-0.06518		1895	32.3	1863.95	31.05
Limuru DO's Offic	36.63955	-1.10977	C4899	2256	112.4	2182.06	73.94
Eastern flour mills	37.25857	-1.50236	C13745	1635	41.14	1613.79	21.21
Machakos sch. for Hand.	37.2613	-1.51658	C1478	1601	18.1	1591.32	4.68
Bishop Kioko Hosp.	37.26497	-1.51656	C13549	1614	27.18	1604.5	3.5
Alphega sisal estate	35.95284	0.05274	C8466	1532	82	1464	68
Ravine Roses	35.75464	0.05604	C8258	1993	53	1944.5	48.5
Subati	36.18447	0.03781	C2303	1954	36	1918	22
Kabatini	36.1347	-0.26279	C7384	1898	74.04	1858.71	39.29
St. Mary's	36.09182	-0.28252	C1805	1852	89.8	1795.12	56.88

Baharini	36.12477	-0.30545		1828	64.35	1786.2	41.8
Naivasha MW&I	36.42183	-0.69607	C4397	1896	39.2	1859	37
Marula	36.3806	-0.6555		1898	18.9	1882.83	15.17
Panda flower farm	36.45883	-0.65347	C13355	2188	66.6	2146.4	41.6
Kinyanjui/Naivasha	36.43043	-0.71475	C9679	1890	19.6	1873.1	16.9
Mayflower/Naivasha	36.39584	-0.80958	C13283	1892	39.9	1881.2	10.8
Ushirika	36.49348	0.74473	C13623	1908	124.51	1894.4	13.6
Rubiri	36.4405	0.80258	C13090	1866	97.96	1863.1	2.9
Ayub suleiman	35.88525	1.09542	C5504	1125	86	1043	82
M.O.W.D.	35.87847	1.07281	C6807	1085	63.52	1059.7	25.3
Katakala	35.76914	1.08981	C3299	1146	55	1095.1	50.9
Kodich BH	35.06451	1.6536		1279	129.9	1244.7	34.3
Konyao BH	35.08341	1.8212		1225	98	1182.2	32.8
Kacheliba Hospital	35.00991	1.49137		1312	60.26	1256.1	55.9
Cherombai pri sch	35.19119	1.29908		1775	34.22	1770.8	4.2
St Cecilia girls	35.19688	1.29722	C11674	1767	9.3	1762.7	4.3
kacheliba mixed	35.00804	1.4798	C4634	1282	16.76	1278.72	3.28
Chepkopegh BH	35.23539	1.45831		1323	21.05	1317.42	5.58
cheptianga comm bh	35.2457	1.41715		1488	34.85	1482.87	5.13
BCFC	35.07877	1.25451		1545	20.08	1530.9	14.1
Ngoswani comm.bh	35.59418	-1.41298		2037	36	2001.99	35.01
Rift Valley academy	36.59963	-0.94535		1938	102.2	1867.99	70.01
Sirinyo BH/marigat	35.97559	0.48515	P120	1065	30	1022	13
Magurin	36.05186	0.08451	P138	1557	112	1447	110
Magurin	36.02	0.1	C285	1536	111	1434	102
Magurin	36.03	0.08	C2484	1525	122	1412	113
Ngubereti	35.9	0.05	P148	1601	95	1522	79
Legetewet	36.00941	0.16751	C478	1431	123	1353	78
Legetewet	35.89798	0.03453	C1406	1631	143	1544	87
Eldama	35.75249	0.04119	C626	1890	152	1769	121
Eldama_Toniok Pekkerra	35.76527	0.0764	C708	1954	177	1841	113
Eldama	35.71542	0.05084	C722	2134	140	2084	50
Nandi	35.75	0.2	C711	1646	141	1599	47

Eldama	35.71432	0.08099	C3433	2134	128	2101	33
Totonjo	35.58367	0.12843	C2124	2606	134	2551	55
Chereta	36.39037	0.29812		2034	20.43	2013.59	9.41
Familia Takatifu	36.53929	0.26803		1845	68.6	1810.84	34.16
	36.53929	-0.26803		2998.5	81.4	2967.16	20.84
Namanga Girls Sec. Sch	36.82623	-2.52619		1299	15.5	1297.71	1.29
PCEA Kibwezi	37.96813	-2.41387		898	80.5	892.95	5.05
Makindu D. Hospital	37.82507	-2.28344		1004	20.96	989.33	14.67
Tawa D. Hospital	37.46647	-1.5484		1302	20.61	1280.35	9.65
Nzueni	37.61782	-1.83786		1178	60.93	1130.05	47.95
	37.61669	-1.83318	C1885	1173	134	1108	65
	37.69999	-1.88318	C398	1108	145	1092	16
	37.71668	-1.89988	C414	1102	135	1055	47
	37.59998	-1.76659	C437	1220	123	1205	15
	37.59998	-1.76659	C446	1128	123	1110	18
	37.73329	-1.78319	C454	1000	84	984	16
Mwaani BH	37.66669	-1.76659	C461	1047	124	999	48
	37.71668	-1.89988	C482	1067	135	1020	47
	37.58329	-1.78319	C488	1170	123	1145	13
	37.64998	-1.96657	C518	1009	132	948	65
	37.66668	-1.78319	C1578	1100	79	1079	21
Makueni Boys BH_unoa	37.65803	-1.84804	C1945	1144	125	1083	61
	37.74999	-1.79989	C1856	987	68	969	18
	37.66669	-1.89988	C1886	1126	136	1071	55
	37.54998	-1.76659	C2451	1189	78	1147	6
	37.53329	-1.81658	C2454	1219	110	1205	14
Kathonzeni BH	37.73328	-1.91658	C3977	1080	152	1039	41
	37.64998	-1.76659	C4009	1096	134	1067	29
	37.64251	-1.76788	C4016	1098	92	1076	3
	37.53328	-1.94988	C4275	1040	80	998	42
Kyamusoi BH	37.66911	-1.79209		1074	83	1050.5	23.5
Kaiti BH	37.93333	-1.76667		980	75	937.5	42.5
Mitinyani	37.94207	-1.25979		1221	37.3	1194.42	26.58

Kiambani	37.79972	-1.95011		1042	59	1024.58	7.42
Tabor Hill 2	36.38412	-0.00576		2380	42.85	2344.71	35.29
karimenu_new city	36.75489	-0.22571		2039	46.48	2014.8	24.2
Matabathi	37.03424	0.0371		1875	29.28	1847.3	27.7
Kikuyu Water & Sew. Co.	36.6614	-1.24136		2061	116.3	1969.3	91.7
Kiambu Water & Sew. Co.	36.83168	-1.17119		1705	117	1608.76	96.24
KMC	36.99154	-1.44714	C4053	1521	143.3	1496.3	24.7
Devki steel	36.99074	-1.44534	C12473	1512	106.6	1456.9	55.1
Athi Leather Works	36.99864	-1.45318	C4734	1521	110	1506.5	4.5
Bawazir Tanneries	36.99208	-1.43927	C10533	1495	152	1427	68
Bawazir Tanneries	36.98659	-1.44152	C10724	1496	106	1438	58
Namanga water users trust	36.78785	-1.84594	C4247	1729	0	1682.5	16.5
Olooitikoshi	36.79283	-1.55038	C13737	1701	87	1668.25	32.75
Kisaju	36.87199	-1.64327	C14177	1633	115	1610.26	22.74
Nkama	36.42	-1.87		829	87	776.25	32.75
Naserian BH_Olturoto	36.90927	-1.61261		1621	115	1598.26	22.74
	37.597	0.3383	C7924	1132	184	1114	18
	37.3375	0.3515	C9385	1486	102	1450	26
Boji1 Borehole	38.34175	0.56757		620	0	617.45	2.55
Boji2 Borehole	38.33849	0.57365	C9640	607	0	601.77	5.23
Kulamawe 1 Borehole	38.21082	0.57436	C16523	694	110	667.7	26.3
Kula Mawe	38.19786	0.57061	C9641	741	0	701.35	39.65
Yamicha Borehole	38.60992	1.73085	C4699	314	0	284	30
Urura Borehole	38.77897	1.54561	C4643	289	0	216	73
Kone Gurbato	39.1225	1.08528		294	140	226.1	67.9
Sericho water supply	39.09694	1.17111		234	22.95	222.35	11.65
Gambela new BH	37.6843	0.40613	C12284	1029	60	1009	20
Manyatta	37.66411	0.52957	C9575	935	18	917.27	7
Eskot_Waliyana BH	38.49767	0.12762	C10786	359	30	338.95	10.05
Bissan Biliqo	38.47618	0.87158	C16525	330	56	314.42	15.58
Malkagala	38.48479	0.86369	C16524	348	161	304	44
Badana	38.99778	1.18694		243	60	213.57	29.43

Badana 2	38.97546	1.10994		219	66	202.66	16.34
Eraso Boru	38.86667	1.15972		257	80	237	20
Sareti water supply	38.77111	1.17556		269	150	162.2	106.8
Oldonyiro	36.98361	0.60767		1553	140	1548	5
Burat 2	37.50503	0.33951		1191	102	1179	12
Game community BH	37.56175	0.36778		1074.3	139.9	1038.905	35.36
Ngaremara Childrens home	37.64072	0.51891		937	213.5	884.9	52.1
D.C. Isiolo	37.58975	0.34767		1128.1	83.52	1065.654	62.48
Mlango 1 BH	37.44115	0.45509		1086	190	946	140
Mlango 2 BH	37.44121	0.45512		1078	150	1018	60
Rapsu comm. BH	38.24224	0.25869		613	74	593.11	19.89
Qone	38.85304	1.06132		240	48	225.5	14.5
Belegesh community	38.72915	0.83457		328	83.2	304	24
Dadache Lafe BH	38.8957	1.36487		254	200.5	151	103
Malkadaka Old BH	38.20957	0.929	C4475	572	0	567.7	4.3
Allango BH	39.09554	1.41651		242	0	159.48	82.52
Isiolo	37.32617	0.3579	RTC	1801	70	1762	25
Isiolo	37.33126	0.35391	C10557	1733	40	1718	8
Isiolo	37.31315	0.31594	C10558	1943	101	1911.6	31.4
Isiolo	37.30762	0.3046	C10574	1924	104	1908.3	15.7
Isiolo	37.30122	0.302	C10575	1938	79.8	1924.6	13.4
Isiolo	37.3049	0.30779	C10576	2000	102	1978.1	21.9
Isiolo	37.34584	0.34427	C11339	1235	91	1187	25
Isiolo	37.33486	0.34923	C11340	1542	45	1497	15
	37.03638	0.0034		1895	18.8	1877.5	17.5
Isiolo district hosp	37.58586	0.35467	C15703	1107	80	1063	44
Kiwanjani pri sch	37.58665	0.35126		1128	80	1098	30
Ramdhan sch	37.60314	0.3628		1083	51.1	1071	12
Daaba comm	37.73888	0.58259	C7632	908	50	885	13
Lairangi BH	37.31562	0.27481		1937	77	1907	30
IWASCO	37.5613	0.33272		1128	0	1102.1	25.9
Gadisa lodge	37.60319	0.36078		1086	70	1059.1	26.9
Tana BH (ENNDA)	38.39641	0.68756		537	138.2	501.8	35.2

Ashnil Camp BH	37.58603	0.58597			845	0	820.27	24.73
Ngare Ndare BH	37.43481	0.36616			1174	72	1144	30
Longopito BH	37.12427	0.69926			1163.5	0	1136.96	26.5
Arimawoi BH	37.68959	0.46132			980	0	940	29.8
Pepo la Tumaini	37.5733	0.34141			1130	120	1088	42
Galbatura High sch	38.52497	0.53618			505	0	489.84	15.16
Borana Ranch	37.30535	0.24332			1925	0	1891	15
Kamwaki	37.0816	0.02391			1927	30.245	1901.8	25.2
Kamura	36.60333	-0.76667			2564.9	45.415	2526.792	38.1
Thika Muslim College	37.11374	-1.05797	C1196		1477	139	1439	38
Githunguri	36.83389	-1.0396	C3359		1768	153	1722	46
Riftvalley	36.525	-0.96333	P42		1844	165.506	1756.53	87.51
Ngendalel	36.12147	0.07125	P84		1533	62	1490.13	42.87
Riftvalley	36.53333	-0.865	P97		2499.4	123.139	2377.44	121.92
	36.60417	-0.77083	P69		2575.6	122.834	2491.74	83.82
	36.55583	-0.78083	P80		2621.3	129.54	2533.498	87.78
Poll Hill BH	36.65479	-0.70459	C100		2590.8	148.438	2499.36	88.39
Kijabe	36.55417	-0.89583	C549		2438.4	158.801	2289.76	148.64
Riftvalley	36.54167	-0.86	C1550		2682.2	246.888	2461.38	220.86
Kinangop	36.55	-0.86833	C1551		2682.2	137.16	2577.69	104.55
Kajiado Dam	36.82338	-2.01531	C138		1575	73.152	1559.82	5.18
Kajiado No. 1	36.81017	-1.95242	C155		1595	55.778	1566.226	23.77
Ngorika	36.9124	-2.02966	C998		1603	137.16	1573.434	29.57
Mile 34. Kajiado rd	36.87864	-1.63616	C1368		1626	182.88	1601.616	24.38
Mile 37. Kajiado rd	36.84974	-1.67253	C1387		1618	54.864	1610.99	7.01
Kajiado No.2	36.73873	-1.80347	C1427		1697	137.465	1662.92	24.08
Sajaloni	36.84552	-1.83991	C1539		1708	114.3	1692.15	15.85
Okiloriti/Esukuta /lidamat	36.72813	-1.85835	C587		1736	91.75	1706.226	23.77
Gachanja BH	36.79342	-2.10367	C1569		1565	61.57	1544.34	3.66
Kajiado No.3	36.64972	-2.0497	C2587		1478	182.88	1455.14	22.86
Lorngosua BH	36.61496	-2.16315			1564	160	1457.2	106.8
Uswa BH_Torosei	36.40285	-2.21276			1155	146	1046.5	98.5
Oloperelongo	37.1363	-1.86247			1564	91.44	1515.9	38.1

Olbili BH_Imbirikani	37.6231	-2.54635		1149	70.96	1102.2	46.8
Holy Ghost mis. Mangu	36.97858	-0.98879	C1685	1615.4	125.578	1566.672	48.77
Kangema Police post	36.97193	-0.68748	C1985	1779	153.314	1719.82	59.18
Kigumo Poli post	36.83321	-1.03286	C2008	1783.1	215.494	1766.93	16.15
Ichaki_Maragwa	37.08516	-0.80859	C1158	1429	55	1401	12
Kambiti_Maragwa	37.22811	-0.82842	C1344	1195	53	1152	3
Kahumbu_Maragwa	37.0807	-0.85564	C4110	1487	124	1466	9
Kakuzi	37.27	-1.03	C2013	1408	63	1381	27
Mwangu sec sch	36.8445	-0.86487	C1976	1965	218	1884	81
TD Jakes	36.59318	-0.99497	C2820	1829	301	1553	276
Gatuikira Kiambaa	36.64548	-0.91325	C1601	2631	183	2597	14
Kiamumbi Kiambaa	36.65711	-0.81946	C1616	2542	162	2509	33
Kitibanga	37.17046	-0.94624	C2171	1459	64	1429	30
Kitibanga	37.149	-0.945	C1633	1486	54	1456	30
Majikaboko	37.21972	-0.93349	C494	1417	27	1406	11
Makindi	37.1	-0.97	C2418	1512	104	1477	35
Koorali	37.02	-1.08	C2530	1494	121	1431	63
Kabati	37.09583	-0.92983	C3049	1527	87	1508	12
Kabati	37.1	-0.95	C144	1520	53	1473	38
Gitura	37.13951	-0.92178	C3199	1479	137	1440	39
Gitura	37.11485	-0.91818	C1273	1477	188	1445	17
Githabai prm_Kamuea	36.59865	-0.74937	C3662	2565	153	2553	12
Kamuea	36.63589	-0.75044	C3663	2521	46	2517	4
Kamahuha	37.1704	-0.83668	C2154	1320	172	1290	30
Kahuhia BH	37.05397	-0.71585	C3293	1539	76	1501.4	28.6
Kangema	36.96915	-0.67887	C2392	1710	182.9	1678	32
Kangema	36.88429	-0.65567	C1985	1766	153.3	1735.6	30.4
Sabasaba	37.14667	-0.8524	C4051	1345	140.8	1300.7	24.3
Ithanga	37.34242	-0.90872	C4976	1293	103	1251	8
Wango Estate	37.07051	-0.97967	C1254	1500	194	1474	26
Laikipia	36.71667	0.21667	P125	1861	66	1846	15
Laikipia	37.12986	0.21298	P126	2098	84	2055	43
Laikipia	36.78333	0.36667	P137	1761	76	1734	27

Laikipia	36.80445	0.25348	P141	1789	67	1775	14
Laikipia	36.46667	0.13333	P145	2075	34	2067	8
Laikipia	36.96667	0.06667	P152	1796	70	1753	43
Laikipia	36.78333	0.4	P155	1720	98	1664	56
Laikipia	36.96667	0.03333	P158	1802	76	1755	47
Laikipia	37.05	0.03333	P163	1874	34	1859	15
Laikipia	37.01667	0	P164	1859	87	1813	46
Laikipia	37	-0.01667	P167	1837	64	1794	43
Laikipia	36.81667	0.2	P171	1816	121	1752	64
Laikipia	36.81667	0.41667	P172	1708	81	1664	44
Laikipia	36.85	0.38333	P175	1696	66	1664	32
Laikipia	36.46667	0.31667	C37	1919	158	1873	46
Laikipia	36.5	0.4	C38	1911	186	1888	23
Laikipia	36.65	0.2	C39	1900	69	1844	56
Laikipia	36.63333	0.21667	C40	1891	152	1834	57
Laikipia	36.73333	0.06667	C42	1908	85	1874	34
Laikipia	36.51667	0.11667	C47	2038	85	2020	18
Laikipia	36.48333	0.11667	C65	2089	119	2013	76
Laikipia	36.51667	0.18333	C101	1937	112	1882	55
Laikipia	37.15	0.15	C139	1962	53	1933	29
Laikipia	37.06667	0	C149	1930	122	1875	55
Bomana ranch	37.28333	0.21667	C150	1985	0	1958	27
Laikipia	37.2322	0.23257	C153	1990	107	1942.2	47.8
Laikipia	37.3	0.26667	C154	1938	42.6	1919.2	18.8
Laikipia	37.2667	0.25	C158	1941	60	1915.9	25.1
Laikipia	37.2	0.23333	C159	1922	74	1896	26
Laikipia	37.2	0.21667	C160	2000	67	1977	23
Laikipia	37.08333	0.16667	C187	1873	70	1848.2	24.8
Laikipia	37.1258	0.28811	C193	1822	85	1788	34
Laikipia	37.11879	0.25978	C195	1860	73	1829	31
Laikipia	37.16667	0.2	C207	1929	110	1902	27
Laikipia	37.2253	0.23949	C221	2002	122	1950	52
Laikipia	37.15	0.31667	C228	1787	95	1753	34

Laikipia	37.2	0.15	C233	2063	91	2036	27
Laikipia	36.66667	-0.01667	C237	2062	107	2053	9
Laikipia	37.26667	0.13333	C241	2220	122	2174	21
Laikipia	36.7	-0.01667	C244	2021	131	2014	7
Laikipia	36.71667	-0.03333	C283	2002	58	1979	23
Laikipia	37.16667	0.23333	C289	1880	76	1848	32
Laikipia	36.75	0.1	C296	1863	66	1845	18
Laikipia	36.71667	0.2	C297	1858	308	1808	50
Laikipia	36.81667	0	C308/C309	1906	134	1889	17
Laikipia	36.7	0.3	C337	1833	236	1769	64
Laikipia	36.56667	0.43333	C342	1893	111	1802	37
Laikipia	37.05	0.28333	C346	1855	36	1848	7
Laikipia	37.11667	0.38333	C371	1731	35	1719	12
Laikipia	37.08333	0.38333	C372	1731	33	1715	16
Laikipia	36.98333	0.08333	C373	1811	59	1761	50
Laikipia	36.68333	0.01667	C382	1970	152	1904	66
Laikipia	36.91667	0	C395	1762	61	1730	32
Laikipia	36.83333	0	C396	1873	19	1856	7
Laikipia	36.86667	0.11667	C453	1749	26	1736	13
Laikipia	36.96667	0	C490	1804	38	1774	30
Laikipia	36.96667	-0.2	C508	1933	92	1891	42
Laikipia	36.75	0.11667	C515	1857	105	1823	34
Laikipia	36.75	-0.11667	C522	2062	46	2037	25
Laikipia	37.11667	0.03333	C523	1970	79	1930	40
Laikipia	37.01667	0.05	C527	1853	105	1803	50
Laikipia	36.96667	0.1	C539	1784	48	1744	40
Laikipia	36.81667	0.15	C555	1787	76	1771	16
Larangai Timau	37.31667	0.28333	C571	1919	78	1870	49
Arigshu	37.25667	0.25667	C596	1949	76	1923	6
Laikipia	37.3	0.23322	C599	2033	56	1988	15
Laikipia	37.3	0.25	C600	1945	20	1936.7	8.3
Mamar Ranch	36.68333	0.75	C611	1800	71.62	1782	18
Laikipia	37.16667	0.13333	C674	1988	69	1959	29

Laikipia	36.96667	0.11667	C690	1782	40	1750	32
Laikipia	37.08333	0.06667	C694	1865	108	1813	52
Laikipia	36.96667	0.15	C715	1765	63	1724	41
Laikipia	36.96667	0.13333	C718	1787	132	1737	50
Laikipia	36.98333	-0.21667	C859	1924	76	1869	55
Laikipia	36.78333	0.11667	C876	1843	177	1824	19
Muhonia BH	36.78353	-0.10384	C884	2061	85	2002	59
Laikipia	36.88333	-0.18333	C887	1911	126	1862	49
Laikipia	36.36667	0.4	C913	1990	244	1944	46
Laikipia	37.0167	0.0578	C922	1831	110	1783	48
Laikipia	36.71667	0.03333	C932	1960	183	1915	45
Laikipia	36.83333	0.08333	C954	1815	102	1766	49
Laikipia	36.85	0.15	C957	1776	156	1774	2
Laikipia	36.63333	0.11667	C1008	1902	203	1862	40
Laikipia	36.88333	-0.08333	C1015	1851	140	1793	49
Ol Morani House_Turi	36.46667	0.55	C1018	1990	251	1874.8	115.2
Laikipia	36.95	-0.21667	C1124	1938	104	1856	82
Laikipia	36.91667	-0.25	C1140	1916	122	1860	52
Laikipia	36.63333	0.08333	C1143	1925	208	1877	48
Laikipia	36.86667	-0.2	C1164	1927	92	1890	37
Laikipia	36.85	-0.21667	C1168	2008	126	1924	84
Laikipia	36.28333	-0.3	C1217	2438	111	2340	98
Laikipia	36.33333	0.2	C1230	2272	122	2223	49
Luoniec	36.5	0.75	C1237	1960	138.68	1862.47	97.53
Laikipia	37.33333	0.21667	C1262	1909	122	1858	11
Laikipia	36.5	0.13333	C1381	2074	213	2044	30
Luoniec	36.51667	0.71667	C1397	1970	259.08	1847.17	122.83
Luoniec	36.53333	0.75	C1473	1950	134.1	1904.28	45.72
Laikipia	37.08333	0.25	C1498	1851	92	1802	49
Laikipia	36.86667	-0.06667	C1562	1852	121	1802	50
Laikipia	37	-0.05	C1563	1858	154	1791	67
Laikipia	36.76667	0.76667	C1565	1811	137	1747	64
Laikipia	36.83333	0.83333	C1600	1749	84	1714	35

Laikipia	37.1	0.1	C1679	1879	66	1826	53
Laikipia	36.33333	0.33333	C1684	2153	123	2112	35
Laikipia	36.79965	0.25564	C1697	1802	65	1793	9
Laikipia	36.60164	0.30318	C1698	1806	76	1790	6
Laikipia	36.75	0.25	C1700	1817	183	1763	54
Laikipia	36.81809	0.25663	C1702	1788	61	1721	67
Laikipia	36.83333	0.2	C1703	1796	172	1737	59
Laikipia	36.63	0.3	C1705	1820	62	1781	39
Laikipia	36.75	0.06667	C1706	1905	161	1823	82
Laikipia	36.71667	0.55	C1752	1882	119	1836	46
Laikipia	36.63333	0.15	C1767	1894	127	1870	24
Luoniec	36.55	0.71667	C1785	1950	178.91	1881.42	68.58
Laikipia	36.76667	0.1	C1791	1873	176	1844	29
Laikipia	36.63333	0.2	C1792	1903	101	1847	56
Laikipia	37.16667	0.4	C1813	1822	53	1803	19
Laikipia	36.61667	0.45	C1819	1913	180	1837	76
Laikipia	36.56667	0.51667	C1832	1911	250	1880	31
Luoniec	36.45	0.76667	C1833	1850	182.9	1740.28	109.72
Laikipia	36.68333	0.5	C1845	1859	177	1809	50
Lariak	36.5	0.6	C1882	1985	263.65	1891.12	93.88
Laikipia	36.8	0.8	C1884	1801	183	1716	85
Laikipia	36.41667	0.46667	C1895	1992	239	1929	63
Mamar Ranch	36.71667	0.76667	C1896	1800	103.63	1775.62	24.38
Laikipia	36.36667	0.23333	C1899	2232	135	2193	39
Ngare Ndare	37.31667	0.25	C1918	1901	168	1846	55
Laikipia	36.58333	0.35	C1921	1836	220	1808	28
Githunguchu BH	36.41702	0.02533	C1953	2344	78	2319	25
Laikipia	36.71667	0.36667	C1957	1799	137	1749	50
Laikipia	36.28333	0.38333	C1977	1932	165	1853	79
Ngare Ndare	37.27447	0.24894	C1980	1967	106.7	1910.3	56.7
Laikipia	36.71667	-0.01667	C1984	2014	70	2002	12
Laikipia	36.76667	0.03333	C2003	1935	183	1882	53
Laikipia	37.06667	0.25	C2014	1811	70	1777	34

Laikipia	36.65	-0.06667	C2023	2165	55	2122	43
Laikipia	36.68333	-0.06667	C2036	2086	61	2067	19
Laikipia	37.08333	0.35	C2135	1753	71	1727	26
Laikipia	36.78333	0.6	C2142	1792	247	1666	126
Laikipia	36.28333	0.43333	C2144	2101	244	2057	44
Laikipia	37.01667	0.36667	C2188	1759	153	1716	43
Laikipia	36.26667	0.05	C2218	2465	213	2408	35
Laikipia	36.9	0	C2249	1803	212	1750	43
Laikipia	36.38417	0.21639	C2258	2084	68	2058	26
Laikipia	36.8	0.61667	C2259	1738	110	1665	73
Laikipia	37	0.05	C2277	1821	148	1736	85
Laikipia	36.6	0.51667	C2280	1910	110	1861	49
Laikipia	36.39272	0.21962	C2285	2070	165	2027	53
Timau	37.25	0.11667	C2314	2273	92	2246	27
Laikipia	37.08333	0.08333	C2315	1883	71	1851	32
Laikipia	37.11667	0.11667	C2316	1878	46	1864	14
Banyi Bun_Laikipia	36.51667	0.51667	C2318	1870	152.4	1809.04	60.96
Laikipia	36.18333	-0.18333	C2328	2225	113	2158	67
	36.23333	-0.23333	C2345	2402	114.3	2328.85	73.15
Laikipia	36.06667	-0.06667	C2349	1659	107	1642	17
Laikipia	36.66667	0.66667	C2354	1858	158	1797	61
Laikipia	36.83333	0.01667	C2363	1854	164	1787	67
Laikipia	36.1	-0.1	C2369	1795	157	1742	53
Laikipia	36.95	0.15	C2375	1771	128	1710	61
Laikipia	36.13333	0.13333	C2381	1543	160	1519	24
Laikipia	36.65	0.65	C2400	1874	155	1824	50
Laikipia	36.03333	0.03333	C2414	1645	317	1573	72
Laikipia	36.75	0.75	C2463	1810	107	1764	46
Laikipia	36.01667	-0.01667	C2479	1559	142	1536	23
Laikipia	36.75	0.01667	C2506	1988	244	1899	89
Laikipia	36.8	0.03333	C2509	1884	119	1867	17
Laikipia	36.76667	0.16667	C2561	1823	92	1786	37
Laikipia	36.8	0.18333	C2562	1815	213	1753	62

Laikipia	36.45	0.4	C2574	1933	279	1860	73
Laikipia	37.03333	0.03333	C2576	1864	146	1824	40
Laikipia	36.83333	0.11667	C2594	1801	84	1760	41
Laikipia	36.75	0.03333	C2595	1923	172	1879	44
Laikipia	37.2	0.16667	C2597	2050	107	2006	44
Laikipia	36.93975	0.43039	C2633	1678	61	1652	26
Laikipia	36.78333	0.1	C2634	1842	283	1791	51
Laikipia	36.51667	0.35	C2727	1889	179	1829	60
Laikipia	36.86667	0.68333	C2750	1742	160	1696	46
Laikipia	36.98333	0.11667	C2803	1794	92	1762	32
Laikipia	36.58333	0.48333	C2805	1899	194	1844	55
Laikipia	36.4	0.03333	C2816	2400	18	2375	5
Laikipia	36.5	0.41667	C2833	1922	282	1837	85
Larlak Farm	36.5	0.63333	C2844	1940	285.6	1799.82	140.18
Laikipia	36.35	0.2	C2854	2364	96	2324	40
Laikipia	36.4	0.21667	C2858	2125	107	2084.7	12
Laikipia	36.56667	0.21667	C2889	1838	238	1769	69
Laikipia	36.4	0.4	C2895	2009	122	1960	49
Laikipia	36.48333	0.48333	C2904	1976	118	1964	12
Laikipia	36.38333	0.03333	C2969	2359	34	2325	4
Laikipia	36.92837	0.4439	C3014	1648	43	1614	34
Kisima	37.27	0.26347	C3022	1973	97.5	1911.2	55.8
Kisima	37.2651	0.27	C3023	1997	77.7	1970.2	26.8
Laikipia	36.4	0.2	C3054	2133	92	2072	21
Mugie Ranch	36.78333	0.78333	C3055	1880	91.44	1852.57	27.43
Laikipia	36.58333	0.58333	C3057	1910	196	1846	64
Laikipia	37.21667	0.21667	C3077	2124	99	2117.5	6.5
Laikipia	36.23333	0.23333	C3078	2225	126	2115	0
Laikipia	36.51667	0.43333	C3098	1950	244	1849	101
Laikipia	36.45	0.45	C3115	1976	305	1854	122
Loip. Lanak East	36.48333	0.55	C3119	1970	234.7	1901.72	68.28
Laikipia	36.55	0.58333	C3122	1857	155	1842	15
Laikipia	36.56667	0.56667	C3200	1889	138	1854	35

Laikipia	36.53333	0.53333	C3201	1882	159	1836	46
Laikipia	36.71667	0.48333	C3215	1815	198	1806	9
Timau	37.23333	0.21667	C3310	2012	152	1942	70
Laikipia	36.71667	0.7	C3413	1806	177	1769	37
Laikipia	37.01667	0.48333	C3420	1745	119	1722	23
Laikipia	36.98333	0.53333	C3430	1697	168	1667	30
Laikipia	36.96667	0.5	C3434	1673	91	1634	39
Laikipia	37.2	0.48333	C3450	1270	100	1223	47
Laikipia	36.68333	0.73333	C3533	1818	125	1806	12
Laikipia	37.06667	0.3	C3555	1810	148	1788	22
Laikipia	36.8	0.3	C3563	1782	68	1748	34
Laikipia	36.67521	-0.02854	C3670	2118	213	2036	82
Laikipia	36.28333	0.31667	C3672	1951	104	1897	4
Laikipia	36.68333	0.03333	C3704	1993	33	1990	3
Laikipia	36.48333	0.43333	C3761	1958	258	1843	115
Laikipia	37	0.01667	C3857	1838	152	1779	59
Laikipia	36.28333	0.33333	C3916	1935	132	1885	50
Laikipia	36.85	0.01667	C4683	1843	213	1806	37
Laikipia	36.75	0	C4684	2005	165	1954.6	50.4
Laikipia	36.8	0.08333	C4724	1837	250	1800.5	36.5
Laikipia	36.81667	0.1	C4725	1821	286	1746.09	74.91
Laikipia	36.85	0.08333	C4726	1780	90	1729.8	50.2
sweetwater lodge	36.9555	0.055	C4727	1792	82	1740.8	51.2
Laikipia	36.82	0.08214	C4737	1836	230	1748.7	87.3
Nanyuki mun	37.04	0.03	C5019	1867	180	1826.58	40.42
Meru Show Ground	37.66583	0.04833	C2977	1513	213.3	1397.2	115.8
Rubate Teachers Colleg.	37.67528	-0.30694	C2270	1245	156	1185	60
Timau	37.20718	0.12846	C1215	2096	107	2047	49
Kisima	37.2943	0.16594	C638	2200	83	2125	75
Kisima	37.29751	0.17136	C639	2165	157	2014	151
Oldonya Timau	37.17574	0.15076	C650	2129	88	2066	63
Timau	37.12217	0.16175	C660	2001	82	1942	59
Timau	37.16143	0.07528	C1261	1994	41	1918	76

Buloi Timau	37.16241	0.09804	C1581	2007	128	1906.4	100.6
Shaba Mile post Timau	37.36337	0.10074	C1620	2539	122	2472	67
Timau	37.24966	0.1271	C1710	2263	97	2185	78
Timau	37.24385	0.1102	C2986	2230	166.1	2173.7	56.3
Nkabune	37.71594	0.03175	C3137	1252	21.03	1228.89	13.11
Igoji	37.66269	-0.17989	C3139	1444	91.44	1387.4	46.6
Nkabune	37.69183	0.0313	C3295	1370	21.3	1346.5	8.5
Muthambe	37.66352	-0.27441	C4251	1415	201	1338.8	76.2
Muthambe	37.68389	-0.27292	C4272	1343	123	1282.55	60.45
Kariakomo	37.67564	-0.23774	C3233	1358	153.5	1284.9	73.1
Kanyakine	37.6707	-0.12147	C4348	1402	154	1363	24
Nkunga	37.60719	0.11053	C5404	1801	200	1645	156
Mwerondu prm BH	37.68865	0.23284		1307	0	1229	79
Thinyaine sec BH	37.74243	0.19509		1396	0	1378.5	17.5
Mariara BH/Kangeta	37.86284	0.29217		1617	0	1522.64	94.36
Materini Comm. BH	37.81756	-0.15991		899	97.5	852.43	46.57
Ciakariga	37.91972	-0.24028		640	125	601.3	38.7
St. Francis Assisi-Mitung.	37.80861	-0.09583		925	100.584	873.1	51.9
Ndumuru BH	37.82	0.21457		1805	146	1742.2	62.8
Mbirikine	37.84412	0.01665		960	250	881.8	78.2
Ndoleli Methodist Chuch	38.06444	-0.14861		653	112	598.9	54.1
Kathare Murera	37.55193	0.29884		1239	190	1114.47	124.53
Mbuya SHG	37.68356	0.32477		1117	172	1033	84
Ruiru coffee fact	37.61426	0.14156		1682	131	1660.3	21.7
Njia Borehole	37.78155	0.42063		1085	80	1053.8	31.2
Uringu /Imani Sh_Nkomo	37.71615	0.14255		1421	150	1334.1	86.9
Inono BH/Naathu	37.94979	0.51084		1043	90	1024.6	18.4
Kamweline Kabachi BH	38.05206	0.48741		1325	76	1298.6	21.4
Kithongo/ndoleli BH	38.05306	0.28811		965	0	937.4	27.6
Miuine BH_Antuambui	37.88276	0.46506		1098	0	1056.9	41.1
Theera Antubetwe kiongo	38.0852	0.33692		922	0	897.3	24.7
Nthui BH/Kianjai	37.73387	0.1739		1390	0	1355.2	34.8

Miuine BH	37.93541	0.37384		1749	0	1703.8	45.2
Limbine BH	37.76118	0.18601		1398	0	1346.7	51.3
Kamweline BH	38.00377	0.43797		1528	0	1508.7	19.3
Moringato estate	36.95355	-0.40938	C1643	1794	85	1763	31
Tree tops	36.88291	-0.36443	C3706	2026	152	1953	73
kabaro Est.	37.11333	-0.29233	C2371	2110	121.9	2012.9	97.1
Solio Est	36.93438	-0.20694	C861	1937	91	1854	83
Nyeri high sch	36.91995	-0.40716	C4629	1856	200	1773	83
Kiganjo Community BH	37.00581	-0.39796		1733	220	1627.6	105.4
engineer	37.02908	-0.2686		1973	189	1865.2	107.8
Githiari	37.01878	-0.2686		1937	168	1849.5	87.5
Thome Kiburuti BH	36.96277	-0.06142		1834	178	1729.5	104.5
Kids Alive	37.05307	-0.25175		2032	159	1935.5	96.5
DWD	38.01573	-1.34875	C425	1146	122	1120.3	5
	37.96629	-1.36569	C1738	1153	63	1118	35
	37.98364	-1.3657	C3326	1121	62	1116	5
	37.98358	-1.38357	C3795	1121	60	1077	44
	37.96628	-1.38356	C4136	1130	94	1090	40
Malombe Daniel	38.01301	-1.41569	C7730	1095	66	1056.4	8.6
Matinyani client	37.99417	-1.30985	C10198	1205	100	1193.4	11.6
Kenya forestry	38.01554	-1.36413	C10929	1175	250	1146.7	4
Mulango Bible ins	38.01166	-1.40257	C11043	1123	70	1100.3	2.7
DWD (Mulango girls sch)	38.00986	-1.42112	C13259	1088	160	1069.1	18.9
Ndotto J.K	37.72244	-1.57276	C7844	1098	58	1060.2	27.8
Endui BH	38.09296	-0.77144		1007	155	939.11	67.89
Ivingoni	37.98333	-2.73333	C2779	866	120	836	30
Mangelete	38.01667	-2.73333	C2944	860	110	818	42
Komboyo	37.79583	-2.38333	C1875	1073	130	1058	15
Utithi	37.98205	-2.51214		950	140	940	10
Katangi/ Kuikuni BH	37.71262	-1.3757		1199	90	1127.3	66.7
Kaimu/mutonguni BH	37.95998	-1.18474		1286	70	1227.3	58.7
Makindu	37.825	-2.275	C1650	974	143	938	36
Masii	37.44139	-1.45718	C2266	1320	108.814	1292.942	10.06

Tala/Katine	37.31565	-1.26337	C436	1518	121.92	1501.846	16.15
Ol Doinyo Sapuk	37.23725	-1.06251	C1769	1401	54.254	1370.52	30.48
	37.25101	-1.10742		1515	0	1465.756	47.24
Kianzabe	37.30551	-1.14623	C2132	1419	104.851	1375.13	29.87
Mbuini	37.40814	-1.25285	C2407	1239	103.632	1208.578	20.42
Muisuni	37.37211	-1.31678	C1864	1633	97.536	1607.092	25.91
Muisuni	37.38941	-1.32522	C1949	1545	61.278	1524.578	20.42
	37.38296	-1.33391		1501	82.25	1479.054	21.95
	37.38274	-1.30218		1617	118.872	1570.366	46.63
Ndalani	37.48841	-1.26715	P128	1169	22.25	1156.198	12.8
Ndalani	37.4623	-1.10231	C2169	1172	38.1	1148.226	23.77
Siathani	37.45359	-1.35067	C2406	1256	92.659	1217.407	18.59
Yatta Ranch	37.44551	-1.17796	C1133	1317	152.4	1294.445	22.56
Yatta Ranch	37.37079	-1.10851	C1493	1328	45.72	1300.62	24.38
Kalimoni	37.02308	-1.09845	C2204	1509	183	1457.4	51.6
Thika	37.08935	-1.04007	C2417	1500	204	1421	79
Thika	37.12165	-1.07119	C1421	1463	133	1434	29
Gatanga	36.75	-0.78	C1457	2395	82	2363	32
Juja	37.05872	-1.10873	C1587	1465	124	1424	41
Thika	37.11027	-1.03434	C1660	1472	153	1431	41
Thika	37.03469	-1.02065	C1683	1541	150	1512	29
Thika	37.13163	-1.08316	C1718	1468	178	1431	37
Thika	37.14121	-1.06121	C2002	1463	122	1401	62
Thika	37.20049	-1.07295	C1547	1455	180	1414	41
Thika	37.09377	-1.05517		1486	175	1424.5	61.5
Mitubiri	37.11598	-1.01281	C1169	1483	121	1456	27
Mitubiri	37.16306	-0.98628	C1739	1462	110	1396	66
Mitubiri	37.13311	-0.98219	C1894	1461	69	1437	24
Mitubiri	37.13594	-1.02813	C1900	1473	159	1443	30
Mitubiri	37.28172	-0.94787	C2835	1489	105	1457	22
Don Bosco Mission	37.19487	-0.9092	C2826	1418	61	1388.2	19.8
Kambiti	37.2455	-0.81758	C2802	1153	47	1134	13
Kavambo BH	37.24724	-0.85728	C2868	1335	122	1290	16

Makuyu	37.17984	-0.90813	C3124	1395	185	1375	19
Makuyu Sisal	37.16233	-0.90982	C2783	1460	41	1437	13
Syokimau BH	37.30505	-1.40814		1716	105	1640.2	48.8
Mayuni BH	37.55	-1.22		1308	104	1256	52
Karaba sch/makutano pol.	37.33745	-0.78666		1139	79	1096.9	22.1
Karaba Mission	37.345	-0.74417		1126	52	1106.6	19.4
Karuara/Gachabari	37.82072	-0.60711		701	77.1	659.9	21.1
Mathai BH_siakago	37.62806	-0.54932		1151	49	1128	23
Gwakarigu/Ndune BH	37.53478	-0.80779		1118	76	1091	27
Irimurai_Mbeere	37.69906	-0.7437		1005	68.96	982.57	22.43
Gategi Mkt	37.41131	-0.7465		1101	69	1072	29
Gachoka kiambere	37.81927	-0.71564		895	76	818	40
Kabare girls	37.3239	-0.50718		1469	150	1417.5	51.5
Catholic Mission Carm	37.27392	-0.74188		1115	124	1086	29
karurumo	37.65361	-0.46838		1228	93	1215	13
DWO Muranga	37.15068	-0.72815	C3876	1307	122	1278.5	28.5
Kiru BH_Mathioya	36.93141	-0.61403		1887	107.9	1846.39	20.61
Kiaritha BH	37.27947	-0.48878		1534	145.7	1517.5	16.5
Runyenjes	37.57	-0.42		1498	80.8	1466.2	31.8
MSHG_EWB BH	37.29778	-1.37334		1460	145.7	1420.3	23.7
Kwakoko BH	37.44825	-1.19221		1338	146	1310	22
Dohnholm	36.90118	-1.29469		1619	227	1586	33
Mathangauta/Nyangati	37.35912	-0.60526		1218	137	1195.5	22.5
Ng'Othi BH_Mutithi	37.27845	-0.69468		1149	159	1119	30
Gathigiriri BH/Tebere	37.3976	-0.68201		1131	137	1101	30
Karira BH/Thiba	37.35664	-0.71183		1130	122	1102	28
Kiamugo BH/Gikindu	37.21967	-0.72475		1119	140	1103	16
Kiria Mugoiri BH	37.03278	-0.75375		1552	104	1521.2	15.8
Kamune/Kamacharia	37.00721	-0.59971		1705	72	1680.4	24.6
Kimanzo BH_If'Digiri	37.04255	0.48331		1812	65	1782.3	29.7
Kirimun	36.79	0.81		1803	42	1779.9	23.1
Logorate_Suguta Marmar	36.61812	0.90316		1956	115	1917.3	38.7

Mochongoi BH	36.2181	0.34629		2201	124	2148.91	31.09
Tinomoi BH_Bekibon	35.8783	0.32917		1495	164	1405.5	89.5
Kelewa /Lembus Mogotio	35.94632	0.01772		1575	155	1455.2	119.8
Katumbi BH	38.407	-0.28788		590	75	540.2	29.8
Ekarakara Masinga	37.49354	-0.94847		1082	110	1044.8	37.2
Kangonde/kathui Kata BH	37.65882	-1.02739		1186	120	1096.5	89.5
kikwa Masinga BH	37.54632	-1.0433		1157	155	1037.5	119.5
Kithyoko BH	37.83654	-1.04736		1109	35	1081.8	27.2
Yathui BH	37.5985	-1.44632		1202	105	1123.8	78.2
Kyua	37.73463	-1.43687		1196	100	1130.2	65.8
Nyumbani Village	37.80025	-1.30802		1136	96.5	1082.35	53.65
Kakuthwa	37.7625	-1.09583		1174	147	1091.6	82.4
Kitulani	37.77083	-1.19167		1213	130	1137.8	75.2
Itumba	38.23626	-1.80812		825	152.4	737.1	87.9
Kanyongonyo	37.93176	-1.83006		978	75.29	941.1	36.9
Kyatune	38.10721	-1.77984		844	39.93	828.6	15.4
Yongela/Kyatune BH	38.10422	-1.75701		863	84.21	820.7	42.3
Kamutei BH	38.03395	-1.9293		865	121.92	809.6	55.4
Ikanga	38.07	-1.72		853	174.39	780.7	72.3
Kyangi BH	37.9236	-1.7585		991	81.7	945.1	45.9
Kitise BH	37.89373	-2.06428		889	83.7	826.9	62.1
Kithuki	37.85578	-1.99248		935	73.17	893.8	41.2
Ngumo/katangini	37.98205	-2.32379		838	97.54	788.5	49.5
Mulutu	37.41686	-1.38249		1326	82.6	1282.93	42.07
Kilala	37.55526	-1.73297		1270	78.4	1210.42	36.58
Nzambani BH	37.23006	-1.13136		1527	122	1489.2	37.8
Mavoloni	37.42599	-1.06879		1205	78	1177.2	27.8
Mutyambo pri BH	37.50483	-1.06081		1202	116	1104.5	97.5
Iviani BH	37.51507	-1.08991		1210	104	1141.1	68.9
Matuu	37.55947	-1.13299		1199	87	1145.6	53.4
Nguumo pri BH	37.42021	-1.16855		1328	110	1291.5	31.5
kithimani	37.46319	-1.17616		1254	98	1228.3	25.7

Kamwituo BH	37.51667	-1.18337				1307	104	1272.3	34.7
Kawetur BH	37.51445	-1.19448				1316	95	1288.4	27.6
Ndalasyani BH	37.58969	-1.21972				1299	107	1252.2	46.8
Naivasa BH	37.62158	-1.22423				1301	115	1251.3	49.7
Kwosau BH	37.58073	-1.18132				1279	122	1227.6	51.4
Mwambathaana BH	37.62404	-1.17701				1219	128	1156.6	62.4
Kinyaata	37.59295	-1.27386				1276	89	1241.9	34.1
Ngangani BH	37.61966	-1.30318				1265	85	1228.3	36.7
Kalyambeu BH	37.66756	-1.23761				1175	103	1115.3	59.7
Tinganga /Ikombe BH	37.66498	-1.26481				1194	111	1130.6	63.4
Ikombe sec BH	37.67133	-1.29262				1203	99	1151.3	51.7
Ndovoini BH	37.18455	-1.25242				1486	115	1402.8	83.2
Kisukioni/kalandini BH	37.2874	-1.22584				1482	123	1383.3	98.7
Koma/Nguluni BH	37.26076	-1.27738				1498	118	1421.1	76.9
Malatani /Kivi BH	37.3919	-1.35401				1428	88	1392.3	35.7
kavilingu/kakuyuni BH	37.35374	-1.37452				1435	95	1387.5	47.5
Mitaboni BH	37.25654	-1.36033				1488	103	1435.7	52.3
Ngelani BH	37.23977	-1.40333				1906	121	1802.5	103.5
Mua BH	37.21238	-1.43168				1955	87	1907.8	37.2
Ulu/Mau Hill	37.15	-1.45				1676	104	1624.3	51.7
Mutituni BH	37.25444	-1.43713				1748	83	1702.2	45.8
Tyaa /katalwaBH	37.26651	-1.48636				1698	117	1619.1	78.9
Kombu/Iveti BH	37.33659	-1.49206				1741	127	1643.2	97.8
Mavuti BH	37.31209	-1.53037				1635	98	1550	78.2
Kaluoki /Kiima Kimwe BH	37.26702	-1.53986				1804	112	1717.7	86.3
Katheka BH	37.19635	-1.53927				1634	100	1562.5	71.5
Tawa BH_Kiteta	37.49983	-1.55656				1248	85	1223.5	24.5
Utumoni BH	37.43765	-1.63055				1728	78	1672.2	45.8
Kimutwa BH	37.19145	-1.6631				1684	130	1592.7	91.3
Watema /kaiti	37.31617	-1.73108				1567	84	1517.8	49.2
Malili Konza BH	37.20165	-1.75709				1655	98	1589.1	65.9
Kiima Kiu BH	37.22665	-1.83235				1618	82	1560.4	57.6
Maiani BH_Mukaa	37.31457	-1.82078				1812	125	1704.5	107.5

Nzaini BH_Kataingo	37.33485	-1.86089		1352	78	1316.8	35.2
Kitimbuni BH_Kasikeu	37.36283	-1.90597		1307	73	1275.5	31.5
Sultan Hamud BH_Kiou	37.34222	-1.9722		1299	95	1247.4	51.6
Ndovoini comm. BH	37.62409	-2.02889		1049	102	987.5	61.5
Mukame Wa Mbeu /Nguu	37.63523	-2.08822		1054	105	988.2	65.8
	37.6125	-2.1375	C545	1015	87	956.6	58.4
	37.64167	-2.14861	C2498	969	72	929.6	39.4
	37.61667	-2.175	C2193	1002	97	938.3	63.7
Merrueshi Bh_Kenyewa	37.59134	-2.19494		1039	103	970.3	68.7
Sakuda BH	36.61246	-1.36631		1771	142	1661.2	109.8
Morindat BH	36.59755	-1.30529		1822	236	1653	169
Olokiroret BH	36.49999	-1.34669		1433	256	1229	204
kiiyu BH	36.62027	-1.51609		1621	88	1553.6	67.4
Leshuta pri sch BH	36.63912	-1.52352		1720	77	1658.8	61.2
kabuagi BH	36.58812	-1.53529		1454	114	1366.8	87.2
Inyonyoli BH	36.61466	-1.54877		1480	98	1404.6	75.4
Moses Turere BH	36.48698	-1.55613		1020	125	930.2	89.8
NPC water point	36.77625	-1.50985		1719	104	1691.7	27.3
Kabuya BH	36.80694	-1.55056		1686	90	1646.3	39.7
Naresho BH	36.70153	-1.60929		1797	241	1728.1	68.9
Jamii Bora BH	36.83447	-1.61397		1656	119	1584.6	71.4
kimani BH	36.89304	-1.61911		1611	145	1546.7	64.3
Oldukunyi BH	36.82035	-1.62987		1634	136	1547.5	86.5
nterit BH	36.81311	-1.67369		1656	176	1556.5	99.5
emborioi BH	36.89247	-1.6741		1596	88	1553.7	42.3
Koshaja BH	36.81864	-1.72593		1670	91	1613.9	56.1
Chemagich Bh	36.84699	-1.7245		1657	123	1605.8	51.2
Kisii Bh	36.88503	-1.71924		1644	116	1598.2	45.8
maloe farm BH	36.88	-1.77614		1652	96	1615.8	36.2
osiligi BH	36.86478	-1.77994		1666	112	1604.3	61.7
Ismail BH	36.8271	-1.82515		1753	147	1679.5	73.5
Iseuri BH	36.80697	-1.84147		1698	93	1641.8	56.2
Iltareto BH_Sijiloni	36.86301	-1.84944		1701	105	1637.8	63.2

Olinga Oibor Loodokilani	36.56713	-1.91362		1351	181	1226.7	124.3
Unicef BH	36.69366	-1.94207		1686	156	1596.7	89.3
Olrropil bh	36.78466	-2.01451		1750	90	1687.5	62.5
Enkaron bh	36.73327	-2.05354		1620	78	1573.2	46.8
Sugura Farm BH	36.84859	-2.13019		1451	67	1422.4	28.6
Leken BH	36.85074	-2.13376		1449	72	1419.2	29.8
kima BH	37.24176	-1.9532		1336	103	1279.2	56.8
kilo BH	37.16884	-1.97487		1450	81	1413.8	36.2
lesoit comm BH	37.19322	-1.97901		1406	79	1374.5	31.5
olomaiyani BH	37.19427	-2.0353		1385	96	1339.3	45.7
arroi BH	37.25728	-2.05119		1239	62	1213.7	25.3
Almanie Mashuru Maroro	37.15286	-2.07095		1419	94	1358.8	60.2
mashuru BH	37.14308	-2.10366		1330	102	1262.2	67.8
Mashuru D.O. BH	37.13279	-2.1052		1349	97	1287.6	61.4
oltepesi comm BH	37.15356	-2.13893		1322	100	1285.2	36.8
Enkutoto/Mashuru BH	37.08935	-2.15209		1355	112	1308.7	46.3
ilturot BH_Emali	37.47333	-2.17755		1139	126	1087.6	51.4
Emotoroki comm BH	37.03169	-2.29675		1254	113	1214.2	39.8
Aumiti BH	36.79485	-2.2331		1489	108	1424.3	64.7
Ilmarba BH	36.66577	-2.23365		1526	99	1469.6	56.4
Ngao BH	36.74371	-2.2268		1512	87	1460.1	51.9
Enaibor-Surgumen Mosiro	36.17233	-1.50379		1341	154	1255.4	85.6
Ntuka	35.85573	-1.43212		1762	175	1664.7	97.3
EOR Ekule	36.00313	-1.11519		1889	186	1777	112
Olgolului/Kijito_Lenkism	37.17403	-2.42098		1172	134	1095.2	76.8
enjakita BH	37.28958	-2.55359		1139	95	1097.7	41.3
Koroto BH/Bartum	35.82331	0.61866		2142	125	2096.8	45.2
Kapteberewo BH	35.82331	0.69732		2039	61	1991.2	27.8
Kabarbet BH_Katiorin	35.75426	0.58507		2150	136	2079.6	50.4
Aiyabo BH_Saimo	35.81931	0.64195		2015	87	1987.3	19.7
Moi Kabartonjo_Ossen	35.75538	0.63458		1967	105	1909.2	57.8
Mandina BH_Kiplombe	35.25249	0.6321		2037	45	2024.5	12.5

Siron BH_marmanet	36.41953	0.20835		2067	98	2043.2	23.8
Seiyo_Cheptiret	35.36655	0.36199		2221	66	2177.4	23.6
Mashariki bH_Masaita	35.60061	-0.07175		2333	89	2283.2	49.8
Cheres bH_Sorget	35.55032	-0.06565		2420	78	2383.2	36.8
Lemotit	35.61918	-0.13153		2336	52	2312.5	23.5
Molo	35.72	-0.24		2506	147	2437.3	68.7
Njoro	35.87	-0.31		2222	53	2193.5	28.5
Kanyangia BH	36.47205	-0.08443		2506	173	2454.3	51.7
Ainoptich BH_Barut	36.02977	-0.32835		1879	67	1833.6	15.4
London Gioto Kaptembwe	36.04728	-0.28688		1843	149	1744.5	98.5
Nakuru Tunners	36.05558	-0.29692		1834	105	1777.3	56.7
Mihango Comm_Subukia	36.23083	0.00835		2008	193	1970.2	37.8
Tabuga BH_Dundori	36.1894	-0.2657		1996	108	1956.8	39.2
Maombi_Kabazi	36.18874	-0.06114		2343	167	2293.5	49.5
Lanet	36.13413	-0.32118		1875	163	1785.7	89.3
Kabatini_Bahati	36.18694	-0.27579		1977	78	1950.3	26.7
Kahuho_kiambogo	36.15115	-0.54488		1911	169	1797.5	113.5
Kiungu BH_gilgil	36.26662	-0.51515		1929	238	1772.2	156.8
Shamba_Ndabibi	36.20825	-0.69592		2213	125	2126.6	86.4
Riftvalley WSB BH1	36.42035	-0.65154		1908	110	1848.5	59.5
Malewa Bay Investment	36.32467	-0.66939		2034	207	1860.8	173.2
Moi Ndabi BH_Naivasha	36.22701	-0.77503		1937	194	1824.3	112.7
Oserian Kiangazi	36.27511	-0.83056		1935	147.2	1856.6	78.4
Kenya nut BH2	36.38238	-0.68033		1889	40	1863.9	25.1
	36.33206	-0.85042	C575	2052	95	1987.8	64.2
Upendo village	36.46801	-0.76244		2070	139	1977.7	92.3
Shindano /Mununga Naiva.	36.50843	-0.71666		2243	236	2029	214
Nyamweru BH_Lari	36.61015	-1.04571		2296	175	2190.8	103.2
Ndiuni Limuru	36.64965	-0.97863		2380	164	2282.8	97.2
Nyathuna Kabete	36.74585	-1.01028		2042	141	1957.8	84.2
Kirenga Lari	36.72834	-1.02748		2072	132	1976.4	95.6
Migumo-Ini Kabete	36.75575	-1.19469		1746	111	1726.5	19.5

Chura BH_Kabete	36.71339	-1.22203		1880	157	1850.2	29.8
Soko BH_KinaleLari	36.64027	-1.13707		2290	127.9	2195.5	94.5
Tigoni Limuru	36.68794	-1.14997		2073	115	2030.4	42.6
Ikinu-Rioki Githunguri	36.80459	-1.10362		1811	82	1777.6	33.4
Kamiti BH_Kiambaa	36.67682	-1.21666		1981	99	1939.5	41.5
Kiambaa Waguthu	36.5745	-1.16328		2082	294	1877	205
Kagwe Comm_Gatimayu	36.6798	-1.27157		1938	187	1803	135
Kigumo Githunguri	36.71267	-1.04782		2070	156	2034.3	35.7
Gaitumbi Muguga	36.66262	-1.03273		2366	179	2298.8	67.2
Nyakianda Kikuyu	36.63956	-1.21191		2004	210	1930.4	73.6
Gathwariga BH_Kamae	36.70782	-1.19833		1917	195	1890.6	26.4
Manunga/Mahinga Kipi.	36.49005	-0.44864		2402	182	2278.9	123.1
Manyatta BH	36.55139	-0.60228		2444	169	2329.8	114.2
Gachoka	37.55609	-0.61668		1159	112	1107.9	43.1
Kapsabet Girls Sc	35.126	0.19915		2014	0	2003.1	10.9
Kapsabet Boys Sc Sch.	35.1168	0.20542		1988	0	1977	11
Cereals Board Mois Brid.	35.1298	0.88568	C10604	1806	0	1801.6	4.4
Gathathi BH	36.97289	-1.14327		1549	0	1484.5	64.5
Gatitu BH	36.84781	-1.01688		1804	0	1710.9	93.1
Gatuanyaga BH	37.17551	-1.07193		1461	0	1404.3	56.7
Gatundu BH	36.89864	-1.01088		1640	0	1553.7	86.3
Gatundu hosp. BH	36.90666	-1.01478		1682	0	1604.7	77.3
Githunguri h/s BH	36.93862	-1.15477		1508	0	1401.2	106.8
Ituru sch BH	36.90111	-0.99459		1722	0	1631.9	90.1
Mathanjini BH	36.99959	-1.1364		1464	0	1422.8	41.2
Ngoliba A BH	37.33327	-1.09724		1377	0	1335.3	35.7
Riuriro BH	37.0103	-1.14096		1516	0	1447.7	68.3
Ruiru sch BH	36.95917	-1.14625		1503	0	1405.8	97.2
Ruiru springs BH	36.97278	-1.13667		1547	0	1521.8	25.2
Rurii Grundfos BH	37.00454	-1.14043		1550	0	1476.5	73.5
Upp Kihara chiefBH	36.73892	-1.20892		1794	0	1740.8	53.2
Wangunyu pry sch BH	36.73355	-1.19492		1831	0	1741.4	89.6
dagoreti BH	36.68438	-1.28464		1894	0	1822.5	71.5

dot com BH	36.95773	-1.15979		1504	0	1420.1	83.9
gituamba BH	36.63325	-1.02655		2394	0	2317.8	76.2
kajibi bh	36.90934	-1.15417		1522	0	1442.5	79.5
kenafria bakery bh	36.95773	-1.15979		1504	0	1389.5	114.5
Kiganjo bh	36.8312	-0.98512		1905	0	1803.6	101.4
Kihunguro A.p bh	36.95237	-1.15993		1506	0	1436.8	69.2
Kimunyu sec BH	36.94033	-1.05474		1553	0	1471.7	81.3
Mustard company	37.02531	-1.13618		1501	0	1402.3	98.7
Mustard company	37.02438	-1.13311		1505	0	1397.8	107.2
kwihota comm BH	36.98254	-1.15536		1489	0	1401.7	87.3
Muigai inn chiefs BH	37.00702	-1.12799		1564	0	1478.6	85.4
mathanu proj BH	36.58851	-1.24665		1988	0	1911.6	76.4
mugutha police BH	36.95925	-1.1198		1553	0	1478.5	74.5
muhuhu sch BH	36.8295	-1.00108		1865	0	1762.7	102.3
murera BH	36.97973	-1.13642		1539	0	1457.4	81.6
salama bh_juja farm	37.06886	-1.14438		1498	0	1402.4	95.6
salama bh_muigai inn	37.01506	-1.12439		1502	0	1421.3	80.7
uplands bh_Ruiru	36.95909	-1.12965		1569	0	1489.2	79.8
	36.54087	-0.76921	C1	2450	206.9	2316.6	133.4
	36.38919	-0.66519	C54	1910	46	1895	15
	36.12444	-0.53221	C59	1880	140.2	1776.4	103.6
	36.12354	-0.5304	C79	1880	116.4	1783.7	96.3
	35.75929	-0.2764	C108	2480	39.6	2460.2	19.8
	35.75839	-0.27369	C131	2480	45.7	2466.9	13.1
	35.76108	-0.27731	C132	2480	54.7	2464.2	15.8
	36.11914	-0.28463	C152	1861	66.9	1812.6	48.4
	35.90552	-0.36317	C164	2332	66.5	2313.2	18.8
	35.91629	-0.36588	C202	2320	137.2	2282	38
	36.12093	-0.28553	C204	1860	76	1834	26
	35.92976	-0.33878	C205	2195	140	2091	104
	36.48328	-0.79995	C210	2149.7	67.1	2134.46	15.24
	35.93424	-0.34782	C211	2220	135.3	2130.1	89.9
	35.99708	-0.29454	C214	1880	121.9	1825.1	54.9

	35.93602	-0.3948	C220	2300	152.4	2266.5	33.5
	35.92256	-0.40292	C223	2396	186.8	2342.7	53.3
	35.91628	-0.39118	C227	2367	167.6	2303.9	63.1
	36.43243	-0.72418	C231	1892.8	45.7	1884	8.8
	35.88849	-0.30535	C258	2228	106.1	2172.5	55.5
	36.09568	-0.59906	C261	2120	150	2049.2	70.8
Riftvalley	36.54889	-0.87317	C264	2580	182.88	2436.7	143.3
	36.15765	-0.5259	C266	1880	150	1776	104
	35.80235	-0.28545	C288	2220	182.9	2138	82
	36.44575	-0.66883	C295	1990	86	1952.5	37.5
	36.05719	-0.33882	C306	1773	73.2	1754.1	18.9
	36.0563	-0.32798	C307	1780	70.1	1762.9	10.1
	36.12721	-0.29096	C321	1880	98.1	1813	67
	36.38036	-0.24944	C325	2377	132.6	2336.8	23.2
	35.81671	-0.29539	C376	2411	91.4	2374	37
Kenya marble Qurries	36.69333	-1.92731	C381	1635	128.3	1612.4	22.6
	36.59805	-1.17963	C407	2140	200	2001.9	138.1
	36.11645	-0.28463	C408	1885	138	1788.1	96.9
	36.62321	-1.15434	C416	2140	146	2072.9	67.1
	36.27891	-0.29009	C417	2480	182.1	2341	138.7
	36.0177	-0.34423	C419	1970	182.9	1840.1	129.9
	35.83107	-0.28275	C423	2280	213.4	2216	64
	36.20523	-0.51418	C429	1840	100.8	1769.5	70.5
	36.15046	-0.5521	C431	1940	216	1781	159
	36.62133	-1.25377	C440	2020	167.6	1974.3	45.7
Turoka Mile 4	36.65382	-1.91369	C451	1510	137.2	1466	44
	36.25464	-0.40485	C456	1860	190	1812.6	47.4
	36.41667	-0.61666	C457	2018.5	76.2	1947.5	27
	36.41615	-0.60465	C458	1948	102.4	1891.4	36.6
	35.82385	-0.40018	C463	2760	106.7	2747	13
	36.38554	-0.56591	C465	1974.6	99	1933.2	41.4
	36.22485	-0.75456	C466	1940	77.4	1890.8	49.2
	36.26667	-0.81665	C467	1898	152.4	1885.09	82.91

	36.38559	-0.67151	C468	1900	46.3	1883	17
	35.97822	-0.31983	C485	2087	120.1	2023	64
	36.43327	-0.73325	C531	1893.6	61	1877.6	16
	36.1666	-0.5747	C533	1990	220.1	1784.3	205.7
Kinangop	36.64147	-0.70599	C553	2560.3	106.68	2471.92	88.4
	36.40258	-0.79896	C562	1900	56.4	1877.1	22.9
	36.2679	-0.8079	C563	1905	31	1897.7	7.3
	36.4295	-0.81524	C567	1955	102.1	1899	56.1
	36.32466	-0.40488	C570	2340	142.5	2310	30
Riftvalley	36.50943	-0.77914	C572	2220	228.6	2010	210
	36.26667	-0.79995	C578	1913.3	0	1893.49	19.81
	36.34349	-0.81659	C579	1883.9	42.7	1860.65	22.3
	36.42305	-0.81671	C580	1945	67.1	1899.28	45.72
	36.31667	-0.79995	C581	1882.2	30.5	1859.04	23.16
	36.43327	-0.78325	C582	1944.4	56.1	1883.68	13.72
	36.29997	-0.81665	C594	1894.3	0	1878.45	15.85
	36.64574	-1.91007	C605	1490	149	1368	122
	35.89028	-0.31257	C624	2236	91.4	2175	61
	36.4008	-0.77003	C628	1902.2	45.7	1868.67	33.53
	36.34997	-0.83325	C629	1899	0	1843.89	57.91
	36.39997	-0.76665	C630	1897.4	0	1858.73	99.97
	36.28327	-0.71666	C631	1912.8	46	1885.8	27.4
	36.43328	-0.74995	C632	1894.3	0	1883.3	11
Kinangop	36.58932	-0.83703	C633	2700	182.88	2506	164
Kinangop	36.61808	-0.79005	C634	2603	103.632	2564	39
Kinangop	36.61457	-0.6183	C651	2580	161.544	2419	161
	35.87054	-0.2945	C655	2174	149.4	2098	76
	35.81671	-0.26738	C665	2280	204	2143	137
	36.40439	-0.77275	C667	1898.2	36.6	1876.25	21.95
	36.12811	-0.29276	C670	1850	112.7	1798	52
Kinangop	36.65495	-0.69786	C678	2590	60.96	2557.1	32.9
Kinangop	36.54538	-0.72944	C691	2520	109.728	2410.3	109.7
Kinangop	36.54628	-0.73306	C692	2520	192.024	2361.504	158.5

Kinangop	36.63787	-0.72497	C699	2520	91.44	2443.8	76.2
Kinangop	36.5992	-0.82077	C703	2650	93	2564.656	85.34
	36.27249	-0.64615	C704	2500	152	2424.7	75.3
	36.27429	-0.64163	C707	2480	103	2428.6	51.4
	36.12855	-0.29286	C719	1880	153	1814	66
	36.41611	-0.86923	C729	2059.2	182.9	1899.18	160.02
	36.13978	-0.29999	C732	1870	152.4	1809	61
	36.32192	-0.53772	C733	2042	240.8	1848.8	193.2
	35.98445	-0.47884	C741	2302	133.5	2260	42
	35.92257	-0.35595	C745	2240	182.8	2145.2	94.8
Kinangop	36.54538	-0.73668	C780	2540	210.312	2358.34	181.66
	36.05442	-0.5367	C783	2196	120	2104.6	91.4
	36.37587	-0.26933	C804	2376	100.8	2318	42
	36.03388	-0.2819	C805	1870	166.4	1757.2	112.8
Oloiyankalani	36.70345	-1.74517	C811	1860	200	1838.1	17.9
	36.17118	-0.34247	C813	1900	152.7	1778.7	121.3
	36.48435	-0.68422	C814	2169	102.4	2126.3	42.7
	36.67706	-1.9996	C824	1610	183	1473	137
	36.14606	-0.31626	C836	1890	172.8	1821	69
	36.69494	-1.29904	C839	1878	45.7	1852.7	25.3
	36.08853	-0.52858	C845	1907	217	1781	126
	36.00426	-0.26834	C855	1954	189.9	1771	183
	36.15322	-0.36325	C858	1882	150.5	1766	116
	36.1622	-0.34789	C869	1900	137	1769	131
	36.31752	-0.25305	C870	2620	102.9	2542	78
	36.37318	-0.25306	C872	2400	109.2	2352	48
	36.66983	-2.02581	C875	1540	152	1467	73
	36.03208	-0.26925	C882	1929	182	1769	160
	36.39178	-0.83058	C910	1940	32.9	1927.2	12.8
	35.94411	-0.36589	C916	2140	213.4	2022	118
	35.86334	-0.36586	C921	2500	228.6	2401.9	98.1
	36.4879	-0.7493	C939	2127	150	2000.6	126.4
Riftvalley	36.51666	-0.70864	C946	2330	245.364	2092.3	237.7

	36.41605	-0.79444	C947	1905	49.4	1880.6	24.4
	35.9719	-0.43547	C953	2295	143.2	2200.5	94.5
	35.83645	-0.27462	C984	2240	106.9	2200.4	39.6
Kitabi	36.62347	-0.78101	C994	2580	98	2537.3	42.7
	36.60193	-0.77106	C1000	2600	148	2475	125
Kiasi_Kinangop	36.63156	-0.7783	C1007	2560.3	60.96	2537.32	23
Kinangop	36.5364	-0.7213	C1013	2520	201.8	2354.5	165.5
	36.3184	-0.33438	C1019	2440	217.2	2276.5	163.5
	35.81401	-0.30442	C1021	2403	118.9	2382	21
	36.08407	-0.48069	C1027	1810	106.7	1730.8	79.2
	35.80594	-0.2999	C1033	2414	183	2379.7	34.3
	36.35788	-0.40037	C1043	2260	210	2125	135
Kinangop	36.56872	-0.73217	C1051	2560	194.158	2400	160
	36.28327	-0.63326	C1062	2353.5	32	2332.5	11.3
	36.2904	-0.72026	C1063	1900	40.8	1889.5	10.5
	36.39997	-0.83324	C1068	1980.8	0	1935.69	45.11
	36.1299	-0.30993	C1080	1870	160	1763	107
	36.12721	-0.30089	C1082	1870	110.5	1810	60
	36.32019	-0.33709	C1083	2530	108.9	2470	60
	35.96925	-0.32886	C1125	2100	125	2014.7	85.3
	36.63205	-1.31525	C1126	2020	215.5	1815.8	204.2
	35.96827	-0.51949	C1148	2510	72.5	2495.2	9.8
Riftvalley	36.52194	-0.88219	C1161	2160	216.1	1965	195
	36.17299	-0.30814	C1250	1910	168	1761	149
	36.68107	-1.6787	C1259	2005	142	1970.9	9.1
Riftvalley	36.50762	-0.80625	C1265	2240	256.64	1995	245
Kinangop	36.65313	-0.73402	C1277	2520	114.3	2451.4	68.6
	36.43218	-0.83874	C1279	2000	182.9	1878.1	121.9
	36.3891	-0.80979	C1281	1898	31	1874.2	23.8
	36.19986	-0.46267	C1287	1815	102.7	1766.4	50.6
	36.67504	-1.43733	C1294	1870	182.9	1830.9	9.1
	35.83914	-0.27913	C1325	2270	192	2180	90
	36.40527	-0.79444	C1356	1900	30.8	1887.8	12.2

	36.30134	-0.33347	C1358	2460	204	2313	147
	36.38327	-0.81665	C1359	1891.3	0	1878.8	12.5
	36.35788	-0.40398	C1361	2280	249.9	2094	186
	35.98541	-0.30176	C1362	2040	199.4	1865	175
	36.13798	-0.3009	C1374	1875	105	1814	61
	36.36239	-0.31993	C1379	2380	126	2344	36
	36.1505	-0.46174	C1383	1845	97.5	1790.1	54.9
Turoka Mile 43/2	36.63496	-1.90463	C1391	1480	152	1369	111
	36.12264	-0.52769	C1394	1880	181.8	1790	90
	36.36923	-0.98511	C1402	1740	232	1635.9	104.2
	36.21676	-0.7654	C1404	1940	103.5	1882.4	57.6
Riftvalley	36.51565	-0.8867	C1425	2120	283.464	1859	261
	36.17479	-0.26747	C1434	1960	137.2	1923.4	36.6
	36.17928	-0.25934	C1436	1980	142.2	1934.9	45.1
	36.27962	-0.74104	C1464	1888	31.1	1880.4	7.6
Kinangop	36.5543	-0.8334	C1475	2600	106.68	2539	61
	36.4338	-0.75717	C1481	1905.6	0	1888.6	17
	36.42954	-0.75423	C1482	1893.4	36.6	1882.1	11.3
	36.44998	-0.66666	C1483	2068.2	45.7	2037.2	31
	36.44748	-0.78723	C1486	1974	152.4	1963.3	10.7
	36.44478	-0.78994	C1487	1974	155.4	1882.6	91.4
	36.46667	-0.69995	C1488	2074	91.4	1997.8	76.2
	35.96925	-0.33067	C1491	2120	162.1	2035	85
Riftvalley	36.51924	-0.8867	C1503	2140	296.4	1879	261
	35.77006	-0.25834	C1504	2380	152.4	2289	91
	36.03657	-0.26383	C1535	1950	188.9	1773	177
	35.96468	-0.53213	C1545	2520	46	2513.9	6.1
	36.12721	-0.28915	C1558	1900	135	1775	125
	36.46654	-1.55641	C1559	1010	119.2	926.2	83.8
	36.12627	-0.44005	C1584	1784	86.3	1766.3	17.7
	35.92885	-0.37763	C1585	2270	155	2254.3	8.7
Kinangop	36.57584	-0.85601	C1602	2680	172.212	2530	150
Kinangop	36.50682	-0.63904	C1614	2480	188.976	2361.7	118.3

	35.80774	-0.28364	C1625	2380	91.4	2341	39
	35.80864	-0.25112	C1641	2220	182.9	2143.8	76.2
	36.14337	-0.30361	C1666	1880	187.4	1817.3	62.7
Kibeto	36.69196	-1.57746	C1713	1840	259.7	1785.1	54.9
Riftvalley	36.51475	-0.90026	C1726	2080	283.464	1820.8	259.2
	35.92526	-0.37311	C1749	2280	175.3	2194.7	85.3
Kinangop	36.56866	-0.83883	C1794	2740	236.22	2560.2	179.8
Kinangop	36.57055	-0.67432	C1795	2510	162.8	2378.33	131.67
	36.1361	-0.53764	C1798	1900	186.6	1768	132
Kinangop	36.55798	-0.66708	C1830	2500	170.383	2371.7	128.3
	36.3989	-0.91916	C1843	2070	256	1814	0
Kinangop	36.60017	-0.69964	C1850	2550	192.024	2410.4	139.6
Riftvalley	36.51751	-0.79632	C1851	2340	306.324	2083.4	256.6
	36.18725	-0.56839	C1877	1940	191.1	1782.4	157.6
	36.49685	-0.80715	C1892	2200	256.3	1966.2	233.8
	36.44997	-0.68326	C1898	2033.5	102.4	1972.8	60.7
	36.00231	-0.63967	C1913	2900	147	2861	39
	35.99603	-0.65051	C1914	2890	76.2	2867.1	22.9
	36.3902	-0.3823	C1924	2260	157.5	2137	123
	36.38907	-0.85498	C1926	1970	125	1879.5	90.5
	36.39997	-0.91665	C1927	2088.7	41.8	2070.41	18.29
Kinangop	36.60731	-0.77829	C1929	2600	136.25	2499.72	100.28
	35.94232	-0.33698	C1935	2160	197	2044.8	115.2
	36.12712	-0.54035	C1941	1920	170.1	1780.5	139.5
	36.44998	-0.73325	C1947	1985	67	1947	15
	36.41534	-0.39225	C1951	2220	147.6	2110.5	109.5
	36.42701	-0.38683	C1952	2290	138	2178.1	111.9
	36.18703	-0.91086	C1970	2580	225	2450.5	129.5
	36.20523	-0.51689	C1990	1840	102	1778.2	61.8
Kinangop	36.55345	-0.75385	C1997	2560	223.42	2360.2	199.8
Kinangop	36.5678	-0.77465	C2005	2600	255.12	2372	228
	36.32739	-0.2657	C2033	2600	126.6	2525	75
	36.33327	-0.81665	C2058	1895	46.6	1879.76	15.24

	36.12445	-0.49968	C2059	1830	118.3	1809.6	20.4
	36.45127	-0.30911	C2061	2340	123.9	2278.7	21.3
Kinangop	36.55884	-0.73668	C2062	2620	260.91	2391.68	228.32
Kinangop	36.57945	-0.81443	C2063	2670	129.24	2571	99
	36.38327	-0.81665	C2069	1891.3	79	1845.58	45.72
	36.32984	-0.8206	C2071	1898	18.9	1886.4	11.6
	36.33181	-0.4817	C2076	2020	221.4	1901.2	118.8
	36.34438	-0.48712	C2077	2000	204	1905.8	94.2
	36.34175	-0.30276	C2097	2500	180.9	2381.2	118.8
Kinangop	36.55706	-0.71228	C2108	2530	187.757	2363.6	166.4
	36.3265	-0.25576	C2109	2600	90	2558	42
	36.49344	-0.3986	C2110	2440	129.3	2340.7	99.3
	36.42954	-0.7583	C2117	1900	26.2	1887.8	12.2
	36.25914	-0.36599	C2118	2220	208.8	2071.2	148.8
	36.15235	-0.28915	C2128	1902	135	1869.7	32.3
	36.16491	-0.29187	C2129	1919	183	1870.2	48.8
Kinangop	36.59016	-0.9211	C2138	2200	124.054	2165.25	34.75
Kinangop	36.5885	-0.68337	C2149	2540	198.12	2395.83	144.17
	36.49793	-0.39137	C2160	2480	185.1	2348.6	131.4
Kinangop	36.62891	-0.68068	C2170	2610	228.6	2423.46	186.54
Riftvalley	36.58747	-0.92291	C2172	2180	142.646	2138	42
Kinangop	36.63785	-0.76836	C2176	2540	76.81	2523.54	16.46
Kinangop	36.64236	-0.7313	C2197	2540	182.88	2426.61	113.39
	36.33327	-0.81665	C2220	1895	0	1864.52	30.48
	36.41667	-0.76665	C2221	1887	0	1874.5	12.5
	36.43328	-0.74995	C2222	1894.3	0	1879.3	15
	36.43328	-0.76665	C2223	1920	0	1907.5	12.5
	36.26347	-0.43616	C2234	1860	162.9	1782.6	77.4
	36.21589	-0.72383	C2241	1980	145.5	1871.4	108.6
	36.40849	-0.68146	C2246	1902.7	38.1	1873	13.7
Kinangop	36.56506	-0.85871	C2263	2712.7	274.32	2453.64	259.08
Kinangop	36.57135	-0.85149	C2264	2740	243.84	2590.648	149.35
	36.13709	-0.29999	C2269	1874	150	1814	60

	35.9423	-0.40113	C2276	2315	137.2	2282	33
	36.09299	-0.58731	C2289	2020	139.2	1933	87
	36.37497	-0.26661	C2292	2360	127.2	2297.6	62.4
	36.65808	-1.33697	C2294	1880	155.5	1863.8	16.2
	36.43152	-0.31724	C2296	2327	96	2290	30
	36.21583	-0.81419	C2300	2000	223.5	1899.4	100.6
	36.28327	-0.74995	C2304	1886.5	42	1880.5	6
	36.2852	-0.26659	C2322	2540	138	2427.8	112.2
	36.28519	-0.29099	C2332	2480	119.1	2424.5	55.5
	36.69047	-1.27643	C2338	1876	238	1680.9	195.1
	36.46906	-0.73573	C2347	2060	41	1940.5	119.5
	36.59533	-1.20403	C2358	2160	311	1895	265
	36.32643	-0.48621	C2388	2030	264	1788.3	241.7
	36.12991	-0.29367	C2402	1872	99.1	1804.9	67.1
Kinangop	36.60908	-0.82258	C2420	2638	123.6	2569.725	68.28
Kinangop	36.61626	-0.82801	C2421	2631	193.548	2442.024	188.98
	36.41668	-0.73326	C2430	1887	31	1881	6
	35.98988	-0.35416	C2432	2060	173	1944	116
	36.61599	-1.19501	C2447	2080	213	1878	202
	35.99254	-0.4427	C2448	2180	288	2023.1	156.9
	36.63125	-1.98779	C2466	1446	98	1391	55
	36.63756	-0.18228	C2468	2685	179	2553	132
	36.13254	-0.47077	C2480	1810	71.6	1770.4	39.6
	36.19632	-0.30905	C2493	1930	146.9	1836.1	93.9
	35.96461	-0.65952	C2496	2820	167.6	2675.5	144.5
	35.90359	-0.64684	C2497	2760	158.5	2655.5	104.5
	36.24119	-0.37141	C2499	1928	213.4	1822	106
	36.18017	-0.28735	C2504	1940	167.6	1869.6	70.4
	36.23116	-0.71119	C2521	1940	102.6	1865.9	74.1
	36.2509	-0.72475	C2522	1940	51.5	1894	46
	36.29997	-0.71665	C2523	1907.1	56.7	1876.6	30.5
	36.3909	-0.81341	C2534	1910	22.3	1892.91	17.09
	36.33327	-0.69996	C2535	1895.9	12.8	1889.2	6.7

	36.33051	-0.70141	C2536	1900.6	9.7	1896.3	4.3
	36.31667	-0.71665	C2538	1886.4	13.7	1876.6	9.8
	36.32579	-0.71625	C2539	1889.8	12.5	1885.2	4.6
	35.84094	-0.25023	C2564	2120	218	2011	109
	36.22853	-0.58286	C2600	2020	213	1834	186
	36.72187	-1.3081	C2620	1820	152.4	1752.9	67.1
	36.39539	-0.80528	C2636	1895	30.5	1890.43	4.57
	36.72387	-1.93277	C2646	1680	91.4	1628.8	51.2
	36.6508	-2.14058	C2647	1600	104	1582	18
	36.25804	-0.79073	C2657	1904	32.6	1880.5	23.5
	36.38327	-0.81665	C2659	1891.3	24.4	1873.94	17.36
	36.27734	-0.79571	C2660	1922	28.3	1902.19	19.81
	36.28327	-0.78325	C2661	1923.5	0	1902.47	21.03
Riftvalley	36.55609	-0.84063	C2662	2612	256.032	2470.38	141.62
Kinangop	36.58214	-0.81895	C2663	2665	137.16	2567.464	97.54
Riftvalley	36.53997	-0.7656	C2667	2420	205.9	2265.2	154.8
	35.99618	-0.29996	C2670	2000	192.7	1833.3	166.7
	35.76377	-0.26647	C2680	2440	85.3	2391.8	48.2
	36.45217	-0.31996	C2697	2339	165	2270	30
	36.26664	-0.64996	C2701	2530.2	25.9	2523.2	7
	36.12355	-0.50239	C2704	1840	76.2	1779.7	60.3
	36.28327	-0.71666	C2705	1902.8	31	1886	16.8
	36.29997	-0.69996	C2706	1949	62.5	1910.3	38.7
	36.18979	-0.82863	C2709	2170	225	1974.3	195.7
	36.58361	-1.25735	C2717	1940	324	1700.7	239.3
Kinangop	36.56329	-0.81171	C2720	2660	301	2384.156	275.84
	35.92347	-0.35595	C2745	2240	178.3	2147.6	92.4
	36.37132	-0.4546	C2753	2207	210	2084	123
	36.58725	-1.1977	C2758	2054	177.1	1951.9	102.1
	36.36863	-0.46092	C2773	2170	159	2098	72
	36.28142	-0.71935	C2813	1920	63.1	1878.5	41.5
	36.48117	-0.88078	C2823	2132	305.5	1871.6	260.4
	36.11902	-0.58913	C2851	2040	259	1809	231

	36.54755	-1.39381	C2866	1585	147.5	1496	89
	36.42243	-0.64215	C2883	1926.5	106.7	1873.8	52.7
Njoro	35.95128	-0.38306	C2894	2230	180.4	2218.4	11.6
	36.63123	-1.22847	C2902	2020	110	1960.6	59.4
	36.59362	-1.1046	C2910	2185	305	2008.2	176.8
	36.3956	-0.35609	C2966	2260	123	2206	54
	36.15414	-0.28916	C2970	1910	53	1884.4	25.6
	36.39353	-0.90424	C2997	2145	320	1864.6	280.4
	36.54857	-1.26907	C3003	1790	295.6	1550	240
	35.80771	-0.35681	C3005	2403	124	2364.9	38.1
	36.12974	-0.68853	C3024	2370	105	2278.2	91.8
	36.12615	-0.6795	C3032	2397	225	2355	42
	36.12183	-0.3036	C3047	1822	73.2	1762.6	59.4
	36.30297	-0.72027	C3064	1904	118	1889.1	14.9
	36.35971	-0.25215	C3066	2460	93	2390	70
	36.39291	-0.3335	C3067	2300	96	2240	60
	36.63032	-1.24384	C3087	1990	76	1949	41
	36.25556	-0.32262	C3136	2320	180	2275	45
	36.1477	-0.67951	C3164	2402	73.5	2381.1	18.9
	36.1344	-0.28011	C3166	1875	134.4	1798	77
	36.40801	-0.714	C3216	1898	42.7	1893.1	4.9
	36.40711	-0.71942	C3217	1898	42.7	1893.2	4.8
	35.92616	-0.36769	C3243	2260	188.9	2192.4	67.6
	36.62325	-1.10734	C3266	2280	111	2187	93
	36.63208	-1.27909	C3280	2000	137.2	1917.7	82.3
Sunshine Rehab Ctr	36.41801	-0.71105	C3292	1887	76	1879.4	7.6
	36.39816	-0.68327	C3298	1900	39.6	1895.2	4.8
	36.41667	-0.69995	C3299	1896.1	39.4	1894	2.1
	36.02757	-0.35056	C3324	1940	201.2	1749.8	190.2
	36.00413	-0.5972	C3327	2660	141	2592.5	67.5
	35.94577	-0.64325	C3351	2774	186	2621	153
	36.00411	-0.64057	C3352	2900	264	2686.6	213.4
	35.98974	-0.65683	C3353	2880	142.7	2843.4	36.6

	36.65383	-1.90827	C3363	1505	165	1426	79
	36.41551	-0.69839	C3365	1896.2	82	1885.3	10.9
	36.41092	-0.69443	C3366	1895.6	76.8	1879.97	15.63
	35.97641	-0.37403	C3371	2145	185.9	2044.4	100.6
	36.63046	-1.0739	C3377	2340	165	2247	93
	36.00951	-0.61889	C3397	2730	117.3	2622	108
	36.38647	-0.70857	C3417	1900	91.7	1891.8	8.2
	36.63214	-1.21762	C3418	2080	240	1938.3	141.7
	36.6341	-1.01062	C3422	2400	117	2343	57
	36.11002	-0.6316	C3431	2200	174.6	2084.2	115.8
	36.70321	-1.93003	C3436	1620	76	1577.3	42.7
chief Maika BH	36.74045	-2.08326	C3451	1596	122	1541.1	14.9
	36.38327	-0.66666	C3459	1900	0	1883	17
	35.95309	-0.33698	C3490	2150	193.9	2043	107
	36.6878	-1.24208	C3523	1900	61.6	1874.7	25.3
	36.68781	-1.23846	C3524	1920	106.7	1906.9	13.1
	36.13451	-1.37798	C3525	1380	143.3	1293.1	86.9
	36.40533	-0.69773	C3551	1900	76.8	1895.4	4.6
oloseos BH	36.67052	-1.46716	C3576	1907	137.2	1865.5	4.5
	36.65998	-1.21403	C3615	2060	85	1988	72
	36.32445	-0.8215	C3616	1930	57	1908.4	21.6
	35.96745	-0.33699	C3627	2132	138.1	2032.4	99.6
	35.98705	-0.64779	C3650	2830	121.9	2821.8	8.2
	36.33531	-0.676	C3674	1913.5	30.4	1907.7	5.8
	36.41431	-0.70226	C3675	1890	61	1885.2	4.8
	36.41491	-0.69556	C3676	1897.4	0	1883.9	13.5
	36.41252	-0.68328	C3677	1902.7	91.4	1882.26	20.44
	36.40714	-0.67875	C3678	1903.5	72.5	1885.5	18
	36.70847	-1.23577	C3693	1880	122	1869	11
	36.67257	-1.20229	C3694	2070	122	2037	33
	36.65908	-1.21946	C3710	2080	87	2022	58
	36.6932	-1.23395	C3721	1940	140	1901	39
	36.70755	-1.25023	C3739	1900	73	1852	48

	36.41668	-0.77547	C3740	1892.2	35.7	1875.1	17.1
	36.70039	-1.23124	C3763	1920	85	1894	26
	36.67614	-1.22218	C3764	1900	107	1876.5	23.5
	36.67824	-0.80021	C3765	2469	67	2433.3	35.7
	36.26666	-0.81965	C3767	1899	72.2	1872.5	26.5
	36.74623	-1.18156	C3771	1880	91	1841	39
	36.38305	-0.2621	C3779	2355	150.6	2344.3	10.7
	36.38305	-0.26571	C3784	2349	150	2333.9	6.1
	36.64828	-1.24205	C3799	2060	83	2019	41
	36.12093	-0.30631	C3874	1800	71	1745.8	54.2
	36.12272	-0.3018	C3875	1800	73	1746.7	53.3
	36.71579	-1.06492	C3897	2170	105.5	2135	35
	36.72284	-1.23578	C3910	1847	98	1829	18
	36.74901	-1.07218	C3919	1980	152.4	1952.9	27.1
	36.35048	-0.83055	C3924	1898	37.8	1891.5	7.5
	35.79682	-0.62012	C3925	2709	122	2615	94
	36.36143	-0.62089	C3929	1902.3	61	1886.4	15.9
	36.14229	-0.70933	C3932	2210	165	2087.3	122.7
	36.66076	-1.34782	C3937	1915	260.6	1872	3
	36.63372	-2.14417	C3939	1540	152	1458.5	81.5
	36.63678	-1.89107	C3942	1500	152.4	1400	100
	36.7158	-1.92011	C3951	1640	122	1611.3	28.7
	35.81401	-0.30894	C3955	2425	143	2417.4	2.6
	36.19813	-0.26567	C3965	2060	158.5	1997.5	62.5
	36.67179	-1.91101	C3970	1598	137.5	1560.9	27.1
	36.66542	-1.16161	C3976	2151	126.5	2093.6	56.4
	36.7265	-1.14539	C3995	1940	122	1926.6	13.4
	36.66084	-1.26014	C3999	2000	138.5	1951.5	48.5
	36.74805	-1.15354	C4003	1977	183	1970	3
	36.66362	-1.16613	C4037	2152	198.5	2022	45.7
	36.39809	-0.80076	C4057	1900	61	1897	3
	36.28309	-0.91184	C4061	2068	1002	1948	120
	36.29567	-0.89287	C4062	2023	1350	1883	564

	35.98538	-0.39301	C4077	2120	226	2036	84
	36.67569	-0.48182	C4092	3062	143	3054.3	7.7
	36.03844	-1.38418	C4116	1470	251	1326	144
	36.29776	-0.28919	C4121	2480	178	2387	93
	35.92735	-1.19794	C4143	1880	197	1708	172
	36.59749	-0.66374	C4152	2543	144.6	2532	11
	36.43501	-0.6634	C4155	1947.9	128	1920.9	27
	36.42598	-0.69319	C4157	1906	78	1883.3	22.7
	36.42112	-0.69051	C4161	1898.7	52	1881.99	16.71
	36.41252	-0.6896	C4168	1900	52	1883.1	16.9
	36.5774	-1.16696	C4174	2080	68	2023	57
	36.43047	-0.69142	C4177	1910	52	1893.9	16.1
	36.42239	-0.69232	C4178	1902	52	1885.6	16.4
	36.68584	-1.42107	C4179	1865	116	1763	102
	36.68313	-1.43191	C4186	1835	152	1765.1	4.9
	36.68767	-1.38672	C4200	1870	226	1796	74
	36.68409	-1.36773	C4201	1880	155	1864	16
	35.94053	-0.33337	C4206	2160	250	2051.5	108.5
	36.42597	-0.71853	C4208	1890	61	1884.4	5.6
	36.42148	-0.72124	C4209	1889	62	1884.7	4.3
	35.9504	-0.33518	C4214	2152	248	2047	103
	36.29148	-0.26479	C4252	2570	181	2448	122
	36.69154	-1.05677	C4279	2271	141	2194	77
	36.7166	-1.17883	C4292	1925	200	1898.8	26.2
	36.40355	-0.6661	C4301	1916	109.7	1883.3	32.7
	36.42687	-0.70949	C4302	1900	76	1890	10
	36.73089	-1.26924	C4306	1845	232	1791.6	53.4
	36.04324	-1.10139	C4332	1850	112	1788	62
	35.92153	-0.66492	C4350	2790	170	2777	13
	36.70226	-1.13633	C4360	1960	135	1938.2	21.8
	36.13979	-0.25843	C4369	1910	166	1878.8	31.2
	36.12901	-0.28011	C4370	1880	180	1846.1	33.9
	36.3451	-0.82693	C4397	1899	33.5	1892	7

	36.64592	-0.78645	C4403	2540	0	2497	43
	35.91986	-0.39931	C4413	2410	137	2341.5	68.5
	36.33971	-0.82603	C4420	1899	25	1892	7
	36.63752	-1.22667	C4431	2032	240	1971	61
	36.6618	-1.19505	C4461	2040	221	2027.2	12.8
	36.57209	-1.89912	C4484	1380	200	1297.7	82.3
	36.20441	-0.28465	C4491	2030	69	2022	8
	36.20261	-0.28103	C4492	2020	150	1961.5	58.5
	36.19274	-0.28374	C4493	1960	75	1947.8	12.2
	36.72674	-1.79627	C4498	1720	100	1695	25
	36.25896	-0.76091	C4499	1940	213	1727	0
	36.27241	-0.77357	C4500	1902	61	1886.8	15.2
	36.26972	-0.77899	C4501	1910	58	1888.7	21.3
	36.0078	-0.43819	C4502	2096	112	2045.3	50.7
	36.33711	-0.67058	C4504	1890	30.5	1878.1	11.9
	36.13979	-0.25933	C4510	1893	150	1865.3	27.7
	36.13979	-0.25753	C4511	1910	148	1882.4	27.6
	36.13889	-0.25662	C4512	1910	150	1882.4	27.6
	35.92078	-0.35956	C4517	2280	188	2183	97
	36.37564	-1.70633	C4531	885	150	790	70
	36.67626	-1.08297	C4554	2280	86	2234	46
	36.39639	-0.61729	C4555	1923	128	1890.6	28.4
	36.09393	-0.49877	C4564	1840	0	1787	53
Kilonito Council BH	36.62395	-1.33423	C4575	1950	196	1828	122
	36.26613	-0.76633	C4591	1904	45.7	1882.6	21.4
	36.23115	-0.72926	C4594	1940	213.6	1834.3	105.7
	36.64027	-1.15707	C4597	2242	260	2127.4	114.6
	36.42329	-0.69322	C4610	1890	53	1874	16
	36.65011	-1.2086	C4615	2100	157	2037.8	62.2
	36.71194	-1.36505	C4624	1824	230.2	1791	33
RVA	36.59643	-0.93918	C4634	2237	110	2218.4	18.6
	36.71752	-1.14086	C4665	1940	153	1903.2	36.8
	35.93334	-0.3686	C4669	2240	214	2219.4	20.6

	36.65909	-1.2059	C4685	2080	122	1999	81
	36.71009	-1.42109	C4687	1827	102	1805	15
	36.74694	-1.39491	C4713	1748	150	1707	43
	36.66701	-1.39031	C4743	1985	104	1958.8	6.2
	36.63303	-1.22576	C4792	2060	204	1968.2	91.8
	36.67428	-1.29992	C4804	1930	140	1866.2	63.8
	36.63035	-1.21491	C4807	2060	206	1890	170
	36.62944	-1.22305	C4812	2060	193	1980.5	79.5
	36.66808	-1.19777	C4850	2070	80	1990	5
	36.65912	-1.17245	C4855	2148	150	2112	8
	36.68673	-1.42378	C4863	1852	94	1805	15
	36.70656	-1.35781	C4881	1840	137	1786	54
	36.18173	-0.79248	C4897	2220	297	2007	213
	36.68319	-1.37044	C4907	1870	60	1862.6	7.4
	36.59979	-1.23296	C4909	2060	300	1924.5	135.5
	36.13888	-0.30271	C4924	1870	177	1724	146
	36.7012	-1.32345	C4927	1880	180	1763.2	116.8
	36.70743	-1.38764	C4966	1840	230	1767	73
	36.68387	-1.36954	C4967	1872	150	1750	109
	36.6886	-1.35418	C4968	1860	240	1801	59
	36.5792	-1.16605	C4974	2080	320	1861	219
	36.69034	-1.41022	C4981	1855	100	1805	35
	36.38101	-0.82063	C4986	1895	54	1889.6	5.4
	36.69985	-1.33272	C4987	1866	94	1826	40
	36.38191	-0.81973	C4989	1895	25	1893.6	1.4
	36.69034	-1.41203	C4997	1875	201	1804.3	70.7
	36.48168	-0.63902	C5002	2310	186	2204	106
	35.94141	-0.36499	C5029	2210	210	2122	88
	36.19991	-0.31628	C5111	1900	188.8	1799.7	100.3
	36.66075	-1.35415	C5117	1927	117	1918	9
	36.11555	-0.2765	C5143	1890	165	1855	35
	36.7092	-1.41386	C5161	1800	150	1775.2	24.8
	36.67083	-1.12816	C5175	2160	51	2121.7	38.3

	35.94231	-0.37222	C5206	2215	220.2	2180.3	34.7
	35.89908	-0.6902	C5257	2680	200	2568.5	111.5
	36.64294	-1.1869	C5343	2120	152	2022.6	97.4
	36.64922	-1.20046	C5348	2100	154	1976	124
	36.66086	-1.23844	C5375	2060	96	1984	76
	36.66357	-1.22488	C5411	2140	116	2057	83
	36.54996	-0.53692	C5520	2458	100	2394	64
	36.66966	-1.43009	C5564	1924	160	1904	16
	36.23223	-0.2955	C5754	2240	0	2232.3	7.7
	36.6625	-1.40839	C5798	2010	134	1972	38
	35.95114	-0.67577	C6056	2770	150	2726.2	13.8
	36.23493	-0.28737	C6095	2237	120	2227.3	9.7
	36.70036	-1.26469	C6186	1880	31	1872.5	7.5
	36.66612	-1.38218	C6211	1980	100	1938	42
	36.64744	-1.17786	C6213	2134	185	2004	130
	35.91988	-0.3713	C6271	2318	74.8	2283.4	34.6
	36.31204	-0.53953	C6290	2030	208	1833	197
	36.54177	-0.76921	C6300	2490	200	2357.1	132.9
	36.28943	-0.84316	C6301	1970	126	1870.3	99.7
	36.66074	-1.37132	C6377	1956	200	1907.7	48.3
	36.63569	-1.26011	C6378	2000	131	1899.7	100.3
	36.65534	-1.37584	C6494	1970	160	1964	6
	36.67155	-1.33337	C6524	1880	134	1817.3	62.7
	36.64204	-1.18961	C6613	2109	204	2019	90
	36.33717	-0.54767	M1	1960	183	1805	155
	36.64999	-1.34329	P2	1953	82.6	1936.5	16.5
	36.65177	-1.35324	P12	1962	96.9	1937.6	24.4
	36.54488	-1.36759	P16	1560	147.5	1465.5	94.5
	36.53592	-1.34499	P23	1510	82.9	1440	70
Riftvalley	36.54164	-0.95903	P53	1859.3	228.905	1645.88	213.4
	36.61179	-0.79366	P65	2620	100.58	2559	60.96
	36.57911	-1.26006	P71	1940	189.8	1751	189
	36.57141	-0.74031	P89	2575.6	42.1	2538.4	37.16

	36.11734	-0.28282	SA58	1856	98.5	1808.8	47.2
Karunga ndumberi	36.61169	-0.95908	P65	2322	100.6	2108.6	213.4
	36.57946	-0.79364	P71	2614	189.8	2553	61
	36.11714	-0.74003	SA58	2501	98.5	2453.8	47.2
Manera	36.40745	-0.71051		1888	0	1885.25	2.75
	36.42615	-0.68213	C11527	1910	0	1881.9	26.05
	36.33928	-0.68564	C11691	1890	0	1885.8	4.2
	36.43345	-0.78375	C11093	1945	0	1885.14	59.86
Kigome	36.42938	-0.79531	C11841	1944	110	1883.85	60.15
	36.31908	-0.6646	C11494	2070.4	0	1879.4	191
	36.41674	-0.66674	C8994	1919.2	0	1903.96	15.24
	36.42912	-0.70678	C11351	1900	0	1885	15
	36.43874	-0.75288	C11548	1912.3	0	1885.3	27
	36.45873	-0.74024	C11600	2023.5	0	1929	94.5
	36.41855	-0.7409	C11688	1886.9	0	1878.9	8
	36.31548	-0.81291	C11889	1899	0	1875.17	23.83
	36.46732	-0.62794	C12287	2383.5	0	2244.5	139
	36.42777	-0.71446	C11906	1895	0	1872	23
Three Ostrich Farm	36.4281	-0.67309		1915	0	1884.615	29.46
BH B	36.4279	-0.67807		1910	0	1884.82	25.18
BH C	36.42562	-0.6785		1908.8	0	1881.31	26.69
BH D	36.42495	-0.67987		1908.7	0	1882.06	26.64
Delamer BHO	36.42202	-0.68109		1906	0	1882.14	23.86
BH green Hs	36.43052	-0.67244		1918	0	1884.35	33.65
TANINI	36.42639	-0.67135		1917.4	0	1884.19	33.21
w16(M6)	36.37603	-0.67073		1897	0	1887.9	9.1
BH 7	36.40561	-0.67838		1903	0	1882.87	20.13
	36.40745	-0.71051		1891	0	1885.71	5.29
	36.41175	-0.68278		1903	0	1890.55	12.45
	36.41793	-0.68903		1902	0	1882.95	19.05
	36.38975	-0.64661		1898	0	1895.01	17.99
	36.39883	-0.6422		1900	0	1872.89	27.11
	36.3305	-0.70682		1895	0	1887.96	7.04

	36.32867	-0.70937		1898.2	0	1894.63	3.57
	36.42262	-0.70816		1894.3	0	1889.5	4.8
	36.41491	-0.69556		1897.4	0	1883.23	14.17
	36.38338	-0.64212		1897.2	0	1885.89	11.31
	36.37397	-0.67192		1897	0	1884.78	12.22
	36.34102	-0.64303		1925	0	1896.05	28.95
	36.35304	-0.68063		1889.4	0	1862.29	27.11
	36.44361	-0.74939		1925.8	0	1888.73	37.07
	36.43246	-0.73047		1892.8	0	1886.08	6.72
	36.43116	-0.71923		1894.3	0	1884.25	10.05
	36.33635	-0.68477		1891	0	1885.83	5.17
	36.33741	-0.67743		1890.8	0	1887.11	3.69
	36.36912	-0.67454		1894	0	1885.84	8.16
	36.40145	-0.71647		1889	0	1887.23	1.77
	36.25852	-0.81411		1901.7	0	1894.54	7.16
	36.37997	-0.81554		1888.9	0	1887.58	1.32
	36.38482	-0.81458		1901.1	0	1887.96	13.14
	36.42179	-0.77256		1906	0	1890.86	15.14
	36.41843	-0.76741		1888.2	0	1886.55	1.65
	36.40528	-0.79105		1894.3	0	1885.6	8.7
	36.43052	-0.74327		1890	0	1887.67	2.33
	36.42388	-0.77448		1910	0	1885.93	24.07
	36.32657	-0.8163		1895.9	0	1889.81	6.09
	36.26856	-0.82281		1893	0	1887.15	5.85
	36.27647	-0.76037		1890	0	1888.13	1.87
	36.28375	-0.73242		1900	0	1897.6	2.4
	36.44643	-0.79214		1980	0	1884	96
	36.44734	-0.78201		1979	0	1898	81
	36.40033	-0.72012		1889.2	0	1887.14	2.06
	36.40095	-0.71715		1889.4	0	1886.27	3.13
	36.40248	-0.7156		1889.6	0	1871.54	18.06
	36.40328	-0.71374		1889.6	0	1885.8	3.8
	36.40527	-0.71237		1889.6	0	1886.27	3.33

	36.42821	-0.74003		1889.8	0	1886.48	3.32
	36.4294	-0.73956		1889.9	0	1883.03	6.87
	36.43057	-0.7393		1890	0	1885.1	4.9
	36.43035	-0.73944		1890	0	1883.24	6.76
	36.4318	-0.73839		1894	0	1888.57	5.43
	36.43288	-0.73719		1892.4	0	1884.09	8.31
	36.43322	-0.73582		1893.4	0	1881.45	11.95
	36.4335	-0.73389		1893.8	0	1880.35	13.45
	36.42693	-0.74034		1888	0	1886.7	1.3
	36.33496	-0.6755		1900.4	0	1848.4	52
Maralal	36.6035	1.09828	C444	2060	121.92	2021.66	38.34
Maralal	36.67537	1.06489	C479	1950	90.2	1939.03	10.97
Maralal	36.69869	1.10197	C1505	1945	105.46	1922.44	22.56
Samburu	36.7126	1.59557	C1553	1370	135.63	1310.57	59.43
Nkichita	36.77413	1.97804	C1613	1320	120.4	1254.78	65.22
Nkurei	36.71393	1.97796	C1639	1600	102	1539.7	60.3
DCs Off Maralal	36.69331	1.09383	C1723	1935	121.92	1904.83	30.17
Lonkewan	36.54171	0.86322	C2434	2080	182.9	1933.7	146.3
Sukuta Mamar	36.55155	0.91565	C2847	2040	179.83	1969.29	70.71
Samburu Ranch	36.60457	0.85783	C2972	2005	259	1955.6	49.4
Tangulbei commun	36.26251	0.81242	C3437	1180	182.9	1087.04	92.96
Baragoi settlement	36.78516	1.78278	C3456	1240	152.4	1225.98	14.02
Losikiriumoi	36.17969	1.0961	C3461	800	134.1	698.5	101.5
Nyaunyau_Chepkonghio	36.0901	0.90085	C3466	870	76.2	832.2	37.8
Chemolingot	35.98501	0.97575	C3470	860	121.92	830.13	29.87
Kabarnet	35.73498	0.49589	C3506	1957	152.4	1927.4	9.6
Kabartonjo	35.78963	0.63592	C3526	2175	166.1	2119.84	55.16
Mission Maralal	36.70948	1.09565	C3609	1920	71	1884.65	35.35
Lesirikan	36.95497	1.78479	C3651	1500	64.31	1455.2	44.8
Marar Township	36.70141	1.07033	C3692	1880	49.37	1840.38	39.62
Sirata Oirobi	36.65742	1.05584	C3833	1959	122.5	1946.84	12.16
Baragoi	36.8067	1.79727	C3855	1260	182.88	1249.29	10.71
Nginyang	36.00748	0.94957	C3868	840	122.22	830.72	9.28

Baragoi (catholic mission)	36.79864	1.77828	C3869	1268	91.44	1232	36
Baragoi settlement	36.78158	1.76832	C4417	1260	120	1228.7	31.3
Kabarnet	35.73408	0.49769	C4722	1975	155	1959.1	15.9
Kabarnet Town	35.75292	0.50131	C4780	1970	150	1913.35	6.65
Kamnorok/Kabluk	35.65777	0.57984	C4838	1106	143	1071	13
	36.29593	0.40758	C5069	2032	154	2030.05	1.95
Kiboino	35.68385	0.46425	C5170	1420	120	1351.6	18.4
Kolowa	35.7559	1.22303	C5333	960	75	950	10
Tot Brigde	35.69847	1.21302	C5349	940	23	933	7
Mkorwa	35.71531	0.31162	C5370	1375	55	1335	30
Kinyach	35.67544	0.93481	C5487	1107	55	1081	10
Salabani	36.04724	0.55205	C6362	976	60	965	12
Kositei	35.94377	0.92693	C6363	1050	107	1039.8	10.2
Chesirimion	36.02372	0.83484	C6364	905	120	819.3	85.7
ngambo	36.05803	0.50598	C6365	980	60	957.8	22.2
Kapsoo	35.76729	0.46519	C6970	2010	138	1973	34
Tangulbei	36.28497	0.80069	C7122	1210	91	1197	13
Katangora	36.24541	0.88109	D1	1180	160	1074	106
Orus mission	36.30909	0.95795	D4b	1325	68.58	1274.71	50.29
Kokwototo	36.29926	0.89468	D7	1235	0	1207.57	27.43
Marigat	35.93062	0.43364	C4077	1234	226	1118	116
Mukutan	36.26801	0.62988	C2115	1226	61	1202	24
Natai	36.30464	0.90372	D5	1255	111.25	1226.1	28.9

## Appendix B: Description GPS landslide points

FID	Longitude	Latitude	Area	Comments
1	36.999981	-0.700045	Koimbi	Shallow debris flow
2	37.596922	-0.113534	baya-karuma nthi2	landslide
3	37.596831	-0.113671	bayakaruma nthi 3	landslide
4	37.596953	-0.113304	mtuma1	soil SURVEY
5	37.664216	-0.066164	nkubu1	landslide near town
6	37.665559	-0.067585	nkubu2	Human induced
7	37.662099	-0.142371	gihubu/rd	landslide rd
8	37.646317	-0.145049	giumpu 1	landslide 1997
9	37.646142	-0.14554	giumpu2	landslide
10	37.664943	-0.142797	giumpu-rd3	along the road
11	37.663731	-0.211531	egoji4	quary activity after river Mutonga, human induced landslide
12	37.649528	-0.266534	nthi1	nthi bridge
13	37.665394	-0.290599	Meru-Embu highway	Bus washed on a bridge, January 1998
14	37.66173	-0.305382	chuka	chuka
15	37.658584	-0.328061	chuka town	Human induced
16	37.645831	-0.339073	bridge	Effect of water flow
17	37.614402	-0.381435	bridge 2	Effect of water flow
18	37.460547	-0.51105	embu town junction	Shallow slide
19	37.015528	-0.739043	waciru1	land slide 2013
20	37.015318	-0.739191	waciru2	landslide
21	37.015447	-0.739302	waciru3	Landslide 2014
22	37.015431	-0.739316		3 Visible cracks
23	37.015558	-0.739519	waciiku4	Landslide scar
24	37.015589	-0.739501		5 Landslide crown
25	37.015708	-0.739393	waciku6	landslide that is in making
26	36.969662	-0.736885	kirikoini1	crack 2013

27	36.970332	-0.737415	homestead/kilikoini2	landslide
28	36.970826	-0.738182	kilikoini4	at the slopes
29	36.971127	-0.73812	kilikoini/slopes6	landslide
30	36.971261	-0.737774	kilikoini 6	extend
31	36.971106	-0.737124	kilikoini 7	homestead area
32	36.97095	-0.736438	kilikoini 7	Near the road
33	36.971433	-0.736423	kilikoini /gatuya	crack at the road
34	36.971508	-0.736138	kilikoini /maina8	maina homestead
35	36.971531	-0.736125	8	Visible cracks
36	36.971592	-0.736155	kirikoini/maina	homestead
37	36.969014	-0.737188	kirikoini -soil1	soil SURVEY
38	36.97003	-0.73687	kirikoini 10	near mama janet
39	36.969556	-0.736771	shamba/soil2	mama mercy
40	36.906235	-0.750219	gathaihi tea1	tea collection centre
41	36.906464	-0.750287	nyangathia2	buying centre
42	36.904662	-0.750176	nyagathia3	landslide in 2009-10
43	36.874051	-0.723297	exposed-pipes1	pipes-water
44	36.871986	-0.720817	gatara1	sinking ground
45	36.872266	-0.720722	gatara2	crack
46	36.872066	-0.720475	gatara3	crack
47	36.87179	-0.72047	gatara5	crack near the road
48	36.872009	-0.720848	gatara1/1	at the road
49	36.872098	-0.721239	gatara1/2	eroded area
50	36.871766	-0.720961	gatara2/1	inside the area, 3 people dead, tea bushes destroyed, earthflow
51	37.596917	-0.113369	baya/karuma nthi	landslide in a tea shamba 2008
52	36.882092	-0.762449	Irati Border	Tea farm, blocked road
53	37.018752	-0.952335	Rugaita	Buried Families, rehabilitated
54	36.960955	-0.829709	Kariua Road landslide	Still active though attempts to rechannel water are underway
55	36.927998	-0.813369	Kariua/Rugaita landslide	15-20 yrs ago, rehabilitated
56	36.839478	-0.659606	Tuthu landslide	Catchment area

57	36.879209	-0.776967	Karingaini	10 families affected
58	36.896252	-0.785644	Ikumbi area 1	Ikumbi area 1
59	36.904152	-0.773026	Ikumbi area 2	Landslide crown
60	37.158778	-0.713317	Kiharu	5 May 2010, houses destroyed
61	36.859161	-1.260818	Mathare landslide	40 houses destroyed, 6 killed
62	37.02036	-0.628384	Gakurwe	Landslide crown
63	36.882092	-0.762449	Irati Border	Road blocked, rock slide
64	36.813864	-0.795922	Rwanyaga	rehabilitated, families relocated, 2 killed
65	36.617085	-0.950343	Magina, Lari	3 killed, families relocated
66	36.591005	-0.94813	Kijabe	destruction of property
67	36.60268	-1.002499	Mai Mahiu Narok Road	Risk of road being cut off
68	37.080642	-0.588928	Kiagathi	Debris slide
69	37.081078	-0.588525	Kiagathi	Debris slide
70	37.080692	-0.658539		Landslide crown
71	37.086322	-0.587922	Kiagathi	mudflow
72	37.081186	-0.588753	Kiagathi	Debris flow
73	37.564069	-0.107936	Kwa mbaya	Debris slide
74	37.606556	-0.179858	kionyo	Debris flow
75	37.609228	-0.181475	kionyo	Landslide toe
76	37.609383	-0.181758	kionyo	Debris flow
77	37.103719	-0.553536	Kimondo village	Landslide crown
78	37.093025	-0.549344	Kimondo	earthflow
79	37.096167	-0.542881	Kimondo	Debris slide
80	37.105544	-0.556214	Kimondo	Earth flow
81	37.013125	-0.430278		Debris flow
82	37.040403	-0.442733		Debris slide
83	36.829989	-0.669884	Tuthu	23rd March 2013, translational landslide
84	36.268178	-0.09874	Ngano village	5 families affected, houses washed away
85	36.271989	-0.111922	Ngano village	April 16, 2013
86	36.467874	-0.484282	Gathiriga, Gatundu	Debris slide

87	36.467101	-0.499541	Gathiriga	earthflow
88	36.474507	-0.502128	Gathiriga village	Earth flow
89	36.268175	-0.098753	Karatu village, Gatundu	More than 700 tea bushes destroyed , Sep 2014
90	37.080553	-0.588267	Kiagathi village, Mukurweini	5 May 2010, 2 dead, mudslide
91	37.104422	-0.55315	Kimondo village	5 May 2010, 13 houses destroyed
92	36.271978	-0.111923		Debris flow
93	35.774961	-0.297882	Elburgon	Debris flow
94	35.633197	-0.165366	Mau summit	Shallow debris
95	35.661119	-0.168225	Mau summit	Landslide crown
96	35.661832	-0.167718	Mau summit	Landslide toe
97	36.158945	-0.751163		Rock slide
98	35.594309	0.339181	Kimwarer	Earth flow
99	35.614234	0.334483	Kimwarer	Debris flow
100	35.626195	0.336049	Kimwarer	Landslide toe
101	35.631493	0.34771	Kimwarer	Landslide head
102	35.635291	0.345378	Kimwarer	Landslide debris
103	35.733865	-0.227871	Elburgon	Debris flow
104	36.858304	-0.579173	Mucharage 1	Landslide crown
105	36.869441	-0.574946	Mucharage 2	Debris slide
106	36.866656	-0.583324	Mucharage 3	Debris flow
107	36.852817	-0.662495	Tuthu	Debris slide
108	36.933354	-0.68331		Landslide head
109	36.93325	-0.687493		Landslide toe
110	35.865482	-0.299407		Debris slide
111	35.744316	-0.397466		mudflow
112	35.564236	-0.393233		Debris flow
113	35.64299	-0.137932		earthflow
114	35.646661	-0.184023		Debris slide
115	36.286541	0.085934		Rock slide
116	36.302862	0.095794		Debris flow

117	36.351757	-0.062854		earthflow
118	37.171028	-0.369902		Landslide crown
119	37.197732	-0.404879		Debris flow
120	37.335031	-0.410528		debris slide
121	37.25942	-0.39776		earthflow
122	37.241967	-0.457819		Landslide toe
123	37.587562	0.053398		Landslide crown
124	36.623576	-1.196308		Debris flow
125	36.805218	-1.318189		Debris flow
126	36.762481	-0.873385		earthflow
127	36.809316	-0.898694		Mudflow
128	36.757484	-0.985797		Debris flow
129	36.855152	-0.751571		Debris slide
130	36.976656	-0.784993		Landslide crown
131	35.785197	-0.645766		Landslide debris
132	37.436332	-1.799371		Landslide head
133	36.815919	-0.416514		Debris slide
134	36.774216	-0.93948		earthflow
135	37.016035	-0.701194		Debris flow
136	36.964091	-0.541136		Debris flow
137	37.128994	-0.557737		Debris slide
138	37.106624	-0.569394		Debris flow
139	37.138691	-0.568048		earthflow
140	35.793436	0.408467	Kabasis	2 dead, August 2012
141	35.811375	0.410486	Timboiywo	Cracks identified
142	35.811761	0.412789	Timboiywo	Ground sinking
143	35.812128	0.41015	Timboiywo	2 people buried alive
144	35.817428	0.399636		House, crop, pasture destroyed
145	35.789539	0.404928		2002 - 2008
146	35.781542	0.457206	Kinyo	earthflow
147	35.771683	0.423756		Landslide crown

148	35.772511	0.4243		Landslide toe
149	35.765903	0.441239		Landslide crown
150	35.765406	0.440731		Landslide deposit
151	35.764342	0.441394		Landslide crown
152	35.784775	0.43985	Kabasis	13 households affected in four villages
153	35.784128	0.4409	Kapkorombo village	12yr old pupil killed
154	35.783119	0.445772		House caved in
155	35.783542	0.445692	Kimungur village	A teenager killed, siblings evacuated
156	35.843978	0.630097	Kasisit	May 2012, Several acres of crops destroyed
157	35.844881	0.629558	Kasisit	People relocated
158	35.838331	0.638303	Kasisit	Rock/debris slide
159	35.830294	0.230617	Cheberen	People displaced
160	35.830178	0.230889	Cheberen	Debris slide
161	35.802553	0.440903	Bosin	Run-off trigger shallow landslides
162	35.802647	0.441367	Bosin	Debris flow
163	35.780103	0.416725		Landslide crown
164	35.815833	0.400739	Ngetmoi	Landslide toe
165	35.815931	0.399636	Ngetmoi	mudflow landslide
166	35.817964	0.399522	Ngetmoi	Landslide crown
167	35.820808	0.394072	Ngetmoi2	Landslide crown
168	35.821508	0.393011	Ngetmoi2	Landslide toe
169	35.792125	0.491969	Kituro	Landslides accompanied by ramblings
170	35.749536	0.439731		Landslide crown
171	35.751019	0.438933		Landslide toe
172	35.749108	0.436311		Debris slide
173	35.775119	0.477147	Kipturo	Debris flow
174	37.433719	-1.087839	Mavoloni, Yatta	3 people died, houses destroyed
175	37.43315	-1.083664	Mavoloni, Yatta	April 2013
176	37.424775	-1.078933	Mavoloni, Yatta	Debris slide
177	37.426306	-1.083319	Mavoloni, Yatta	earthflow

178	36.955519	-0.930839	Gatanga	Landslide crown
179	36.95435	-0.932739	Gatanga	Landslide rehabilitation
180	36.955175	-0.931819	Gatanga	Landslide toe
181	36.901067	-1.005528	Gatanga	earthflow
182	37.406014	-1.433592	Masii	Masii-Makueni highway, 2km road section and bridge destroyed, 16/03/1998
183	36.5735	-0.917361	Kijabe1	Mudflow
184	36.574697	-0.916778	Kijabe1	Mudflow
185	36.574067	-0.916594	Kijabe1	April 2013
186	36.573311	-0.916	Kijabe2	Landslide crown
187	36.573933	-0.910733	Kijabe2	Landslide crown
188	36.573967	-0.915453	Kijabe3	Landslide crown
189	36.574389	-0.915311	Kijabe3	Debris flow
190	36.574253	-0.916114	Kijabe3	Landslide toe
191	36.571025	-0.908967		Debris flow
192	36.536772	-0.875233		Debris flow
193	36.49925	-0.874342	Longonot	Landslide toe
194	36.499811	-0.875164	Longonot 2	Debris flow
195	36.500531	-0.876883	Longonot 3	Landslide crown
196	36.499592	-0.877097	Longonot 3	Debris material
197	36.497764	-0.875322	Longonot 4	Landslide toe
198	36.497597	-0.875697	Longonot 4	Earth flow
199	36.496947	-0.875689	Longonot 4	Landslide crown
200	36.958386	-0.523889	Othaya	April 2004, 6 family members dead
201	37.113933	-0.554144	Mukurweini	Nano village, 8 families affected, earth flow
202	37.124667	-0.552344	Kigathi village	5th May 2010
203	37.119936	-0.537083		9th May 2015
204	37.084961	-0.655314		Shallow landslides, 5 families affected, 1 child dead, May 6, 2012
205	37.859181	0.273839	Nkinyang'a	mudflow
206	37.861661	0.271347		Landslide crown
207	37.862614	0.271058		Landslide toe

208	37.805742	0.237978		mudflow
209	37.777536	0.206931		mudflow
210	37.623222	-0.206467		Debris slide
211	37.622892	-0.205089		Debris slide
212	37.623892	-0.209817		Landslide debris
213	37.623667	-0.208953		Debris flow
214	37.624131	-0.209222		Landslide debris
215	37.658178	-0.192914		mudflow
216	37.659433	-0.196617		Debris slide
217	37.6591	-0.197289		Landslide toe
218	37.660436	-0.200158		Earth flow
219	37.659739	-0.2011		Landslide toe
220	37.684053	-0.207483		Debris flow
221	37.681428	-0.208986		earthflow
222	37.682769	-0.209139		earthflow
223	37.678369	-0.2074		Landslide crown
224	37.663208	-0.213469		mudflow
225	37.637844	-0.323892		Shallow slide
226	37.806433	-0.328189		Debris slide

## Appendix C: Curriculum Vitae

### Ms Mercy Wanjiru Mwaniki

---

<b>Permanent Address</b>	Jomo Kenyatta University of Agriculture and Technology (J.K.U.A.T) % Department of Geomatic Engineering and Geospatial Information Systems P.O. Box 62000-0200 City Square, Nairobi, Kenya Email: mercimwaniki@yahoo.com / mmwaniki@jkuat.ac.ke Mobile contact: +254721 630669
<b>Current Address</b>	Storkower Strasse 219, 10367 Berlin, Germany Mobile contact: +49157318089923

---

#### Personal Details

GENDER:	FEMALE
NATIONALITY:	KENYAN
RELIGION:	CHRISTIAN
LANGUAGES:	ENGLISH, SWAHILI



#### Broad Research Interests

- Remote Sensing, GIS and Environmental modeling
- Disaster, hazard management using GIS
- Climate Change

#### Research Activities

Current	PhD candidate Dissertation title: Modeling the impacts of predicted environmental change on the frequency and magnitude of rainfall induced landslides in Central Kenya
Past research studies	JKUAT Research Assistant <ul style="list-style-type: none"><li>- Rainfall Induced Landslide Probability Mapping for Central Province</li><li>- Determination of safe distances between shallow wells and soakpits within plots in Juja</li></ul>

## Education Background

April 2013 – September 2016 Otto-Friedrich-Universität Bamberg (Germany)	A PhD Doctoral student under the supervision of Prof. Dr. Matthias S. Möller
2009 – 2010 J.K.U.A.T (Kenya)	Msc in Geospatial Information Systems and Remote Sensing
2003 – 2008 J.K.U.A.T (Kenya)	Bachelor of Science in Geomatic Engineering and Geospatial information Science (First class Honours)

## Professional Experience

<b>2011 May - September 2012</b>	Working as an Assistant Lecturer in the department of GEGIS (JKUAT) <i>Main Responsibilities:</i> <ul style="list-style-type: none"> <li>- Teaching and administering Examinations of Undergraduate students</li> <li>- Supervising Bsc project research</li> <li>- Undertake research activities</li> </ul> <i>Other responsibilities:</i> <ul style="list-style-type: none"> <li>- Department of Geomatic Engineering &amp; Geospatial Information Systems (GEGIS) and School of Civil &amp; Environmental Geospatial science Website coordinator</li> </ul>
<b>2008 Dec - May 2011</b>	Working as a teaching assistant in the department of GEGIS (JKUAT) <i>Main Responsibilities:</i> <ul style="list-style-type: none"> <li>- Assist in the preparation of teaching materials, administer practicals and marking of Continuous Assessments Tests</li> <li>- Assist in Research activities</li> </ul>
<b>2010 Sep – Nov</b>	Undertaking traineeship at the Bavarian Office for Surveying and Geoinformation, where I worked in the following departments: Photogrammetry and Remote Sensing, Cadastre and Digital Terrain Model.
<b>2008 Aug - Nov 2008</b>	Practiced with Gath Consulting Engineers as a GIS technician. Main duties included data editing (GPS data), processing and map production in a GIS environment.

## List of Publications

Mwaniki, M.W. and Moeller, M.S. (2015). Knowledge based multi-source, time series classification: A case study of central region of Kenya. *Applied Geography*, 60, 58–68. DOI: 10.1016/j.apgeog.2015.03.005

Mwaniki, M.W., Moeller, M.S., and Schellmann, G. (2015). Application of Remote Sensing Technologies to Map the Structural Geology of Central Region of Kenya. *IEEE Journal of Selected*

*Topics Application Earth Observation Remote Sensing, PP, 1–13. DOI: 10.1109/JSTARS.2015.2395094*

Mwaniki, M.W., Moeller, M.S., and Schellmann, G. (2015). A comparison of Landsat 8 (OLI) and Landsat 7 (ETM+) in mapping geology and visualising lineaments: A case study of central region Kenya. *ISPRS - International Archives of the Photogrammetry, Remote Sensing and Spatial Information Sciences - XL-7/W3*, 897–903. DOI: 10.5194/isprsarchives-XL-7-W3-897-2015

Mwaniki, M.W., Moeller, M.S., and Schellmann, G. (2015). Landslide inventory using knowledge based multisources classification time series mapping: A case study of central region of Kenya. *GI Forum – Journal of Geographic Information Science 1*, 209–219. DOI: 10.13140/RG.2.1.1645.4241

Mwaniki, M.W., Agutu, N.O., Mbaka, J.G., Ngigi, T.G., and Waithaka, E.H. (2015). Landslide scar/soil erodibility mapping using Landsat TM/ETM+ bands 7 and 3 Normalised Difference Index: A case study of central region of Kenya. *Applied Geography. 64*, 108–120. DOI: 10.1016/j.apgeog.2015.09.009

Mwaniki, M.W. (2015). Effects of climate change variables on land-use land-cover changes in the central region of Kenya. In Dresden Nexus Conference 2015, (Dresden, Germany).

Mwaniki, M.W., Kuria, D.N., and Boitt, M.K. (2016). Image enhancements of Landsat 8 (OLI) and SAR data for Preliminary Landslide identification and mapping applied to the central region of Kenya. *Geomorphology*. Accepted

Mwaniki, M.W. (2016). Landslide susceptibility mapping for the central highlands of Kenya. *CATENA journal*, Accepted.

Mwaniki, M.W. (2016). Rainfall induced shallow landslide susceptibility mapping using combined hydrological stability model for the central region of Kenya. *Environmental Earth Sciences Journal*. under review

Mwaniki, M.W. (2016). Geology mapping and lineament visualization using image enhancement techniques: comparison of Landsat 8 (OLI) and Landsat 7 (ETM+). Researchgate resource